Earthquake rupture around stepovers in a brittle damage medium

Joseph Flores Cuba

Sorbonne Université

Ecole Doctorale GRNE - ED N° 398

Institut des Sciences de la Terre de Paris

Earthquake rupture around stepovers in a brittle damage medium

Par

Joseph M. FLORES CUBA

Thèse de doctorat de Géophysique

Dirigée par Laurent JOLIVET, Harsha S. BHAT and Marion Y. THOMAS

Présentée et soutenue publiquement le 18 Septembre 2023

devant un jury composé de :

Mme Cécile DOUBRE Physicienne (Université de Strasbourg)	Rapporteuse
M. Ioan IONESCU Professeur (Université Sorbonne Paris-Nord)	Rapporteur
Mme Nadaya CUBAS Maître de conférences (Sorbonne Université)	Examinatrice
M. Yann KLINGER Directeur de recherche (IPGP)	Président
Mme Marion Y. THOMAS Chargé de recherche (Sorbonne Université)	Co-encadrant de thèse
M. Harsha S. BHAT Chargé de recherche (ENS Paris)	Co-directeur de thèse
M. Laurent JOLIVET Professeur (Sorbonne Université)	Directeur de thèse

"Great things are done by a series of small things brought together."

Vincent van Gogh

Acknowledgements

A mis queridos padres, José Flores Torres y Gladys Cuba Raque, quiero expresar mi inmenso agradecimiento por brindarme su apoyo y aliento para alcanzar mis metas en las diferentes etapas de mi vida. Ahora que estoy a punto de completar uno de los objetivos más importantes, en cuanto a mi carrera, siento que son los que merecen los honores. Esto va dedicado a ustedes José y Gladys.

To my dear parents, Jose Flores Torres and Gladys Cuba Raque, I would like to express my immense gratitude for giving me their support and encouragement to achieve my goals at different stages of my life. Now that I am about to complete one of the most important of those goals, careerwise, and I feel like they are the ones that deserve the honours. This is dedicated to you Jose and Gladys.

I would also like to extend my gratitude to my sisters, Rosario and Yvonne, for their love, support and encouragement.

I am deeply indebted to my advisors, Dr. Laurent Jolivet, Dra. Marion Y. Thomas and Dr. Harsha S. Bhat, for their unwavering support and expert guidance throughout the entire duration of my research work. I thank their willingness to invest time in my project and bringing it to a full accomplishment. I thank them for addressing the challenges encountered during my research. Their deep insight to solve them has been crucial for me to learn and benefit from their expertise.

Furthermore, I would like to extend my heartfelt appreciation to the Doctoral School for their invaluable support and resources throughout my research journey. I greatly thank the members of my thesis committee for their support, encouragement, and thorough review of this research work.

Undertaking a PhD has been one of the most challenging experiences of my life. It has been a long journey that goes back to the moment when I took the decision to pursue a physics degree at San Marcos University in Lima, Peru. It was such a valuable decision that I will consider it pivotal in my life. I have gone through many challenges that prompted in me invaluable lessons and personal growth. Now, it is time to jump to the next step, to embrace new opportunities.

My sincere thanks also extend to my friends, professors, researchers, and colleagues with whom I had the privilege of interacting during my professional journey. This journey started at San Marcos University in Lima, Peru, and further continued at IGP and CISMID in Peru, GNS Science in Wellington, New Zealand, Lab Geoazur-UCA, ENS, IPGP, and ISTeP-SU in France. I am deeply grateful for their unwavering support. Their assistance and encouragement in various situations I encountered along the way will forever be etched in my memory. Each help and opportunity I received has played a significant role in my success in the Doctoral program.

I would like to express particular gratitude to Rafael Benites, my advisor in New Zealand during my Bachelor's degree in Physics. His mentorship over the years since I left San Marcos has been an integral part of my scientific foundation in this exciting field of applied physics. Likewise, my deepest appreciation goes to Jean-Paul Ampuero, my Master's advisor in France. Even after completing my master's

degree, Jean-Paul has continued to provide guidance and support, for which I am profoundly thankful. Their unwavering dedication to my academic and professional growth has served as a constant source of inspiration.

Last but not least, special thanks to my wife, Claudia Rubio. Claudia, you know well how challenging this journey has been at different times of my life. Thanks for sharing my ideals and goals, and for all the big and little efforts that you have made in order to cope with this -not always pleasant- period of our life.

The author acknowledges the full support of this work provided by the European Research Council grant PERSISMO (grant 865411) and the Agence National de la Recherche (ANR) IDEAS contract ANR-19-CE31-0004-01. The computations presented here were conducted on the MADARIAGA cluster, which is supported by the European Research Council grant PERSISMO.

Abstract

Strike-slip fault systems consist of a variety of geometrical complexities like branches, kinks and step-overs. Especially, the presence of a step-over structure can strongly determine the final size of the earthquake rupture. Thus understanding the dynamics of a rupture through such a complexity is crucial for seismic hazard assessment. A few studies have looked at this question within the context of a linear elastic medium. However, during an earthquake off-fault damage is generated, especially at the ends of a fault, which significantly changes the overall dynamics of a rupture. Using a micromechanical model, that accounts for crack growth and opening and its impact on the dynamic evolution of elastic moduli, we evaluate how dynamic off-fault damage can affect the capability of a rupture to navigate through step-over fault structures. We show that, sometimes, accounting for this energy sink, off-damage suppresses the ability of the rupture to jump from one fault to another. Whereas, in some specific cases, the dynamically created low-velocity zone may aid the rupture to jump on the secondary fault. Combing this numerical study with an analytical analysis we set the contours for a systematic approach useful for earthquake hazard assessments.

Keywords: Earthquake dynamics, stepover faults, fault damage zone, physical properties of fault zones.

Résumé

Les systèmes de failles décrochantes sont constitués d'une variété de complexités géométriques telles que des branchements de failles, des plis et des zones de relais. En particulier, la présence d'une structure de relais peut fortement déterminer la taille finale de la rupture sismique. Ainsi, comprendre la dynamique d'une rupture à travers une telle complexité est crucial pour l'évaluation des risques sismiques. Quelques études ont examiné cette question dans le contexte d'un milieu élastique linéaire. Cependant, lors d'un séisme, des zones d'endommagement sont générées, notamment aux extrémités d'une faille, ce qui modifie considérablement la dynamique globale d'une rupture. En utilisant un modèle micromécanique prenant en compte la croissance et l'ouverture de fissures et leur impact sur l'évolution dynamique des modules élastiques, nous évaluons comment l'endommagement dynamique peut affecter la capacité d'une rupture à se propager au travers des structures de relais. Nous montrons que, parfois, en tenant compte de cette dispersion de l'énergie sur les microstructures formées, les zones endommagées suppriment la capacité de la rupture à passer d'une faille à une autre. Mais, dans certains cas spécifiques, la zone de faible vitesse créée dynamiquement peut au contraire aider la rupture à sauter sur la deuxième faille. En combinant cette étude numérique avec une approche analytique, nous établissons les contours d'une approche systématique utile pour l'évaluation des risques sismiques.

Mots-clés: Dynamique des tremblements de terre, zone de relais, zones endommagées, propriétés physiques des zone de failles.

Contents

List of Figures

Chapter 1

Introduction

Strike-slip faults are constantly evolving and interacting, in long-term and short-term processes, with surrounding faults. The presence of a step-over structure due to the interaction of nearby strike-slip faults can impact on the earthquake rupture behavior (e.g. *Wesnousky*, 1988, 2006). Rupture propagation can jump across the step-over due to consequent stress readjustment that activates the sliding dynamics on a second fault. Understanding the capability of step-overs to allow rupture jumping is crucial for estimating the magnitude and rupture length of earthquakes, a challenge for seismic hazard assessment. To thoroughly analyse the role of stepover faults on earthquake rupture behavior, it is fundamental to take into account its complex fault zone structure. This ensures that we properly capture their essential characteristics and key features. Fault zone structure of stepovers is characterised not only by its geometrical features, but also by its intricate damage zone formed by fractures and micro-cracks heterogeneously distributed due to its mechanical, physical and hydrostatic properties. Thus, the key question is how the evolution of dynamic off-fault damage impacts on the role of stepovers in earthquake rupture dynamics. To approach this investigation, the following section provides the geological characterisation of fault zone structure of stepovers and the current understanding of their role on rupture dynamics.

1.1 Fault zone structure

The presence of deeply exhumed faults have allowed the geological observation of fault zone structure. One of the most studied exhumed faults is the rigth-lateral strike-slip Punchbowl fault. This fault with a total displacement of 44 km was active from 4 Ma to 1 Ma. Punchbowl fault is one of the exposed inactive traces of the San Andreas system (southern California) and is exhumed from up to 4 km depth (e.g. *Chester and Logan*, 1986; *Chester et al.*, 1993; *Schulz and Evans*, 2000). *Chester and Logan* (1986) presented a geological description of the Punchbowl Fault where the fault zone was characterized by three main units: The main gouge zone, the damaged host rock and the undeformed-host rock (see figure 1.1):

The gouge, or cataclasite layer, up to 1 m thick, represents the fault core where most of the fault displacement is localized and accommodated. The damaged host rock, displaying a thickness of about 100 m, bounds the gouge zone and is composed of a dense network of mesoscopic-scale fractures and microfractures. The length of these off-fault fractures is on the order of microscopic scale up to some greater than 15 m. *Wilson et al.* (2003) identified exponential decrease of the off-fault fracture density from the shear zone up to the underformed-host rock. Most of these fractures are oriented nearly perpendicular to the shear sense of the Punchbowl fault. The preferred orientation of the off-fault fractures suggested that the average direction of the maximum principal stress σ_1 is oriented nearly perpendicular to the fault strike. This damaged host rock forms a transition zone between the intense deformation in the gouge zone and the regional, background level of deformation in the host rock. Due to the complex structure of the damaged host rock, there is a significant variation of the mechanical, hydrological and physical properties as shear modulus, strength and permeability.

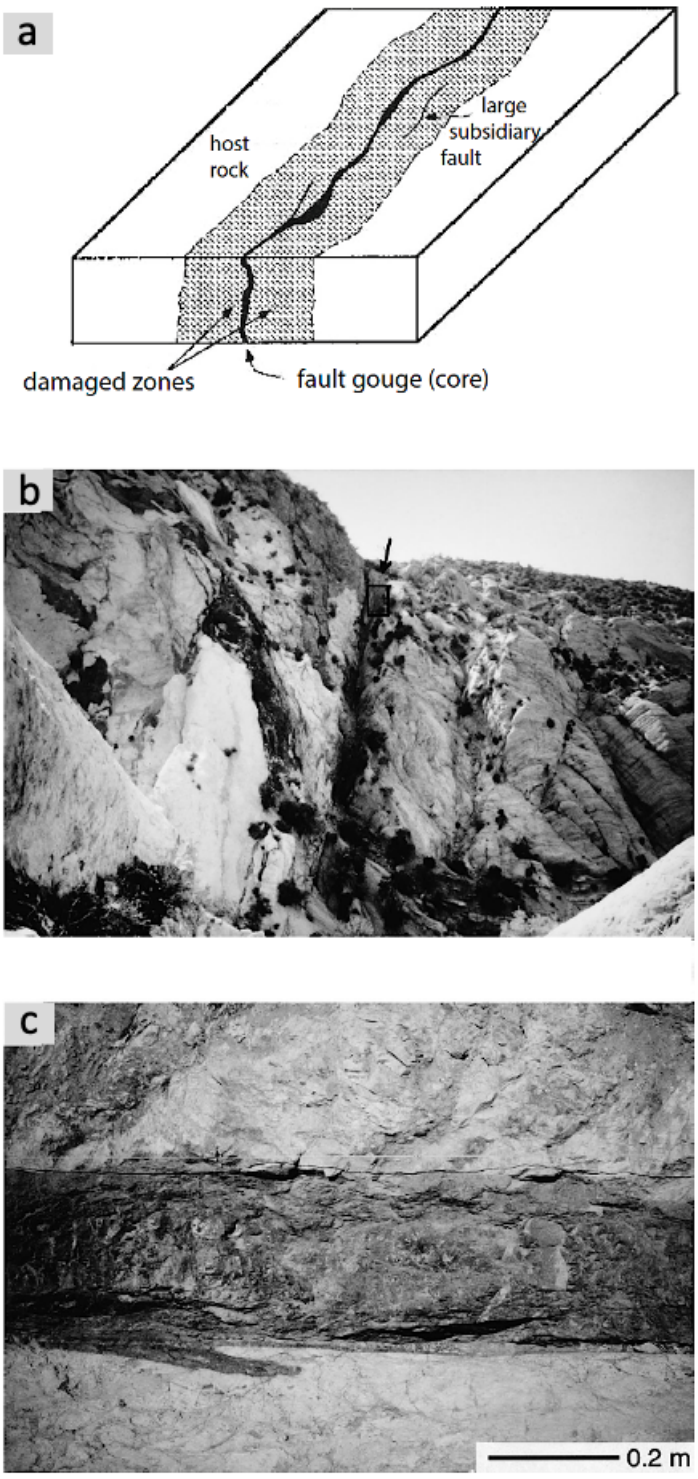

Figure 1.1: **Schematic and photographs of the Punchbowl fault zone and the gouge layer (*Chester and Logan*, 1986; *Yang*, 2015).** **(a)** Schematic of the Punchbowl fault zone. **(b)** View of the Punchbowl fault zone. White aplite of the San Gabriel basement complex (left) and Punchbowl formation sandstones (right) are juxtaposed along the gouge layer. **(c)** A portion of the slip-parallel exposure of the gouge layer. Basement at the top and sandstone at the bottom.

The description of the Punchbowl fault has been considered as a conceptual model for crustal fault zones. The width and the complexity of fault zone structure depend on the faulting mechanism (i.e. whether normal, strike-slip or reverse) and can be affected by the presence or absence of sedimentary layers as well as by other free surface effects. For instance, a case of complex structure of a low-angle normal fault gouge layer of Mykonos fault is presented in figure 1.2. Displacement is accommodated by a 1m-thick gouge and cataclasites, as well as by steeper normal faults in the hanging-wall rooting in the main fault core. The hanging-wall is made of sediments and the footwall of metabasites and a granite, introducing a strong asymmetry of mechanical properties on either sides of the fault plane.

Based on field observations of the left-lateral strike-slip Carboneras fault in southeastern Spain, *Faulkner et al.* (2003) proposed a more complex model of fault zone structure than the previous-mentioned model based on Punchbowl fault (see figure 1.3). The essential difference between the two models is that the Carboneras fault has a much wider and more complex shear zone with width $\sim$ 1 km. This slip zone is composed of two main geological elements that allow a combined style of fault deformation: (1) multiple strands of phyllosilicate-rich fault gouge (each of them with thickness up to 5m) that allow distributed deformation due to fault creeping and (2) dolomite blocks containing ultracataclasite layers formed by localized deformation due to recurrent earthquakes. This complex shear zone is surrounded by damaged host-rock on the order of 100 m in thickness.

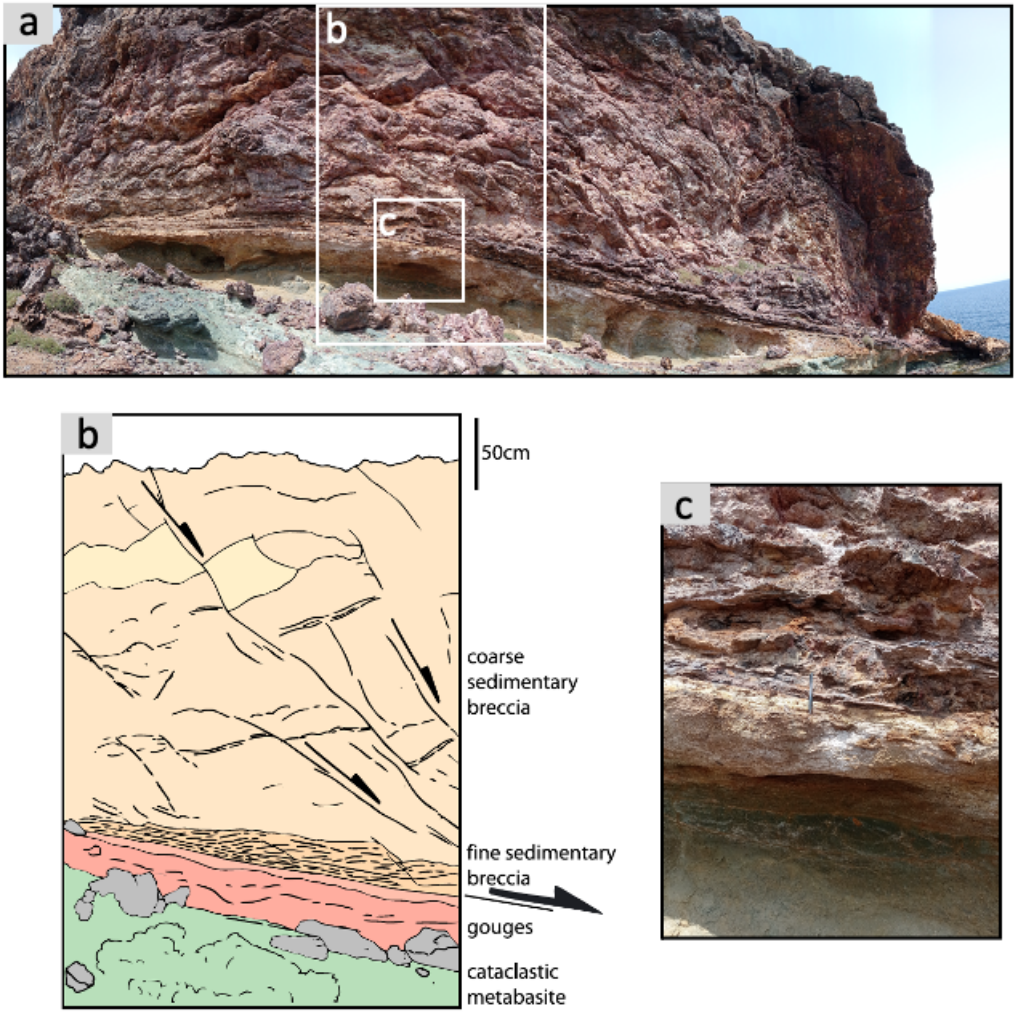

Figure 1.2: **Photographs and schematic of geological units of Mykonos detachment fault**. **(a)** Mykonos detachment fault gouge separating a sedimentary material (top) from the metabasites (bottom) at Cape Evros. **(b)** Schematic of geological units (*Lecomte et al.*, 2010). **(b)** Zoom on the Mykonos gouge layer.

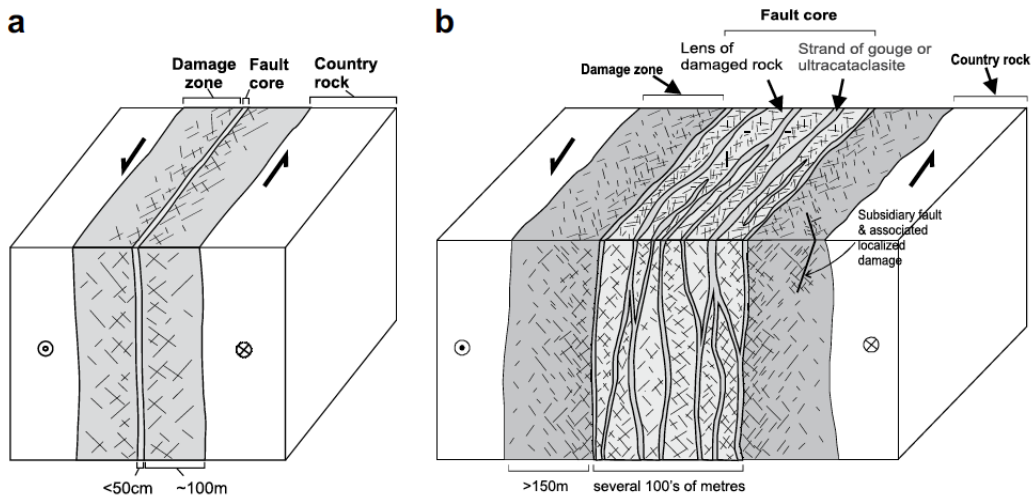

Figure 1.3: **Strike-slip fault zone models (***Mitchell and Faulkner***, 2009)** considering a (a) single fault core (e.g. *Chester and Logan*, 1986) and (b) multiple fault core (e.g. *Faulkner et al.*, 2003), surrounded by a damage zone.

Other examples of complex fault zone structure for strike-slip faults were studied by *Mitchell and Faulkner* (2009). They explored the damage zone structure of six strike-slip faults exhumed from 6 to 10 km depth in the Atacama fault zone, northern Chile. Total displacements of these faults range over 4 orders of magnitude ($\sim$ 0.12 - 5000 m). Damage zone is mainly characterized by a density of macro-and-micro fractures that decreases exponentially with perpendicular distance from the slip zone (see figure 1.4).

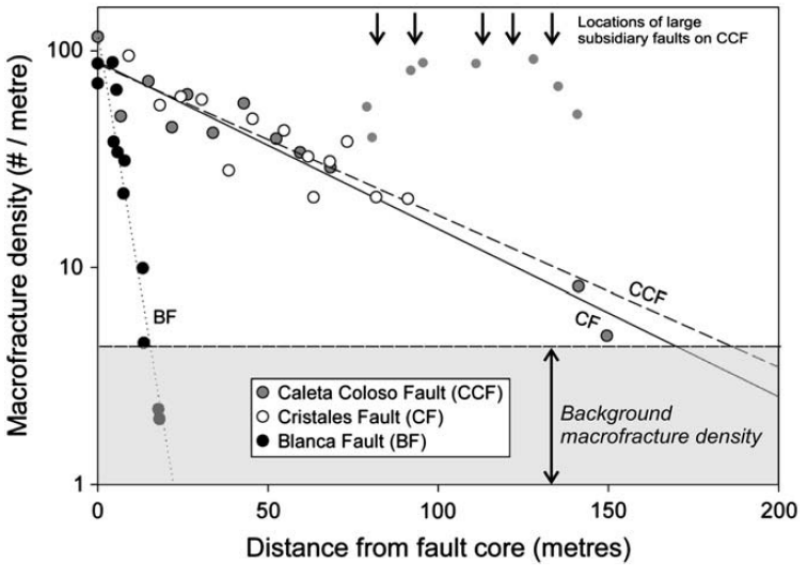

Figure 1.4: **Exponential decrease of off-fault fracture density from the fault core (*Mitchell and Faulkner*, 2009)**. Graph considers data from the three largest strike-slip faults of the Atacama fault zone (northern Chile) studied by *Mitchell and Faulkner* (2009).

Whether in a simple or complex fault zone, different lithologies on each side of the fault can give rise to a highly asymmetric fault zone structure. This is an important feature that makes the understanding and prediction of fluid flow difficult. *Wibberley and Shimamoto* (2003) studied the permeability behavior of the Median Tectonic Line (MTL) which is the longest arc-parallel strike-slip fault system in southwest Japan. The MTL has an asymmetric complex fault zone. The fault separates the Ryoke mylonite rock in the north from Sambagawa schists in the south. As a consequence, the permeability and damage zone structure are asymmetric. On the north side, the MTL presents a highly heterogeneous permeability structure influenced by mineralisation, re-fracturing of cemented fault rocks and degree of fracturing. On the south side, instead, one observes no significant damage zone but a progressive grain size reduction and compaction towards to the centre of the fault zone, which leads to a systematic decrease in permeability (see figure 1.5).

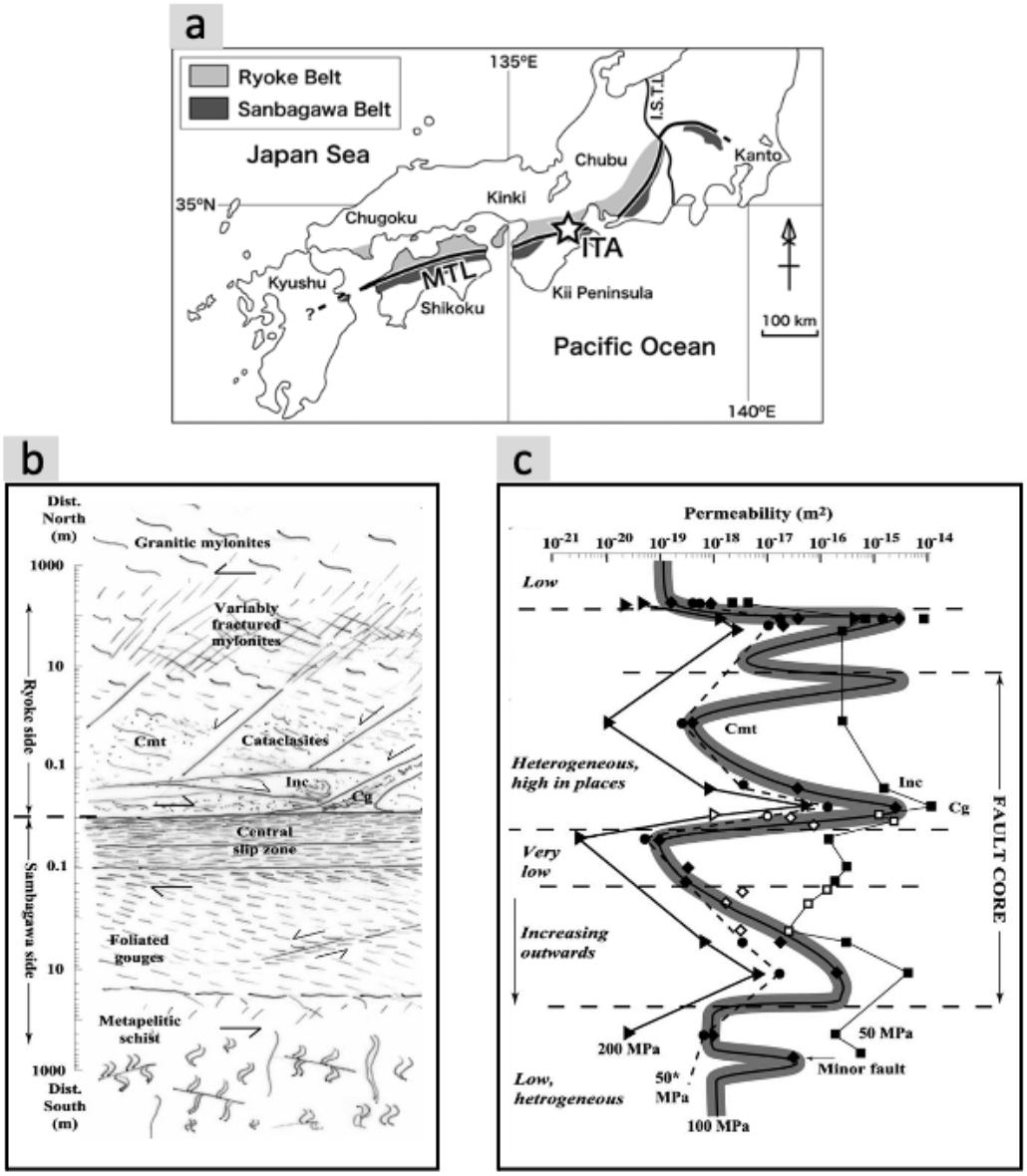

Figure 1.5: **Sketch summary of the main elements of permeability structure across The Median Tectonic Line (***Wibberley and Shimamoto***, 2003) (a)** Map location of The Median Tectonic Line (*Mori et al.*, 2015). **(b)** Summary of the fault zone structure. **(c)** Summary permeability data distribution for different confining pressures. Cmt and Inc denote cemented and incohesive foliated cataclasites, respectively, and Cg denotes crenulated gouge.

Fault zone structure is also modified by dynamic processes during earthquake ruptures. Laboratory experiments in Westerly granite (e.g. *Reches and Lockner*, 1994; *Moore and Lockner*, 1995) and numerical studies (e.g. *Yamashita*, 2000; *Dalguer et al.*, 2003; *Bhat et al.*, 2012; *Suzuki*, 2012) have shown that the growth of off-fault micro-cracks is larger at the tensional sides than at the compressional sides of the shear rupture propagation on a strike-slip fault. Furthermore, *Templeton and Rice* (2008) found that, prior to an earthquake, the angle Ψ between the maximum principal stress σ_1 and the fault strike can strongly modulate the asymmetry of the damage fault zone. *Templeton and Rice* (2008) conducted a series of rupture simulations in off-fault plastic medium varying the angle Ψ. It was observed that the lower the angle Ψ, the lower the evolution of damage at the tensional side of the fault (see figure 1.6).

Evolution of fault zone structure takes into account both (1) different lithology (or elastic properties) compared to the fault gouge and (2) the impact of earthquake ruptures (e.g. *Ben-Zion and Shi*, 2005a; *Thomas et al.*, 2017; *Thomas and Bhat*, 2018). One of the numerical experiments conducted by *Thomas et al.* (2017) corresponds to the evolution of damage fault zone due to an earthquake on a strike-slip fault that separates two different materials: granite and gabbro. They used a micromechanical model (*Bhat et al.*, 2012) that accounts for off-fault micro-crack growth and opening and its impact on the dynamic evolution of elastic moduli. It is observed that the asymmetry of the damage fault zone due to an earthquake is sensitive to the material contrast leading to a larger spatial extent of damage in the softer material. Previously mentioned observations let us observe how dynamic stresses during an earthquake can significantly impact on the fault zone structure.

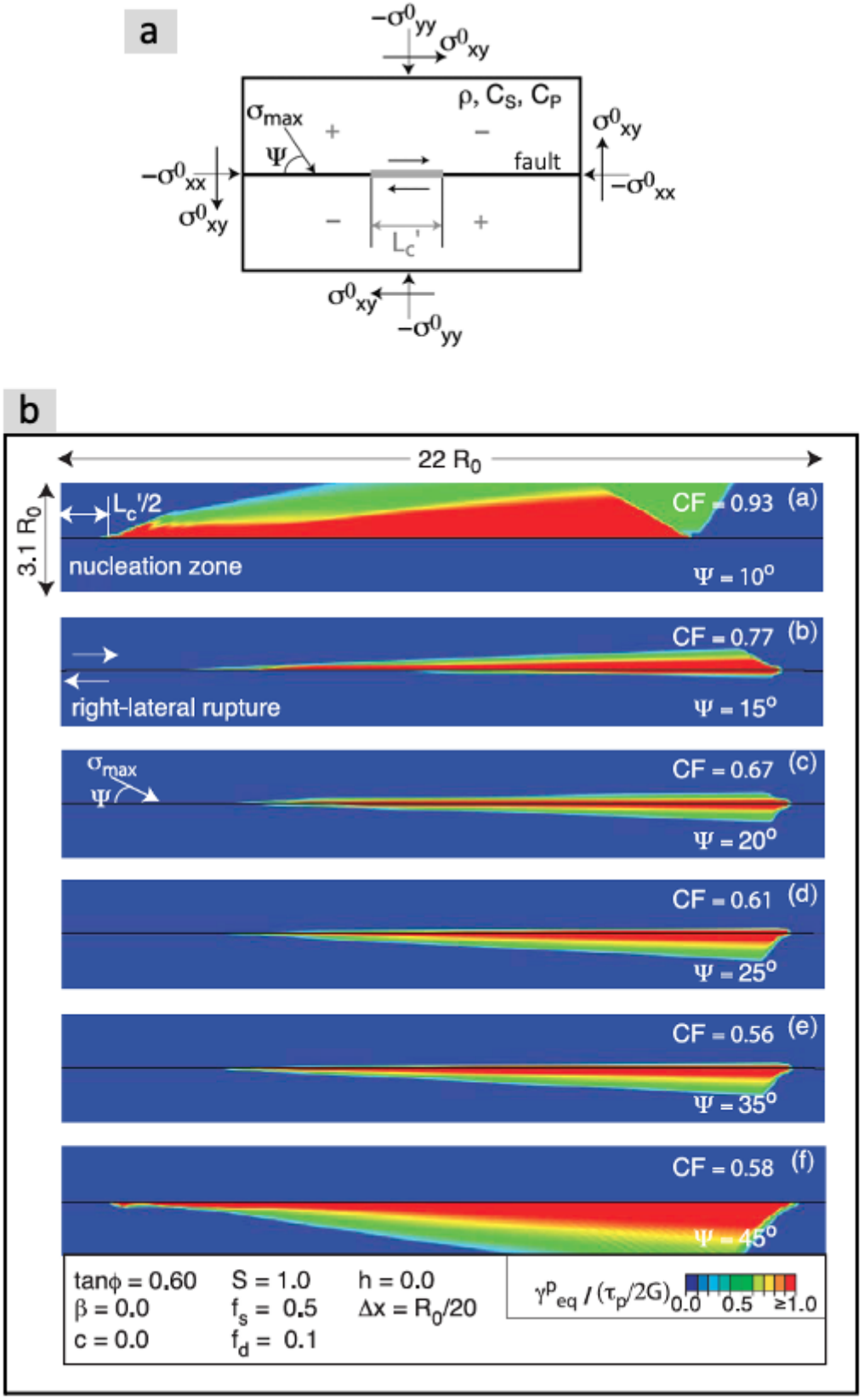

Figure 1.6: **Plastic strain during dynamic shear rupture in a strike-slip fault (*Templeton and Rice*, 2008). (a)** Model setup for 2D earthquake rupture simulations. **(b)** Results of plastic strain for angles Ψ range from 10^o to 45^o. Ψ is the initial angle between the maximum principal stress σ_{max} and the fault strike.

1.2 Step-over structure in strike-slip faults

Active strike-slip faults are not only constantly evolving but also interacting with surrounding faults leading to the formation of geometrical complexities like branches, kinks and step-overs. The presence of a step-over structure due to the interaction of nearby strike-slip faults can impact on the earthquake rupture behavior. Before discussing the impact in the rupture dynamics, we describe the structure of a step-over fault system. Our main concern on this description considers the following questions: what are the main elements of stepover faults?, how do stepover faults geologically evolve? and how is the fault zone structure of stepover faults characterised?

Stepover faults are characterized by two elements: (1) main strike-slip faults or bounding faults and (2) stepover region or transverse structure (see figure 1.7). Based on the system setting they can be extensional or compressional stepovers, as observed in figures 1.7 A and 1.7 B respectively. Stepover region develops internal fractures. The type of faulting of internal fractures depends on the stepover system (e.g. *Sibson*, 1986; *Gamond*, 1987; *Kim et al.*, 2004). For extensional systems, the transverse structure is mainly composed of open fractures and normal faults leading to crustal extension and consequent formation of pull-apart bassins (tensile bridges) (e.g. *Mann et al.*, 1983; *Peacock and Sanderson*, 1995b; *Dooley and McClay*, 1997). In compressional systems, the transverse structure predominantly develops reverse faults and shear fractures allowing topographic uplift (pressure bridges) (e.g. *Peacock and Sanderson*, 1995a; *Dooley et al.*, 1999; *McClay and Bonora*, 2001).

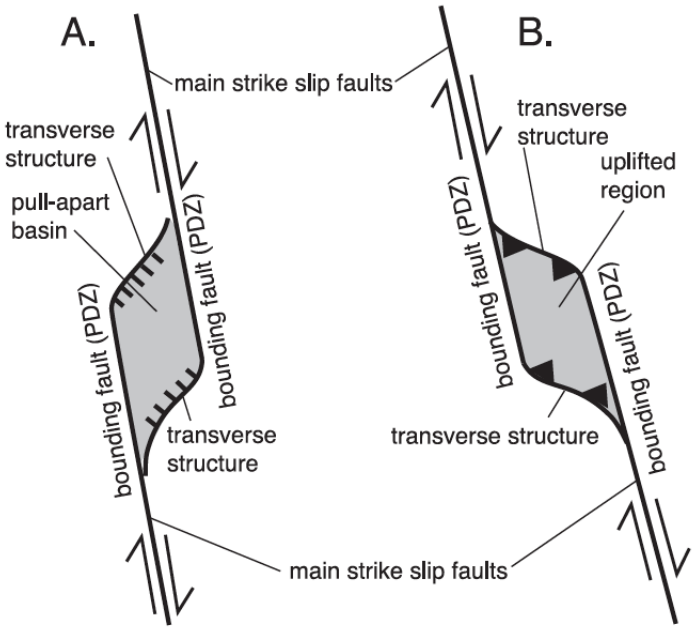

Figure 1.7: **Classification of stepover structures based on the system configuration of two right lateral (dextral) strike-slip faults (** *Wakabayashi et al.*, **2004)**. (A) Extensional and (B) Compressional stepover faults. Two main features characterise an step-over system : (1) main strike slip faults or bounding faults (also known as principal displacement zones, PDZs and (2) stepover region or transverse structure.

Analogue-models have been used as alternative to analyse long-term tectonic evolution of strike-slip stepover faults (e.g. *McClay*, 1990; *Jolivet et al.*, 1991; *Dooley and McClay*, 1997; *Dooley et al.*, 1999; *McClay and Bonora*, 2001; *Wu et al.*, 2009; *Dooley and Schreurs*, 2012; *Visage et al.*, 2022). *Jolivet et al.* (1991) used an analogue-model to analyse the extensional tectonic process that occurred in the Japan Sea area in Miocene time. They used a brittle-ductile model described by *Faugere and Brun* (1984) and *Vendeville et al.* (1987) and simulated an extensional stepover system considering two materials contained in a 70x50cm rectangular box. The upper brittle crust is simulated by Fontainebleau sand, whereas silicone simulates the ductile crust. This analogue-model allowed to analyse 3D fault zone features of the extensional process due to strike-slip motion. *Jolivet et al.* (1991) used this model showing extension and block rotations to discuss the opening of the Japan Sea as a pull-apart basin (see figures 1.8 and 1.9).

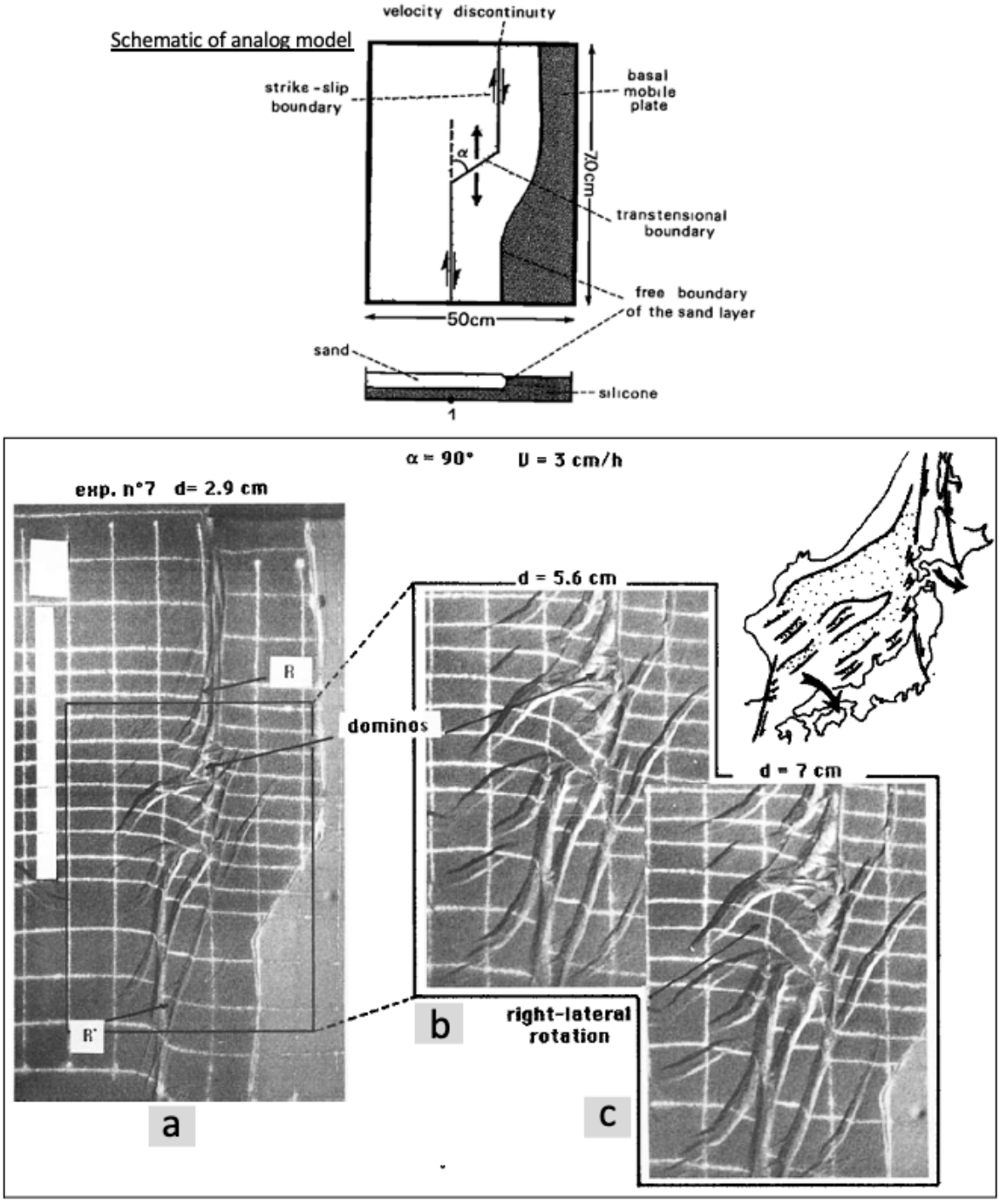

Figure 1.8: **Domino system and clockwise rotation in small-scale analog model of right-lateral extensional stepover system (*Jolivet et al.*, 1991).** This experiment is used to analyse the Japan Sea structure. $\alpha = 90^o$ and velocity $v = 3$ cm/h Stepover zone structure is shown after **(a)** 2.9 **(b)** 5.6 and **(c)** 7 cm of displacement. Progressive block rotation is allowed as the displacement increases. At the right side, an sketch of Japan Sea structure is shown as a reference for comparison.

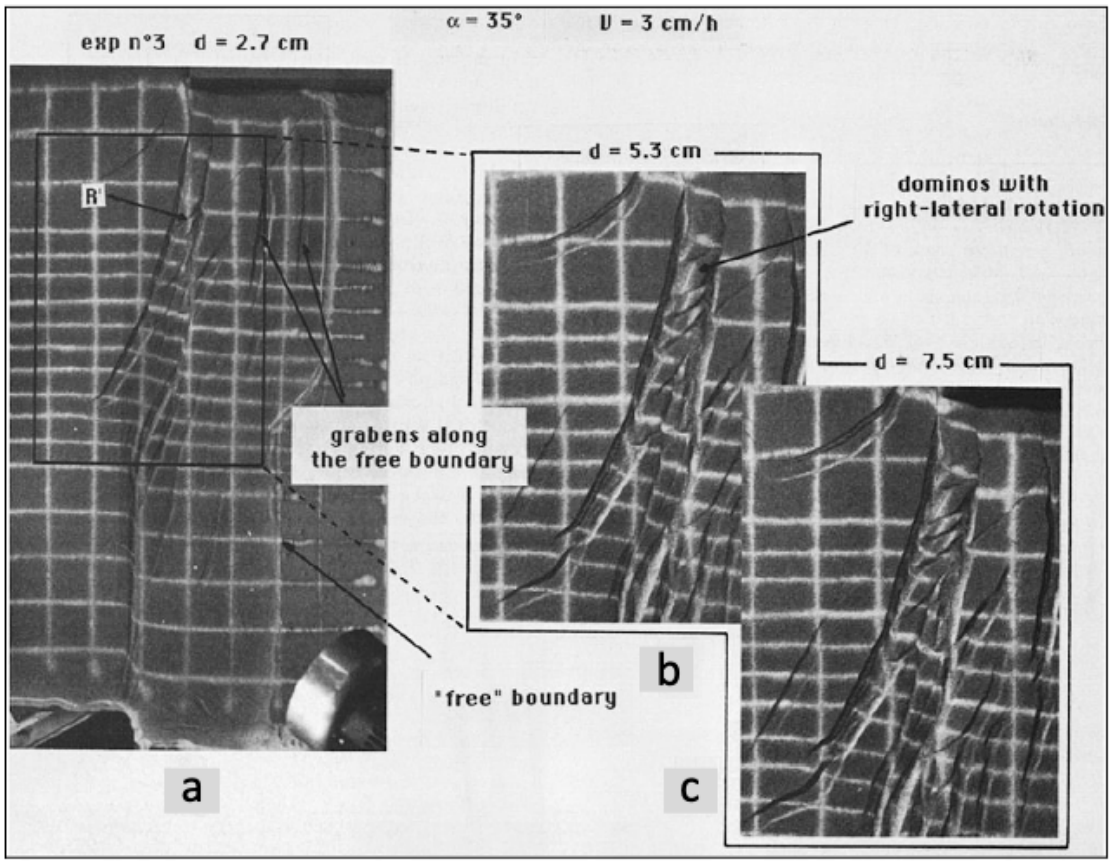

Figure 1.9: **Domino system and clockwise rotation in small-scale analog model of right-lateral extensional stepover system (*Jolivet et al.*, 1991).** This experiment is used to analyse the Japan Sea structure. $\alpha = 35^o$ and velocity $v = 3$ cm/h (see schematic of the model in figure 1.8). Stepover zone structure is shown after **(a)** 2.7 **(b)** 5.3 and **(c)** 7.5 cm of displacement. In (a), R Riedel shears of strike-slip system evolve to oblique normal faults. In (b) and (c), with increase of displacement, formation of R' left-lateral shears is allowed with block rotation like dominos.

Dooley et al. (1999) developed scaled analogue-models for extensional and compressional strike-slip faults in a 100x60x10cm deformation apparatus (see figure 1.10). Dry quartz sand is used to simulate the brittle material in the upper crust, whereas the base of the model is made of thin aluminium. The model is scaled so that 1 cm in the model is equivalent to 1 km in nature. Tectonic loading is driven by two worm screws deforming at a constant displacement rate of 4x10^{-3} $cm\ s^{-1}$. These analogue-models allowed to analyse the evolution of the stepover region for both the extensional and compressional stepover system. Once initial configuration of the fault system (extensional or compressional) is setup, the fault system deforma-

tion causes stress-field modifications around the stepover region. This overall stress evolution leads to formation of new structures (pull-apart basins similar to those observed by *Jolivet et al.* (1991) or pressure bridges), fractures and block rotation (see horizontal sections in figure 1.10).

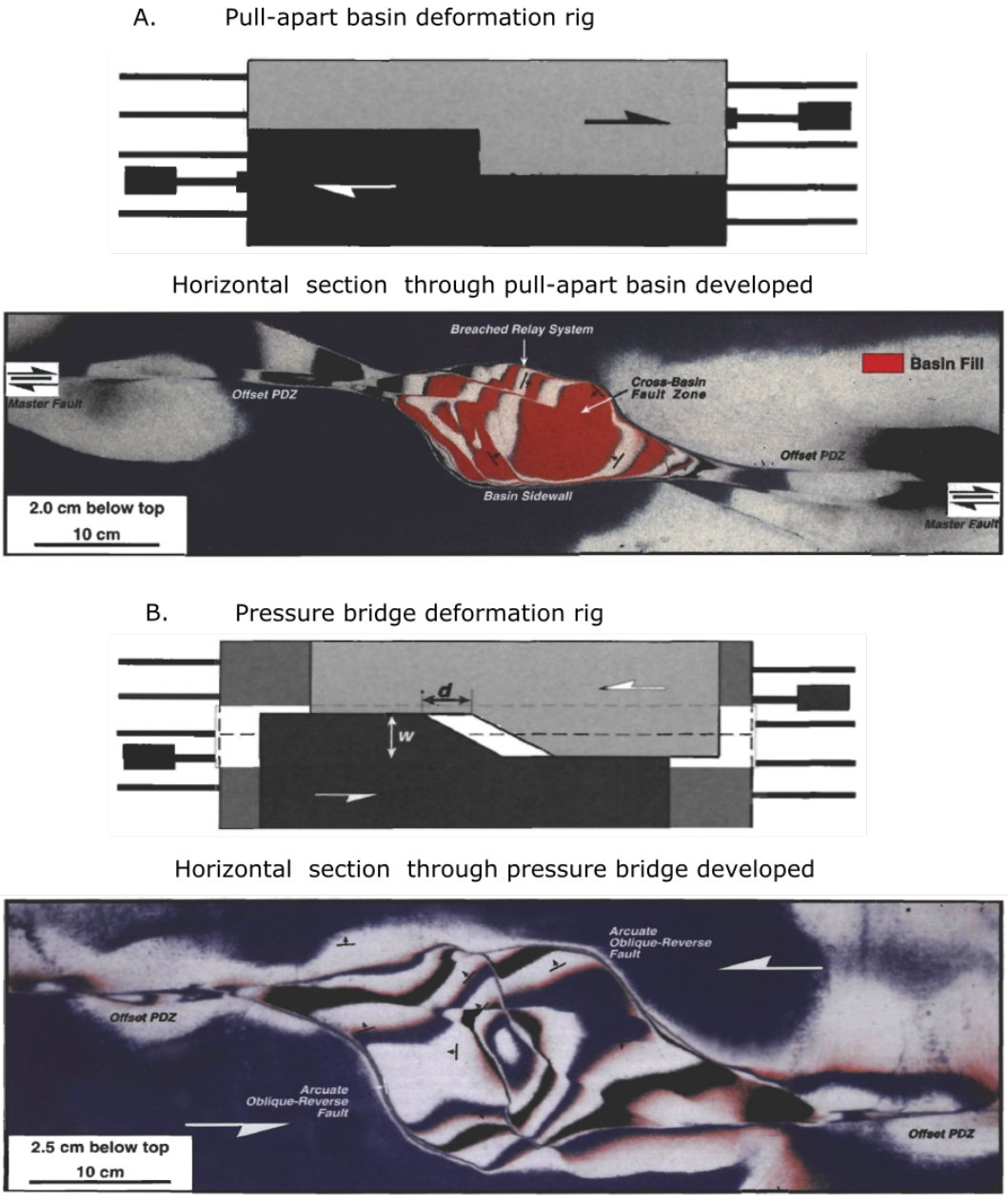

Figure 1.10: **Structures of stepover region for (A) extensional and (B) compressional stepover faults based on analogue-models by** *Dooley et al.* **(1999).** The pre-deformation stage of the deformation rig is presented at the top of each figure (A) and (B). The width of the stepover, w= 10 cm. The horizontal displacement, d= 10 cm. The model is scaled so that 1 cm in the model is equivalent to 1 km in nature.

The long-term spatial evolution of pull-apart basins and pressure bridges at stepover structures is modified as the bounding faults continue increasing their motion (e.g. *Aydin and Nur*, 1982, 1985). Some studies have analysed the geological evolution of extensional and compressional stepover systems (e.g. *Mann et al.*, 1983; *Wakabayashi*, 2007). *Wakabayashi et al.* (2004) proposed a geological description of different cases from San Andreas fault system and also outside of this region such as the Dead Sea pull-apart basin, Gulf of Paria pull-apart basin in the north of Venezuela, and cases from the Alpine fault and Hope fault of New Zealand. This study remarked that in some cases, as the strike-slip deformation increases, the stepover region migrates from its initial position towards the direction of strike-slip deformation (see figure 1.11), whereas in other cases, this transverse structure gradually grows as reported in analogue-models (for further discussion of the geological evolution of stepover faults in different active and ancient strike-slip systems, see *Mann* (2007) and references therein).

Fracture patterns in stepover faults are not only limited to the stepover region but are also developed along the off-fault region as discussed in section 1.1. Geological studies have described different features of the damage fault zone around small-and-large scale stepover faults (e.g. *Rispoli*, 1981; *Cruikshank et al.*, 1991; *Petit and M*, 1995; *Kim et al.*, 2000, 2003, 2004; *Ostermeijer et al.*, 2020). *Kim et al.* (2004) carried out a detailed characterisation of the overall damage zone of strike-slip stepover faults based on geological observations. This study pointed out three zones of damage, according to their location around the bounding faults: (1) tip damage zone, (2) wall damage zone and (3) linking or interacting damage zone (see figure 1.12). They remarked that fracture patterns vary around the bounding faults and mostly depend on their location, deformation mode, amount of slip, and type of stepover system (compressional or extensional). Nonetheless, other factors such as lithology, fluid pressure and temperature can also modify the damage zone structure. A schematic view of this heterogeneity in the damage distribution around strike-slip

stepover faults is shown in figure 1.13.

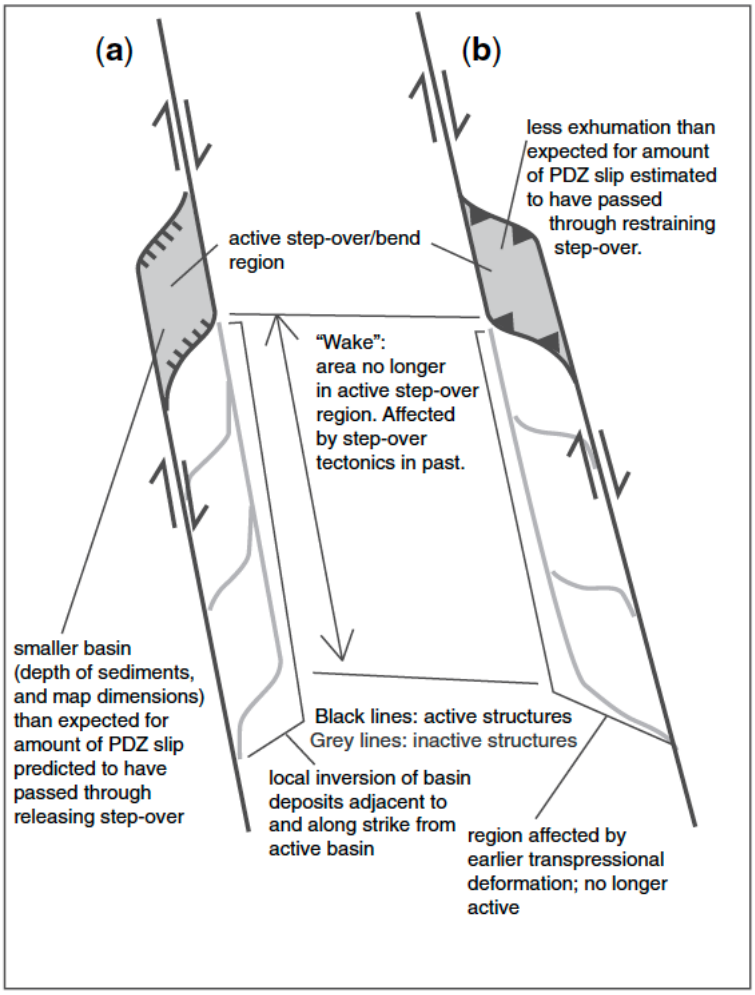

Figure 1.11: **Diagrams showing process of stepover migration (*Wakabayashi*, 2007)** for **(a)** extensional and **(b)** compressional stepover systems. PDZ: principal displacement zones.

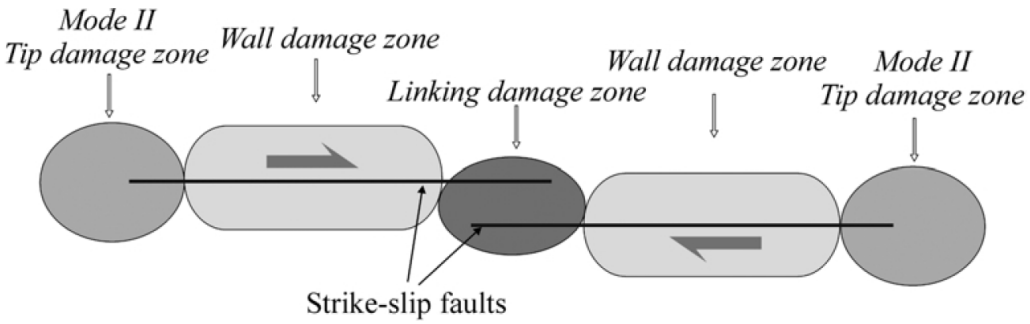

Figure 1.12: **Schematic of locations of damage zones around stepover faults defined by (*Kim et al.*, 2004).**

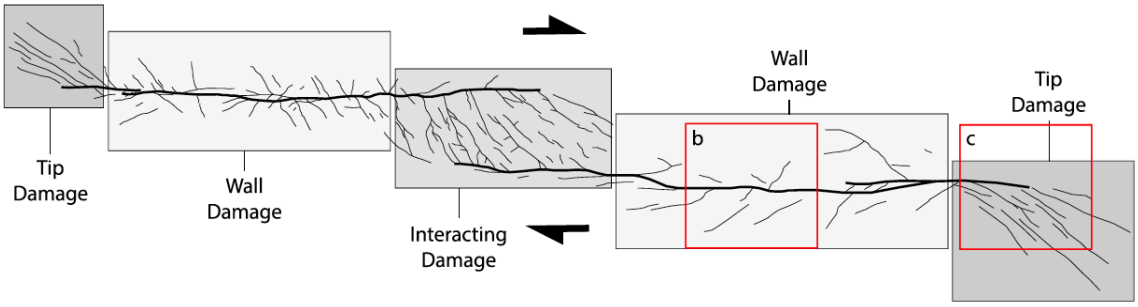

Figure 1.13: **Schematic of damage fault zone in stepover faults (***Ostermeijer et al.***, 2020).**

An important question that raises at this stage is how this complex off-fault fracture features of stepover faults dynamically evolve and interact with earthquake rupture propagation? A first-order exploration of this question have been approached in geological studies of earthquake ruptures in stepover faults (e.g. *Wesnousky*, 1988; *Lettis*, 2002; *Wesnousky*, 2006, 2008; *Biasi and Wesnousky*, 2016). These studies focused on whether or not a stepover structure allows an earthquake rupture to propagate (or jump) from one fault to the next one. *Wesnousky* (2006) analysed 22 continental strike-slip earthquakes of magnitude Mw between 6 and 7.9. Data collection considered earthquakes from different locations as Japan, Turkey and California. Rupture traces range between 10 and 420 km. According to observations, most stepover structures with a stepwidth greater than 3 o 4 km do not allow jumping rupture (see figure 1.14). It was suggested that this maximum stepwidth value is independent of the rupture length from the earthquake nucleation to the stepover structure. Instead, It was proposed that this threshold for jumping rupture is mostly linked to the stress state released by previous earthquakes and the complex geometrical volume at the stepover zone. This remark was supported by studies based on more extended data of earthquake-rupture observations (*Wesnousky*, 2008; *Biasi and Wesnousky*, 2016).

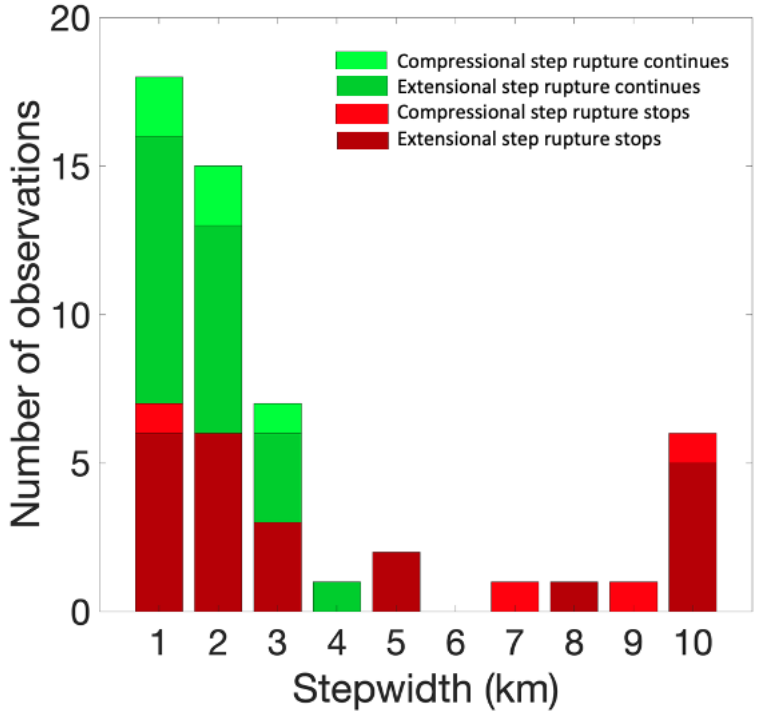

Figure 1.14: **Number of observations as a function of stepwidth size for stepover faults (*Wesnousky*, 2006).** This study analysed 22 surface rupture maps of historical strike-slip earthquakes.

1.3 Rupture dynamics on stepover faults

As we previously mentioned, earthquake rupture propagation can be modified by the complex stepover structure. In some cases, stepovers can act as a barrier arresting an earthquake, whereas in other cases, rupture propagation can jump across the stepover structure due to consequent stress readjustment that activates the sliding dynamics on the second fault (e.g. *Wesnousky*, 2006). Understanding the capability of stepovers to allow rupture jumping is fundamental for estimating the magnitude and rupture length of earthquakes, a challenge for seismic hazard assessment.

1.3.1 Analysis in physical modeling

Segall and Pollard (1980) carried out 2D static stress analysis of stepover faults in elastic medium. According to this study, once an earthquake is given on a first bounding fault, we have two scenarios: (1) in extensional stepover faults, the fault deformation reduces the normal stress around the stepover zone. This process reduces the frictional resistance at the second fault favoring rupture jumping (see figure 1.15), whereas (2) in compressional stepover faults, the deformation of the first fault develops increase of the normal stress around the stepover zone. This process increases the fault strength at the second fault inhibiting rupture jumping. Considering fluid-saturated crust, *Sibson* (1985, 1986) hypothesized that extensional system may also behave as a barrier or at least delay earthquake rupture jumping by the following reason. During earthquake propagation on the first fault, the stepover region generates extension fractures. The short duration of the earthquake does not allow the fluid pressure to re-equilibrate leading to the increase of the effective normal stress around the stepover zone. This process increases the fault strength on the secondary fault leading to arrest the earthquake.

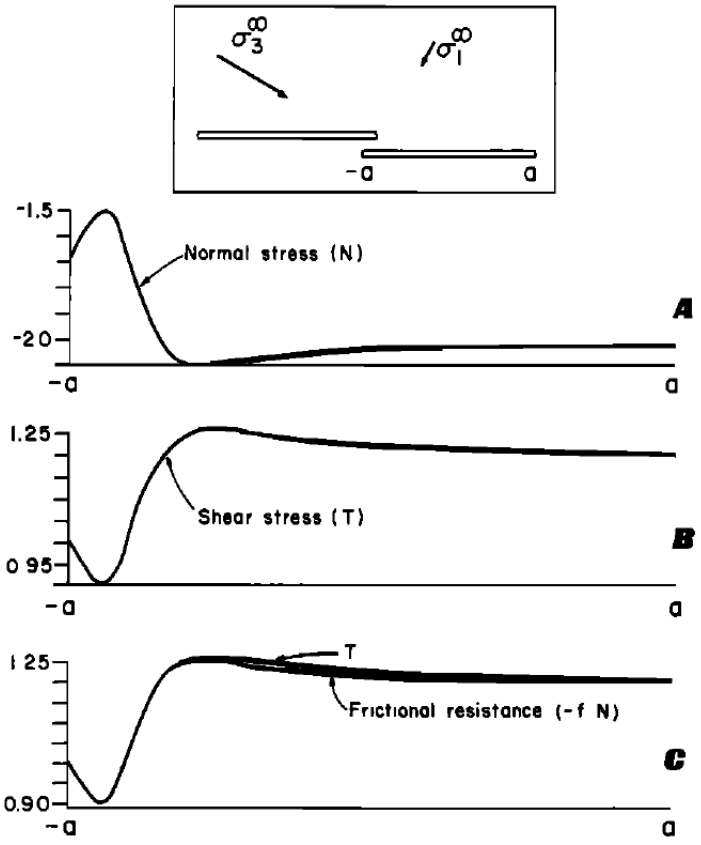

Figure 1.15: **2D static analysis of fault deformation on right-lateral strike-slip stepover faults (*Segall and Pollard*, 1980).** Setup of the stepover system is shown at the top of the figure. Considering dynamic sliding of the first bounding fault, results of (A) Normal stress, (B) Shear stress and (C) Frictional resistance on the second bounding fault are shown.

Some numerical studies on 2D dynamic earthquake rupture simulations have analysed the impact of an earthquake rupture in parallel strike-slip stepover faults within the context of a linear elastic medium (e.g. *Harris et al.*, 1991; *Harris and Day*, 1993, 1999). *Harris and Day* (1993) reported a potential threshold for jumping rupture on stepover faults. They conducted a set of 2D numerical simulations for stepover faults embedded on an elastic medium. By overstressing a determined region (nucleation patch) on a fault overcoming the frictional resistance, an earthquake is initiated at the first fault in the model (see figure 1.16). They evaluated the capability of rupture jumping to the second fault at different stepwidths (per-

pendicular distance between the faults) from 0.5 km to more than 5km. Simulations were set up for different values of S parameter [0.49, 1.65] and stress drop [3 MPa, 10 MPa]. The S parameter is the ratio between the shear stress increment required to failure and the static stress drop (*Andrews*, 1976; *Das and Aki*, 1977). Based on their numerical results, 5km-stepwidth was considered the limit at which stepover structures arrest earthquakes. Figure 1.16 shows the results between two cases (a) and (d) with different S values and stress drops. This maximum stepwidth value (5 km) that allows rupture jumping is compatible with previously mentioned geological observations reported by *Wesnousky* (2006). This remark lets us to pose the following question. Stepover with stepwidth larger than 5km acts as a barrier: is it a rule of thumb? The observation of earthquake rupture jumping at larger step width (e.g. *Xu et al.*, 2002) can help us to answer the previous question. This proves that the impact of stepovers has been underestimated and remains to be studied.

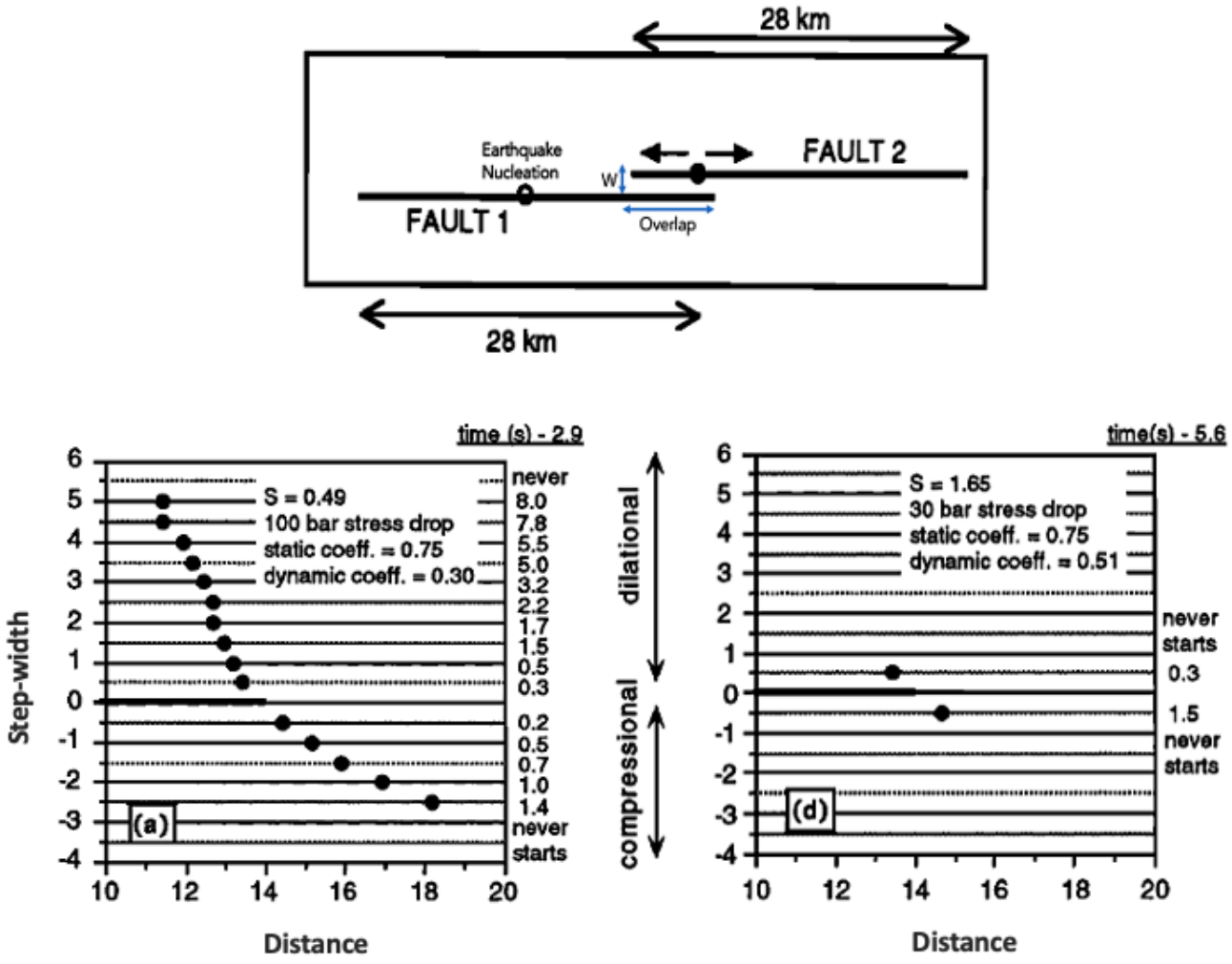

Figure 1.16: **Schematic for simulations of dynamic rupture in stepover faults (top figure) and summary results of triggering location at the second fault for two different cases of S parameter and stress drop values (bottom figures) (*Harris and Day*, 1993).** For bottom figures, x axis indicates the distance (in km) from the middle of the first fault, whereas y axis indicates the stepwidth (in km) (positive value for extensional stepover system, negative value for compressional stepover system).

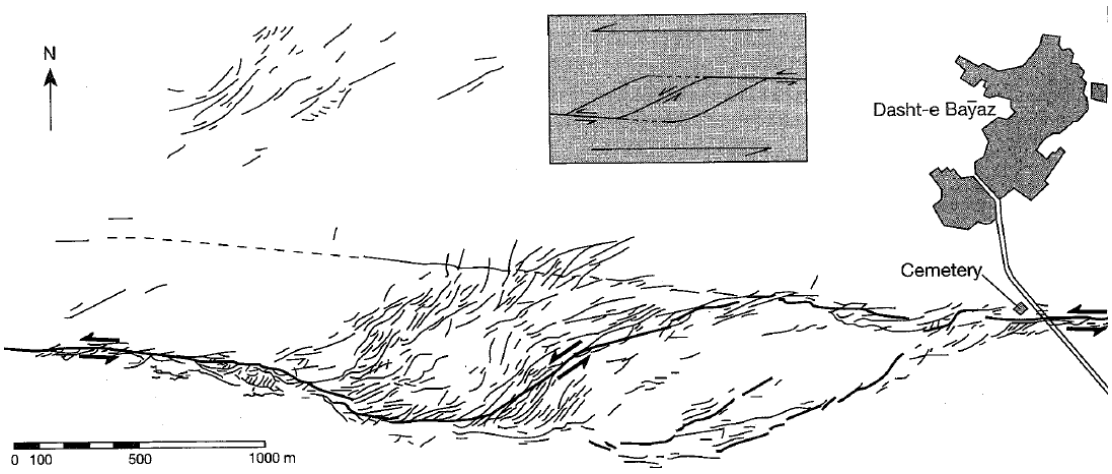

Figure 1.17: **Strike-slip step-over structure: surface rupture map, western section for Dasht-e-Bayaz earthquake (M_w 7.2), Iran (1968) (*Tchalenko and Ambraseys*, 1970).** Step-over faults are not only characterized by geometrical features but also by the presence of a density of secondary fractures (damage).

As we discussed in section 1.2, stepover structures are characterized not only by their geometrical features but also by the presence of a step-over damage zone (e.g. see figure 1.17). Hence, if we investigate the role of stepovers on earthquake rupture propagation, we need to capture and consider its complex structure. Some 2D numerical studies have analysed the effect of damage considering low velocity fault zones at the stepover zone (*Finzi and Langer*, 2012a,b) and off-fault elastoplastic material (*Liu and Duan*, 2014).

Based on 2D finite element method, *Finzi and Langer* (2012a) analyzed the effect of a constant, uniform damage level (rigidity reduction) within an extensional stepover zone (see figure 1.18). The geometrical setup of the model consisted on two parallel faults of lengths 60 and 40 km with the ratio between the overlap and stepwidth equals 1.5. Sliding on the faults is governed by a velocity-weakening friction law (e.g. *Cochard and Madariaga*, 1994). It was reported that significant level of damage (or low velocity fault zone) can promote rupture jumping at larger stepwidth than the previous-mentioned threshold value (5 km) suggested by *Harris and Day*

(1993) and *Wesnousky* (2006). It suggests that damage (contrast of rigidity) changes initial stress state at the second fault, favoring jumping rupture. These models can explore the effect of a prescribed damage zone (or low velocity fault zone) on the earthquake rupture but do not account for the dynamic inelastic deformation of the off-fault medium.

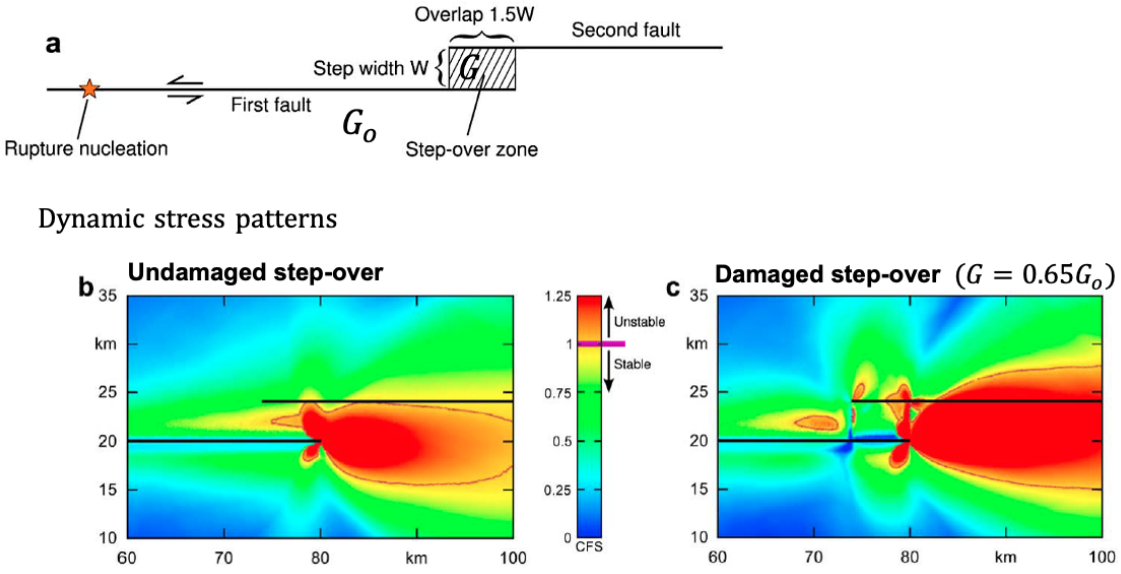

Figure 1.18: **Rupture jumping due to the presence of pre-existing damage zone at the stepover region (*Finzi and Langer*, 2012a).** (a) Setup of the strike-slip stepover fault system. Dynamic stress pattern for (b) undamaged and (c) damaged stepover.

Liu and Duan (2014) used 2D finite element method to conduct rupture simulations in extensional and compressional stepover faults. Sliding of the bounding faults is governed by a slip-weakening friction law (e.g. *Andrews*, 1976). This model includes dynamic generation of plastic deformation off the fault where the failure of the plastic material is governed by the Coulomb yielding criterion. They reported that in extensional stepover faults, damage (off-fault plastic deformation) allows jumping rupture at larger stepwidth than observed in elastic case. No significant effect of damage was reported in compressional stepover faults. Models with off-fault elastoplastic material can provide the plastic deformation but it does not account

for the dynamic changes of elastic moduli in the medium and therefore it can't fully evaluate the interaction of the off-fault damage and the seismic rupture.

The role of stepover on earthquake rupture propagation is not yet fully explored since important questions are still opened such as the following. Do we fully understand the complex off-fault fracture network observed in nature (e.g. see figure 1.17)? How does damage control the jumping rupture? Does damage always favor jumping rupture? Accounting for the energy sink, does off-fault damage suppress the rupture jumping ability? Can dynamic damage change drastically the expected strong ground motion scenario in stepover faults?

1.3.2 Analysis in seismic hazard assessment

Seismic hazards assessment (SHA) aims to estimate the most hazardous strong ground motion at a certain site due to an expected earthquake. To do this analysis, SHA deals with the uncertainties involved on future ground shaking. There are two types of analysis: Deterministic Seismic Hazard Analysis (DSHA) and Probabilistic Seismic Hazard Analysis (PSHA) (*Baker et al.*, 2021). DSHA considers that the worst strong ground motion is determined by estimating the maximum earthquake magnitude for a significant nearby fault. PSHA considers a probabilistic approach to estimate the worst strong ground motion during a certain period of time, i.e. earthquake recurrence time, taking into account all possible events with different factors such as distance from the source, earthquake magnitude and site effects.

It is evident that a crucial uncertainty considered in seismic hazards assessments, not only for deterministic but also for probabilistic approach, is the earthquake magnitude. The magnitude of an earthquake is strongly related to the rupture length as we can deduce from the seismic moment (M_o) equation:

$$M_o = \mu D A \tag{1.1}$$

where μ is the rigidity of the medium, D is fault slip and A is the earthquake rupture area, $A = W.L$ (W: seismogenic width, L: rupture length). Therefore, the longer the rupture length, the larger the earthquake magnitude and potentially larger slip. As we already discussed, faults can be surrounded by secondary faults, e.g. stepover faults, where rupture can jump to the surrounding fault (e.g. *Wesnousky*, 2006, 2008) changing dramatically the expected longest rupture length. Hence, rupture length, determined by the jumping rupture ability in stepover faults, is also an uncertainty that can substantially impact on the seismic hazard assessment modifying drastically both the deterministic and probabilistic earthquake-magnitude assessment.

Different seismic hazard studies have focused on estimating earthquake rupture magnitudes across step-over faults. For instance, *Armijo et al.* (2005) investigated the morphology of the most prominent submarine faults that hosted earthquakes at the north Marmara extensional stepover zone. This area is located between the right-lateral strike-slip Izmit and Ganos faults (see figure 1.19). This analysis aimed to estimate the magnitude of possible large future earthquakes through this stepover fault system based on the tectonic loading state. They deduced that only a potential fault segment located between the Cinarcik and Central basins would be able to host a large-magnitude earthquake (Mw 7.2).

As we already mentioned, geological and numerical studies have provided further insights on the impact of stepover faults in rupture earthquake propagation and potential estimation of large-earthquake magnitude. Indeed, *Wesnousky* (1988), *Harris and Day* (1993), and *Wesnousky* (2006) are among the most referenced studies in seismic hazard analysis for earthquake rupture propagation across step-over structures (e.g. *Scholz and Gupta*, 2000; *Field et al.*, 2009, 2014; *Mignan et al.*, 2015; *Liu et al.*, 2020; *Cheng et al.*, 2021). However, the current exploration of the role of stepovers in earthquake rupture is still not fully characterized which could drastically impact on seismic hazard assessment. Thus, this review of long-and-short

term analysis of stepover faults attempt to pave the way for further analysis that can help to improve multisegment seismic hazard assessment.

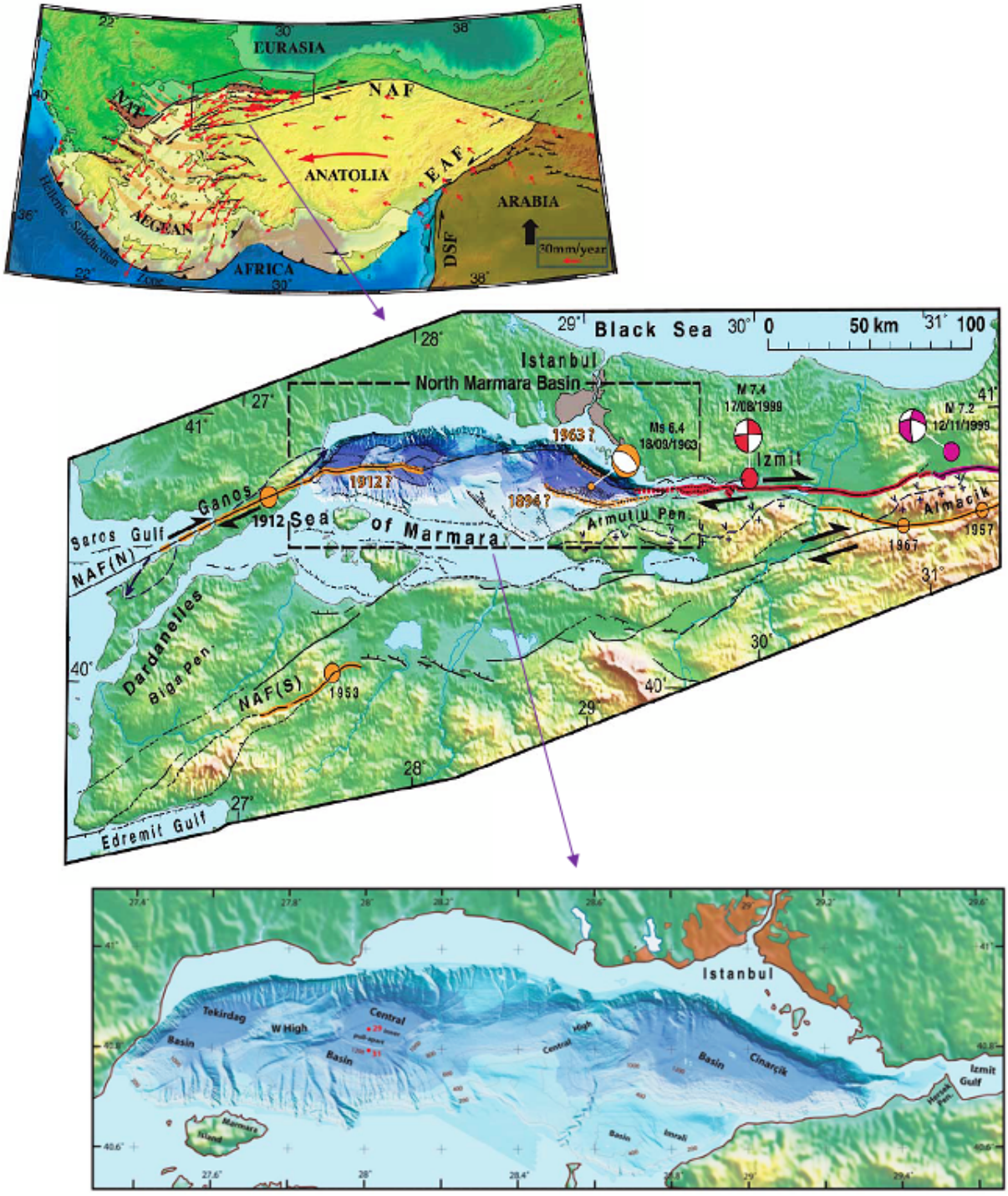

Figure 1.19: **The Sea of Marmara pull-apart basin (*Armijo et al.*, 2005).**

1.4 Problem statement

The objective of this thesis is to investigate the dynamics and radiation of ruptures around stepover faults. In particular, I consider the evolution of bulk properties around stepover faults during the coseismic deformation. One of the important questions I approach is how the evolution of dynamic off-fault damage at step-over faults impacts on the earthquake rupture behavior. This numerical analysis will be developed in a 2D earthquake dynamic rupture model (*Thomas et al.*, 2017) that takes into account the coseismic evolution of elastic properties around the step-over faults. I also combine this numerical study with an analytical analysis so that I can set the contours for a systematic approach useful for earthquake hazard assessments.

Chapter 2

Methodology: Model Description

This chapter describes the model applied to conduct dynamic earthquakes rupture simulations in strike-slip step-over faults, in either elastic and dynamic-damage mediums. We used a 2D spectral element code SEM2DPACK implemented with a dynamic damage model (*Ampuero*, 2012; *Thomas et al.*, 2017). The spectral element approach solves the earthquake rupture dynamics and the elastic wave equation on a 2D spatially discretised domain that contains the fault zone of the step-over faults. *Thomas et al.* (2017) implemented in the SEM2DPACK code a dynamic damage model based on a micromechanical approach developed by *Ashby and Sammis* (1990) and *Bhat et al.* (2012) to allow for off-fault damage evolution during the coseismic deformation. Through this chapter, we describe the friction law, the rheology (micromechanical damage model), the initial stress field and the geometrical features.

2.1 Friction law

The frictional strength $\mathcal{T}$ on the fault can be expressed as a function of the friction coefficient f and the normal stress σ_n (stress negative in compression),

$$\mathcal{T} = f[-\sigma_n] \tag{2.1}$$

In our models, the evolution of the friction coefficient f is governed by the slip-weakening friction law (e.g. *Ida*, 1972; *Palmer and Rice*, 1973; *Andrews*, 1976) where f is a function of the cumulative slip δ at the rupture tip (see figure 2.1). Slip starts when the shear stress τ reaches the static frictional strength $\mathcal{T}_s$,

$$\tau = \mathcal{T}_s \equiv f_s[-\sigma_n] \tag{2.2}$$

where f_s is the static friction coefficient. Then the friction coefficient is linearly characterised by a drop to its dynamic value f_d over a characteristic slip δ_c. This friction drop represents the slip-weakening effect on the friction coefficient. After this drop, dynamic friction coefficient f_d governs the fault sliding.

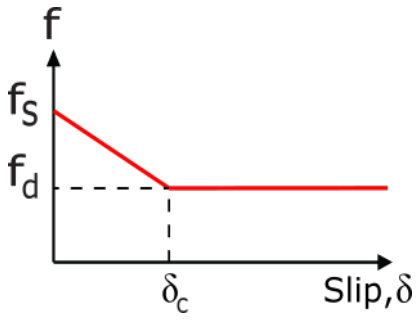

Figure 2.1: **Slip-weakening friction law**. Friction evolution as a function of the cumulative slip, $f(\delta)$. δ_c is the characteristic slip.

The region behind the rupture tip where shear stress drops from its static value to its dynamic value is called the process zone. The process zone size varies dynamically

during the dynamic rupture process (e.g. *Thomas et al.*, 2017). The static value of the process zone size R_0 for in-plane rupture is defined by (*Day et al.*, 2005):

$$R_0 = \frac{9\pi\delta_c\mu}{32(1-\nu)(f_s - f_d)(-\sigma_n^0)} \tag{2.3}$$

where μ is shear modulus, ν is Poisson ratio and σ_n^0 is initial normal stress.

An earthquake, i.e. a dynamic instability, occurs on a fault when the slipping length is greater than the nucleation length L_{nuc}, defined as (e.g. *Kame et al.*, 2003):

$$L_{nuc} = \frac{64}{9\pi^2}\left(\frac{\sigma_n^0(f_d - f_s)}{\tau^0 + \sigma_n^0 f_d}\right)^2 R_0 \tag{2.4}$$

where τ^0 is the initial shear stress.

2.2 Rheology - Micromechanical damage model

This section initially gives a brief summary on how the damage zone is represented in numerical models that use different frameworks such as elastic low velocity fault zones, plasticity and damage model. Then, we describe the micromechanical damage model (*Bhat et al.*, 2012; *Thomas and Bhat*, 2018) applied in this thesis.

2.2.1 Review of previous models for damage zone

2.2.1.a Elastic Low Velocity Fault Zones (LVFZ)

The LVFZ is a linear elastic isotropic material representing the damage zone that surrounds the fault (see figure 2.2) (e.g., *Huang and Ampuero*, 2011; *Huang et al.*, 2014). LVFZ is defined by two properties that are assumed fixed and uniform in the model: its thickness and its damage level. The latter is defined as the relative contrast of the wave velocity between damaged and country rock, and can also be expressed in terms of the shear moduli contrast. This model can explore the effect of the LVFZ on the seismic rupture (e.g. speed and directivity) and final slip (e.g., *Cappa et al.*, 2014) but it does not consider dynamic inelastic deformation of the off-fault medium.

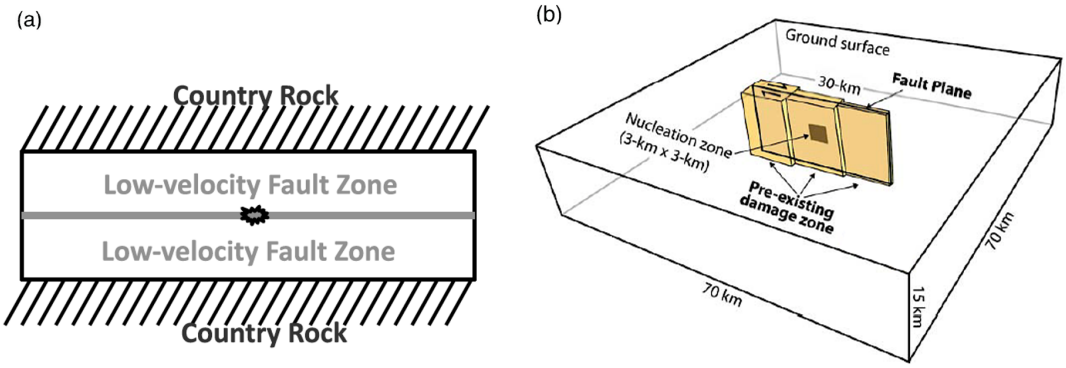

Figure 2.2: **2D and 3D Models of fault zone. (a)** Model setup of 2-D dynamic rupture on a fault bisecting a low-velocity fault zone *Huang and Ampuero* (2011). **(b)** Model setup of a 3-D dynamic rupture on a fault plane surrounded by a triangular low velocity fault zone (*Cappa et al.*, 2014).

2.2.1.b Plasticity

The off-fault material is considered as an elastic-plastic solid (e.g., *Andrews*, 2005). Failure criteria have been used to model the spontaneous dynamic plastic deformation, i.e. off-fault damage, during the dynamic rupture propagation. For instance, *Andrews* (2005) performed 2D calculations of dynamic rupture on a fault plane in a medium that yields plastically off the fault when the stress state reaches a Coulomb yield condition. This study allowed to analyse how the energy loss in the off-fault medium affects the rupture velocity. *Ben-Zion and Shi* (2005b) studied the response of a 2D model with in-plane ruptures on a fault between different materials. This model includes dynamic generation of plastic strain off the fault where the failure of the plastic material is governed by the Coulomb yielding criterion. Numerical results showed that when the fault is a bimaterial interface, plastic strain is generated only on the stiffer side of the fault, in the tensional quadrant of the radiated field. On the other hand, Drucker-Prager yield criterion has been also applied to model the off-fault plastic deformation during coseismic sliding (e.g., *Templeton and Rice* (2008), *Kaneko and Fialko* (2011)).

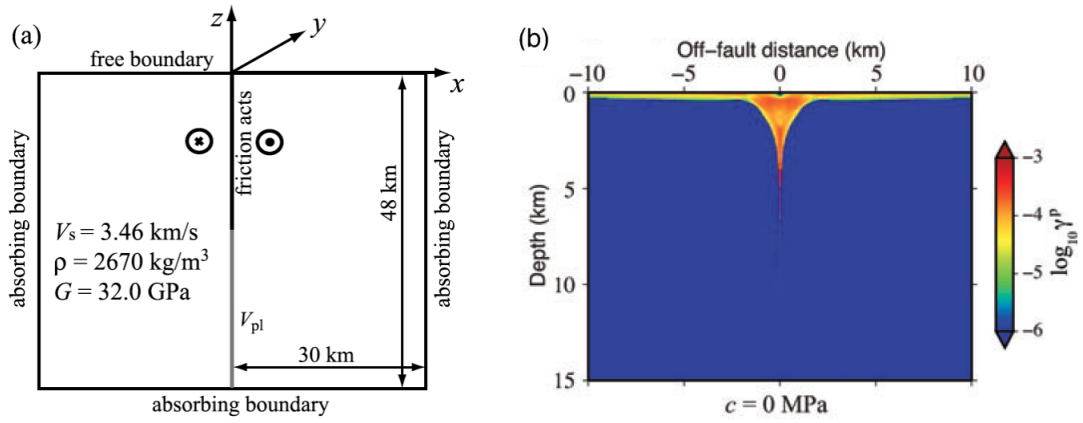

Figure 2.3: **2D Model of fault zone and distribution of the accumulated plastic strain (*Kaneko and Fialko*, 2011). (a)** Model setup of 2-D dynamic rupture on a vertical strike-slip fault embedded in an elastic-plastic medium. **(b)** Distribution of the accumulated plastic strain γ^p at the end of an event with no cohesion and internal rock friction 0.98.

Elastoplastic constitutive theory

Following the model formulation of stress-strain relation presented by *Erickson et al.* (2017). Letting the total strain be $\varepsilon_{ij} = \varepsilon^e_{ij} + \varepsilon^p_{ij}$, where ε^e_{ij} and ε^p_{ij} are the elastic and plastic strain, respectively; the elastoplastic constitutive law can be generally expressed as follows

$$\sigma_{ij} = C_{ijkl}(\varepsilon_{kl} - \varepsilon^p_{kl}) \tag{2.5}$$

where σ_{ij} is the stress tensor and C_{ijkl} is the fourth order elasticity tensor. Plastic yielding criteria determine when the material has undergone plastic yielding, i.e. $\varepsilon^p_{ij} > 0$. The Drucker-Prager yielding criterion has the form:

$$F_{DP}(\sigma, \gamma^p) = \bar{\tau} - (\sigma_Y + h\gamma^p) \tag{2.6}$$

where h is the plastic hardening modulus and γ^p is the plastic hardening paramater

(equivalent to plastic strain). $\bar{\tau}$ is the second invariant of the deviatoric stress and σ_Y is the yield stress.

$$\begin{aligned} s_{ij} &= \sigma_{ij} - \sigma_{kk}\delta_{ij}/3 \\ \bar{\tau} &= \sqrt{\frac{1}{2}s_{ij}s_{ij}} \\ \sigma_Y &= -(\sigma_{kk}/3)\sin\phi + c\cos\phi \end{aligned} \tag{2.7}$$

where c is the cohesion and ϕ is the internal friction angle. δ_{ij} is the Kronecker delta.

The yielding condition states that when $F_{DP} \geq 0$, there is plastic deformation; otherwise, the deformation of the medium is elastic. Plastic strain can be obtained from the flow rule that expresses the plastic strain rate,

$$\dot{\varepsilon}^p_{ij} = \lambda \frac{\partial F_{DP}}{\partial \sigma_{ij}} \tag{2.8}$$

where λ is the deviatoric plastic strain rate.

Overall, This damage model can provide the plastic deformation but it does not account for dynamic changes of elastic moduli in the medium and therefore it can not fully evaluate the interaction of the off-fault damage and the seismic rupture.

2.2.1.c Damage model

Using an energy-based approach that considers a damage evolution law allows to develop a new constitutive law. (see figure 2.4, comparison with plasticity).

Two damage models have been reported in the literature, where the off-fault damage is initially represented by a density of micro-cracks (see figure 2.5). In the

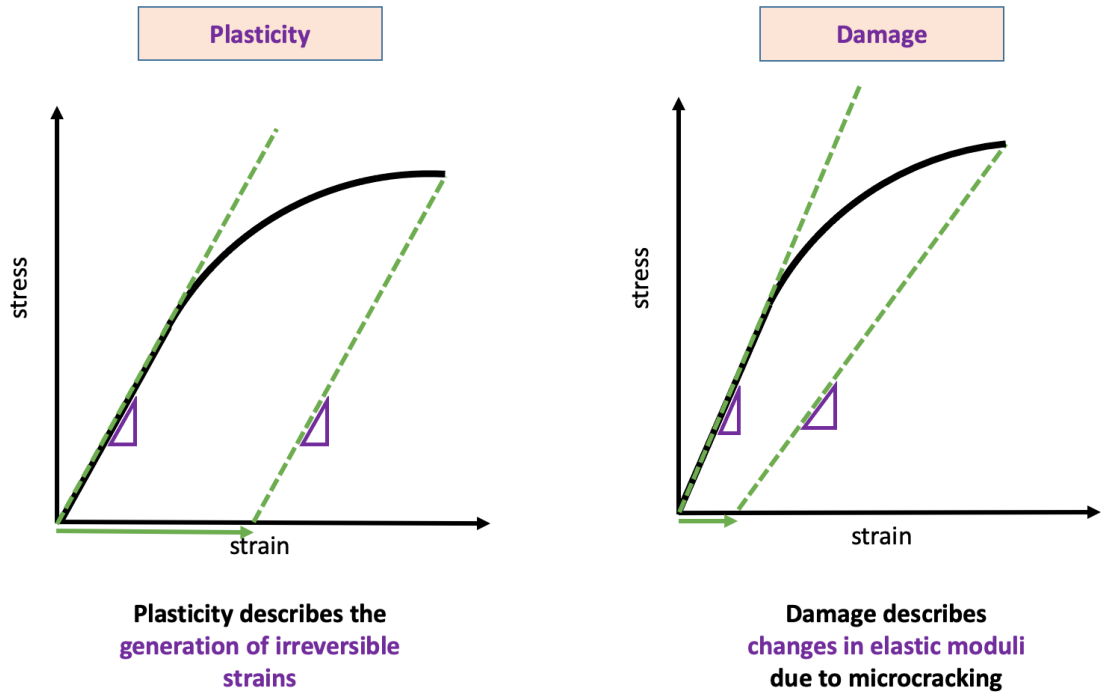

Figure 2.4: **Scheme comparing the stress-strain response for plasticity and damage.**

following part, we discuss the damage model proposed by *Lyakhovsky et al.* (1997b). Then, in a next section, we discuss the micromechanical damage model, applied in this thesis, proposed by *Ashby and Sammis* (1990), extended by *Bhat et al.* (2012).

The model proposed by *Lyakhovsky et al.* (1997b) considers a medium with a low density of non-interacting cracks allowed to accommodate small deformation (see figure 2.5a). The set of cracks have same initial length and are oriented perpendicular to the orientation of the maximum compressive stress σ_1. Damage in the medium is interpreted as the non-dimensional measure of crack density, defined by the scalar α ($0 < \alpha < 1$). Non-linear elastic deformation is generated by the opening and closing of the cracks. This deformation is taking into account through an energy balance to get a non-linear constitutive law. The energy-based approach to develop the non-linear constitutive response of the medium considers the change of the elastic

moduli λ, μ, γ due to the evolution of damage α. λ and μ are the Lame constants. The additional modulus, γ, includes the effects of microcrack opening and closure (*Lyakhovsky et al.*, 1997a).

The rheological constitutive law is expressed by

$$\sigma_{ij} = \left(\lambda - \gamma\frac{\sqrt{I_2}}{I_1}\right) I_1\delta_{ij} + \left(2\mu - \gamma\frac{I_1}{\sqrt{I_2}}\right)\varepsilon_{ij} \tag{2.9}$$

where $I_1 = \varepsilon_{kk}$ and $I_2 = \varepsilon_{ij}\varepsilon_{ij}$ are two independent invariants of the strain tensor ε_{ij}. δ_{ij} is the Kronecker delta. The elastic moduli λ, μ, γ have the following explicit connection to the scalar damage, α:

$$\begin{aligned} \lambda &= \lambda_0 \\ \mu &= \mu_0 + \xi_0\gamma_r\alpha \\ \gamma &= \gamma_r\alpha \end{aligned} \tag{2.10}$$

where λ_0 and μ_0 are the Lamé parameters of the intact medium, γ_r is a scaling factor that maps damage into elastic moduli and defines the maximum damage level α at 1. ξ_0 is a material parameter linked to the start of damage generation and can be related to the internal friction angle ϕ:

$$\xi_0 = \frac{-\sqrt{2}}{\sqrt{1 + (\lambda_0/\mu_0 + 1)^2\sin^2\phi}} \tag{2.11}$$

Damage evolution law has the form:

$$\frac{d\alpha}{dt} = -C\frac{\partial F}{\partial\alpha} \tag{2.12}$$

where F is the free energy of the brittle medium and C is a positive function of the state variables (macroscopic temperature T and damage α) that characterizes the rate of damage evolution.

Table 2.1: Summary table of damage zone models

Type	Medium	Implications
Low Velocity Fault Zones (LVFZ)	Elastic.	No change in elastic modulus, $\sigma_{ij} = C_{ijkl}\varepsilon_{kl}$
Plasticity	Elastic-plastic, Atomistic dislocations or cracks.	No change in elastic modulus, $\sigma_{ij} = C_{ijkl}(\varepsilon_{kl} - \varepsilon^p_{kl})$
Damage	Inelastic , Density of micro-cracks.	
Lyakhovsky et al. (1997a)	Growth of micro-cracks.	Change in elastic moduli, $\mu(\alpha), \gamma(\alpha)$ α: damage
Ashby and Sammis (1990), *Bhat et al.* (2012)	Growth and interaction of micro-cracks.	Change in elastic modulus, ΔC_{ijkl}

2.2.2 Micromechanical damage model

The micromechanical damage model, applied in this thesis, is formulated by *Ashby and Sammis* (1990) and extended by *Bhat et al.* (2012) to a wide range of loading rates ($\dot{\varepsilon} \sim 10^{-6}s^{-1}$ to $10^{3}s^{-1}$) that includes the cases of aseismic creep and dynamic earthquake rupture. This model reproduces the off-fault damage evolution in brittle solids via an energy-based approach that consider the presence of off-fault micro-cracks that grow, open and interact with each other (see figure 2.5b). From this inelastic deformation, that comes from the off-fault microcracks rearrangements, the model takes into account the dynamic evolution of elastic properties.

In the following part, we explain key characteristics of the model. Further details can be found in *Bhat et al.* (2012) or *Thomas et al.* (2017). We will initially describe

how the dynamic growth of cracks is given. Then, we explain the energy-based approach that aims to capture the inelastic deformation so that we can determine the constitutive strain-stress relationship in a damaged solid.

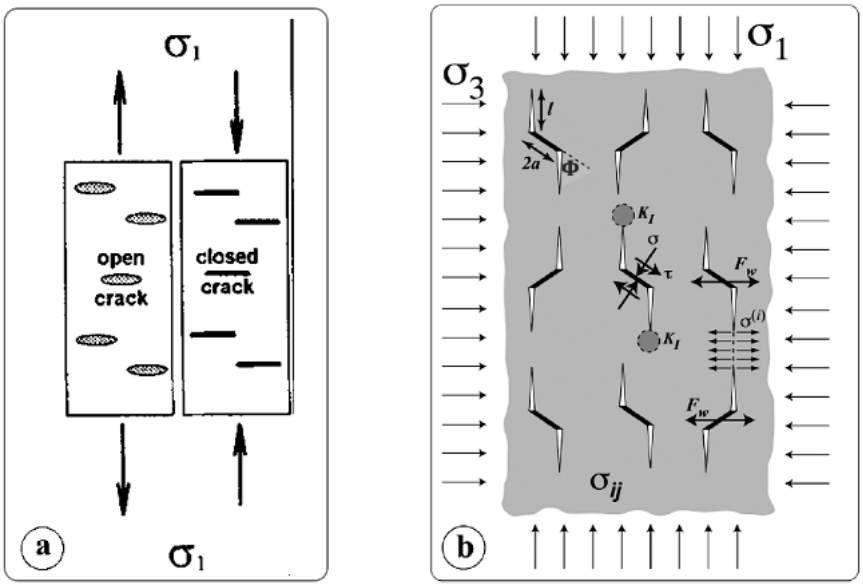

Figure 2.5: **Scheme comparing damage models. (a)** Damage model by *Lyakhovsky et al.* (1997b).**(b)** Micromechanical Damage model by *Bhat et al.* (2012).

We start from an isotropic elastic solid under loading. The solid contains an initial density of monosized penny-shaped microcracks with radius **a** and a fixed orientation (relative to the axis of principal compression σ_1, see figure 2.5b). This volumen density represented by the scalar N_ν is a constant value since no nucleation of new cracks are taken into account. The initial damage state that is the initial density of microcracks per unit volume is defined by the scalar D_o :

$$D_o = \frac{4\pi}{3} N_\nu (\mathrm{a}\cos\Phi)^3 \tag{2.13}$$

where $\mathrm{a}\cos\Phi$ is the projection of the cracks radius to an orientation parallel to the axis of the maximum compressive stress σ_1. The angle $\Phi = \frac{1}{2}\tan^{-1}(1/f_{s,crack})$, with $f_{s,crack}$ the friction coefficient. During loading, the additional damage is generated

by the form of tensile "wing cracks" of lenght l that nucleate at the tips of the initial cracks and grow parallel to σ_1 (see figure 2.6). Then, the current damage state can be expressed as follows:

$$D = \frac{4\pi}{3} N_\nu (\mathrm{a}\cos\Phi + l)^3 \tag{2.14}$$

$D \in [0\ 1]$, $D = 1$ is the coalescence state that represents the macroscopic fracture of the solid. The damage evolution law defined by *Bhat et al.* (2012) is expressed as follows:

$$\frac{dD}{dt} = \left(\frac{3D^{2/3} D_0^{1/3}}{\mathrm{a}\cos\Phi} \right) v \tag{2.15}$$

where $v = \dfrac{dl}{dt}$ is the instantaneous wing-crack tip speed.

Two important fracture parameters are involved in the evolution of damage: (1) The stress intensity factor, K_I and (2) the fracture toughness, K_{IC}. The stress intensity factor K_I measures the stress state at the crack-tip whereas the fracture toughness K_{IC} measures the resistance of the material to fracturing. K_{IC} is obtained through experimental measurements. During loading, these fracture parameters evolve to a dynamic terms referred as follows. For the first parameter, we have the dynamic stress intensity factor, K_I^d; whereas for the second parameter, we have two terms: the dynamic initiation toughness, K_{IC}^D (for dynamic crack initiation) and the dynamic propagation toughness, K_{IC}^d (for dynamic crack propagation).

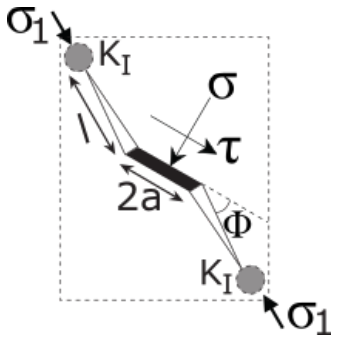

Figure 2.6: **Scheme of crack growth (***Thomas et al.***, 2017).** K_I: Stress intensity factor.

The micromechanical model considers 3 regimes, during loading, to define the inelastic deformation (see figure 2.7). Under Regime I, frictional resistance on the microcracks is not overcome. Then, the material behaves as elastic medium. Under Regime II, frictional sliding on the microcracks is allowed leading to the nucleation and growth of the wing-cracks. At this regime, the stress intensity factor, K_I, takes into account three contributions: (1) A wedging force F_w, generated by the sliding on the initial microcracks, tends to open the wing-cracks. F_w is normal to the maximum principal stress, σ_1. (2) The wedging force, F_w, generates tensile stress, $\sigma^{(i)}$, on the surrounding area between neighboring wing-cracks. This tensile forces tend to open the whole microcrack. (3) The remote compressive stress, σ, tries to close the wing-cracks (see figure 2.5b). Expressions for F_w, $\sigma^{(i)}$ and σ are defined in (*Bhat et al.*, 2012). The stress intensity factor, K_I, in regime II is related to the previously mentioned forces, as follows:

$$K_I^{R-II} = \frac{F_w}{[\pi(l+\beta \mathrm{a})]^{3/2}} + \frac{2}{\pi}\left(\sigma + \sigma^{(i)}\right)\sqrt{\pi l} \tag{2.16}$$

Factor $\beta = 0.1$ is defined by *Ashby and Sammis* (1990) to assign a limiting value of K_I when the length of the wing-cracks is zero. Since, microcracks are uniformly distributed, we can express the stress intensity factor related to the current damage state D, considering a unit volumen of density cracks of size $(l + \alpha \mathrm{a})$,

$$K_I^{R-II}(\sigma, D) = \sqrt{\pi \mathrm{a}}[A(D)\sigma + B(D)\tau] \tag{2.17}$$

where

$$\begin{aligned} A(D) &= f_{s,crack}c_1(D) + c_3[f_{s,crack}c_2(D) + 1] \\ B(D) &= c_1(D) + c_2(D)c_3(D) \end{aligned} \tag{2.18}$$

and

$$
\begin{aligned}
c_1(D) &= \frac{\sqrt{1-\alpha^2}}{\pi\alpha^{3/2}[(D/D_o)^{1/3}-1+\beta/\alpha]^{3/2}} \\
c_2(D) &= \left(\frac{\sqrt{1-\alpha^2}}{\alpha}\right)\left(\frac{D_o^{2/3}}{1-D^{2/3}}\right) \\
c_3(D) &= \frac{2\sqrt{\alpha}}{\pi}[(D/D_o)^{1/3}-1]^{1/2}
\end{aligned}
\tag{2.19}
$$

Under Regime III, it corresponds when the remote loading turns tensile, inducing opening to both the wing-cracks and the initial microcracks. In this regime, the stress intensity factor is related to the current damage state, D, as follows:

$$
K_I^{R-III}(\sigma, D) = \sqrt{\pi \mathrm{a}}[C^2(D)\sigma^2 + O^2(D)\tau^2]^{1/2} \tag{2.20}
$$

with

$$
\begin{aligned}
C(D) &= A + \Omega\sqrt{\alpha[D/D_o]^{1/3}} \\
O(D) &= \sqrt{\frac{B^2C^2}{C^2-A^2}}
\end{aligned}
\tag{2.21}
$$

The essential difference that the micromechanical damage model has with respect to pre-existing models is that, the dynamic evolution of K_I and K_{IC} is based on their sensitive not only to the initial damage but also to the loading rate and the crack-tip velocities, observed in experimental studies (e.g. *Chen et al.*, 2009; *Wang et al.*, 2010; *Zhang and Zhao*, 2013; *Gao et al.*, 2015). The dynamic evolution of these parameters determines the crack growth (evolving damage).

During loading, crack growth criterion stipulates that a crack starts growing when the dynamic stress intensity factor overcomes the material resistance to fracturing defined by the dynamic initiation toughness, i.e. $K_I^d > K_{IC}^D$. Then, crack

propagation is controlled by the dynamic propagation toughness, K_{IC}^{d}. In other words, the crack keeps propagating provided that $K_I^d = K_{IC}^d$. This crack growth criterion can be expressed in its rate-sensitive non-linear equation:

$$\frac{K_I(1 - v/c_R)}{\sqrt{(1 - v/c_p)}} = K_{IC}^{SS} \left\{ \frac{1 + (v/v_m)^5}{\sqrt{(1 - v/c_p)}} \right\} \tag{2.22}$$

where the left hand side defines the dynamic stress intensity factor, K_I^d and the right hand side defines the dynamic propagation toughness, K_{IC}^d. K_I is the quasi-static stress intensity factor. K_{IC}^{SS} is the quasi-static limit of K_{IC}^D. c_R is the Rayleigh wave speed. c_p is the P wave speed of the medium. v_m is the branching speed. v_m is a material dependent value used to prevent crack branching. The wing-crack tip speed v is solved by the rate-sensitive non-linear equation 2.22, and then used to get the current damage state D by solving the damage evolution equation 2.15.

Let us now describe the energy-based approach applied to determine the constitutive strain-stress relationship of a damaged solid, i.e. the rheological constitutive law that takes into account the dynamic evolution of elastic properties of the medium. This energy-based approach is explained as follows.

Considering isothermal conditions, an equilibrium state of the solid is defined by its current strain ε and damage state D. During loading, the solid passes from one equilibrium state to another through energy variations due to inelastic deformation. Hence, the total Gibbs free energy $W(\sigma, D)$ of the solid at the next equilibrium state is expressed as follows:

$$W(\sigma, D) = W^e(\sigma) + W^i(\sigma, D) \tag{2.23}$$

The term, $W^e(\sigma)$, corresponds to the elastic strain energy. Whereas $W^i(\sigma, D)$, represents the inelastic strain energy. Since the all microcracks have the same orientation, the contribution of inelastic deformation can be expressed as the contribution

per microcrack, $\Delta W^i(\sigma, D)$, times the volume density of microcracks, N_ν :

$$W(\sigma, D) = W^e(\sigma) + N_\nu \Delta W^i(\sigma, D) \tag{2.24}$$

$\Delta W^i(\sigma, D)$ is the Gibbs free energy per microcrack. The steps described thus far are illustrated on the following sketch, considering the initial equilibrium state at damage D_o.

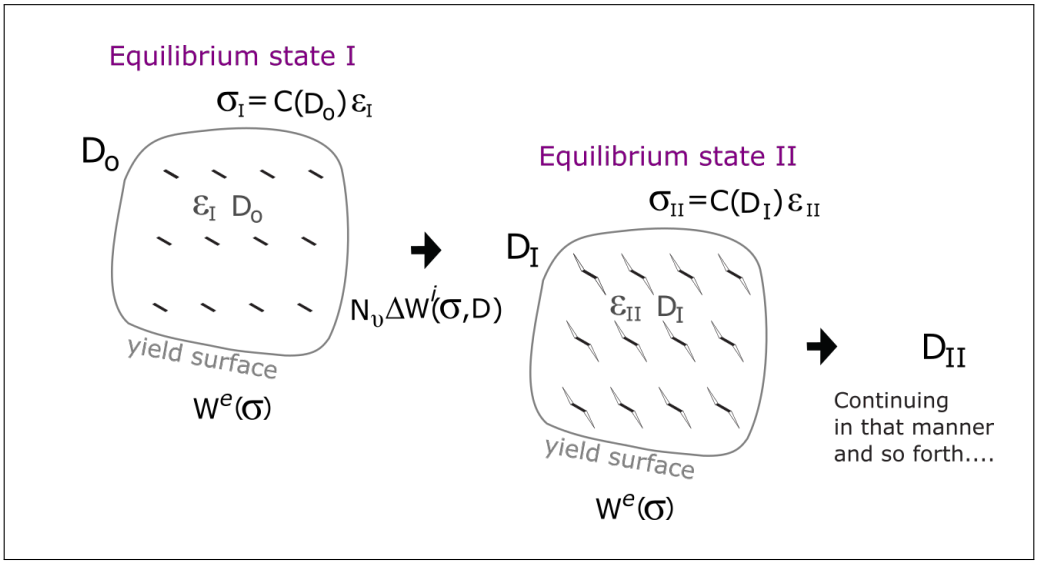

The Gibbs free energy per microcracks, $\Delta W^i(\sigma, D)$, can be expressed by its relation with the fracture energy release rate, $G(\sigma, D)$, and the surface energy, γ_s.

$$\Delta W^i(\sigma, D) = \int_\Gamma [G(\sigma, D) - 2\gamma_s] ds \tag{2.25}$$

$G(\sigma, D)$ is the rate at which energy is consumed by crack growth. γ_s is the energy required to create a unit area of a new fracture surface. d_s corresponds to the position along the microcrack. Γ describes the locus of all microcracks fronts. Based on linear elastic fracture mechanics, the fracture energy release rate, $G(\sigma, D)$, depends on the three modes (I,II and III) of the stress intensity factor, as follows :

$$G(\sigma, D) = \frac{1 - \nu^2}{E} \left[K_I^2 + K_{II}^2 + \frac{K_{III}^2}{(1 - \nu)} \right] \tag{2.26}$$

where E is the Young's modulus and ν is the Poisson's ratio. Stress intensity factors mode II and mode III (K_{II} and K_{III}) are neglected since the contribution of these modes are relevant only when the microcrack starts growing. Then, the fracture growth becomes purely tensile. For this reason, only mode-I stress intensity factor, K_I, is taken into account for the crack growth criterion.

By reeplacing equation 2.26 in 2.25, we obtain the Gibbs free energy per microcracks, $\Delta W^i(\sigma, D)$, as a function that depends on the mode-I stress intensity factor, K_I:

$$\Delta W^i(\sigma, D) = \int_\Gamma \left[\frac{1-\nu^2}{E} K_I^2(\sigma, D) - 2\gamma_s \right] ds \tag{2.27}$$

Therefore, the total Gibbs free energy, $W(\sigma, D)$, of the solid, under ineslatic deformation, can be expressed as follows:

$$W(\sigma, D) = W^e(\sigma) + N_\nu \int_\Gamma \left[\frac{1-\nu^2}{E} K_I^2(\sigma, D) - 2\gamma_s \right] ds \tag{2.28}$$

As a result, the constitutive stress-strain relationship for a damaged solid can be derived from the total Gibbs free energy, W:

$$\epsilon_{ij} = \frac{\partial W}{\partial \sigma_{ij}} \quad \text{and} \quad M_{ijkl} = \frac{\partial^2 W}{\partial \sigma_{ij} \sigma_{kl}} \tag{2.29}$$

The rheological constitutive law is expressed depending on the overall stress-state (loading regime):

Linear elasticity (Regime 1): In this regime, the remote compressional stresses are not high enough to allow sliding along the initial microcracks. The material behavior corresponds to an isotropic linear elastic solid. Therefore, the

consitutive law is written as its linear elastic expression:

$$\sigma_{ij} = 2\mu \left[\varepsilon_{ij} + \frac{\nu}{1-2\nu} \varepsilon \delta_{ij} \right] = 2\mu \varepsilon_{ij} + \lambda \varepsilon \delta_{ij} \tag{2.30}$$

where μ and λ are the elastic moduli, δ_{ij} is the Kronecker delta, ν is the Poisson's ratio and ε is the strain invariant, $\varepsilon = \varepsilon_{kk}$

Compressive loading (Regime 2): It is reached when the shear stress overcomes the frictional resistance acting on the microcracks. Inelastic deformation is then accounted for by the growth of tensile wing-cracks at the tip of the initial microcracks. Then, the constitutive law is expressed as follows:

$$\begin{aligned} \sigma_{ij} = \frac{\mu}{\Gamma} \Bigg\{ & \left[\frac{3(1-2\nu)}{(1+\nu)} + A_1^2 - \frac{A_1 B_1 \varepsilon}{\gamma} \right] \varepsilon_{ij} + \\ & \left[\frac{3\nu}{(1+\nu)} + \frac{B_1^2}{2} - \frac{A_1^2}{3} + \frac{A_1 B_1 \varepsilon}{3\gamma} \right] \varepsilon \delta_{ij} - \left[\frac{A_1 B_1}{2} \right] \gamma \delta_{ij} \Bigg\} \end{aligned} \tag{2.31}$$

with

$$\begin{aligned} \Gamma &= \left[\frac{3(1-2\nu)}{2(1+\nu)} + \frac{3(1-2\nu)B_1^2}{4(1+\nu)} + \frac{A_1^2}{2} \right] \\ A_1 &= A_{(D)} \sqrt{\frac{\pi D_0 (1-\nu)}{\alpha^3}} \\ B_1 &= B_{(D)} \sqrt{\frac{\pi D_0 (1-\nu)}{\alpha^3}} \end{aligned} \tag{2.32}$$

γ is the strain invariant, $\gamma = \sqrt{2 e_{ij} e_{ij}}$ with $e_{ij} = \varepsilon_{ij} - \frac{1}{3}\varepsilon \delta_{ij}$. $A_{(D)}$ and $B_{(D)}$ are parameters that depend on the current damage variable D (cf. *Bhat et al.*, 2012).

From equation 2.31, we can express the equivalent Lamé parameters μ^* and λ^*:

$$\mu^* = \frac{\mu}{2\Gamma}\left(\frac{3(1-2\nu)}{(1+\nu)} + A_1^2\right) \quad \text{and} \quad \lambda^* = \frac{\mu}{\Gamma}\left(\frac{3\nu}{(1+\nu)} + \frac{B_1^2}{2} - \frac{A_1^2}{3}\right) \tag{2.33}$$

and we can approximate the change in waves speed in the medium:

$$c_p^* = \sqrt{\frac{\lambda^* + 2\mu}{\rho}} \quad \text{and} \quad c_s^* = \sqrt{\frac{\mu^*}{\rho}} \tag{2.34}$$

Tensile loading (Regime 3): This regime considers the case when the remote compressional stresses turn tensile leading to the opening of both initial microcracks and wing-cracks. Therefore, we have the following constitutive law:

$$\sigma_{ij} = \mu\left\{\left(\frac{4}{2+O_1^2}\right)\varepsilon_{ij} + \left(\frac{2}{\frac{3(1-2\nu)}{(1+\nu)} + C_1^2} - \frac{4}{3\left[O_1^2+2\right]}\right)\varepsilon\delta_{ij}\right\} \tag{2.35}$$

with

$$\begin{aligned} C_1 &= C_{(D)}\sqrt{\frac{\pi D_0(1-\nu)}{\alpha^3}} \\ O_1 &= O_{(D)}\sqrt{\frac{\pi D_0(1-\nu)}{\alpha^3}} \end{aligned} \tag{2.36}$$

where $C_{(D)}$ and $O_{(D)}$ are parameters that depend on the current damage variable D.

From the equation 2.35, we can obtain the equivalent Lamé parameters to get the change in wave speed in the medium:

$$\mu^* = \mu\left(\frac{2}{2+O_1^2}\right) \quad \text{and} \quad \lambda^* = \mu\left(\frac{2}{\frac{3(1-2\nu)}{(1+\nu)} + C_1^2} - \frac{4}{3[O_1^2+2]}\right) \tag{2.37}$$

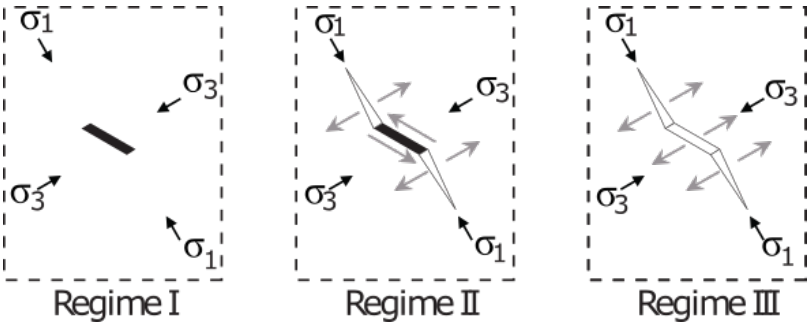

Figure 2.7: **Micromechanical damage model : Regimes of inelastic deformation**.

Transition between regimes is given following *Bhat et al.* (2012):

- For Regime I, the stress intensity factor related to regime II and III must be negatives: $K_I^{II}, K_I^{III} < 0$. Since the stress intensity factor for both regimes II and III are related to the factor $A_{(D)}\sigma + B_{(D)}\tau$, the criteria for being at Regime I is based on satisfying the following inequality:

$$A_{(D)}\sigma + B_{(D)}\tau < 0 \tag{2.38}$$

- For Regime II and III, stress intensity factor must be positives: $K_I^{II}, K_I^{III} > 0$ since inelastic deformation is developed. Additionally, by assuring that tensile deformation is greater for regime III than regime II, criteria for each regime can be defined by the following inequalities:

$$\begin{aligned} &\text{For Regime II} : A_{(D)}\sigma + B_{(D)}\tau > 0 \text{ and } (A_{(D)}^2 - C_{(D)}^2)\sigma + A_{(D)}B_{(D)}\tau > 0 \\ &\text{For Regime III} : A_{(D)}\sigma + B_{(D)}\tau > 0 \text{ and } (A_{(D)}^2 - C_{(D)}^2)\sigma + A_{(D)}B_{(D)}\tau < 0 \end{aligned} \tag{2.39}$$

2.3 Initial stress state

To conduct earthquake rupture simulations, we need to define the initial stress field at which both faults are subjected. To simplify the analysis, we can describe the initial stress field for the first fault of a step-over system. Consider a strike-slip fault in 2D plane-strain condition as shown in figure 2.8. The its in-plane principal stresses σ_1 and σ_3 follow the inequality $\sigma_1 < \sigma_3$ (stresses are negative in compression). The orientation of the stress field is defined by the angle Ψ between the maximum principal stress σ_1 and the fault strike.

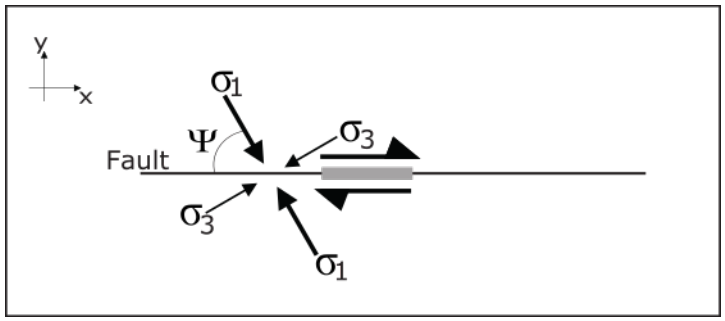

Figure 2.8: **Initial stress state**. Ψ is the angle between the maximum principal stress σ_1 and the fault strike. This schematic corresponds to the first fault of a step-over system. The thick grey line corresponds to the nucleation prone-patch where the initial shear stress is set up to be just above the frictional strength to allow fault sliding.

Jeandet-Ribes et al. (2023) pointed out the importance of 3D stress state on the evolution of off-fault damage in 2D plane-strain simulation. They remarked that if the inequality for 3D stress state $\sigma_1 < \sigma_2 < \sigma_3$ (σ_2 is the principal stress with out-of-plane direction) is not satisfied in 2D in-plane simulations, it will significantly impact the off-fault damage evolution. They provide a condition to constrain the initial stress field that favors the strike-slip faulting.

Consider the initial stress state σ_{ij}^0 expressed as follows (coordinate system as in

figure 2.8):

$$\sigma_{ij}^{0} = \begin{pmatrix} \sigma_{xx}^{0} & \sigma_{xy}^{0} & 0 \\ \sigma_{xy}^{0} & \sigma_{yy}^{0} & 0 \\ 0 & 0 & \sigma_{zz}^{0} \end{pmatrix} \tag{2.40}$$

The initial stress state σ_{ij}^{0} that favors the strike-slip motion must satisfy the following inequality:

$$1 - 2\nu < \sqrt{\left(\frac{\gamma - 1}{\gamma + 1}\right)^{2} + \frac{4\mu_o^2}{(\gamma + 1)^2}} < 1 \tag{2.41}$$

where ν is the Poisson ratio and

$$\gamma = \frac{\sigma_{xx}^{0}}{\sigma_{yy}^{0}} \;\; \& \;\; \mu_o = \frac{\sigma_{xy}^{0}}{-\sigma_{yy}^{0}} \tag{2.42}$$

An important rupture parameter that relates the frictional parameters and the initial stress state is the seismic ratio S. This is a ratio between the shear stress increment required to failure and the static stress drop (*Andrews*, 1976; *Das and Aki*, 1977):

$$S = \frac{f_s(-\sigma_{yy}^{0}) - \sigma_{xy}^{0}}{\sigma_{xy}^{0} - f_d(-\sigma_{yy}^{0})} \tag{2.43}$$

where σ_{xy}^{0} and σ_{yy}^{0} are the shear and normal stresses, respectively.

In our model, to verify the inequality 2.41, we consider the following procedure,

Some parameters are defined as constants, such as: Material density, ρ ; P wave speed, c_p; S wave speed, c_s; hydrostatic pore pressure, pp; depth, z; seismic ratio, S; static friction coefficient, f_s; dynamic friction coefficient, f_d, angle Ψ (see figure 2.8).

Other expressions to obtain μ_o and γ are:

$$\begin{aligned} \mu_o &= \frac{(f_s + S f_d)}{1 + S} \\ \gamma &= \frac{2\mu_o}{\tan(2\Psi)} + 1 \end{aligned} \tag{2.44}$$

From the elastic properties (ρ, c_p and c_s), we can compute the following parameters: Lamé parameter, λ; shear modulus, μ and Poisson's ratio, ν

$$\begin{aligned} \lambda &= \rho(c_p^2 - 2c_s^2) \\ \mu &= \rho c_s^2 \\ \nu &= \frac{\lambda}{2(\lambda+\mu)} \end{aligned} \tag{2.45}$$

The stress components can be computed as follows:

$$\begin{aligned} \sigma_{zz}^o &= (1-pp)\rho g z \\ \sigma_{yy}^o &= \frac{\sigma_{zz}^o}{\nu(\gamma+1)} \\ \sigma_{xx}^o &= \gamma \sigma_{yy}^o \\ \sigma_{xy}^o &= -\mu \sigma_{yy}^o \end{aligned} \tag{2.46}$$

We can then calculate the maximum and minimum compressive principal stresses:

$$\begin{aligned} \sigma_1 &= \frac{\sigma_{xx}^o + \sigma_{yy}^o}{2}\left(1 + \sqrt{\left(\frac{2\mu_o}{\gamma+1}\right)^2 + \left(\frac{\gamma-1}{\gamma+1}\right)^2}\right) \\ \sigma_3 &= \frac{\sigma_{xx}^o + \sigma_{yy}^o}{2}\left(1 - \sqrt{\left(\frac{2\mu_o}{\gamma+1}\right)^2 + \left(\frac{\gamma-1}{\gamma+1}\right)^2}\right) \end{aligned} \tag{2.47}$$

Taking into account, for strike-slip faulting, that the intermediate compressive principal stress $\sigma_2 = \sigma_{zz}^o$, we can directly verify the stress inequality:

$$\sigma_1 < \sigma_2 < \sigma_3 \tag{2.48}$$

2.4 Model scheme

Once the friction law, rheology and the initial stress state are setup, we can build a 2D model to conduct earthquake rupture simulations on step-over faults (see model scheme in figure 2.9). To initiate an earthquake, on a determined region (nucleation patch) on the first fault, we set the stresses so it overcomes the frictional strength. The earthquake propagates through the first fault generating seismic waves, and is arrested at the fault edges. If the system allows off-fault damage evolution during the coseismic deformation, off-fault microcracks grow and interact with each-other according to the evolution of the stress state at their crack tips, following the micromechanical damage model explained in section 2.2.2 (*Bhat et al.*, 2012).

Whether a rupture jumps on the second fault depends on the stresses readjustment occurring during the dynamic faulting. Therefore, it is sensitive to the impact of dynamic wave propagation (e.g. *Harris and Day*, 1993). Hence, it implies that artificial reflections that come from numerical domain boundaries can also influence the mechanisms that allow jumping ruptures. A usual procedure in numerical modelling is to apply absorbing boundary conditions to prevent reflections. Within SEM2DPACK is implemented with absorbing boundary conditions proposed by *Clayton and Engquist* (1977) for in-plane 2D motion. At normal incidence on the domain boundaries, the absorbing boundary conditions reduces consistently the artificial reflections. However, at grazing angles, spurious reflections are not adequately minimized.

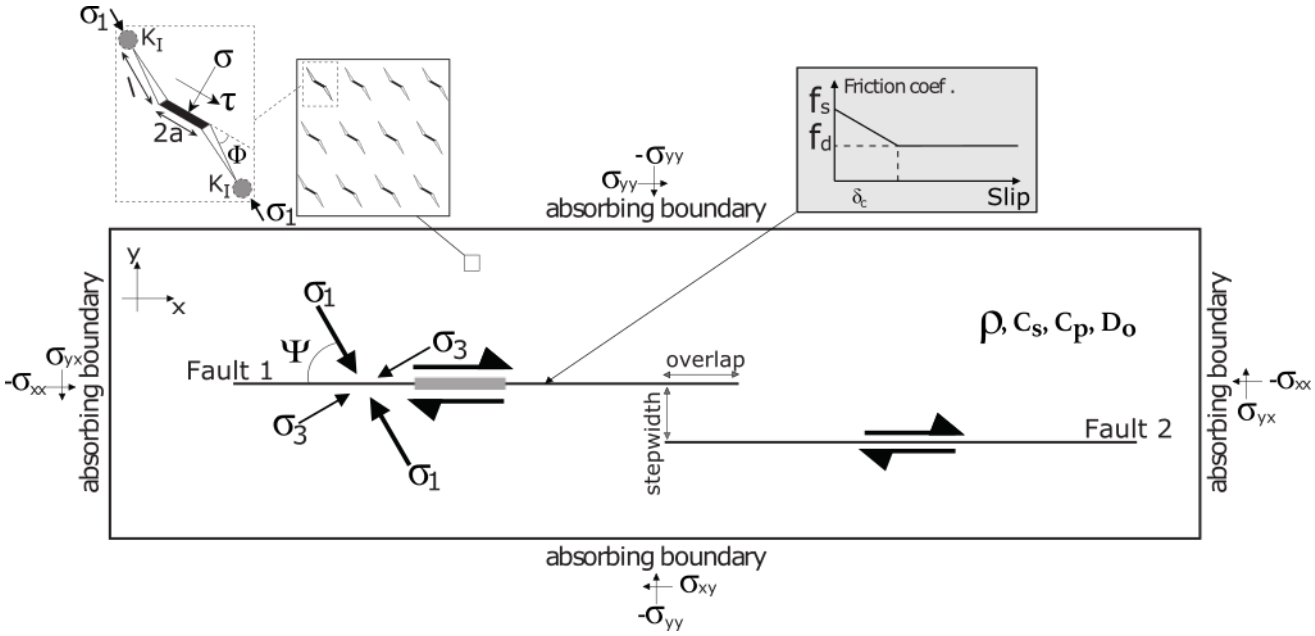

Figure 2.9: **2D Model Scheme**. Schematics for simulations of dynamic ruptures in a 2-D in-plane model. We consider two right-lateral planar faults labeled as Fault 1 and Fault 2, embedded in a brittle off-fault medium with a damage-constitutive law. Material properties are defined by the density (ρ), the S and P-waves speed (c_s and c_p) and the initial damage density (D_o). Slip-weakening friction (grey box) acts on the two faults. The medium is loaded by uniform background stresses with the maximum compressive stress σ_1 making an angle ψ with the fault strike. The thick grey line corresponds to the nucleation prone-patch where the initial shear stress is set up to be just above the frictional resistance so that an earthquake can be triggered on the first fault.

Rupture dynamics across stepover structure generates seismic waves from different sources such as rupture propagation, rupture arrest, damage generation and wave reflection within the low velocity zone (LVZ) nearly created (*Thomas and Bhat*, 2018), etc. Hence, seismic waves can have a wide range of incident angle at the domain boundaries. Therefore, we set the domain size such that no reflected waves may interact with the faults. This criteria is developed as follows:

Let us analyse the case of an extensional step-over fault system as shown in figure 2.10 for any orientation ω of the second fault. Considering full rupture of both faults due to rupture jumping, we can express the distance d_1 and d_2 on fault 1 and fault

2 , respectively, where earthquake rupture is propagated.

$$\begin{aligned} d_1 &= L_{F1} - L_{nuc1} \\ d_2 &= \sqrt{(X_{F2R} - X_{L_{nuc2}})^2 + (Y_{F2R} - Y_{L_{nuc2}})^2} \end{aligned} \tag{2.49}$$

Where L_{F1} and L_{nuc1} are the length and the nucleation size of fault 1, respectively. X_{F2R} and Y_{F2R} are the x and y values of the right end of fault 2. $X_{L_{nuc2}}$ and $Y_{L_{nuc2}}$ are the x and y values, respectively, where triggering is expected to be allowed on fault 2. Nucleation size is computed considering equation 2.4. Then, we need to consider additional distances (W_L,W_R,H_1 and H_2) away from the faults so that the artificial reflections of the fastest seismic wave, P wave (c_p), do not reach the faults (see figure 2.10). To do so, we can express these distances as follows:

$$\begin{aligned} W_L &= 0.5 \left(c_p \frac{d_1 + d_2}{v_{rup}} + X_{F1L} \right) \\ W_R &= 0.5 \left(c_p \frac{d_1 + d_2}{v_{rup}} - X_{F2R} \right) \\ H_1 &= 0.5 \left(c_p \frac{d_1 + d_2}{v_{rup}} \right) \\ H_2 &= 0.5 \left(c_p \frac{d_1 + d_2}{v_{rup}} + Y_{L_{nuc2}} \right) \end{aligned} \tag{2.50}$$

where v_{rup} is the rupture velocity. We can constrain the upper limit of v_{rup} to S wave speed in subshear rupture. X_{F1L} is the x value of the left end of fault 1. Domain size is then limited considering the distances W_L, W_R, H_1 and H_2.

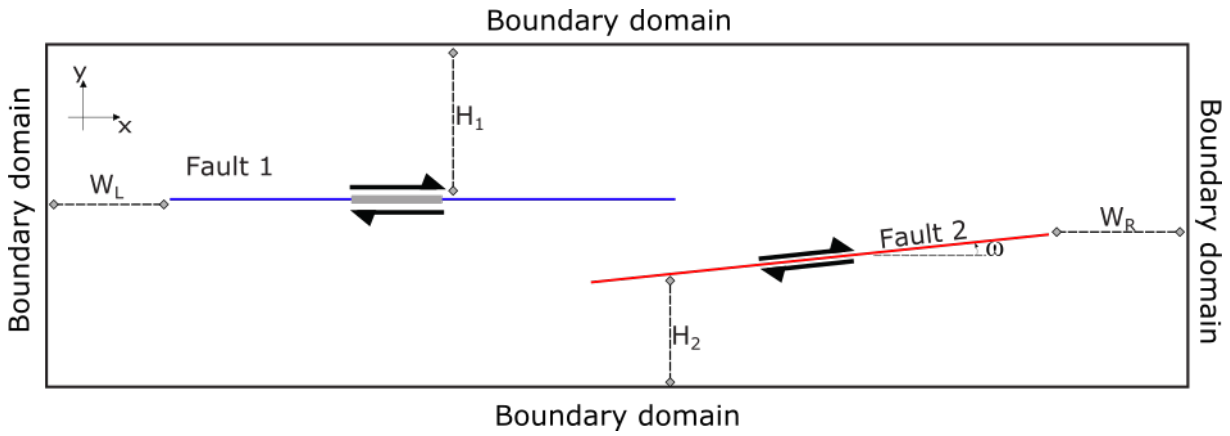

Figure 2.10: **2D Domain**. We consider additional distances (W_L,W_R,H_1 and H_2) away from the faults to define a criteria that aims to prevent the influence of artificial reflections on rupture propagation around stepovers.

Chapter 3

Benchmarking of 2D dynamic earthquake rupture modeling in step-over faults

3.1 Introduction

Wesnousky (1988), *Harris and Day* (1993) and *Wesnousky* (2006) are among the most referenced studies in seismic hazard analysis for earthquake rupture propagation across step-over structures (e.g. *Scholz and Gupta*, 2000; *Field et al.*, 2009, 2014; *Mignan et al.*, 2015; *Liu et al.*, 2020; *Cheng et al.*, 2021). *Harris and Day* (1993) conducted a set of 2D dynamic earthquake simulations in step-over faults embedded on linear elastic medium. *Wesnousky* (2006) analysed 22 continental strike-slip earthquakes of magnitudes Mw between 6 and 7.9 associated with step-over structures, from different locations as Japan, Turkey and California. Both studies suggest that an earthquake rupture is unlikely to jump from one fault to a secondary fault at distances greater than 5 km. Numerical analysis performed by *Harris and Day* (1993) mainly focused on 4 cases considering different values of seismic ratio $S \in [0.49, 1.65]$ and stress drop $\Delta\tau \in [3, 10]$ MPa. S is a value that represents the ratio between the

stress increment required to initiate an earthquake and the overall stress drop (*Andrews*, 1976; *Das and Aki*, 1977). In 2D in-plane motion, for an earthquake rupture propagating bilaterally in a fault, transition from subshear to supershear rupture velocity is allowed when $S < 1.77$ (*Andrews*, 1976, 1985). According to this limiting value of S, the analysis of maximum jumpable distance in dynamic simulations of *Harris and Day* (1993) were based on exploring dynamic earthquake ruptures at supershear regime.

Case A, one of the four cases analysed by *Harris and Day* (1993), produced the largest jumpable distance considering seismic ratio $S = 0.49$ and stress drop $\Delta\tau = 10$ MPa. Figure 3.1 shows the location at which the earthquake initiates at the second fault due to jumping rupture. The overlap length is set up as 5 km. Values of stepwidth is analysed between 0.5 km and 5km in both extensional and compressional system. They reported that the largest jumpable distance is allowed at stepwidth equals 5 km and this case corresponds to extensional stepover structure. Conversely, The largest jumpable distance in compressional stepover structure corresponds to 2.5 km. Besides, it is observed that earthquake nucleation at the second fault in compressional stepover occurs at further distance away from the edge of the first fault. It is associated with the fact that during the coseismic deformation there is an increase of shear and normal stresses around the compressional stepover structure whereas at further distance the increase of normal stress no longer influence on the second fault allowing the earthquake nucleation. A particular difference between extensional and compressional system in figure 3.1 that we can remark is that the compressional system does not require an overlap length to develop jumping rupture. Regarding triggering time at the second fault, *Harris and Day* (1993) reported that jumping rupture had larger time delay in extensional system than in compressional system. This implies there is significant dynamic effect that keeps interacting with the stress state around the second fault allowing its sliding. Based on this numerical

analysis often referred in seismic hazard assessments, we plan to benchmark our own dynamic rupture simulations.

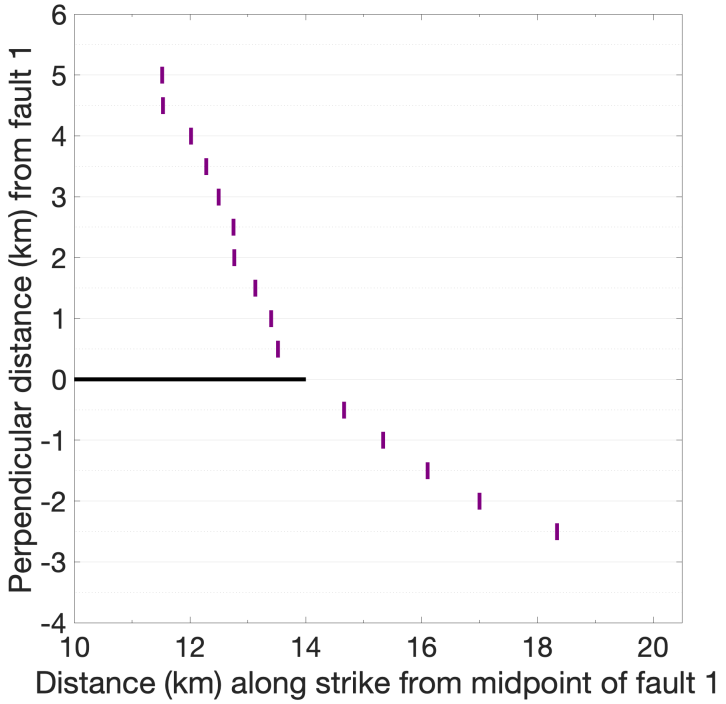

Figure 3.1: **Triggering location at the second fault, results from case A of *Harris and Day* (1993).** For this case, seismic ratio $S = 0.49$, stress drop $\Delta\tau = 10$ MPa, static friction $f_s = 0.75$ and dynamic friction $f_d = 0.3$. In axis Y, negative values of perpendicular distance represent stepwidth for step-over compressional setup, positives values represent stepwidth for step-over extensional setup. Black horizontal line represent the right edge of the first fault.

In this chapter, we conducted dynamic earthquake rupture simulations on step-over faults with model parameters from *Harris and Day* (1993). The objective of this chapter follows two approaches: firstly, we run simulations considering linear elastic medium in order to benchmark with results reported in *Harris and Day* (1993); secondly, we run simulations considering dynamic off-fault damage with initial damage state $D_0 = 0.1$ to evaluate the impact of damage effects on earthquake rupture propagation. Additional parameters than those provided in *Harris and Day*

(1993) are discussed further on. Besides, as presented in *Harris and Day* (1993), we evaluated different values of stepwidth. For extensional stepover system, we analysed cases with stepwitdh from 0.5km to 5.5km whereas for compressional stepover system, we explored cases with stepwidth from 0.5km to 3.5km. Detailed list of parameters is presented in table 3.1. Parameters correspond to the case A from *Harris and Day* (1993). We chose case A since it corresponds to the case with the largest jumpable distance for both compressional and extensional systems (see figure 3.1).

To conduct earthquake rupture simulations in linear elastic medium, we required to get the additional following parameters: angle ψ (orientation of the initial maximum principal stress σ_1 respect to the fault strike), depth z, process zone size R_0 and nucleation size L_{nuc}. We obtained the value of these parameters based on the following relations:

Considering a certain value of depth and that initial stress state σ_{ij}^0 is given by:

$$\sigma_{ij}^0 = \begin{pmatrix} \sigma_{xx}^0 & \sigma_{xy}^0 & 0 \\ \sigma_{xy}^0 & \sigma_{yy}^0 & 0 \\ 0 & 0 & \sigma_{zz}^0 \end{pmatrix} \tag{3.1}$$

we can get the value of the angle ψ as follows

$$\begin{aligned} \sigma_{zz}^0 &= (1-\gamma)\rho g z \\ \sigma_{xx}^0 &= \frac{\sigma_{zz}^0}{\nu} - \sigma_{yy}^0 \\ \psi &= 0.5 \arctan\left(\frac{2\sigma_{xy}^0}{\sigma_{yy}^0 - \sigma_{xx}^0}\right) \end{aligned} \tag{3.2}$$

where $\gamma = 0.4$ is the pore pressure parameter, $g = 9.8 m.s^{-2}$ is acceleration due

to gravity, ρ is material density and ν is Poisson's ratio. To set up a proper value of depth we considered the following aspects. On one side, we require to assure that the value of angle ψ does not correspond to the case with free-surface effect that can influence on jumping rupture mechanism (e.g. *Xu et al.*, 2015; *Hu et al.*, 2016; *Bai and Ampuero*, 2017). On the other side, since off-fault damage zone thickness decreases with depth (e.g. *Cochran et al.*, 2009; *Okubo et al.*, 2019b), shallow values of depth are required so that we can evaluate off-fault damage effect on the jumping rupture mechanism at large spatial extent of damage zone. According to the previous-mentioned aspects, we consider a proper value of depth $z = 2$ km. Based on this value of depth and following the expression 3.2, we obtain the value of angle $\psi = 15^o$.

Quasi-static process zone size (*Poliakov et al.*, 2002) that characterizes the scale of dynamic rupture is defined by

$$R_0 = \frac{9\pi D_c \mu}{32(1-\nu)(f_s - f_d)(-\sigma^0_{yy})} \tag{3.3}$$

where D_c is the characteristic distance, μ is the shear modulus, f_s and f_d are static and dynamic friction coefficient respectively. Nucleation size (*Palmer and Rice*, 1973) that represents the minimum required size on the fault for dynamic instability is given by

$$L_{nuc} = \frac{64}{9\pi^2}(1+S)^2 R_0 \tag{3.4}$$

where S is the seismic ratio.

To perform earthquake rupture simulations with dynamic off-fault damage, we needed to set up the following parameters related to the micromechanical damage approach presented in chapter 2 (detailed in *Bhat et al.*, 2012) : quasi-static fracture

toughness K_{IC}^{SS}, branching speed v_m, initial crack size $2a$, initial damage state D_0 and the static friction coefficient for off-fault microcracks $f_{s,crack}$. We set up the values of material properties such as quasi-static fracture toughness K_{IC}^{SS} and branching speed v_m according to granite (see Table 3.1). Since fault damage zone has been characterized with lengths of off-fault fractures on the average interval from 10 m to 150 m (*Faulkner et al.*, 2008; *Vallage et al.*, 2015; *Ostermeijer et al.*, 2020), we consider a minimum value of the initial cracks' radius $a = 25$ m. Some studies have shown that in fault damage zone, minimum crack density close to the damage zone-host rock boundary is in the range between 10% and 25% of its maximum value observed close to the fault core (e.g. *Schulz and Evans*, 2000; *Mitchell and Faulkner*, 2009, 2012; *Ostermeijer et al.*, 2020). Hence, our initial damage state D_0 that represents the initial crack density (background damage) is set up as $D_0 = 0.1$. Maximum value of damage state $D = 1$ corresponds to the extreme damage state or pulverized rock as characterized in field studies (e.g. *Rempe et al.*, 2013; *Aben et al.*, 2017). On the other side, since high content of low-coefficient-of-friction minerals (e.g. clays, reader is referred to experimental studies of friction coefficient in *Summers and Byerlee* (1977); *Byerlee* (1978)) is usually found at the fault surface, we consider that the static friction coefficient for off-fault microcracks $f_{s,crack}$ is greater than the static friction coefficient at the fault f_s (according to *Harris and Day* (1993), for this case of study $f_s = 0.75$). Besides, the upper limit of $f_{s,crack}$ is constrained to 1.0 based on experimental studies (*Jaeger*, 1979). Therefore, we define $f_{s,crack} = 0.8$.

Parameter	Symbol	Value
Initial Shear stress	τ_{xy}^0	20 MPa
Initial Normal stress	σ_{yy}^0	33.3 MPa
Seismic ratio	S	0.49
Stress drop	$\Delta\tau$	10 MPa
P wave velocity	c_p	6.00 $km.s^{-1}$
S wave velocity	c_s	3.46 $km.s^{-1}$
Density	ρ	2700 $kg.m^{-3}$
Orientation of maximum principal stress σ_1^0	Ψ	15°
Depth	z	2.0 km
Static friction coefficient	f_s	0.75
Dynamic friction coefficient	f_d	0.3
Characteristic distance	D_c	0.1 m
Process zone size	R_0	0.25 km
Nucleation size	L_{nuc}	0.40 km

Parameter for dynamic damage	Symbol	Value
Initial damage state	D_0	0.1
Static friction coefficient for microcracks	$f_{s,crack}$	0.8
Initial cracks' radius	a	25 m
Branching speed	v_m	1.1 $km.s^{-1}$
Quasi-static fracture toughness	K_{IC}^{SS}	1.2 MPa$\sqrt{m}$

Table 3.1: Parameters based on Case A from *Harris and Day* (1993) used to evaluate earthquake rupture simulations on step-over faults.

3.2 Results

In this section, we show results with parameters listed in table 3.1. These results correspond to the case of extensional secondary fault. Regarding the geometrical setup, both faults have the same length equal to 28 km. The overlap distance is 5 km. We conducted earthquake rupture simulations with different stepwidth (perpendicular distance between faults) up to 5.5 km. In this section, we show two cases with stepwidth 0.5 km and 4.5 km to analyse the role of stepovers at distances close and far away from the first fault. In all the figures, values of distance along and perpendicular to the fault are normalized by the process zone size $R_0 = 250$ m.

For the first case with stepwidth=0.5 km, we show the particle velocity at a time before and after the jumping rupture in Figure 3.2 and 3.3 respectively. Plot (a) corresponds to the case with dynamic off-fault damage. Plot (b) corresponds to the case with elastic medium. Plot (c) is the difference between the two cases. Dynamic earthquake rupture is developed as follows: A sized region (nucleation size, L_{nuc}) on the first fault is overstressed overcoming the frictional resistance which leads to an earthquake nucleation. Then, sliding on the fault is governed by the slip-weakening friction law, explained in chapter 2. Shortly after its initiation (at time < 1 s), there is a transition from subshear to supershear rupture that propagates along the fault until reaching the right edge (see Figure 3.2). Right after the rupture arrests, a secondary nucleation is triggered on the second fault (at time ~ 3 s). Then, there is a transition to supershear rupture which propagates along the second fault (see Figure 3.3). A characteristic remark is that there is no significant difference in particle velocity between both dynamic damage and elastic cases as observed in plot(c) for each time step. This observation is attributed to the lack of significant off-fault damage shown in figure 3.4. Besides, we observe that in this case there is no any crucial effect of damage such as inhibiting or delaying the jumping rupture. Slip-rate on faults are superimposed, as black curves, on the plots.

Figure 3.4 shows the evolution of damage state at different times during the jumping rupture. The first plot (a) corresponds to the same time as figure 3.2, before jumping rupture. Plot (b) and (c) correspond to the time after the earthquake nucleation at the second fault. We observe an slight increase of damage at both compressional and extensional side of the first fault. Besides, there is damage generated at the edge of the fault that comes from the rupture arrest and dynamic impact of the stopping phase. Nonetheless, the overall off-fault spatial extension of damage and level of damage around the fault are quite negligible. Since the particle velocity for damage case behaves quite similar to the elastic case, we consider that the lack of damage evolution does not allow significant damage effects. The absence of significant evolution of damage is observed in all dynamic off-fault damage simulations. This behavior is discussed in the last section of this chapter.

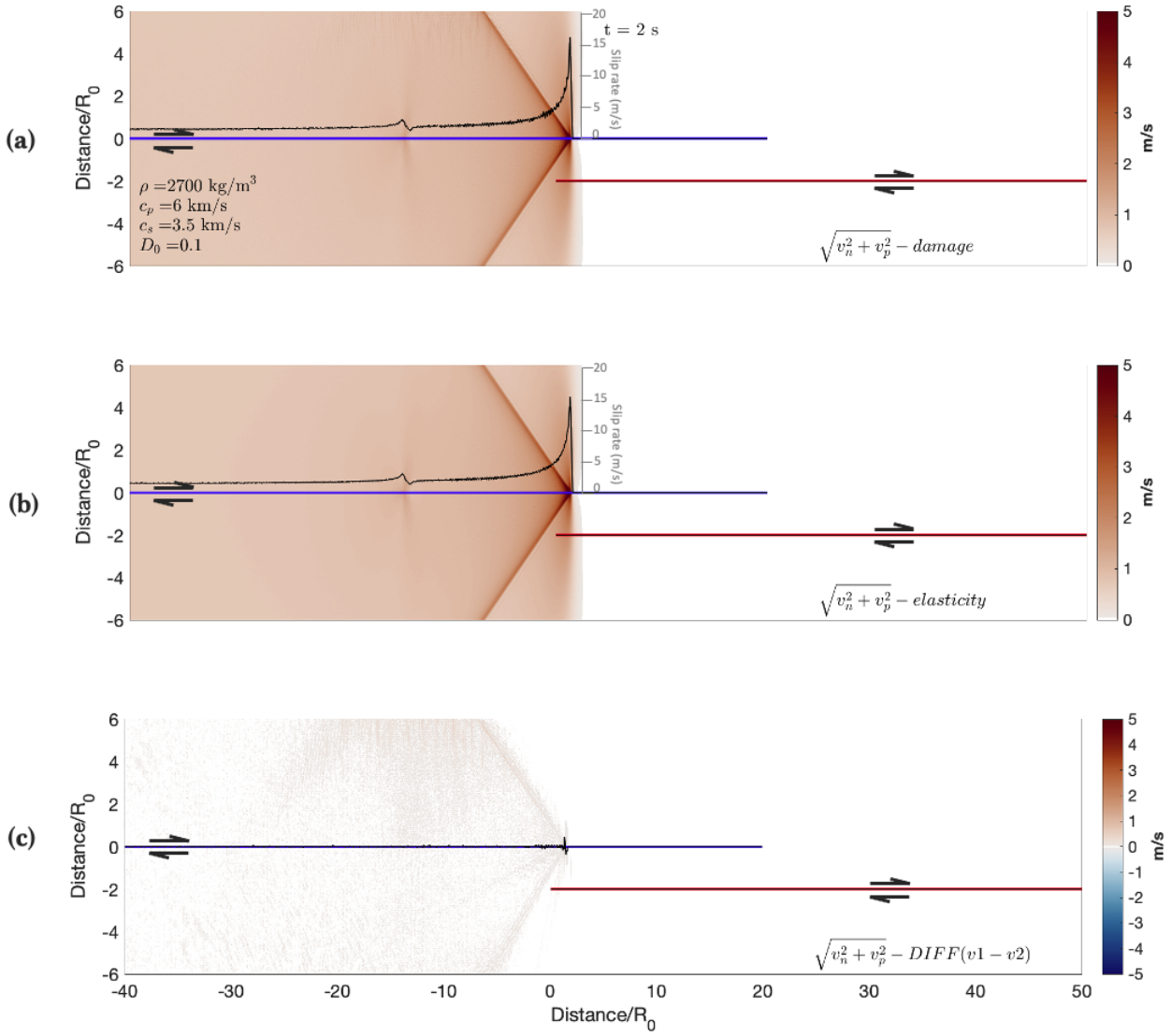

Figure 3.2: **Snapshot of particle velocity for dynamic earthquake rupture simulations in strike-slip step-over faults at a time before the earthquake arrest at the first fault**, for case with (a) dynamic off-fault damage and (b) elastic off-fault medium. Plot (c) shows the difference between the two models. Parameters are based on Case A **(stepwidth=0.5km)** from *Harris and Day* (1993). Strike-slip faults are represented by straight lines colored in blue (first fault) and red (second fault). Slip-rate on the fault (black curves) is superimposed on the snapshots.

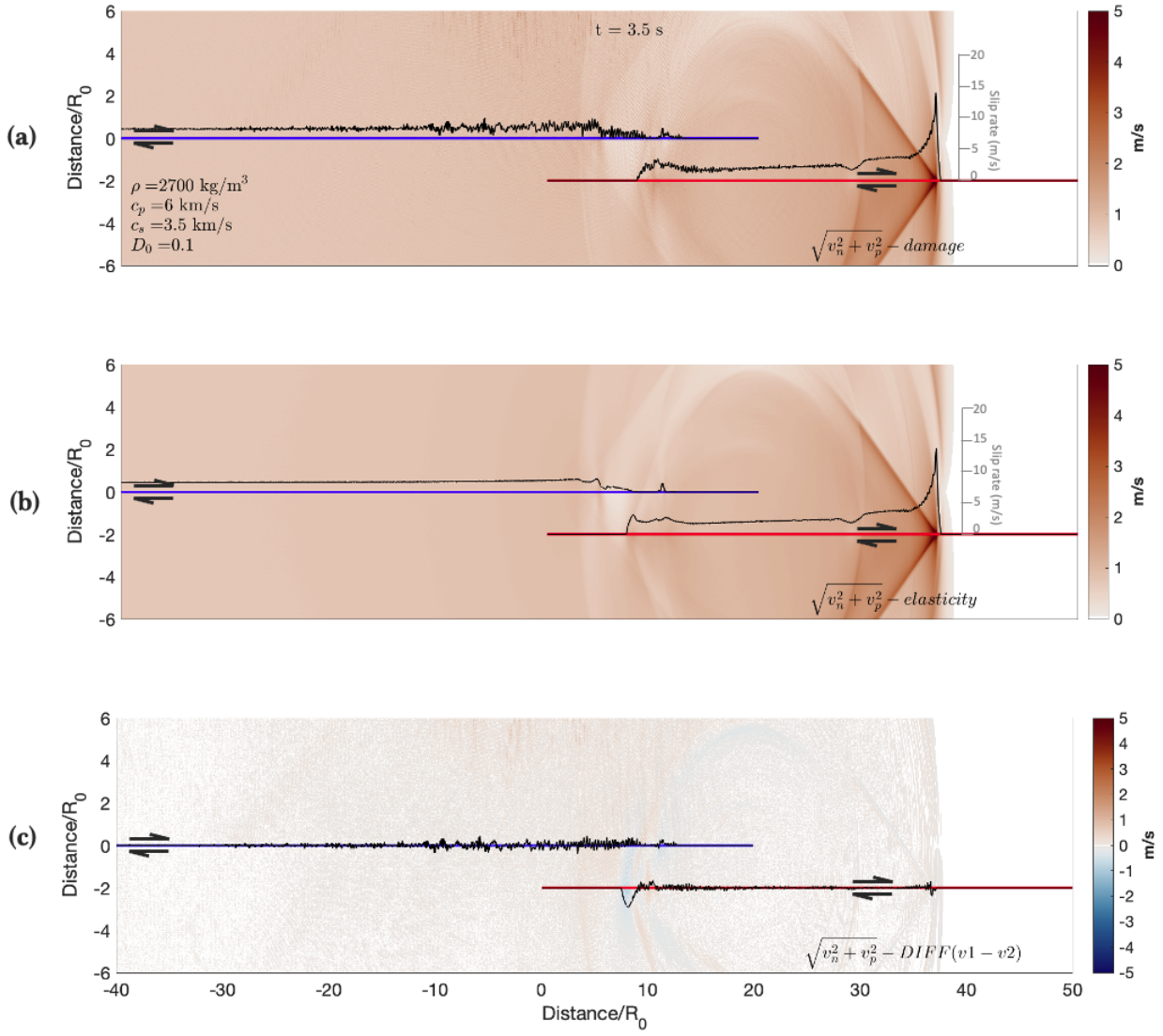

Figure 3.3: **Snapshot of particle velocity for dynamic earthquake rupture simulations in strike-slip step-over faults at a time after the earthquake nucleation at the second fault**, for case with (a) dynamic off-fault damage and (b) elastic off-fault medium. (c) Difference between the two models. Parameters are based on Case A **(stepwidth=0.5km)** from *Harris and Day* (1993). Strike-slip faults are represented by straight lines colored in blue (first fault) and red (second fault). Slip-rate on the fault (black curves) is superimposed on the snapshots.

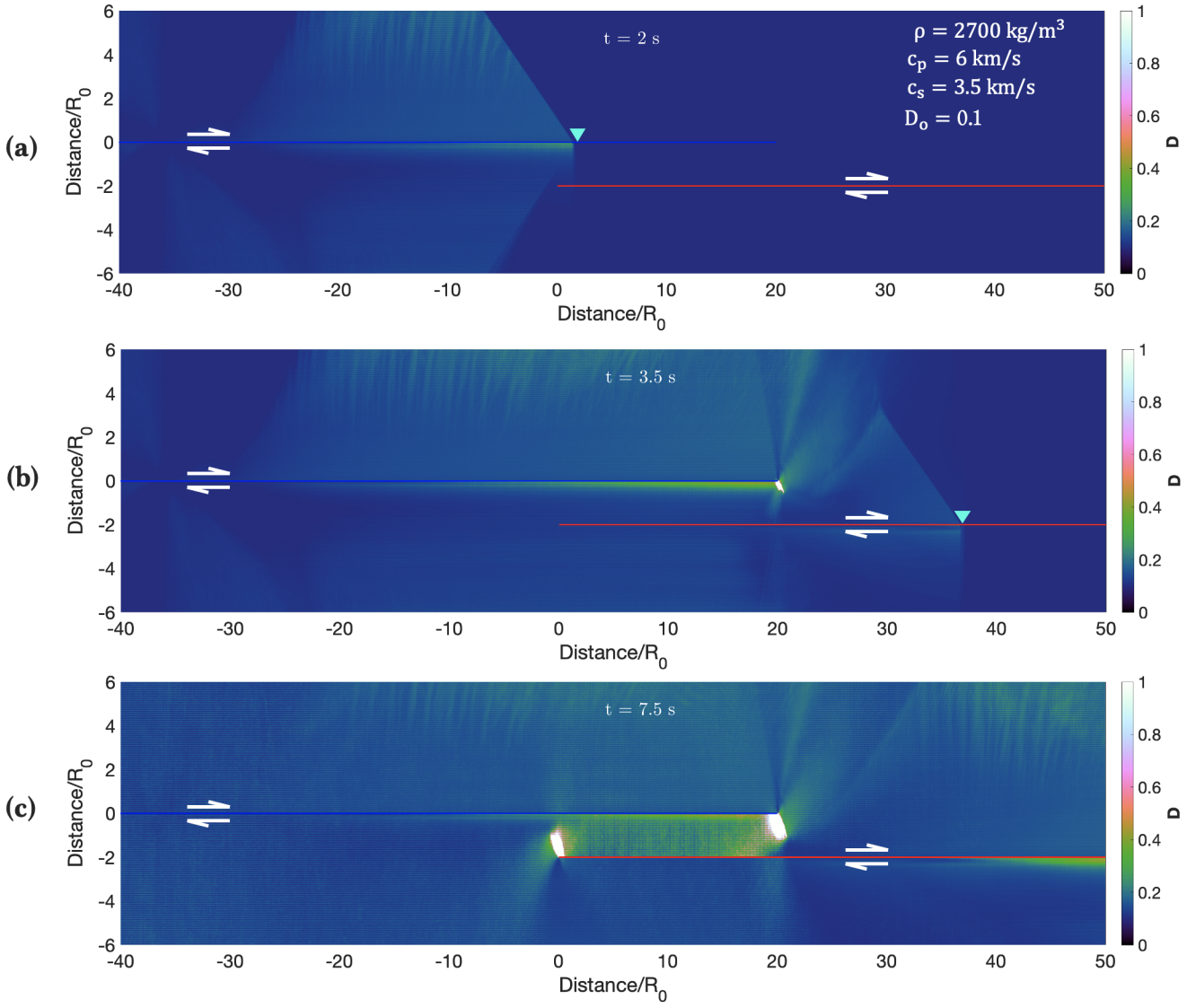

Figure 3.4: **Snapshots of damage state for dynamic earthquake rupture simulation in strike-slip step-over faults** at a time (a) before the earthquake arrest at the first fault, (b and c) after the earthquake nucleation at the second fault. Strike-slip faults are represented by straight lines colored in blue (first fault) and red (second fault). Rupture tips are denoted by the inverted (cyan) triangle. Process zone size, $R_0 = 250$ m.

For the second case with stepwidth=4.5 km, we show the particle velocity at a time before and after the jumping rupture in Figure 3.5 and 3.6 respectively. Elastic and damage cases are compared at the plot (c) for each time step. Jumping rupture at the second fault is allowed at time > 6.5 s (see triggering time in figure 3.9). This overall time delay respect to the previous case with shorter stepwidth indicates that jumping rupture at larger stepwidth is at least influenced by the dynamic effect of the stopping phase. In another aspect, we remarkably notice a certain time delay of jumping rupture in elastic case with respect to the damage case (see figure 3.6). Earthquake nucleation at the second fault for elastic case is allowed at time ~ 8.5 s whereas in damage case jumping rupture is given at time ~ 7 s. This time difference is related to the influence of dynamic stress transfer that allows jumping rupture. We suspect that the stopping phase is sped up in the extensional side of the first fault due to dynamic off-fault damage. This generates a time delay in elastic case with respect to the damage case for extensional step-over faults, whereas in compressional system, both elastic and damage cases allow jumping rupture at the same time (see figure 3.9). Figure 3.7 shows the evolution of damage state at different times during the jumping rupture. We observe that there is quite similar absence of damage evolution as in the case with stepwidth = 0.5 km. There is a particular damage increase far away from the fault at the compressional side of the first fault. This damage feauture is discussed later in the next section.

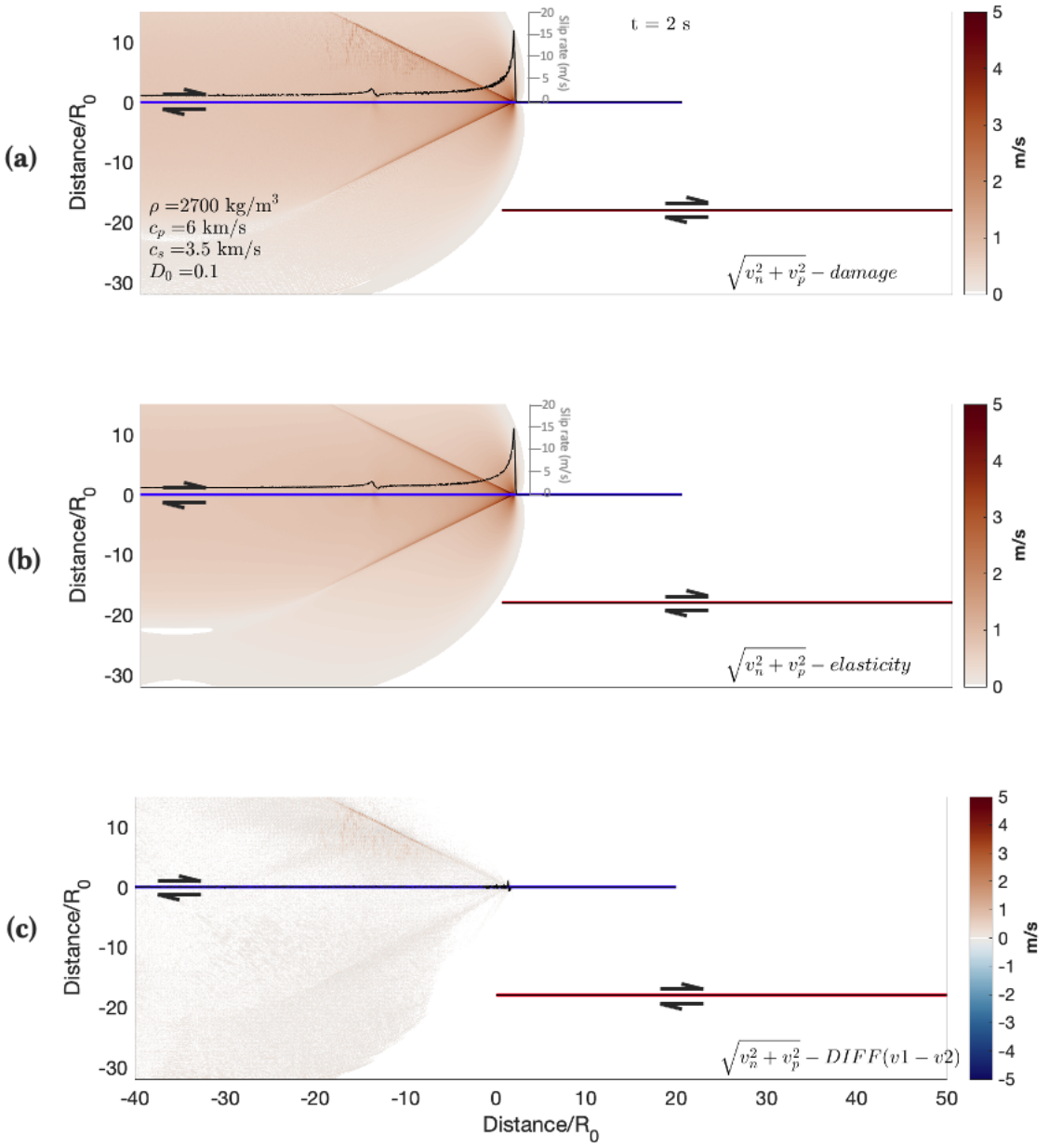

Figure 3.5: **Snapshot of particle velocity for dynamic earthquake rupture simulations in strike-slip step-over faults** at a time before the earthquake arrest at the first fault, for case with (a) dynamic off-fault damage and (b) elastic off-fault medium. (c) Difference between the two models. Parameters are based on Case A **(stepwidth=4.5km)** from *Harris and Day* (1993). Strike-slip faults are represented by straight lines colored in blue (first fault) and red (second fault). Slip-rate on the fault (black curves) is superimposed on the snapshots.

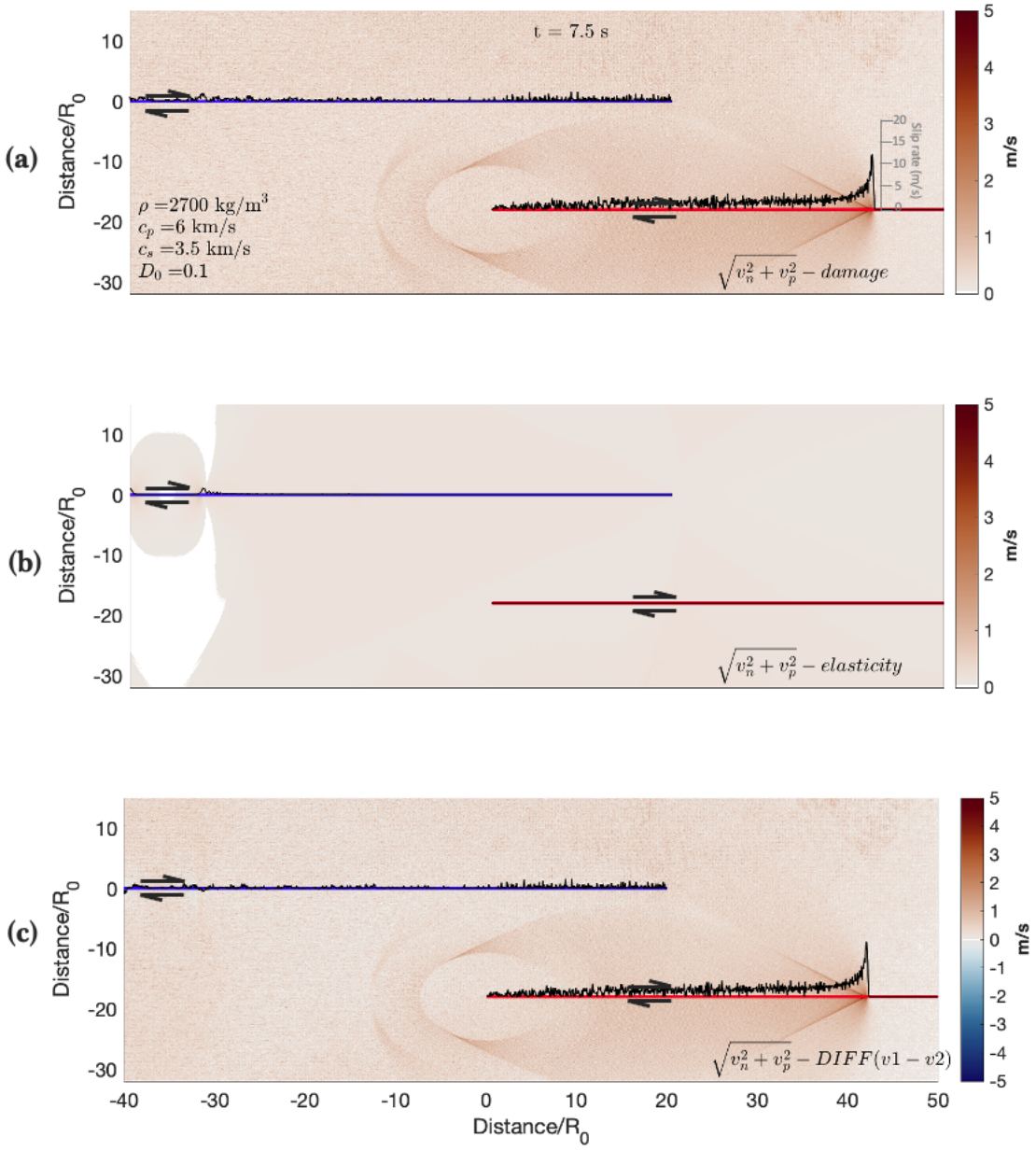

Figure 3.6: **Snapshot of particle velocity for dynamic earthquake rupture simulations in strike-slip step-over faults** at a time after the earthquake nucleation at the second fault, for case with (a) dynamic off-fault damage and (b) elastic off-fault medium. (c) Difference between the two models. Parameters are based on Case A **(stepwidth=4.5km)** from *Harris and Day* (1993). Strike-slip faults are represented by straight lines colored in blue (first fault) and red (second fault). Slip-rate on the fault (black curves) is superimposed on the snapshots.

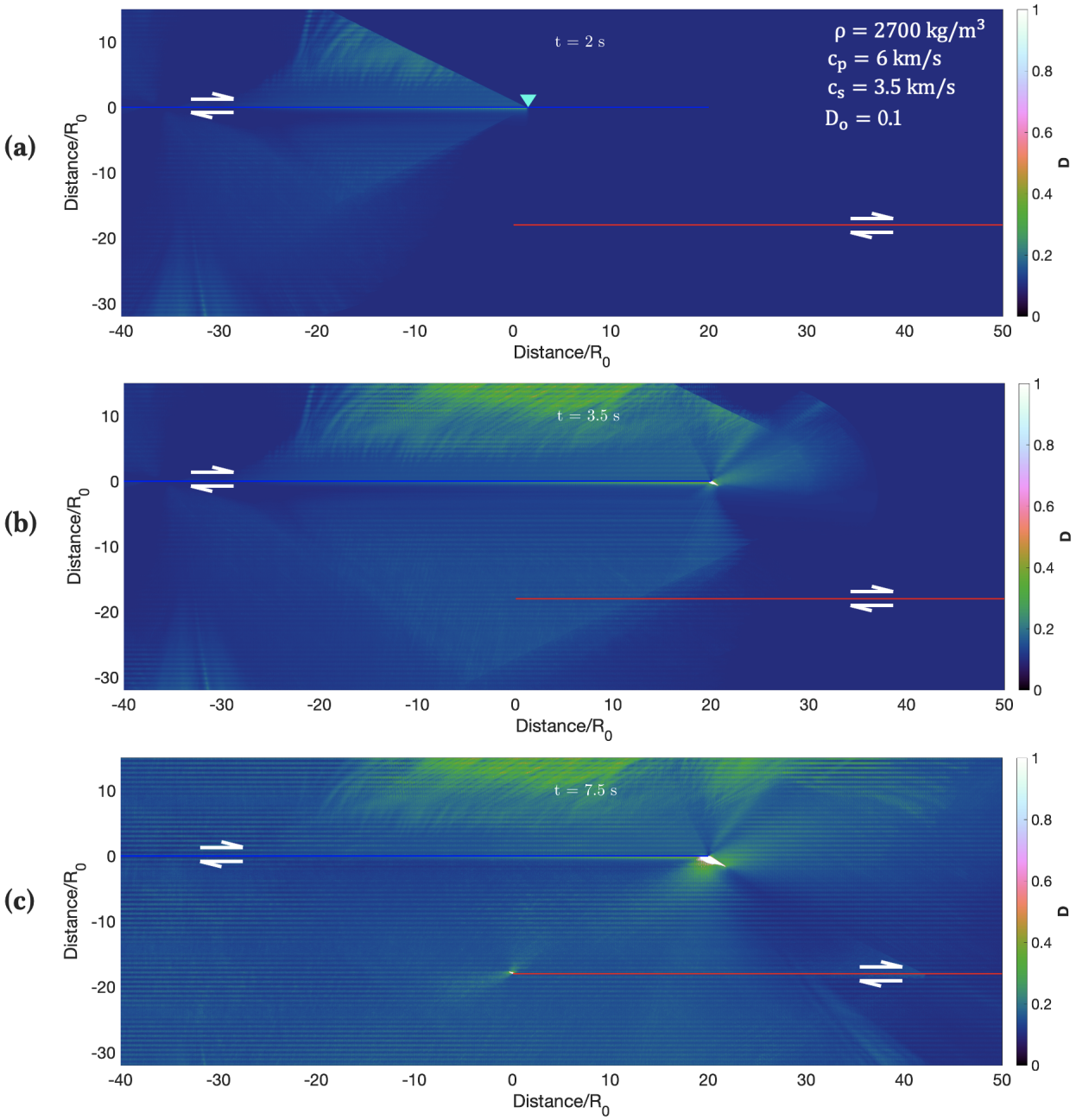

Figure 3.7: **Snapshot of damage state for dynamic earthquake rupture simulation in strike-slip step-over faults** at a time (a) before and (b) during the earthquake arrest at the first fault, and (c) after the earthquake nucleation at the second fault. Strike-slip faults are represented by straight lines colored in blue (first fault) and red (second fault). Rupture tips are denoted by the inverted (cyan) triangle.

3.3 Discussion

We now can discuss with the all results of jumping rupture for different cases of stepwidth at both compressional and extensional system. The location and time at which rupture jumped at the second fault are shown in summarising figures 3.8 and 3.9, respectively. In y-axis, negative sign of the perpendicular distance (i.e. stepwidth) from fault 1 corresponds to compresssional system whereas positive sign corresponds to extensional system. Regarding the earthquake rupture simulations for elastic medium, the overall comparison shows that there is a quite good match between our simulations and results from *Harris and Day* (1993). The slight mismatch between both models of elastic cases are related to the difference of spatial and time resolution. For instance, the grid spacing for our own simulations is 25 m ($= R_0/10$) whereas grid spacing in *Harris and Day* (1993) is 250 m. It means that the spatial resolution of our own simulation is 10 times larger than resolution in *Harris and Day* (1993). On the other side, damage cases, in general, do not show significant difference with respect to simulations of elastic cases. This is attributed to the absence of significant damage evolution so that the off-fault medium behaves quite close to elastic material. Besides, comparing damage and elastic cases there is slight difference in location and time of earthquake nucleation at the second fault for cases of extensional step-over faults with stepwidth greater than 4 km. We consider that at shorter stepwidths, stress distribution at the edge of the first fault due to the overall deformation (related to static effects) dominates the mechanism for jumping rupture but at larger stepwidth, dynamic effects predominates on the influence for jumping rupture. Dynamic effects can impact in different ways since they are sensitive to different dynamic mechanisms such as the impact of supershear rupture front on the off-fault damage medium, the stopping-phase propagation through the off-fault damage zone or the impact of the stopping phase from the left end of the first fault.

The lack of significant off-fault damage evolution in all dynamic simulations does not allow to proper analyse the damage effects on earthquake rupture. *Poliakov et al.* (2002) analysed the influence of the angle ψ on the stress distribution around a crack tip in static and dynamic crack models based in linear elastic fracture mechanics (LEFM). The aim of this study focused on estimating the favored direction of right-lateral shear along fault bends or secondary faulting by analysing at which orientation around a crack tip the Coulomb failure criteria is satisfied. This favored direction can be related to predict the spatial extent of off-fault damage evolution in our study. They stated that at low angle $\psi < 45^o$, compressional and extensional side are encouraged to allow rupture propagation through fault branching; whereas at high angle $\psi > 45^o$, only extensional side is favored and higher encouraged than in lower angle ψ. Furthermore, based on dynamic crack models, *Poliakov et al.* (2002) observed that the difference between the two cases of angle ψ is remarkably stronger at higher rupture velocity at the crack tip. *Templeton and Rice* (2008) conducted a series of rupture simulations based on dynamic finite element method to analyse the spatial extent of off-fault plastic deformation varying the angle ψ. They provided similar conclusion as *Poliakov et al.* (2002), the lower the angle ψ, the lower the extension of off-fault damage at the tensional side of the fault. Based on previous studies, the absence of significant damage in our simulations can be attributed to the value of the angle ψ. In our case with $\psi = 15^o$, it implies almost negligible damage evolution at the tensional side. Hence, we needed to propose another set of parameters so that the evolution of dynamic damage can be properly analysed.

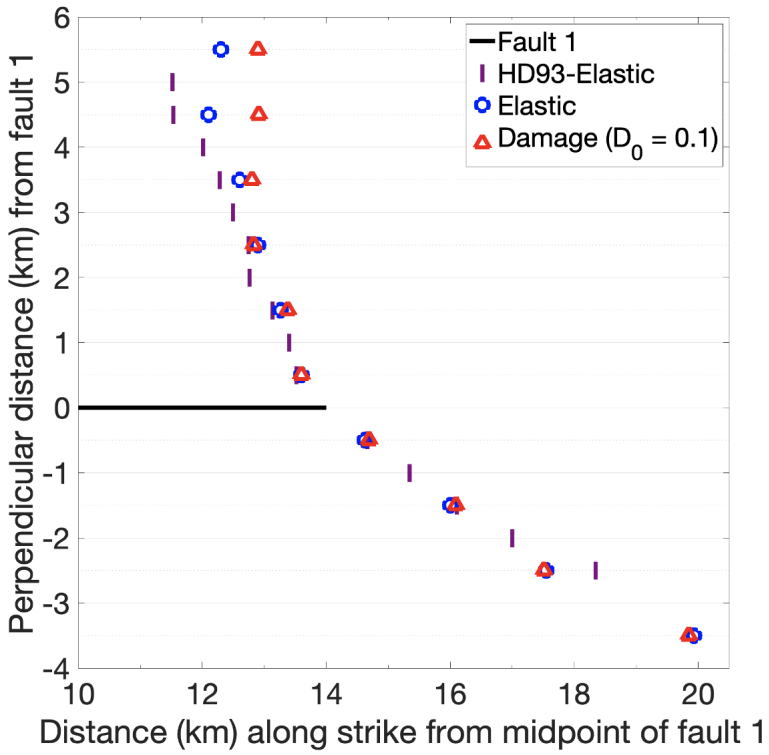

Figure 3.8: **Triggering location at the second fault**. Comparison of elastic-case results (in colour purple) from *Harris and Day* (1993) with my own results for elastic case (in colour blue) and damage case (in colour red). In axis Y, negative values of perpendicular distance represent stepwidth for step-over compressional setup, positives values represent stepwidth for step-over extensional setup.

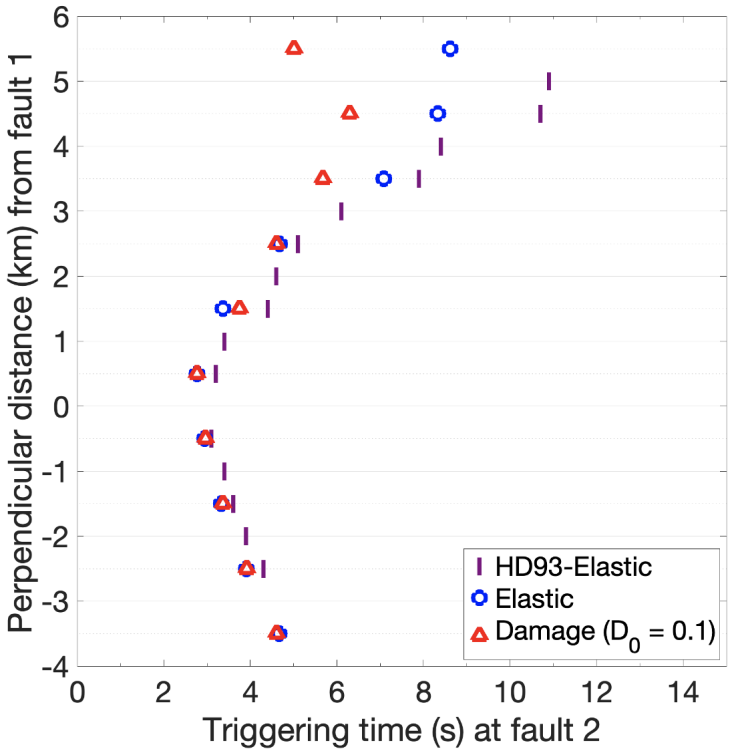

Figure 3.9: **Triggering time at the second fault**. Comparison of elastic-case results (in colour purple) from *Harris and Day* (1993) with my own results for elastic case (in colour blue) and damage case (in colour red). In axis Y, negative values of perpendicular distance represent stepwidth for step-over compressional setup, positives values represent stepwidth for step-over extensional setup.

Regarding damage evolution at the compressional side, we observe a particular damage feature that corresponds to an increase of damage at distances ($> 2R_0$) far away from the fault at the compressional side of the first fault. This damage feature is observed in all our simulations (see figure 3.10). We consider that this emergence of off-fault damage can be attributed to two factors: 1. Initial off-fault microcracks are highly prone to fracturing and 2. Supershear Mach front can potentially contribute as a additional source of off-fault damage.

The first factor is related to the initial damage condition which considers that stress loading at the off-fault microcracks is not high enough to allow them to slide, i.e. initial state of the off-fault medium corresponds to an elastic material. This condition corresponds to Regime 1 in the micromechanical model explained in chapter 2 (also in *Bhat et al.*, 2012), whereas Regime 2 corresponds to the growth of damage by the sliding of the microcracks. At the initial damage state, the closeness to the transition from Regime 1 to Regime 2 is sensitive to the angle ψ (initial stress field orientation) and the static friction coefficient at the microcracks $f_{s,crack}$ since they influence in determining whether or not the failure criteria at the initial off-fault microcracks is satisfied. These two values have been already rigorously constrained in this study ($\psi = 15^o$ and $f_{s,crack} = 0.8$) and they correspond to the most appropriate case that allows the initial state of damage to be at Regime 1. However, we notice that the initial state of off-fault microcracks are close to the transition to Regime 2; i.e. off-fault microcracks are highly prone to fracturing.

The second factor is associated to a potential source of damage: Supershear Mach front. As observed in this chapter, the growth of damage can be allowed due to three sources: 1. Velocity rupture tip, 2. Supershear Mach front and 3. Stopping phase. We focused in this part at the effect of the second source of damage. Some studies have remarked that there is a potential influence of the Supershear Mach front on

far-field features such as on the strong ground motion and off-fault damage at larger distances away from the fault (*Bernard and Baumont*, 2005; *Bhat et al.*, 2007; *Dunham and Bhat*, 2008). *Bhat et al.* (2007) studied a region of damage away from the fault using a elastodynamic supershear slip pulse model analysing the perturbation of normal stress around the rupture tip. In figure 3.11, we did a similar exploration for our study. This figure shows the normal stress perturbation (normalized by the dynamic stress drop) at three time steps from the earthquake nucleation at the first fault. Colorbar indicates that normal extensional stress perturbation corresponds to positive values (in colors, from white to red) and normal compressional stress perturbation corresponds to negative values (in colors, from white to blue). We observe that behind the Mach front at the compressional side, there is a band that allows tensional deformation. *Bhat et al.* (2007) suggested that this non-attenuated tensional band formed behind the supershear Mach front could potentially trigger off-fault damage far away from the fault. We observe in our results that close and parallel to the fault there is no damage due to the presence of a high compressional stress (colored in darker blue) close to the rupture tip. However, at a distance away from the fault, there is the attenuation of the compressional stress allowing the tensional band to generate damage. In particular, at time t = 1.0 s (see figure 3.11 a), there is not still evolution of damage since the tensional band is not enough defined due to the compressional stress influence (colored in darker blue) from the subshear front. But as time passes (see figure 3.11 b-c), there is no longer influence of the subshear front on the tensional band so that damage away from the fault can evolve. It worth mentioning that if off-fault microcracks are highly prone to sliding (previous-mentioned first factor), there is higher impact of the tensional band of the Mach front on damage evolution. This generation of off-fault damage away from the fault can potentially influence on the earthquake rupture propagation and on the role of stepovers.

In overall, previous discussion helps us to define some conditions to proper analyse the effect of damage on stepover faults. First, we require to constrain the angle ψ (initial stress field orientation) so that it can allow significant evolution of damage. Second, we require to explore the regime of subshear rupture because not only the most observed type of rupture is subshear ($S > 1.77$) but also to avoid any additional complex damage features involved in supershear rupture that can influence on the role of stepovers.

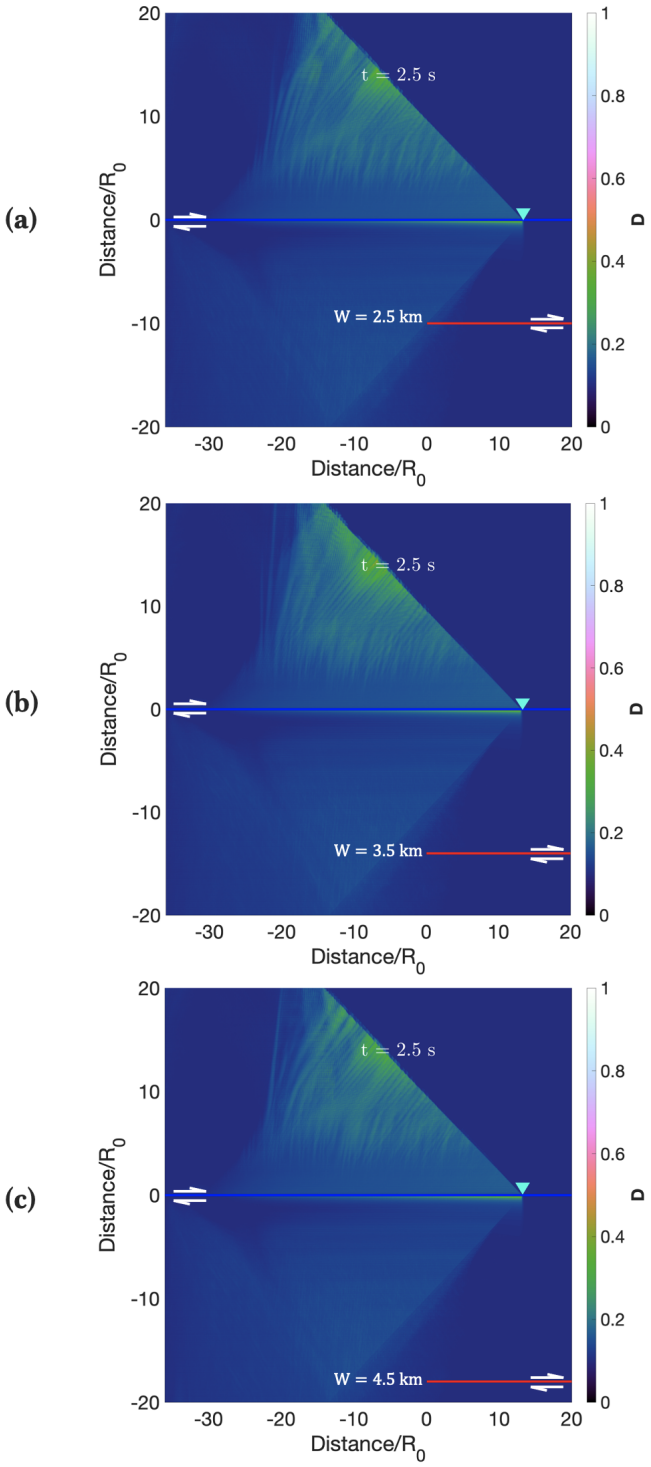

Figure 3.10: **Damage state for dynamic earthquake rupture simulation with dynamic off-fault damage in step-over faults: Observation of dynamic off-fault damage away from the fault**. Snapshots of damage state at time = 2.5 s (before jumping rupture) for three different cases with stepwidth (a) 2.5 km, (b) 3.5 km and (c) 4.5 km. Strike-slip faults are represented by straight lines colored in blue (first fault) and red (second fault). Rupture tips are denoted by the inverted (cyan) triangle.

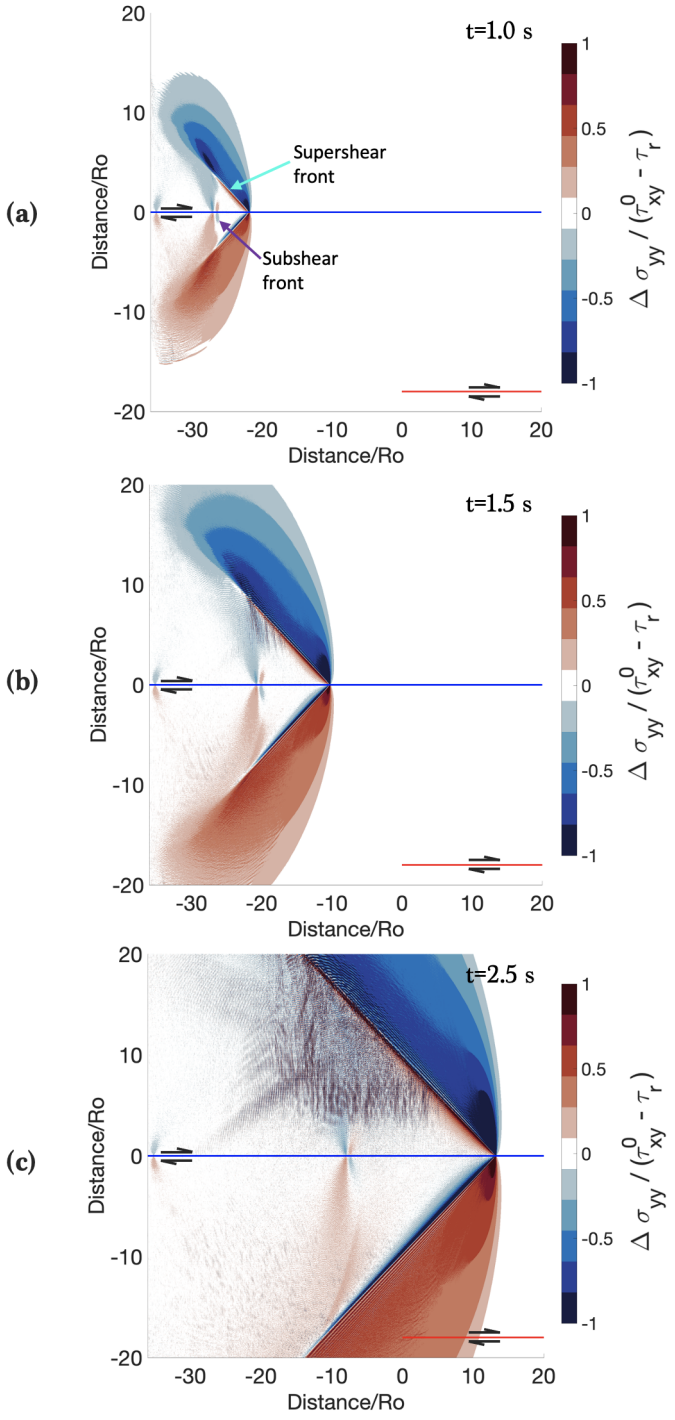

Figure 3.11: **Perturbation in fault normal stress $\Delta\sigma_{yy}$ for earthquake rupture simulation with dynamic off-fault damage in step-over faults: Observation of dynamic off-fault damage away from the fault**. Perturbation in fault normal stress (normalized by the dynamic stress drop) for case of step-over fault with stepwidth 4.5 km at time (a) 1.0 s, (b) 1.5 s and (c) 2.5 s. Strike-slip faults are represented by straight lines colored in blue (first fault) and red (second fault).

Chapter 4

Theoretical analysis for jumping rupture on step-over faults

4.1 Introduction

As discussed in chapter 3, we observed two main issues in the evaluation of dynamic earthquake rupture simulations with off-fault damage based on parameters from *Harris and Day* (1993): 1. Lack of significant off-fault damage evolution attributed to the influence of the angle ψ (orientation of the initial stress field respect to the fault strike) and 2. Supershear rupture provides an additional complexity on the evolution of off-fault damage. Due to these conditions, we need to propose another set of parameters to properly analyse the effect of dynamic damage. Since there is an enormous set of parameters, we require to apply a theoretical analysis in order to constrain their values. Besides, the strongest change of stress is due to accumulation of slip (static effect) at the first fault. Therefore, we perform an static analysis that allows us to estimate the stress field at the tip of the first fault at the rupture arrest. This theoretical analysis based on linear elastic fracture mechanics (LEFM) follows the analytical approach presented in *Fliss et al.* (2005).

Fliss et al. (2005) analysed the mechanisms that relates earthquake rupture directivity and fault branching. A backward branch is a branch fault oriented with an obtuse angle respect to the direction of the main rupture propagation. In particular, this case of fault branching is analysed for the 1992 Landers, California, earthquake. The research question in *Fliss et al.* (2005) aimed to provide the mechanisms that allows the main rupture to propagate through a backward branch. Since theoretical work by *Poliakov et al.* (2002) does not support this behavior of rupture propagation for backward branching, *Fliss et al.* (2005) addressed this study by assuming that the branch fault is a neighboring strand disconnected from the main fault. From this condition, it was proposed that after the earthquake arrests at the main fault, the stress distribution around the main-fault edge allows the earthquake triggering at the neighbouring strand. This mechanism is analysed numerically by two models: 1. Elastostatic singular crack modeling based on linear elastic fracture mechanics (LEFM) and 2. Elastodynamic rupture modeling based on boundary integral equation (BIE) method. The first model corresponds to a theoretical approach that aims to analyse the stress distribution around a crack tip after its motion (static solution) so that a maximum distance of jumping rupture can be constrained. The second model explores the dynamic solution so that they could analyse the influence of dynamic effects for the earthquake nucleation and propagation at the second fault. By this analysis, *Fliss et al.* (2005) provided the guidelines to analyse the mechanism that allows the earthquake rupture to propagate to a backward branch.

In this chapter, the theoretical approach proposed by *Fliss et al.* (2005) is applied for the analysis of jumping rupture in step-over faults and extended to the cases of a secondary fault with different horizontal orientation respect to the strike of the first fault. This orientation is defined by the angle ω with values that correspond to the interval $[-\pi/2, \pi/2]$. For a fault oriented at an angle ω (see Figure 4.2), we define the Coulomb stress and the stress drop as a function of the stress field σ_{ij}, the static

friction coefficient f_s and the residual friction coefficient f_r. The Coulomb stress is given by $\sigma_c(f_s, \omega) = \sigma_{r\omega} + f_s\sigma_{\omega\omega}$ with its initial value $\sigma_c^0(f_s, \omega) = \sigma_{r\omega}^0 + f_s\sigma_{\omega\omega}^0$. Besides, the stress drop is defined as $\sigma_c^0(f_r, \omega) = \sigma_{r\omega}^0 + f_r\sigma_{\omega\omega}^0$.

The theoretical analysis is done in 2 steps:

- Firstly, based on linear elastic fracture mechanics for sliding mode (e.g. *Rice*, 1968), we can get the stress field σ_{ij} around the tip of a finite brittle crack embedded in a linear elastic material subjected to an initial stress field σ_{ij}^0 (see Figure 4.1). This approximation of the stress field corresponds to the state after the sliding of the crack, i.e. at the arrest of the motion. This static study allows us to analyse how the stress state at the rupture arrest can potentially trigger a dynamic rupture on a secondary fault.

- We then calculate the Coulomb stress $\sigma_c(f_s, \omega)$ for any case of second fault orientation ω by rotating the stress field at angle ω (see Figure 4.2). Where $\sigma_c(f_s, \omega) = \sigma_{r\omega} + f_s\sigma_{\omega\omega}$. We can get the expression of the maximum jumpable distance, for compressional and extensional system, $H_{max}^{c/e}(\sigma_{ij}^0, \omega, f_s, f_r)$ as a function of the initial stress field, the second fault orientation and the frictional parameters (see Equation 4.11).

4.2 Methodology

4.2.1 Linear Elastic Fracture Mechanics

Consider the presence of a finite crack of lenght L embedded in a elastic medium subjected to an initial stress field σ_{ij}^0. We consider the in-plane shearing mode which corresponds to the sliding of the crack faces in a direction perpendicular to the crack front (see Figure 4.1).

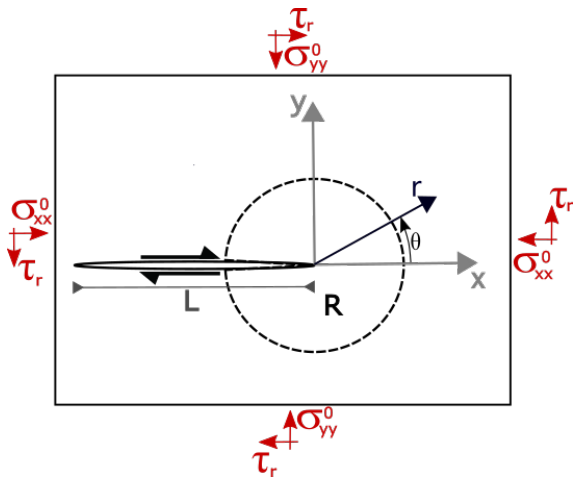

Figure 4.1: **Crack of finite length L subjected to an initial stress field σ_{ij}^0 under plane strain conditions (*Rice*, 1968).** R represents near crack tip region.

Following the elastic crack theory (e.g. *Rice*, 1968), at the stage that represents the rupture arrest, we can get the stress field σ_{ij} around the crack tip for a singular crack model.

$$\sigma_{ij} = \frac{K_{II}}{\sqrt{2\pi r}}\Sigma_{ij}(\theta) + \begin{pmatrix} \sigma_{xx}^0 & \tau_r \\ \tau_r & \sigma_{yy}^0 \end{pmatrix} + O(\sqrt{r}) \tag{4.1}$$

where r, θ are polar coordinates with the origin of the coordinate plane located at the crack tip. Regarding the initial stress state, this theoretical approximation considers that residual stress is set up all along the crack. Based on this condition, residual stress $\tau_r = -f_r\sigma_{yy}^0$ is used as initial shear stress. Moreover, as we can observe in the equation 4.1, singularity refers to the infinite stresses located at the

crack tip, .i.e. $r \sim 0$. $\Sigma_{ij}(\theta)$ is a dimensionless function that represents the angular dependence of the stress field at the crack-tip region,

$$\begin{pmatrix} \Sigma_{xx} \\ \Sigma_{xy} \\ \Sigma_{yy} \end{pmatrix} = \begin{pmatrix} -\sin\frac{\theta}{2}[2+\cos\frac{\theta}{2}\cos\frac{3\theta}{2}] \\ \cos\frac{\theta}{2}[1-\sin\frac{\theta}{2}\sin\frac{3\theta}{2}] \\ \sin\frac{\theta}{2}\cos\frac{\theta}{2}\cos\frac{3\theta}{2} \end{pmatrix} \tag{4.2}$$

K_{II} is a mode II (inplane sliding) stress intensity factor

$$K_{II} = \Delta\tau\sqrt{\frac{\pi L}{2}} \tag{4.3}$$

where $\Delta\tau$ is the stress drop.

$O(\sqrt{r})$ represents higher order terms.

4.2.2 Maximum jumpable distance

We can get an analytical expression for maximum jumpable distance H_{max} for a potential secondary fault oriented at angle ω. We start considering an analysis for two parallel faults so that the orientation of the second fault defined by the angle $\omega = 0^o$. Following the analytical approach by *Fliss et al.* (2005), we can expand the Coulomb stress ($\sigma_c(f_s, 0) = \sigma_{xy} + f_s\sigma_{yy}$) using the equation 4.1

$$\sigma_c(f_s, 0) = \frac{K_{II}}{\sqrt{2\pi r}}\Sigma_{xy}(\theta) + \tau_r + f_s\left[\frac{K_{II}}{\sqrt{2\pi r}}\Sigma_{yy}(\theta) + \sigma^0_{yy}\right] \tag{4.4}$$

then we use equation 4.3 for the stress intensity factor K_{II} and consider the peak stress $\tau_p = -f_s\sigma^0_{yy}$ to obtain the expression

$$\sigma_c(f_s, 0) = \frac{\Delta\tau}{2}\sqrt{\frac{L}{r}}\left[\Sigma_{xy}(\theta) + f_s\Sigma_{yy}(\theta)\right] + \left(\tau_r - \tau_p\right) \tag{4.5}$$

Considering $|y| = r|\sin\theta|$ and noting that

$$1 + S = \frac{\tau_p - \tau_r}{\Delta\tau} \tag{4.6}$$

where S is the seismic ratio defined by *Andrews* (1976) and *Das and Aki* (1977), we obtain the following expression

$$\frac{\sigma_c(f_s, 0)}{\Delta\tau} = \sqrt{\frac{L}{|y|}} F(f_s, \theta) - (1 + S) \tag{4.7}$$

where

$$F(f_s, \theta) = \frac{\sqrt{|\sin(\theta)|}}{2} \left[\Sigma_{xy}(\theta) + f_s \Sigma_{yy}(\theta)\right] \tag{4.8}$$

The largest distance $|y|$ designated hereafter as the maximum jumpable distance H_{max} corresponds to the case when the right side of the equation 4.7 is zero. In other words, it corresponds at the largest distance where there is enough shear stress to overcome the frictional strength at a potential secondary fault, i.e. where Coulomb stress is zero. The expression 4.7 is also a function of θ as encapsulated by $F(f_s, \theta)$. This function is bounded and has two local maxima in the $(0, \pi]$ and $[-\pi, 0)$ intervals. These correspond to the compressional and extensional sides of the fault respectively. Let F^c_{max} be the value on the compressional side and F^e_{max} on the extensional one. This implies to consider the maximum values of equation 4.8, $F^{c/e}_{max}$, leading to an expression for the maximum jumpable distance, as expressed by *Fliss et al.* (2005)

$$\frac{H^{c/e}_{max}}{L} = \left(\frac{F^{c/e}_{max}}{1 + S}\right)^2 \tag{4.9}$$

From previous equation, we can observe the influence of the S ratio and the fault length L on the maximum jumpable distance. For instance, the lower the S ratio is, the larger the maximum jumpable distance $H^{c/e}_{max}$ is allowed. We can generalize the expression 4.9 for $H^{c/e}_{max}$ to any orientation ω of the second fault by expressing the stress field σ_{ij} around the crack-tip respect to the angle ω (see Figure 4.2).

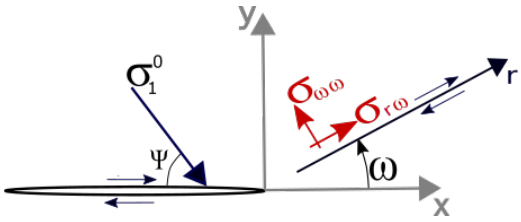

Figure 4.2: **Stresses $(\sigma_{\omega\omega}, \sigma_{r\omega})$ on a potential secondary fault oriented at angle ω.** The orientation of the maximum principal stress σ_1 at the crack is defined by the angle ψ.

To get the stress field for an orientation ω, we can apply the following relations

$$\begin{aligned} \sigma_{rr} + \sigma_{\omega\omega} &= \sigma_{xx} + \sigma_{yy} \\ \sigma_{\omega\omega} - \sigma_{rr} + 2i\sigma_{r\omega} &= e^{2i\omega}(\sigma_{yy} - \sigma_{xx} + 2i\sigma_{xy}) \end{aligned} \tag{4.10}$$

After taking into account the above equation, we get the maximum jumpable distance $H_{max}^{c/e}$ for any orientation ω of the second fault as a function of the initial stress field σ_{ij}^0, static friction coefficient f_s, residual friction coefficient f_r and the orientation ω

$$\frac{H_{max}^{c/e}(\sigma_{ij}^0, \omega, f_s, f_r)}{L} = (F_{max}^{c/e})^2 \left[\frac{\sigma_c^0(f_r, 0)}{\sigma_c^0(f_s, \omega)}\right]^2 \tag{4.11}$$

Note that

$\sigma_c^0(f_r, 0) = \Delta\tau$ is the stress drop on the first fault,

$\sigma_c^0(f_s, \omega) = \sigma_{r\omega}^0 + f_s\sigma_{\omega\omega}^0$ is the initial Coulomb stress for a potential secondary fault oriented at angle ω

We consider three conditions to constrain the values of $H_{max}^{c/e}$

1. We reject cases with positive values of initial Coulomb stress ($\sigma_c^0(f_s, \omega) = \sigma_{r\omega}^0 + f_s\sigma_{\omega\omega}^0 > 0$) because this condition means that the second fault is prone to sliding before the earthquake nucleation at the first fault.

2. We also reject cases with values of initial Coulomb stress close to zero since this condition implies unreal large values of maximum jumpable distance (see equation 4.11). Therefore, we set up the upper limit of $H_{max}^{c/e}$ as 0.3 times the fault length L ($L = 28km$ as in *Harris and Day* (1993)). The factor 0.3, in our case, produces the maximum jumpable distance equals 8.4 km. This value corresponds to the range of largest stepwidths reported and analysed in earthquake rupture studies (e.g. *Klinger*, 2005; *Wesnousky*, 2006, 2008; *Finzi and Langer*, 2012b).

3. The lower limit of $H_{max}^{c/e}$ is set up considering that the lowest stepwidth analysed in geological observations of step-over faults is about 1 km (e.g. *Wesnousky*, 2008; *Biasi and Wesnousky*, 2016). To properly define this value in our numerical analysis, we consider that the lower limit of $H_{max}^{c/e}$ equals the element size of the lowest resolution in dynamic rupture simulation. Hence, the lower limit is $R_o/4$ (R_o is the process zone size). This is the minimum value of the element size that allows the process zone size R_o to be properly solved in dynamic rupture simulations.

Hence we have the following expressions based on the above-mentioned constraints

$$\begin{aligned} \frac{R_o}{4} < H_{max}^{c/e}(\sigma_{ij}^0, \omega, f_s, f_r) < 0.3L \\ \sigma_c^0(f_s, \omega) < 0 \end{aligned} \tag{4.12}$$

4.3 Results

Based on the static analysis developed in previous section, we can now explore the maximum jumpable distance $H^{c/e}_{max}(\sigma^0_{ij}, \omega, f_s, f_r)$ for different cases of initial stress field, second fault orientation and frictional coefficients. For this evaluation, we consider the elastic properties (ρ,c_s,c_p) of granite and depth 2km. Besides, since the most observed type of rupture is subshear ($S > 1.77$), we evaluate the seismic ratio for $S = 2$ (see Table 4.1). After setting the previous parameters, the orientation of the initial stress field respect to the fault strike, defined by the angle ψ, can represent the influence of the initial stress field σ^0_{ij}. Therefore, the maximum jumpable distance is expressed hereafter as $H^{c/e}_{max}(\psi, \omega, f_s, f_r)$.

Figures 4.3 - 4.6 show the exploration of static solution for maximum jumpable distance $H^{c/e}_{max}(\psi, \omega)$. We considered the two cases of stepover system which correspond when the secondary fault is either at the compressional (Figures 4.3 and 4.5) or at the extensional (Figures 4.4 and 4.6) side of the brittle crack. Static friction coefficient f_s is set up as 0.6 since it is an average value observed in brittle faults (e.g. *Byerlee*, 1978; *Yamashita et al.*, 2004). Regarding residual friction coefficient f_r, we explored the values 0.1 and 0.3. These are the limiting values observed in experimental studies when rupture tip approaches the dynamic steady-state which is given when slip rate reaches the range between 0.1 and 1 ms^{-1} (see Figure 7 and 8 in *Wibberley et al.* (2008)). Besides, selected values of residual friction coefficient f_r have been also evaluated in numerical studies on earthquake rupture dynamics (e.g. *Harris and Day*, 1993; *Fliss et al.*, 2005; *Bhat et al.*, 2012; *Thomas and Bhat*, 2018).

Parameter	Symbol	Value
Depth	z	2.0 km
Orientation of maximum principal stress σ_1^0	ψ	$< 0^o, 90^o >$
Orientation of potential secondary fault	ω	$< -90^o, 90^o >$
Static coefficient of friction	f_s	0.6
Residual coefficient of friction	f_r	$[0.1, 0.3]$
Seismic ratio	S	2

Table 4.1: Parameters for evaluation of the static solution of maximum jumpable distance $H_{max}^{c/e}(\psi, \omega, f_s, f_r)$

The maximum jumpable distance is limited as in expression 4.12. Besides, we identify the cases that correspond to strike-slip faulting applying the condition provided by *Jeandet-Ribes et al.* (2023). Consider σ_1 and σ_3 be the maximum and minimum in-plane principal stresses, respectively; whereas σ_2 is the principal stress with out-of-plane direction. *Jeandet-Ribes et al.* (2023) remarked that if the inequality $\sigma_1 < \sigma_2 < \sigma_3$ (stresses are negative in compression) for 3D initial stress state is not satisfied in 2D in-plane simulations, the initial stress field would favor reverse faulting instead of strike-slip motion. This condition was expressed in the following manner:

Consider the initial stress state

$$\sigma_{ij}^0 = \begin{pmatrix} \sigma_{xx}^0 & \sigma_{xy}^0 & 0 \\ \sigma_{xy}^0 & \sigma_{yy}^0 & 0 \\ 0 & 0 & \sigma_{zz}^0 \end{pmatrix} \tag{4.13}$$

and the following ratios

$$\gamma = \frac{\sigma_{xx}^0}{\sigma_{yy}^0} \quad \& \quad \mu_o = \frac{\sigma_{xy}^0}{-\sigma_{yy}^0} \tag{4.14}$$

The initial stress state σ_{ij}^0 that favors the strike-slip motion must satisfy the following inequality (ν is the Poisson's ratio):

$$1 - 2\nu < \sqrt{\left(\frac{\gamma - 1}{\gamma + 1}\right)^2 + \frac{4\mu_o^2}{(\gamma + 1)^2}} < 1 \tag{4.15}$$

Based on previous condition, the grey area in our results represents the forbidden area to analyse strike-slip system since the initial stress field does not verify the inequality 4.15.

On the other hand, the red area corresponds to the cases with positive initial Coulomb stress at the second fault. It means the second fault is already prone to sliding before the earthquake initiates at the first fault. This condition is rejected since does not correspond to the case of jumping rupture.

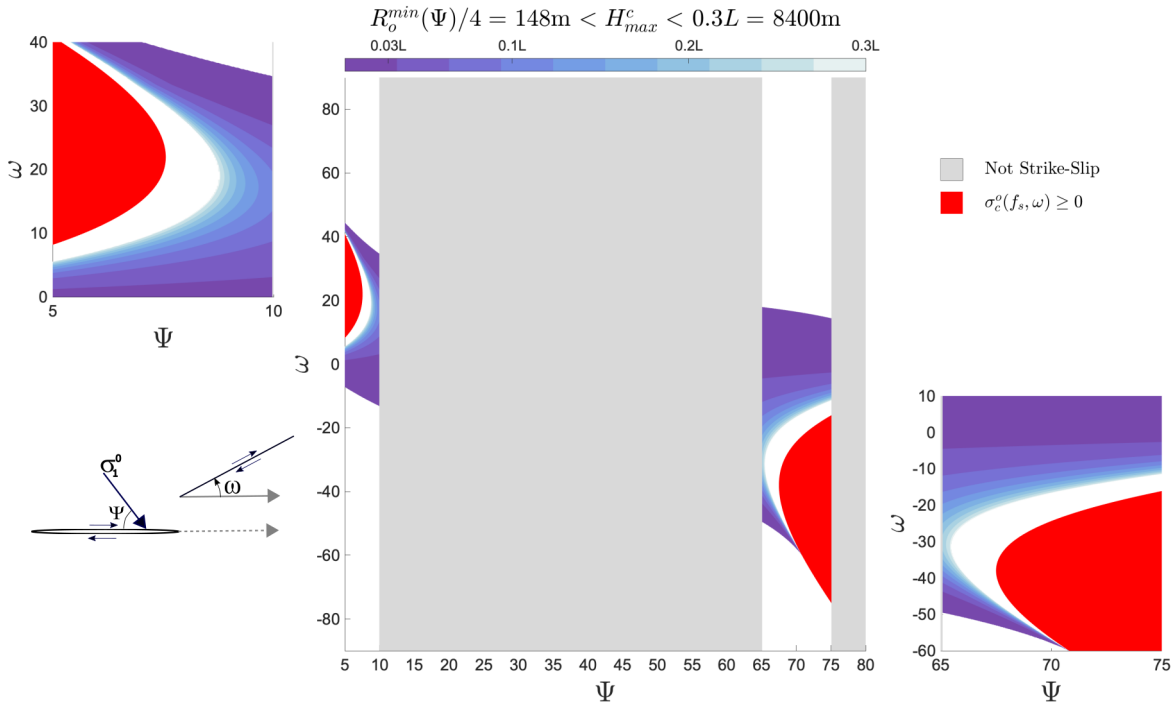

Figure 4.3: **Compressional side: Maximum jumpable distance H^c_{max} respect to initial stress orientation at the first fault (angle Ψ) and orientation of the second fault (angle ω). Case for $S = 2$, $f_s = 0.6$ and $f_r = 0.1$.** Plots show results for cases where the second fault is located at the compressional side of the first fault (see schematic of the step-over system). H^c_{max} is normalized by the length of the first fault L (L=28km). Gray region corresponds to the cases where initial stress field does not favor strike-slip motion (*Jeandet-Ribes et al.*, 2023). Red area represents cases where initial Coulomb stress $\sigma_c^0(f_s, \omega)$ at the second fault is positive. Minimum process zone size $R_o^{min}(\Psi) = 592$ m.

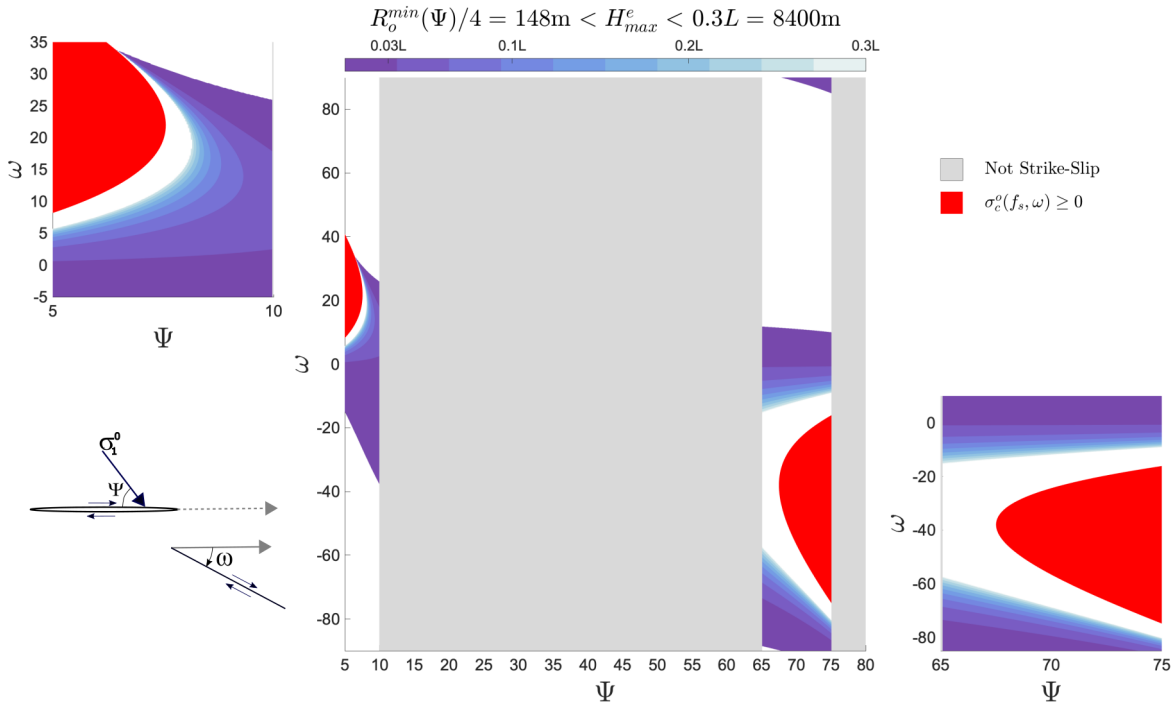

Figure 4.4: **Extensional side: Maximum jumpable distance H^e_{max} respect to initial stress orientation at the first fault (angle Ψ) and orientation of the second fault (angle ω). Case for $S = 2$, $f_s = 0.6$ and $f_r = 0.1$.** Plots show results for cases where the second fault is located at the extensional side of the first fault (see schematic of the step-over system). H^e_{max} is normalized by the length of the first fault L(L=28km). Gray region corresponds to the cases where initial stress field does not favor strike-slip motion (*Jeandet-Ribes et al.*, 2023). Red area represents cases where initial Coulomb stress $\sigma_c^0(f_s, \omega)$ at the second fault is positive. Minimum process zone size $R_o^{min}(\Psi) = 592$ m.

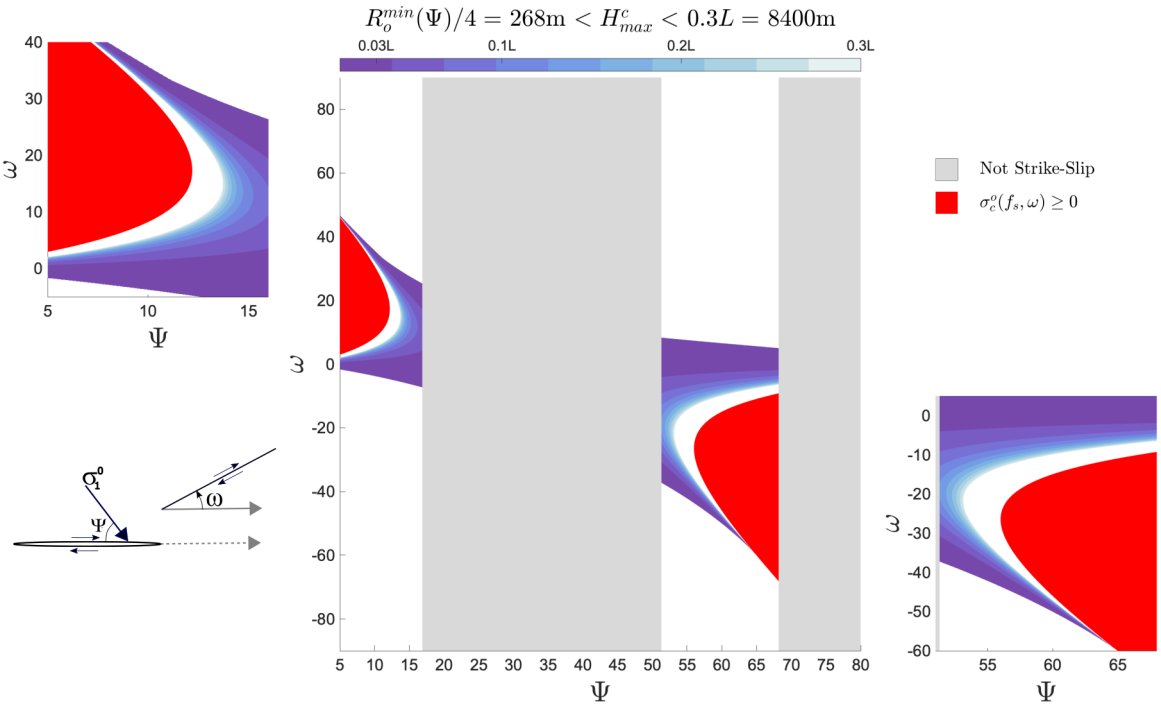

Figure 4.5: **Compressional side: Maximum jumpable distance H^c_{max} respect to initial stress orientation at the first fault (angle Ψ) and orientation of the second fault (angle ω). Case for $S = 2$, $f_s = 0.6$ and $f_r = 0.3$.** Plots show results for cases where the second fault is located at the compressional side of the first fault (see schematic of the step-over system). H^c_{max} is normalized by the length of the first fault L (L=28km). Gray region corresponds to the cases where initial stress field does not favor strike-slip motion (*Jeandet-Ribes et al.*, 2023). Red area represents cases where initial Coulomb stress $\sigma_c^0(f_s,\omega)$ at the second fault is positive. Minimum process zone size $R_o^{min}(\Psi) = 1072$ m.

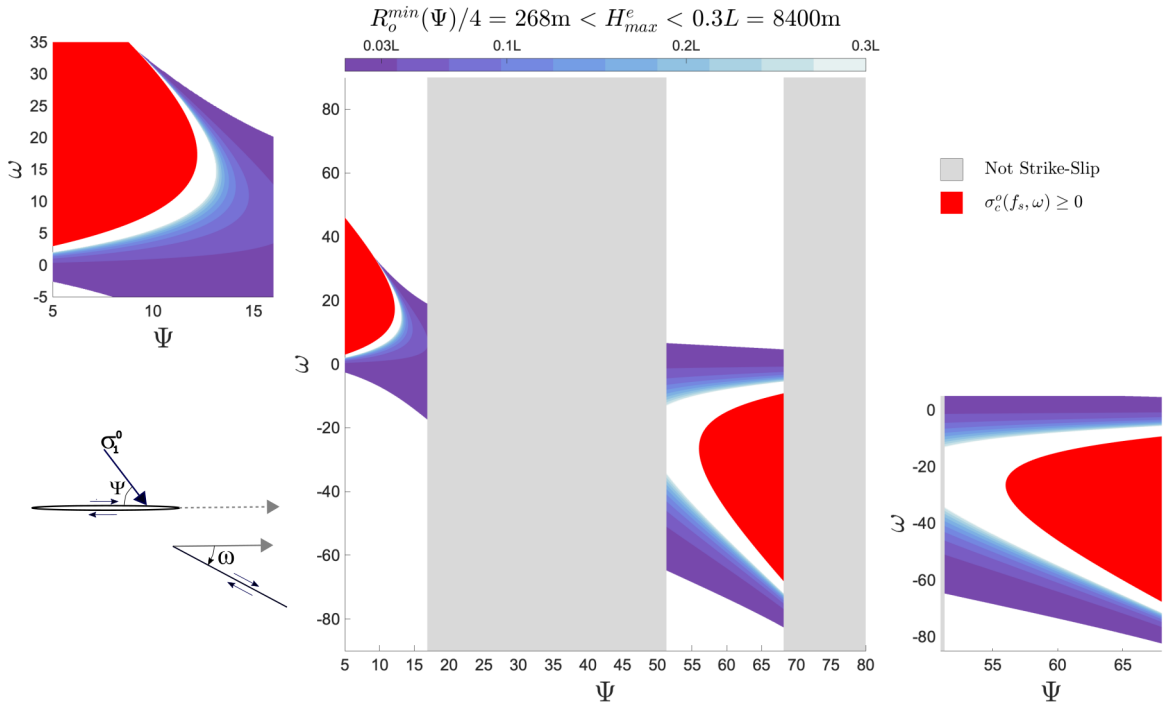

Figure 4.6: **Extensional side: Maximum jumpable distance H_{max}^e respect to initial stress orientation at the first fault (angle Ψ) and orientation of the second fault (angle ω). Case for $S = 2$, $f_s = 0.6$ and $f_r = 0.3$.** Plots show results for cases where the second fault is located at the extensional side of the first fault (see schematic of the step-over system). H_{max}^c is normalized by the length of the first fault L (L=28km). Gray region corresponds to the cases where initial stress field does not favor strike-slip motion (*Jeandet-Ribes et al.*, 2023). Red area represents cases where initial Coulomb stress $\sigma_c^0(f_s, \omega)$ at the second fault is positive. Minimum process zone size $R_o^{min}(\Psi) = 1072$ m.

4.4 Discussion

An interesting analysis is the comparison between the static and dynamic solutions. However, limitations of linear elastic fracture mechanics such as the unrealistic infinite stresses and strains at the crack tip do not allow the direct comparison with dynamic solutions. For a proper comparison, the static solution needs to be adjusted by the maximum cumulative slip obtained on dynamic simulation.

To adjust the maximum cumulative slip Δu_{max} for the theoretical approach, we need to get the expression of Δu_{max} based on linear elastic fracture mechanics. Hence, as the stress field for a singular crack model is expressed by the equation 4.1, the displacement u_x is given by the following equation considering r and θ as polar coordinates (e.g. *Zehnder*, 2012) :

$$u_x = \frac{K_{II}}{2\mu}\sqrt{\frac{r}{2\pi}}\sin\frac{\theta}{2}(\kappa + 2 + \cos\theta) \tag{4.16}$$

Where μ is the shear modulus, ν is the Poisson's ratio and $\kappa = 3-4\nu$. From previous equation we can get the cumulative slip $\Delta u = u_x(\theta = \pi) - u_x(\theta = -\pi)$

$$\Delta u = \frac{K_{II}}{\mu}\sqrt{\frac{r}{2\pi}}(\kappa + 1) \tag{4.17}$$

Replacing κ, K_{II} (equation 4.3) and considering that the stress drop $\Delta\tau = \tau^0_{xy} - \tau_r$, we obtain the following expression

$$\Delta u = 2\frac{(1-\nu)}{\mu}\Delta\tau\sqrt{Lr} \tag{4.18}$$

To get the maximum cumulative slip, we consider $r = L/2$

$$\Delta u_{max} = 2\frac{(1-\nu)}{\sqrt{2}\mu}\Delta\tau L \tag{4.19}$$

We then can compare the approximation of the static solution with dynamic results from earthquake rupture simulations investigated in chapter 3. Parameters of this analysis are based on *Harris and Day* (1993) considering seismic ratio $S = 0.49$ (supershear regime), static friction coefficient $f_s = 0.75$ and dynamic friction coefficient $f_r = 0.3$. Since we are interested on analysing how the stress distribution around the crack tip can influence on the jumping rupture, a comparison of the Coulomb stress is required. Figure 4.7 shows the comparison of the static and dynamic solutions of the Coulomb stress normalized by the stress drop. Dynamic solution is colored from black to yellow that correspond the values from 0 to 1 respectively. Static solution is presented by the curve in cyan color. Region inside this curve represents positive Coulomb stress which means that the Coulomb failure criteria is satisfied. Comparison is evaluated for 6 time steps that correspond to the interval between the earthquake rupture arrest ($t = 2.9$ s) and the time where second fault is prone to sliding ($t = 4.6$ s).

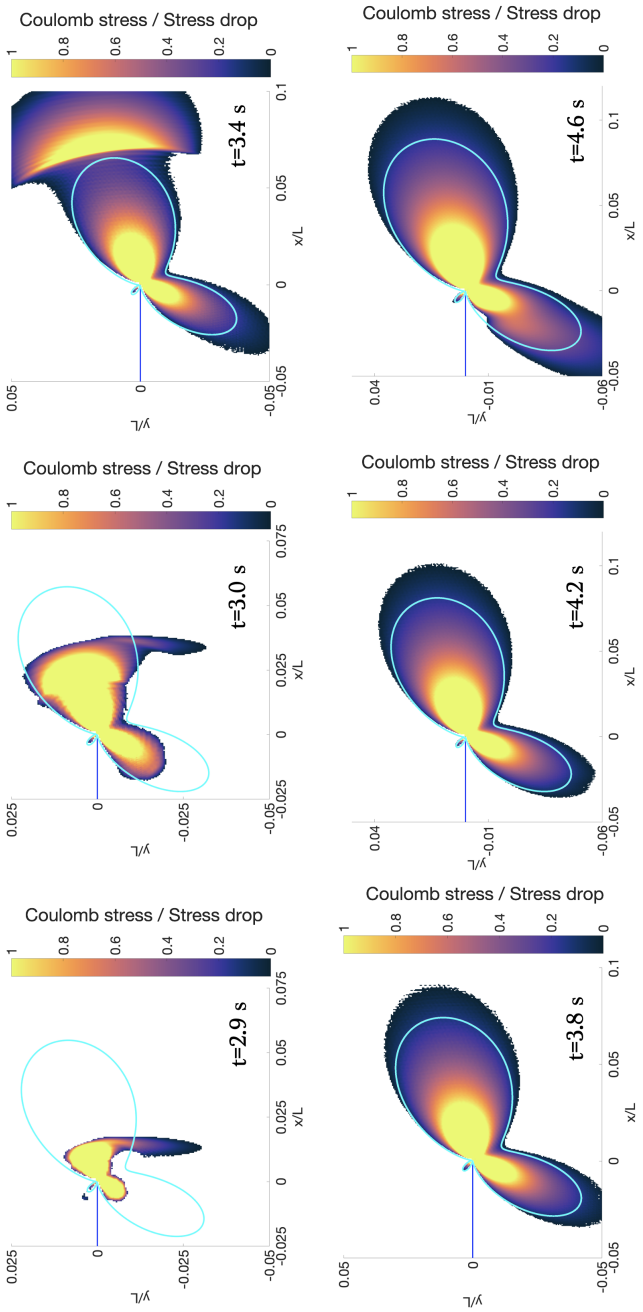

Figure 4.7: **Comparison of static and dynamic results of ratio Coulomb stress/Stress drop for parameters based on extensional step-over case from *Harris and Day* (1993). Case for stepwidth = 2.5 km,** $S = 0.49$**,** $f_s = 0.75$ **and** $f_r = 0.3$**.**. Colored plot (from black to yellow) represents dynamic result whereas the static result is represented by the curve colored in cyan. Static result is adjusted taking into account of the maximum slip for the first fault in dynamic simulation.

During the first two time steps ($t = 2.9s, 3.0s$), The stress distribution is extending around the crack tip and is also affected by the dynamic effect of the supershear rupture front. At this part, there is a mismatch between static and dynamic solutions. Then, in the next two time steps ($t = 3.4s, 3.8s$), the Coulomb stress approaches to a final static stress distribution getting a comparable shape as the static solution. However, in the final two time steps ($t = 4.2s, 4.6s$), the influence of dynamic effects that comes from the back and forth radiation of the stopping phase affect the stress distribution so that the static approximation is no longer comparable. Besides, an important issue that limits the comparison is that dynamic solution for this case is based on supershear regime which leads to a different slip evolution and additional dynamic effects than in subshear ruptures. Hence, If the stress field at the crack-tip is governed by the rupture process zone, the analytical solution is a quite good approximation to compare with dynamic solution. However, if the stress field is perturbed e.g. by dynamic effects from supershear rupture or from the impact of the stopping-phase, the analytical solution does not match to the dynamic solution; i.e. we can not properly compare both solutions. Based on this condition, we consider that subshear rupture dynamic simulation is a good candidate to compare with static solution.

Chapter 5

Dynamic off-fault damage: impacts on the role of step-overs

5.1 Introduction

During an earthquake, a dynamic rupture may jump across a stepover structure due to consequent stress readjustment that activates the sliding dynamics on the next fault. Static stress analysis (e.g. *Segall and Pollard*, 1980) and dynamic earthquake rupture simulations (e.g. *Harris et al.*, 1991; *Harris and Day*, 1993, 1999), within the context of a linear elastic medium, have remarked that the stress readjustment in stepover faults depends on the following factors: (1) the geometrical features of the fault system (e.g. fault length and stepwidth), (2) the sense of shear at the stepover system (extensional or compressional) and (3) the dynamic elements (seismic waves and rupture speed). Nonetheless, during an earthquake an intricate off-fault damage structure is generated and/or enhanced (see figure 5.1), especially at the ends of a fault (i.e. at the stepover zone), that significantly adds complexity to the seismic event. Hence, to investigate the role of stepovers on earthquake rupture propagation, we need to capture and consider its complex off-fault damage structure.

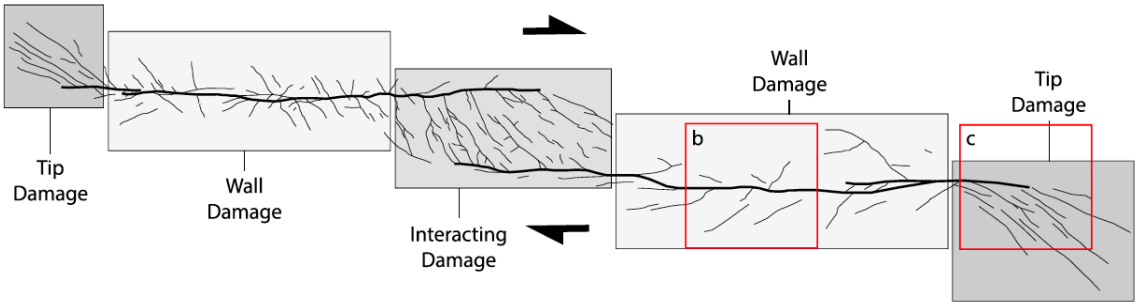

Figure 5.1: **Schematic of damage fault zone in stepover faults based on geological observations (*Ostermeijer et al.*, 2020).**

A few studies have looked at the effect of off-fault deformation on earthquake rupture in step-over systems considering either a pre-existing damage zone (low velocity fault zone) at the stepover zone (e.g. *Finzi and Langer*, 2012a) or off-fault plastic deformation (e.g. *Liu and Duan*, 2014). These studies provided a first order analysis. However, they do not take into account the dynamic changes of elastic properties in the medium, which have an effect on the rupture dynamics, the seismic wave propagation and consequently on the potency for the rupture to jump.

In this chapter, we study the role of damage on fault stepovers dynamics by conducting 2D earthquake rupture simulations around stepovers in a damage medium. In the previous chapter, we performed the static stress analysis of an elastic singular crack model so that we could analyse the stress readjustment influenced by the slip of the fault, where the earthquake initiated. This investigation allowed to obtain a first-order approximation of the largest jumpable distance (H_{max}) due to the fault slip. It provides the guidelines for this study, i.e. we define the geometry so that the stepover width correspond to the largest, estimated, jumpable distance derived from the static analysis. These cases are initially analysed in the context of a linear elastic medium and then using the micromechanical damage model (c.f. chapter 2).

5.2 Model setup

In chapter 4, we estimated the largest jumpable distance H_{max} for a stepover system based on a 2D static stress analysis of an in-plane elastic singular crack model. This crack represents the first fault in an stepover fault system (e.g., see figure 5.3a). H_{max} represents the maximum perpendicular distance measured from the axis of the first fault. We consider the static analysis explored with the following constant parameters: depth = 2 km, seismic ratio S = 2, static $f_s = 0.6$ and dynamic (residual) $f_d = 0.1$ friction coefficients. Figures 5.2a and 5.2b show the static solution of H_{max} as a function of the angles Ψ and ω, for extensional and compressional stepover system, respectively. Ψ is the initial orientation of the maximum principal stress σ_1^o with respect to the strike of the first fault. ω is the orientation of a potential secondary fault. Stepover system schematic is shown in these figures. How H_{max} is computed is explained in section 4.3. In particular, its upper limit is set to 0.3 times the crack length, which corresponds to 8.4 km. This value corresponds to the range of largest stepwidths reported and analysed in earthquake rupture studies (e.g. *Klinger*, 2005; *Wesnousky*, 2006, 2008; *Finzi and Langer*, 2012b). Two restricted areas are defined and depicted in the figures. Gray area corresponds to the cases where initial stress field does not favor strike-slip motion (*Jeandet-Ribes et al.*, 2023). Red area represents cases where initial Coulomb stress $\sigma_c^0(f_s, \omega)$ at the second fault is positive, meaning fault is ready to slip. Hence, cases from these areas do not correspond to the case of jumping rupture in strike-slip stepover faults. The static solution of $H_{max}(\Psi, \omega)$ serves as guideline to explore 2D earthquake rupture simulations. Since jumpable distance is significantly important in earthquake hazard assessment (e.g. *Field et al.*, 2014; *Cheng et al.*, 2021), our focus is on analysing cases that correspond to the upper limit H_{max}. Selected cases (black stars) for 2D earthquake rupture simulations are shown in figure 5.2. Initially, we set the distance, H, between the end of the first fault and the second fault as, H = H_{max} (see Figure 5.3). If no jumping rupture is observed in the simulations conducted in

an elastic medium, we iteratively reduce the value of H in subsequent simulations until nucleation occurs on the second fault. This chapter focuses on the analysis of these specific cases characterized by jumping rupture.

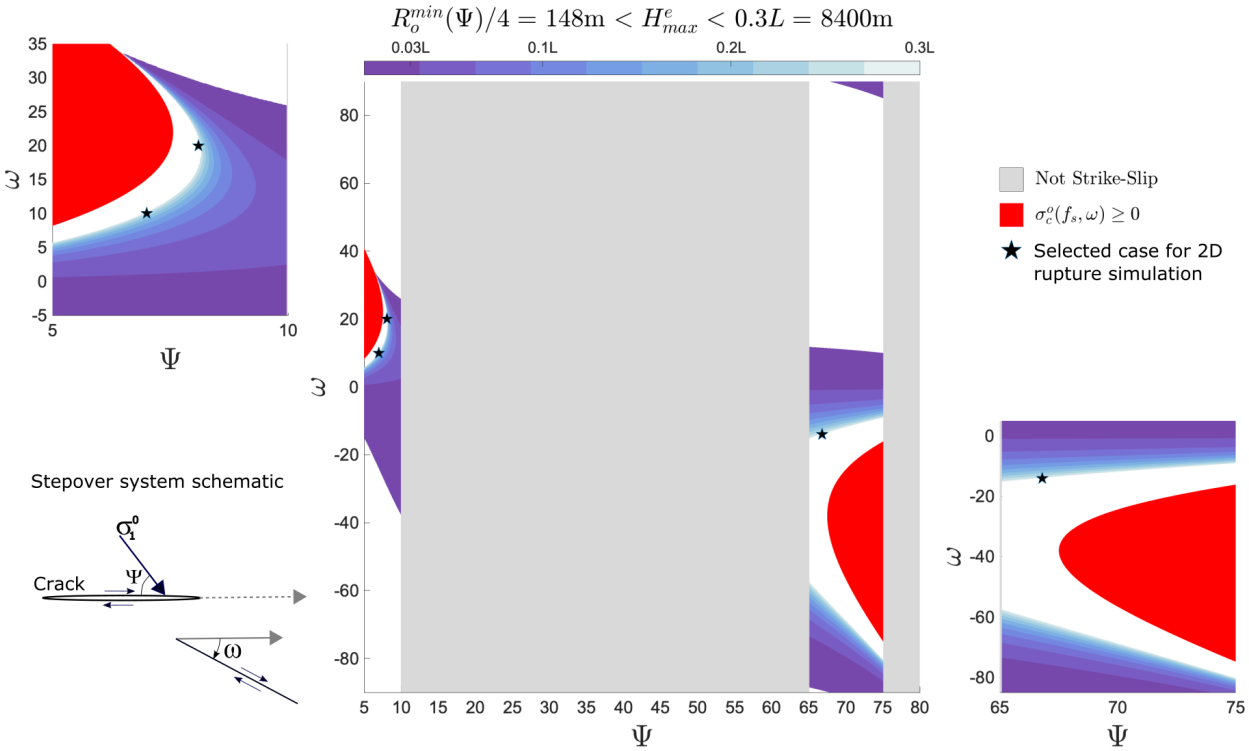

(a) $H_{max}^{e}(\Psi, \omega)$: Maximum jumpable distance at the extensional side of the crack.

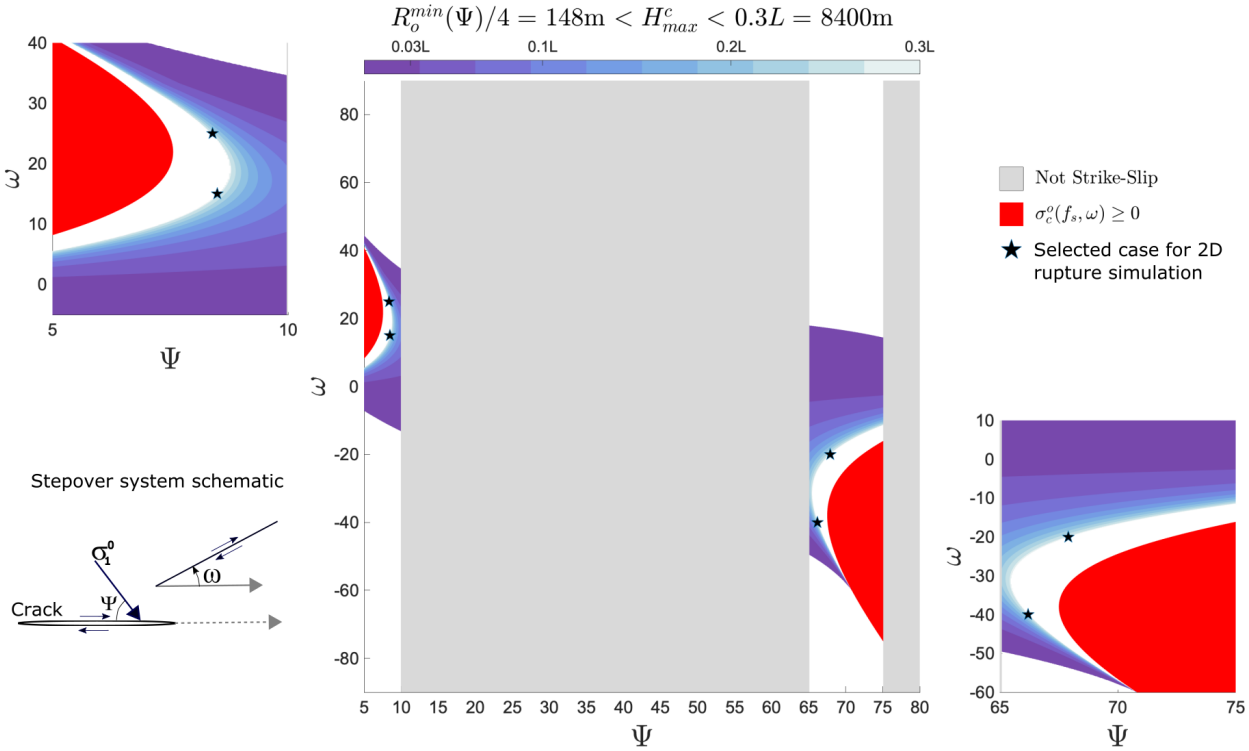

(b) H_{max}^{c} : Maximum jumpable distance at the compressional side of the crack.

Figure 5.2: **Selection of cases (black stars) for 2D rupture simulations in (a) extensional and (b) compressional stepover system. Parameters : depth = 2 km, $S = 2$, $f_s = 0.6$ and $f_r = 0.1$.** $H_{max}^{e/c}$ is obtained from the static analysis of an elastic singular crack model (see section 4.3). Its value is normalized by the crack length L ($L = 28$ km). Minimum process zone size, $R_o^{min}(\Psi) = 592$ m.

2D in-plane model schemes for extensional and compressional stepover faults are shown in figures 5.3a and 5.3b, respectively. We consider two right-lateral planar faults labeled as fault 1 and fault 2. Orientation of fault 2 is defined by the angle ω. The medium is loaded by uniform background stresses with the maximum compressive stress σ_1 making an angle Ψ with the strike of the fault 1. Sliding on the faults is governed by a slip-weakening friction law (grey box in the figures) (e.g., *Ida*, 1972; *Palmer and Rice*, 1973; *Andrews*, 1976). The thick grey line in fault 1 corresponds to the nucleation prone-patch where the initial shear stress is set up to be just above the frictional resistance so that an earthquake can be triggered. The size of nucleation, represented by the variable L_{nuc}, is computed using equation 2.4. It is worth noting the significant impact of the elastic modulus on the size of nucleation, as documented in previous studies (e.g., *Andrews*, 1976; *Campillo and Ionescu*, 1997; *Favreau et al.*, 1999; *Uenishi and Rice*, 2003). 2D earthquake rupture simulations are conducted considering both a linear elastic medium and a medium that allows dynamic crack growth. The applied micromechanical damage approach is presented in chapter 2.

Table 5.1 summarizes the all values of the constant parameters. We consider the elastic properties (density, P and S wave speeds) of a granite, representative of a continental crust, and the previously mentioned parameters used in the static analysis: depth, f_s, f_d and seismic ratio S. To perform earthquake rupture simulations with dynamic off-fault damage, we consider additional parameters: Initial damage density, D_o, static friction coefficient for microcracks, $f_{s,crack}$, initial crack length, 2a, quasi-static fracture toughness K_{IC}^{SS} and branching speed v_m. The values assigned to K_{IC}^{SS} and v_m correspond to those of granite material. Quasi-static process zone sizes R_o are calculated considering the initial stress state at each fault by the equation 2.3 (*Poliakov et al.*, 2002). The length of the initial microcracks are proportional to the minimum quasi-static process zone size R_o. This minimum value is used as length

scale to define the resolution (grid spacing) of the model so that the minimum process zone size is resolved with 20 spatial elements. Table 5.2 shows the geometrical features of the all cases selected for 2D earthquake rupture simulations in stepover faults. The length of fault 1 measures 28 km, since this value is on the average range of fault length reported in nature and evaluated in numerical studies (e.g. *Klinger*, 2010; *Choi et al.*, 2018; *Harris and Day*, 1993). Whereas, we set up the length of fault 2 equals two times its nucleation size. This size is solved considering the initial stress state at the fault 2. The minimum distance between faults is defined by χ (see figure 5.3). This value is determined so that the maximum jumpable distance for each case is achieved. The initial length of the microcracks ranges between 40 and 120 m.

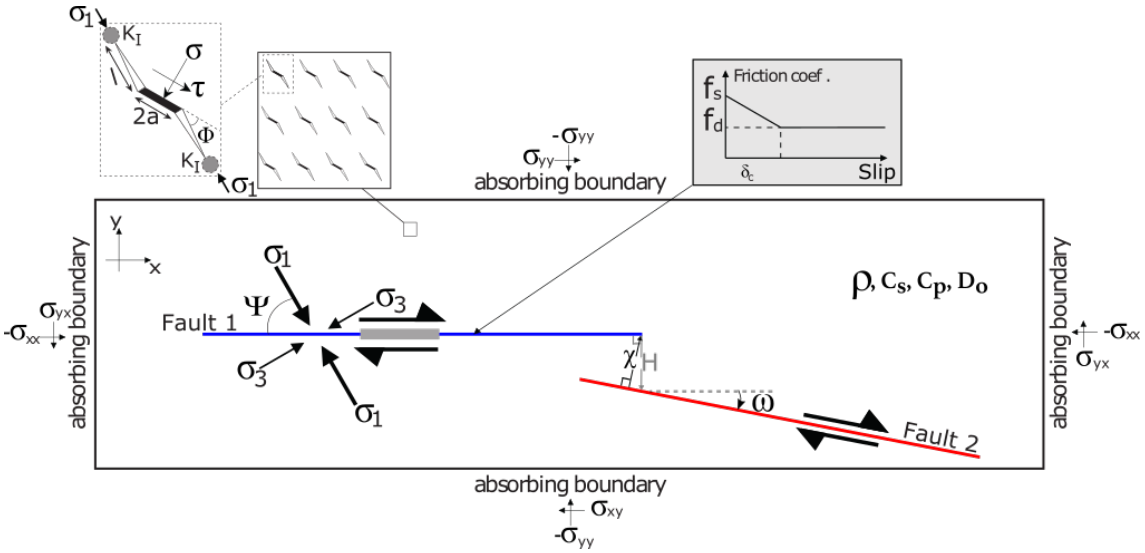

(a) 2D model scheme for extensional stepover faults.

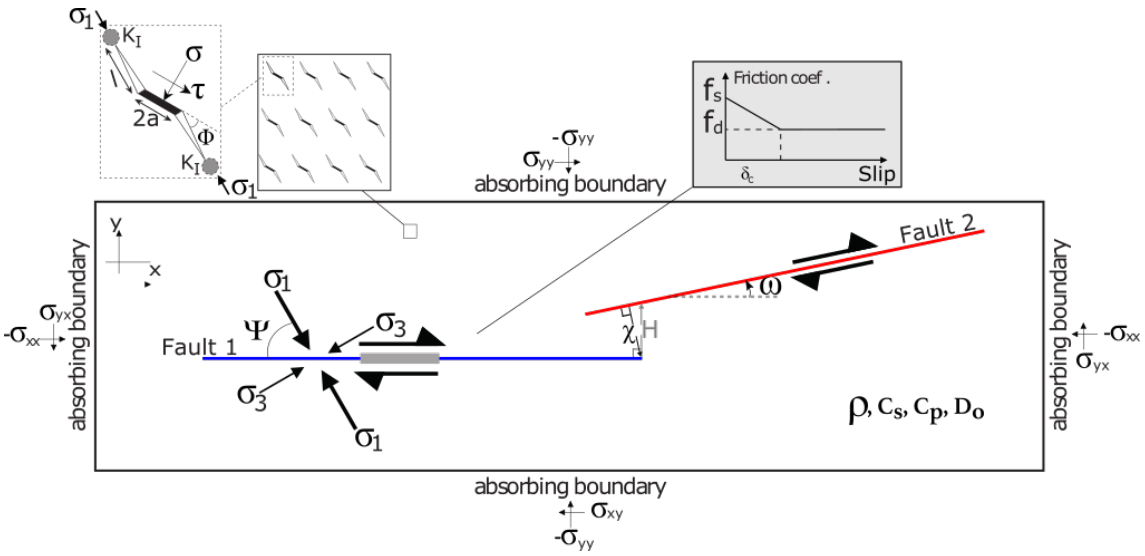

(b) 2D model scheme for compressional stepover faults.

Figure 5.3: **Schematics and parameters for 2D in-plane dynamic rupture simulation around (a) extensional and (b) compresional stepover faults. Modified from** *Thomas and Bhat* **(2018).** Material properties are : density (ρ), S wave speed (c_s), P wave speed c_p and initial damage density (D_o). Frictional parameters: static friction coefficient (f_s), dynamic friction coefficient (f_d) and characteristic distance (δ_c). 2a: initial crack length. H: distance to the second fault from the end of the first fault. To ensure the achievement of the maximum jumpable distance for each case in the 2D dynamic simulation, H is carefully fixed, taking into account an upper limit. This upper limit is the static solution of H_{max}. χ: minimum distance between fault 2 and the end of the fault 1.

Parameter	Notation	Value
material density	ρ	2700 $kg.m^{-3}$
P-wave velocity	c_p	5.60 $km.s^{-1}$
S-wave velocity	c_s	3.12 $km.s^{-1}$
depth	z	2.0 km
Static coefficient of friction	f_s	0.6
Residual coefficient of friction	f_d	0.1
Slip weakening distance	δ_c	1 m
Seismic ratio	S	2

Parameter for dynamic damage	Notation	Value
Initial damage density	D_0	0.1
Static friction coefficient for microcracks	$f_{s,crack}$	0.8
Initial crack length	2a	$\propto R_o^{min}$
Branching speed	v_m	1.5 $km.s^{-1}$
Quasi-static fracture toughness	K_{IC}^{SS}	1.2 MPa$\sqrt{m}$

Table 5.1: **Parameters used for all performed 2D earthquake rupture simulations in stepover faults.** Initial crack length is proportional to R_o^{min}. R_o^{min} is the minimum value between the process zone sizes at each fault in the stepover system.

		Stepover system						
		Extensional			**Compressional**			
	Parameter	case (i)	case (ii)	case (iii)	case (iv)	case (v)	case (vi)	case (vii)
Geometrical features	Angle Ψ	7^o	8.1^o	67^o	8.5^o	8.4^o	66.2^o	67.9^o
	Angle ω	10^o	20^o	-14^o	15^o	25^o	-40^o	-20^o
	Length of F1 (km)	28	28.2	28	28.2	28	28	28
	Length of F2 (km)	25.8	20	12.7	21.5	17.9	20.2	13.6
	Distance χ (km)	8	7.6	3.8	5.9	5.6	6.5	5.7
	Initial crack size 2a (m)	119	92	50	100	82	50	48
Initial stress field F1	Shear stress σ_{xy} (MPa)	7.4	8	20.6	8.2	8.2	20.4	21.2
	Normal stress σ_{yy} (MPa)	27.9	30.1	77.4	30.8	30.6	76.3	79.6
	Stress drop $\Delta\tau$ (MPa)	4.6	5	12.9	5.1	5.1	12.7	13.3

Table 5.2: **Geometrical features and initial stress field at fault 1 for cases used in 2D earthquake rupture simulations.** Schematics for geometrical features are illustrated in figure 5.3a and figure 5.3b for extensional and compressional stepover system, respectively. χ : minimum distance between fault 2 and the right end of the fault 1.

5.3 Elastic results: Earthquake rupture jumping controlled by fault slip and seismic waves

2D earthquake rupture simulation in a linear elastic medium are analysed for 7 scenarios. Parameters are summarized in table 5.1 and 5.2. Cases are grouped considering the background stress orientation defined by the angle Ψ. Cases with low angle Ψ are cases i, ii, iv, v with $\Psi = 7^o$, 8.1^o, 8.5^o and 8.4^o, respectively. Cases with high angle Ψ are cases iii, vi, vii with $\Psi = 67^o$, 66.2^o and 67.9^o, respectively.

Our results show that two main factors influence the stress change, which governs rupture jumping in stepover faults: (1) fault slip and (2) seismic waves. The impact of these factors is modulated by the orientation ω of fault 2. These two factors have been suggested in static stress analysis and dynamic rupture studies for parallel strike-slip stepover faults embedded in a elastic medium (e.g. *Segall and Pollard*, 1980; *Harris and Day*, 1993, 1999). However, in this section we are able to explore the impact of these factors in more complex geometrical structures considering non-parallel faults. A first insight on how even a slight difference in the orientation of the second fault can impact on the maximum jumpable distance can be inferred from the static solution presented in figure 5.2. In that sense, theoretical studies that explore parallel faults have limitations in estimating the maximum jumpable distance and subsequent rupture scenario for stepover structures of non-parallel faults reported in nature (e.g. *Klinger*, 2005; *Klinger et al.*, 2010, 2017; *Choi et al.*, 2018; *Lefevre et al.*, 2018).

An essential observation from all the results, for a linear elastic medium, is that: nucleation, on the second fault, in extensional stepover faults, occurred close to the stepover zone; whereas in compressional stepover faults, rupture jumping happened at farther side on the fault 2 with respect to the stepover zone. This observation is

in a good agreement with previous studies (*Harris and Day*, 1993; *Liu and Duan*, 2014; *Wang et al.*, 2020). It is related to the sense of sliding with respect to the location of the second fault. As suggested by (*Segall and Pollard*, 1980), in compressional stepover system, fault sliding generates increase of normal stress at the stepover zone with consequent increase of frictional strength which prevent jumping rupture close to the stepover zone. Whereas, in extensional stepover system, fault sliding provokes a reduction of normal stress with a resultant reduction of friction, consequently favoring the nucleation of a dynamic event close to the stepover zone. As we can infer, the determination of jumping rupture is affected by the position of the second fault respect to the first fault. This position implies not only the length or the location of the second fault respect to the stepover zone but also its strike orientation respect to the first fault.

Dynamic effects also play a key role on the determination of jumping rupture (e.g. *Harris and Day*, 1993; *Bai and Ampuero*, 2017). From our results, a initial insight can be formed based on the difference of time, Δt_j, between the earthquake triggering on the second fault through jumping rupture and the rupture arrest on the first fault. Δt_j is summarized for the all cases in Table 5.3. Variability on values of Δt_j suggests that jumping rupture is influenced not only by fault slip but also by dynamic effects driven by seismic waves. In the following part, we analyse the different mechanisms that conduct to jumping rupture, for the all cases.

Extensional stepover system				
Case	angle Ψ	angle ω	t_{F1}	Δt_j
i	7^o	10^o	4.4 s	-0.5 s
ii	8.1^o	20^o	4.6 s	-0.8 s
iii	67^o	-14^o	4.9 s	3.6 s
Compressional stepover system				
Case	angle Ψ	angle ω	t_{F1}	Δt_j
iv	8.5^o	15^o	4.5 s	3.5 s
v	8.4^o	25^o	4.5 s	3.1 s
vi	66.2^o	-40^o	4.9 s	1.1 s
vii	67.9^o	-20^o	4.9 s	1.7 s

Table 5.3: **Results for 2D earthquake rupture simulation in stepover faults embedded in linear elastic medium.** Parameters and geometrial features are summarized in table 5.1 and table 5.2, respectively. t_{F1} : time when the rupture propagation reaches the end of fault 1. Δt_j : Difference between the time of triggering nucleation on fault 2 and t_{F1}. Negative values of Δt_j means that the nucleation on fault 2 happened before the earthquake rupture reaches the end of fault 1.

5.3.1 Low angle ψ

From 2D earthquake rupture simulation conducted for case i and case ii, figure 5.4 shows the ratio between the shear stress and the peak stress ($\sigma_{xy(\omega)}/f_s\sigma_{yy(\omega)}$) in the vicinity of the end of fault 1 for any secondary fault with strike orientation ω. Peak stress is the static coefficient of friction times the normal stress on a potential secondary fault. This ratio is designated hereafter as the stress ratio. Darker red color indicates that above this value there is the required stress to overcome the frictional resistance for any fault with the strike orientation ω. Figure 5.5 shows the normal stress normalized by its initial value, denoted as $\sigma_{yy(\omega)}/\sigma^o_{yy(\omega)}$. This figure will be referred to as 'normal stress' for simplicity. In both figures, stresses are rotated with respect to the orientation ω of the fault 2 so that the values of the stress ratio and normal stress correspond to those expected for a fault with the strike orientation of fault 2. Time of the snapshots is t = 4 s. This time corresponds to the moment right after the rupture jumping as we can observe from the slip rate on the faults (curves colored in cyan). Areas in white color have a stress field corresponding to the initial setup.

In these cases of extensional stepovers with a low angle Ψ, the propagation of the rupture wave front facilitates the transfer of a positive perturbation towards the second fault. Additional clues can be obtained from the snapshots of normal stress. It is noticeable that the sense of shear of fault 1 produces two different regions of normal stress changes. Significant increase of normal stress is produced at the compressional side of the fault 1. Whereas, normal stress reduction is strongly localized at the extensional side. The propagation of the rupture wave front facilitates the transfer of these normal stress changes.

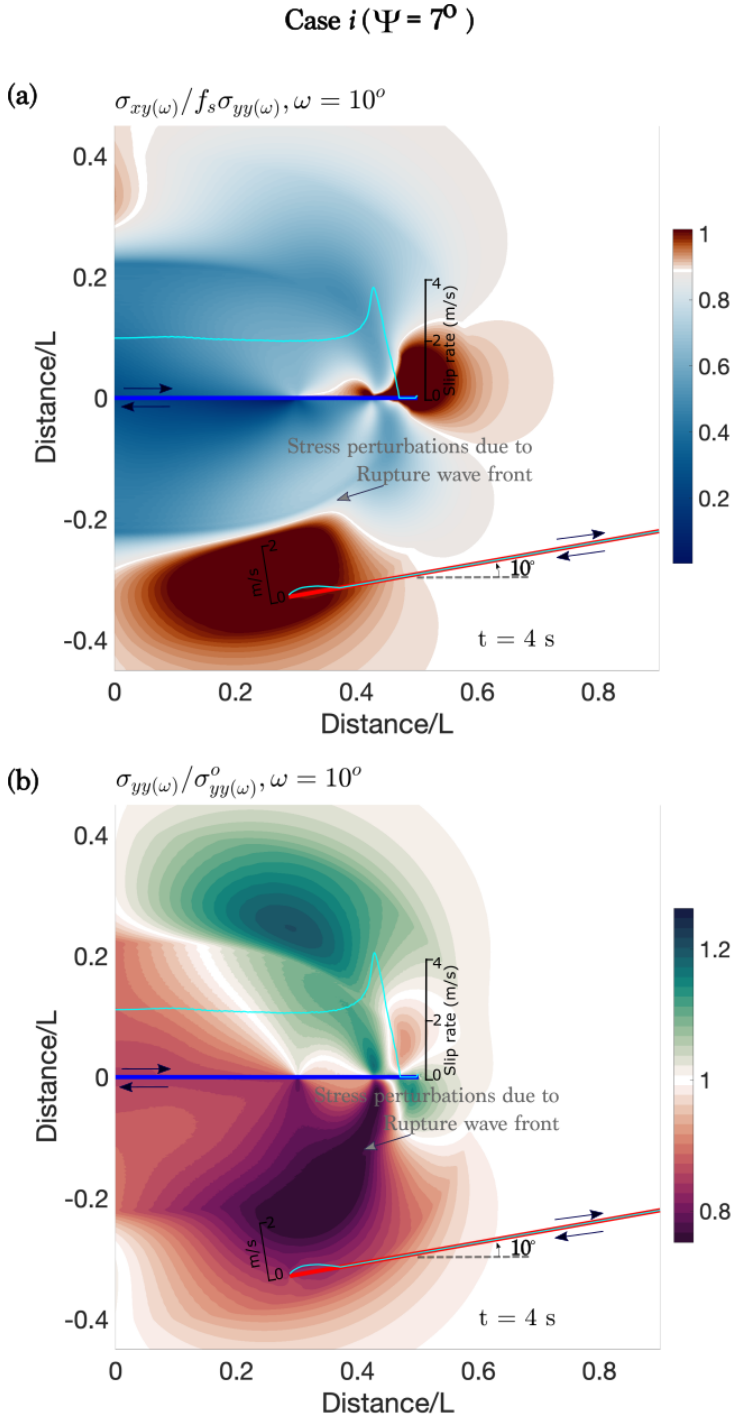

Figure 5.4: **Case** i **(**$\Psi = 7^o$**,** $\omega = 10^o$**) : (a) Ratio Shear stress/Peak stress** $(\sigma_{xy(\omega)}/f_s\sigma_{yy(\omega)})$ **and (b) Normalized normal stress** $(\sigma_{yy(\omega)}/\sigma^o_{yy(\omega)})$ **at time** $t =$ **4 s, for a dynamic rupture on extensional stepover faults embedded in a linear elastic medium.** Strike-slip faults are represented by straight lines colored in blue (fault 1) and red (fault 2). Stresses are rotated respect to the orientation ω of the fault 2. Initial orientation of the maximum principal stress σ_1 defined by angle Ψ is measured respect to the strike of the fault 1. White color labels the value that corresponds to the initial stress state. Slip rate on the faults (curves colored in cyan) is superimposed on the snapshots. Parameters are summarized in table 5.1 and 5.2.

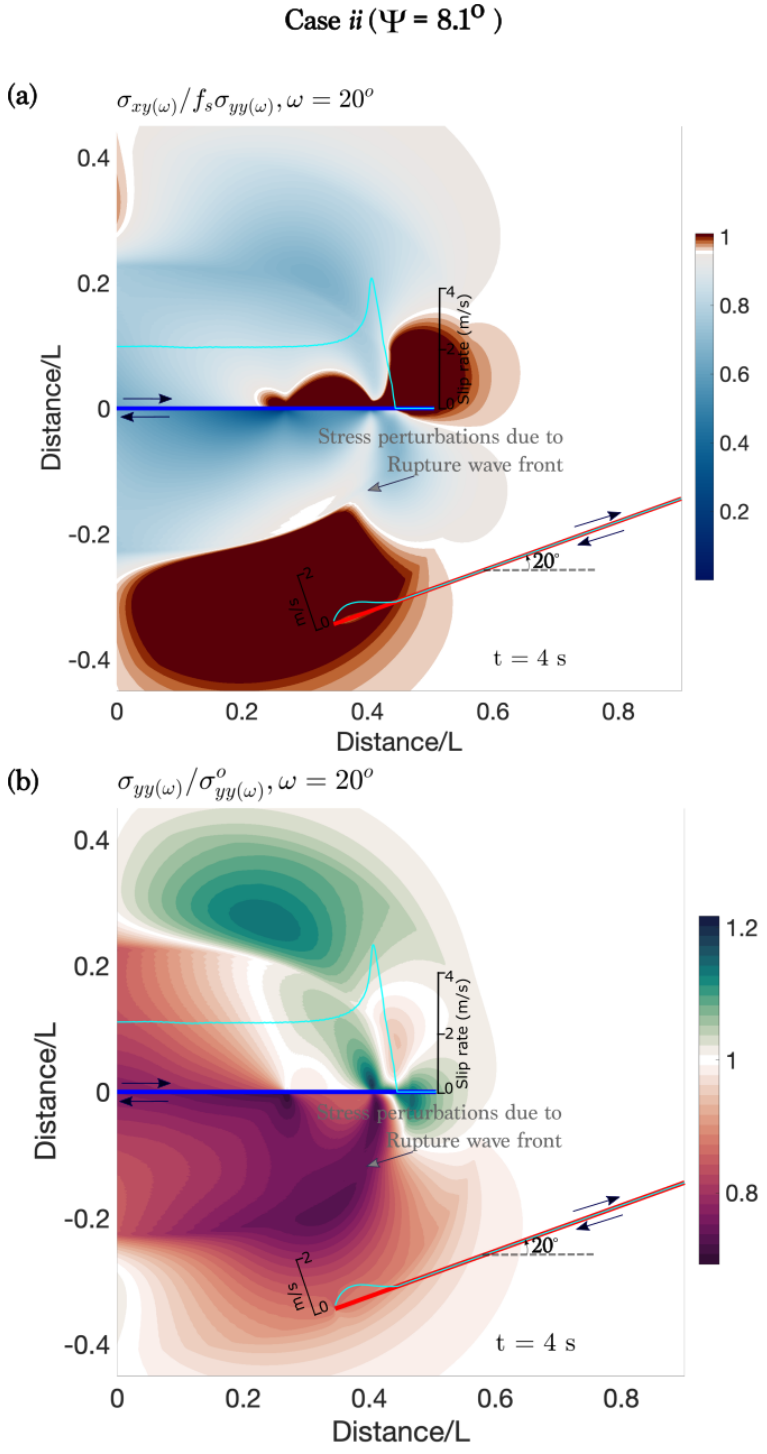

Figure 5.5: **Case *ii* ($\Psi = 8.1^o$, $\omega = 20^o$) : (a) Ratio Shear stress/Peak stress ($\sigma_{xy(\omega)}/f_s\sigma_{yy(\omega)}$) and (b) Normalized normal stress ($\sigma_{yy(\omega)}/\sigma^o_{yy(\omega)}$) at time $t =$ 4 s, for a dynamic rupture on extensional stepover faults embedded in a linear elastic medium.** Strike-slip faults are represented by straight lines colored in blue (fault 1) and red (fault 2). Stresses are rotated respect to the orientation ω of the fault 2. Initial orientation of the maximum principal stress σ_1 defined by angle Ψ is measured respect to the strike of the fault 1. White color labels the value that corresponds to the initial stress state. Slip rate on the faults (curves colored in cyan) is superimposed on the snapshots. Parameters are summarized in table 5.1 and 5.2.

The static analysis provides a first order approximation of the fault slip effect on jumping rupture. Based on linear elastic fracture mechanics, the static solution discussed in chapter 4 provides an approximation of the stress field state due to the sliding of a fault (labeled as fault 1, in our study). For the static solution, figures 5.6a and 5.6b show the stress ratio for the case *i* and *ii*, respectively. Inside the red area in the figure 5.6, values of the stress ratio are higher than 1. According to the static solution, at the extensional side of fault 1, fault slip generates stress perturbation towards the fault 2 potentially facilitating jumping rupture. Moreover, its triggering is likely to occur near the left end of the second fault, i.e. close to the stepover zone.

Figures 5.7a and 5.7b show the temporal evolution of the stress ratio along the second fault for case *i* and case *ii*, respectively. We have adjusted the time and position on the vertical and horizontal axes, respectively, to simplify the interpretation. Time = 0 corresponds to the time when rupture at the first fault reaches its right end (i.e. rupture arrest). Position on the horizontal axis is normalized by the length of the fault 1, L. Normalized position x/L = 0 corresponds to the location at the second fault where the right end of fault 1 is projected. White color in the colorbar corresponds to the initial value of the stress ratio. Darker red color indicates that above this value there is the required stress on fault 2 to allow rupture triggering. Nonetheless, in order to allow rupture propagation on fault 2, a certain region (nucleation size) needs to be subjected to this required stress. Two straight lines, colored in green and magenta, are superimposed on the figures. The slopes of these lines represent the S and P wave speeds, respectively.

Our results show that in extensional stepover faults with low angle Ψ, nucleation on the second fault happens sligthly before the arrest of the rupture on the first fault. Triggering location is close to the left end of the fault 2. Considering that

case i and case ii have nearly same initial parameter values (see parameters in table 5.2), particularly nearly same orientation Ψ of the initial maximum principal stress at the first fault, the discrepancy (timing essentially) depends on the orientation of the second fault. Looking at the initial values of stress ratio at the second fault (see figure 5.7), the increase of the orientation of the second fault from $\omega = 10^o$ (case i) to $\omega = 20^o$ (case ii) sets the initial stress field at the second fault closer to failure. Indeed, the optimal angle between σ_1 and the strike of a fault 2 is 30^o, for a static friction coefficient $f_s = 0.6$ (e.g. *Skoumal et al.*, 2019; *Cochran et al.*, 2020). The static solution of the stress ratio for these two cases supports this statement. In figure 5.6, we can observe that even when considering the complete fault sliding of fault 1, case i is less likely to allow rupture jumping than case ii. Additionally, we can infer that dynamic effects conducted by seismic waves from the rupture front at fault 1 are more required in case i than in case ii to allow earthquake triggering at fault 2. An overall conclusion from our cases of extensional stepovers with low angle Ψ remarks that both effects from fault slip (see static solution in figure 5.6) and seismic waves favor jumping rupture at the second fault and its triggering is located close to the left end of the second fault, i.e. at the stepover zone.

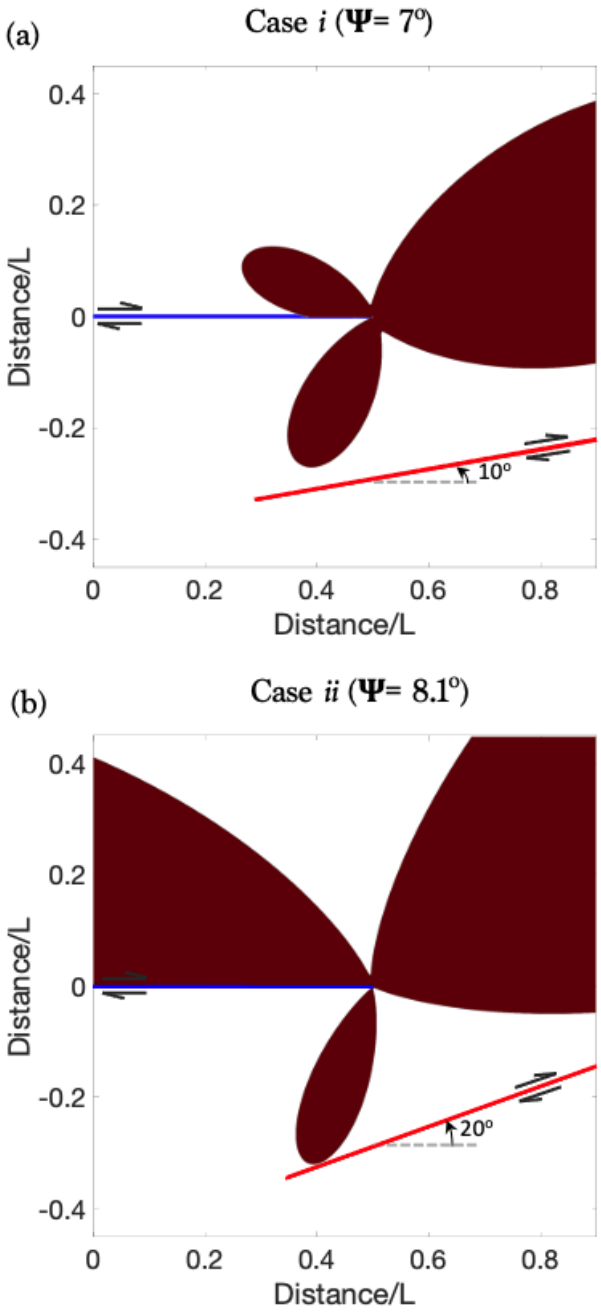

Figure 5.6: **Static solution of the ratio Shear stress/Peak stress for extensional stepover system, (a) case i and (b) case ii , with low angle Ψ.** Strike-slip faults are represented by straight lines colored in blue (fault 1) and red (fault 2). Stresses correspond to the orientation ω of the fault 2. Inside the red area, there is the required stress to overcome the frictional resistance for any fault with the strike orientation of fault 2. Initial orientation of the maximum principal stress σ_1 defined by angle Ψ is measured respect to the strike of the fault 1. L is the length of fault 1. Value 0 of normalized distance corresponds to the middle of the fault 1. Further detailed on the static solution, see chapter 4.

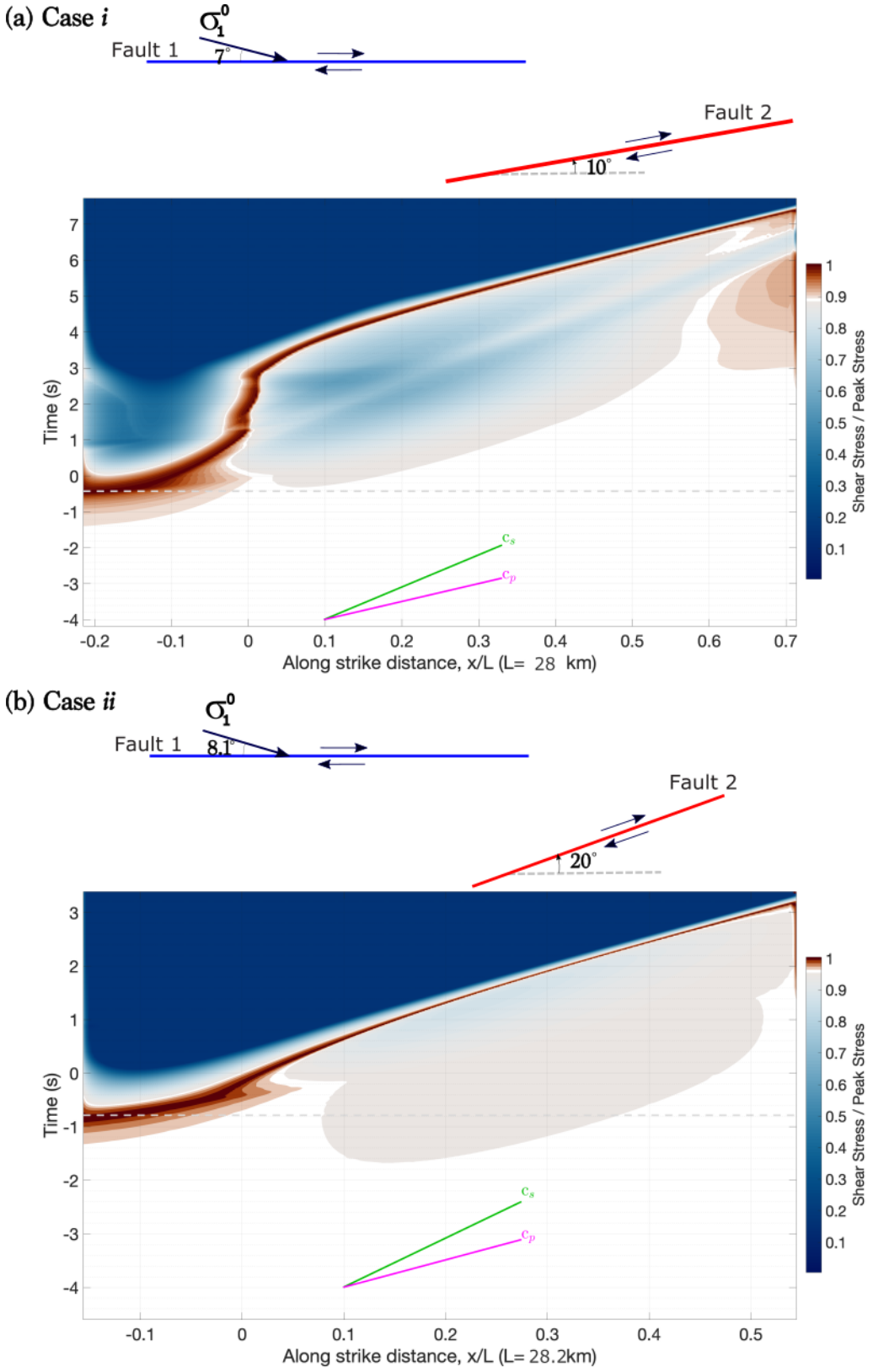

Figure 5.7: **Temporal evolution of the ratio Shear stress / Peak stress at fault 2 for extensional stepover system, (a) case *i* and (b) case *ii* , with low angle Ψ.** Time = 0 : time when rupture reaches the end of fault 1. x/L = 0 : location where the end of fault 1 is projected at fault 2. Gray dashed line represents triggering time at fault 2. White color labels the initial stress state.

Regarding the result of the 2D earthquake rupture simulation in compressional stepover faults, figures 5.8 and 5.9 illustrate the impact of seismic waves that come from the rupture and its arrest at fault 1. When the rupture front reaches the end of the fault 1, i.e. at the rupture arrest, P and S stopping phases are generated and radiated outward from the end of the fault (e.g. *Savage*, 1965; *Madariaga*, 1977; *Bruhat*, 2012). Stopping phases carry high frequency radiation due to the abrupt change of the rupture velocity at the end of the fault (e.g. *Savage*, 1966; *Madariaga*, 1976, 1977). This high frequency radiation as well as the amplitude of the stopping phases are proportional to the stress concentration left at the edge of the fault at the rupture arrest (*Madariaga*, 1977). It has been suggested that stopping phases are a key factor that favors jumping rupture on stepover faults (e.g. *Bai and Ampuero*, 2017). In our results of stress ratio, in figures 5.8a and 5.9a, we can remark that stresses are dynamically perturbed by seismic waves which modulate the stress field state influenced by the fault slip. Results for normal stress in figures 5.8b and 5.9b show that there is an enhanced reduction of the normal stress which led to jumping rupture.

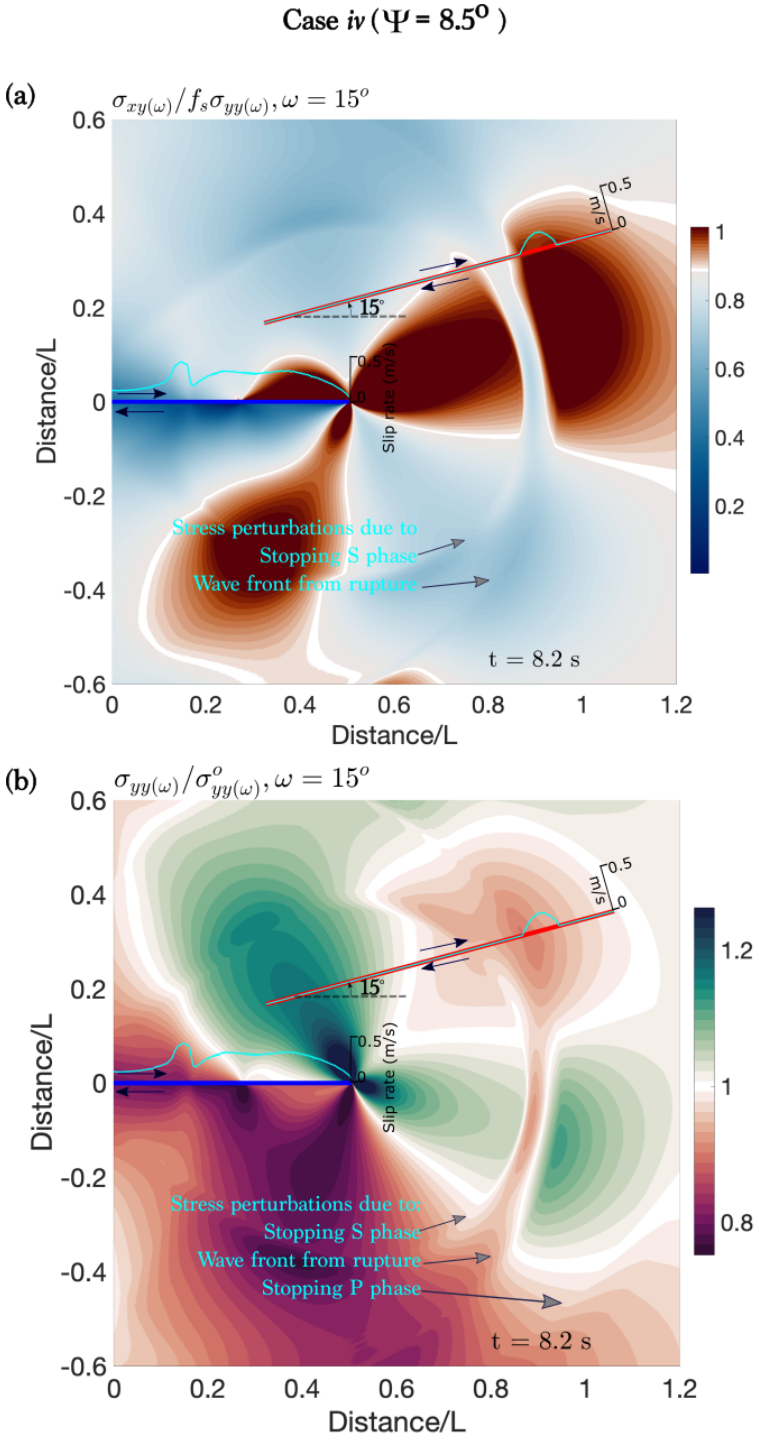

Figure 5.8: **Case** *iv* **($\Psi = 8.5^o$, $\omega = 15^o$) : (a) Ratio Shear stress/Peak stress ($\sigma_{xy(\omega)}/f_s\sigma_{yy(\omega)}$) and (b) Normalized normal stress ($\sigma_{yy(\omega)}/\sigma^o_{yy(\omega)}$) at time t = 8.2 s, for a dynamic rupture on compressional stepover faults embedded in a linear elastic medium.** Strike-slip faults are represented by straight lines colored in blue (fault 1) and red (fault 2). Stresses are rotated respect to the orientation ω of the fault 2. Initial orientation of the maximum principal stress σ_1 defined by angle Ψ is measured respect to the strike of the fault 1. White color labels the value that corresponds to the initial stress state. Slip rate on the faults (curves colored in cyan) is superimposed on the snapshots. Parameters are summarized in table 5.1 and 5.2.

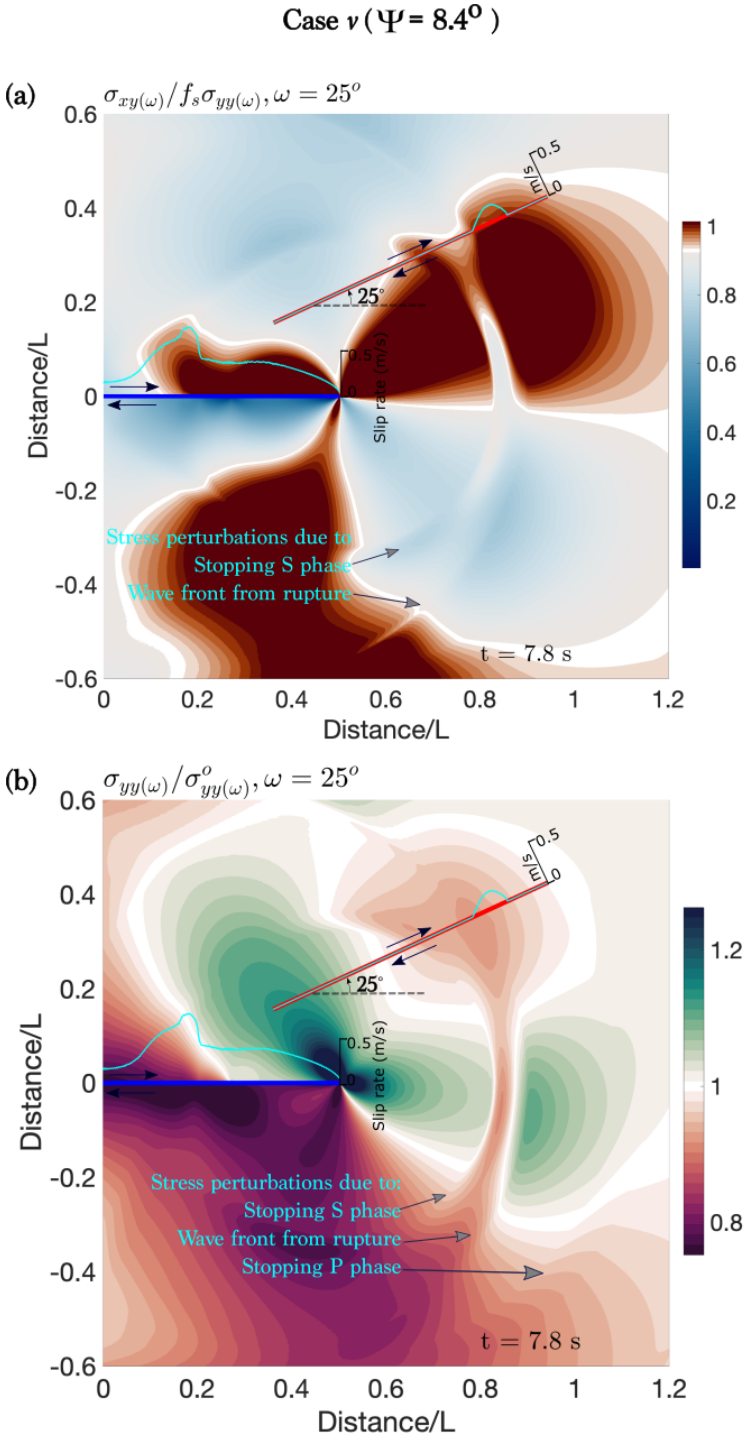

Figure 5.9: **Case** v **(**$\Psi = 8.4^o$**,** $\omega = 25^o$**) : (a) Ratio Shear stress/Peak stress** $(\sigma_{xy(\omega)}/f_s\sigma_{yy(\omega)})$ **and (b) Normalized normal stress** $(\sigma_{yy(\omega)}/\sigma^o_{yy(\omega)})$ **at time** $t =$ **7.8 s, for a dynamic rupture on compressional stepover faults embedded in a linear elastic medium.** Strike-slip faults are represented by straight lines colored in blue (fault 1) and red (fault 2). Stresses are rotated respect to the orientation ω of the fault 2. Initial orientation of the maximum principal stress σ_1 defined by angle Ψ is measured respect to the strike of the fault 1. White color labels the value that corresponds to the initial stress state. Slip rate on the faults (curves colored in cyan) is superimposed on the snapshots. Parameters are summarized in table 5.1 and 5.2.

The sliding of fault 1 promotes a jumping rupture at the right end of the fault, but it is expected to occur closer to the stepover zone than the triggering location in dynamic simulations (see static solution in figure 5.10). It is important to highlight the presence of an elongated red area near the second fault, which aligns closely with the strike orientation of fault 2. This alignment plays a crucial role in facilitating the effective distribution of the necessary stress to overcome frictional resistance along the required nucleation size. As a result, this alignment favors nucleation on the second fault.

For the 2D simulations, figure 5.11 shows the results of stress ratio along the second fault as a function of time. The figures 5.11a and 5.11b show that the rupture in case *iv* was triggered at the normalized position x/L $\sim$ 0.4; whereas in case *v*, it is located at x/L $\sim$ 0.3. For both cases, from x/L= 0.2 to the right end of the fault, for about 2 sec before the rupture nucleates on the second fault, there is a gradual increment of the stress ratio from its background value (white color) to the threshold value (darker red color). The slope of this increment matches with a wave speed between the S and P wave velocity (slopes of the straight lines colored in green and magenta, respectively). It implies that seismic waves from rupture and stopping phases, have played a key role that led to jumping rupture. This comparison between the stress increment rate and the seismic waves velocity is possible since the strike orientation of fault 2 is nearly perpendicular to the seismic waves front (see figures 5.8 and 5.9, for instance). An overall conclusion from our cases of compressional stepovers with low angle Ψ remarks that while fault slip promotes jumping rupture near the stepover zone, dynamic effects through seismic waves can trigger the nucleation further away on the fault.

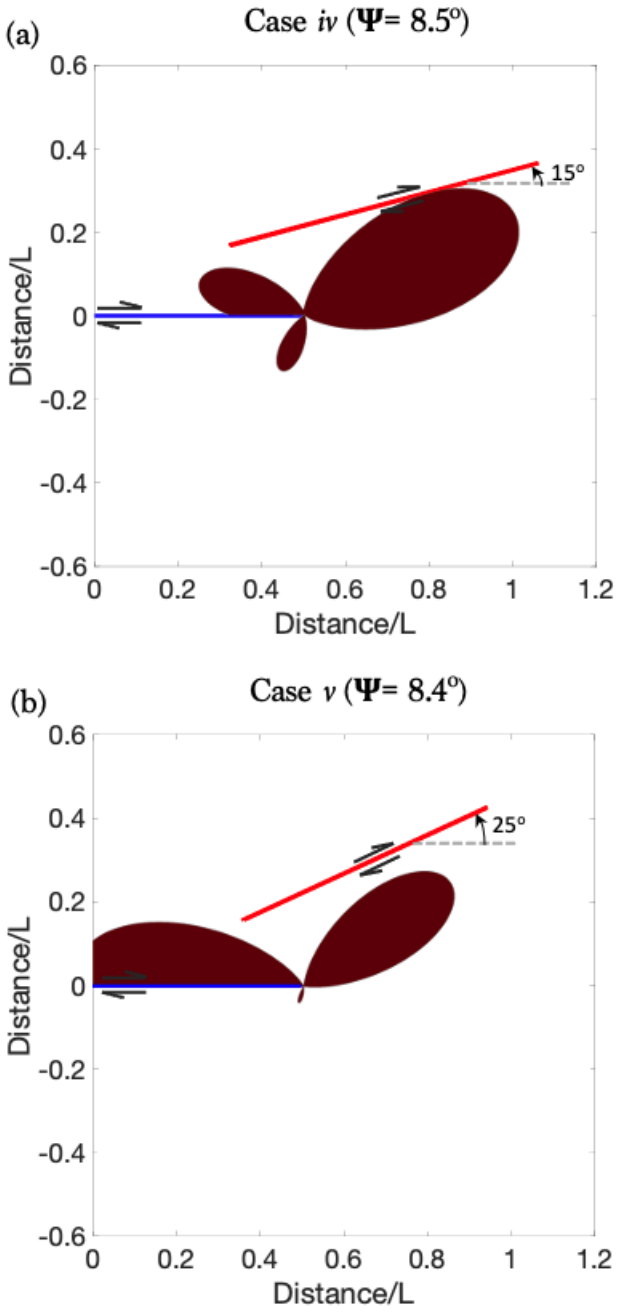

Figure 5.10: **Static solution of the ratio Shear stress/Peak stress for compressional stepover system, (a) case** iv **and (b) case** v **, with low angle** Ψ**.** Strike-slip faults are represented by straight lines colored in blue (fault 1) and red (fault 2). Stresses correspond to the orientation ω of the fault 2. Inside the red area, there is the required stress to overcome the frictional resistance for any fault with the strike orientation of fault 2. Initial orientation of the maximum principal stress σ_1 defined by angle Ψ is measured respect to the strike of the fault 1. L is the length of fault 1. Value 0 of normalized distance corresponds to the middle of the fault 1. Further detailed on the static solution, see chapter 4.

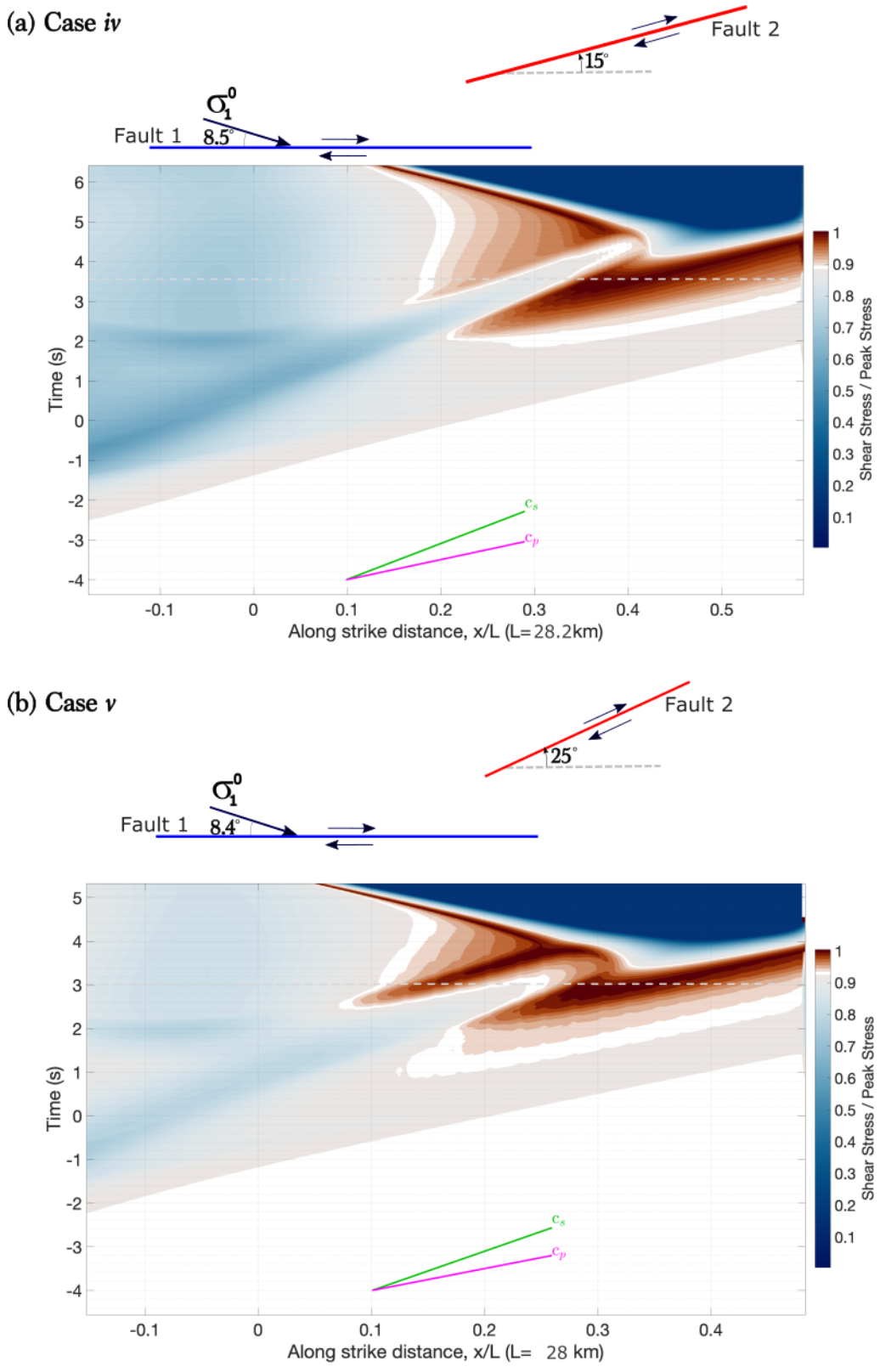

Figure 5.11: **Temporal evolution of the ratio Shear stress / Peak stress at the fault 2 for compressional stepover system, (a) case *iv* and (b) case *v* , with low angle Ψ.** Time = 0 : time when rupture reaches the end of fault 1. x/L = 0 : location where the end of fault 1 is projected at fault 2. Gray dashed line represents triggering time at fault 2. White color labels the initial stress state.

5.3.2 High angle ψ

Figure 5.12 shows the stress ratio and normal stress, for case *iii*, for an extensional stepover fault with high angle Ψ. It is shown that even after the stress perturbation due to seismic waves from rupture and its arrest in fault 1, the stress required to allow jumping rupture is not reached until a certain time delay. During this delay time there is not only the impact of seismic waves but also the influence of the sliding of fault 1, that is still allowed after the initial rupture reaches the end of the fault 1. Additionally, it is observed that the reduction of normal stress at the extensional side of fault 1 is oriented towards the left end of the fault 2 favoring the reduction of the frictional resistance.

In figure 5.13, the static analysis suggests that, jumping rupture is likely to occur at the left end of fault 2, or slightly further away. Nonetheless, in order to initiate dynamic sliding on a fault, the stresses that exceed the frictional resistance must be distributed over an area, the size of the nucleation length. In this particular case, the maximum jumpable distance obtained in dynamic simulations is smaller than the static solution of H_{max}. This indicates that fault 2 is located closer to fault 1 and further into the red region of the static solution. Hence, it is crucial to recognize the significant role played by the nucleation size in determining the maximum jumpable distance.

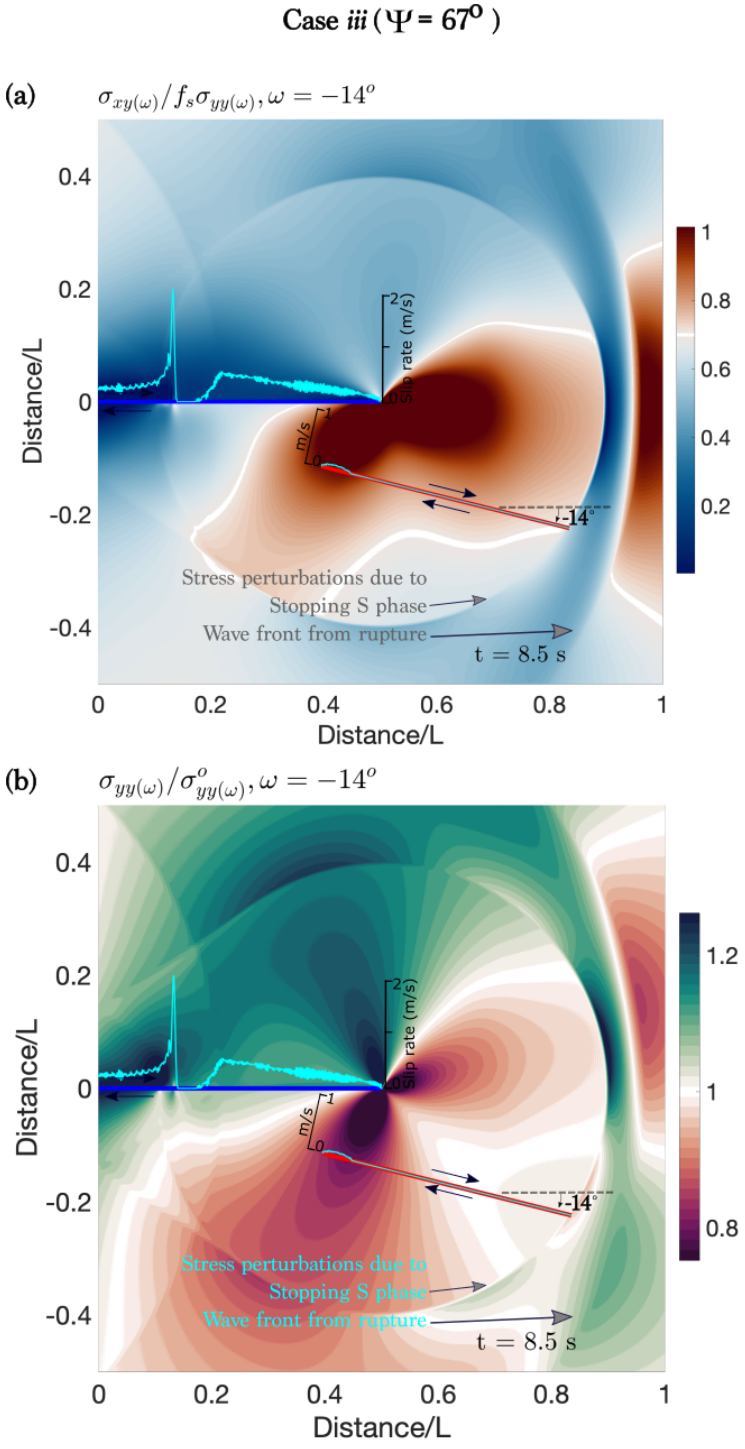

Figure 5.12: **Case** *iii* **($\Psi = 67^o, \omega = -14^o$) : (a) Ratio Shear stress/Peak stress ($\sigma_{xy(\omega)}/f_s\sigma_{yy(\omega)}$) and (b) Normalized normal stress ($\sigma_{yy(\omega)}/\sigma^o_{yy(\omega)}$) at time $t =$ 8.5 s, for a dynamic rupture on extensional stepover faults embedded in a linear elastic medium.** Strike-slip faults are represented by straight lines colored in blue (fault 1) and red (fault 2). Stresses are rotated respect to the orientation ω of the fault 2. Initial orientation of the maximum principal stress σ_1 defined by angle Ψ is measured respect to the strike of the fault 1. White color labels the value that corresponds to the initial stress state. Slip rate on the faults (curves colored in cyan) is superimposed on the snapshots. Parameters are summarized in table 5.1 and 5.2.

Regarding the stress ratio along the second fault, figure 5.14 displays significant stress changes after the rupture arrest (time t $>$ 0 on the vertical axis). Particularly, a notable stress perturbation corresponding to the impact of the seismic waves from rupture and stopping S phase can be observed around time t $\sim$ 1.3 s. However, despite these stress changes, a considerable time delay of Δt_j = 3.6 s is required for nucleation to occur on the second fault. A particular difference with the cases of extensional stepover faults with low angle Ψ can be observed. The initial stress ratio (value represented by white color), is equal to 0.7 for the current case, while it is higher than 0.9 for the previous cases (see figure 5.7). This difference is related to the initial orientation Ψ of the maximum principal stress σ_1 with respect to the strike orientation of fault 2. Angle Ψ on fault 2 for case *iii* is $\sim 52.8^o$; whereas for cases *i* and *ii*, angle Ψ on fault 2 are $\sim 18^o$ and $\sim 28^o$, respectively. Considering that the optimal angle Ψ to failure is 30^o for a static friction coefficient 0.6, we can remark that the stepover in case *iii* requires higher stress change than cases *i* and *ii* to allow jumping rupture.

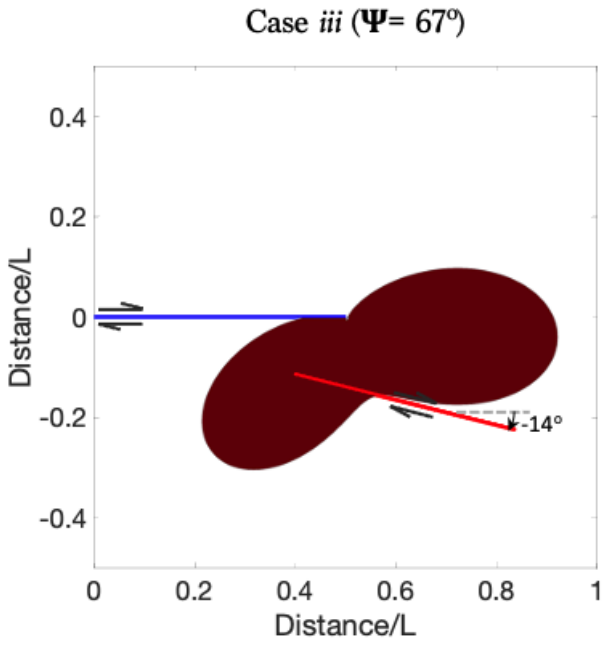

Figure 5.13: **Static solution of the ratio Shear stress/Peak stress for extensional stepover system, case *iii*, with high angle Ψ.** Strike-slip faults are represented by straight lines colored in blue (fault 1) and red (fault 2). Stresses correspond to the orientation ω of the fault 2. Inside the red area, there is the required stress to overcome the frictional resistance for any fault with the strike orientation of fault 2. Initial orientation of the maximum principal stress σ_1 defined by angle Ψ is measured respect to the strike of the fault 1. L is the length of fault 1. Value 0 of normalized distance corresponds to the middle of the fault 1. Further detailed on the static solution, see chapter 4.

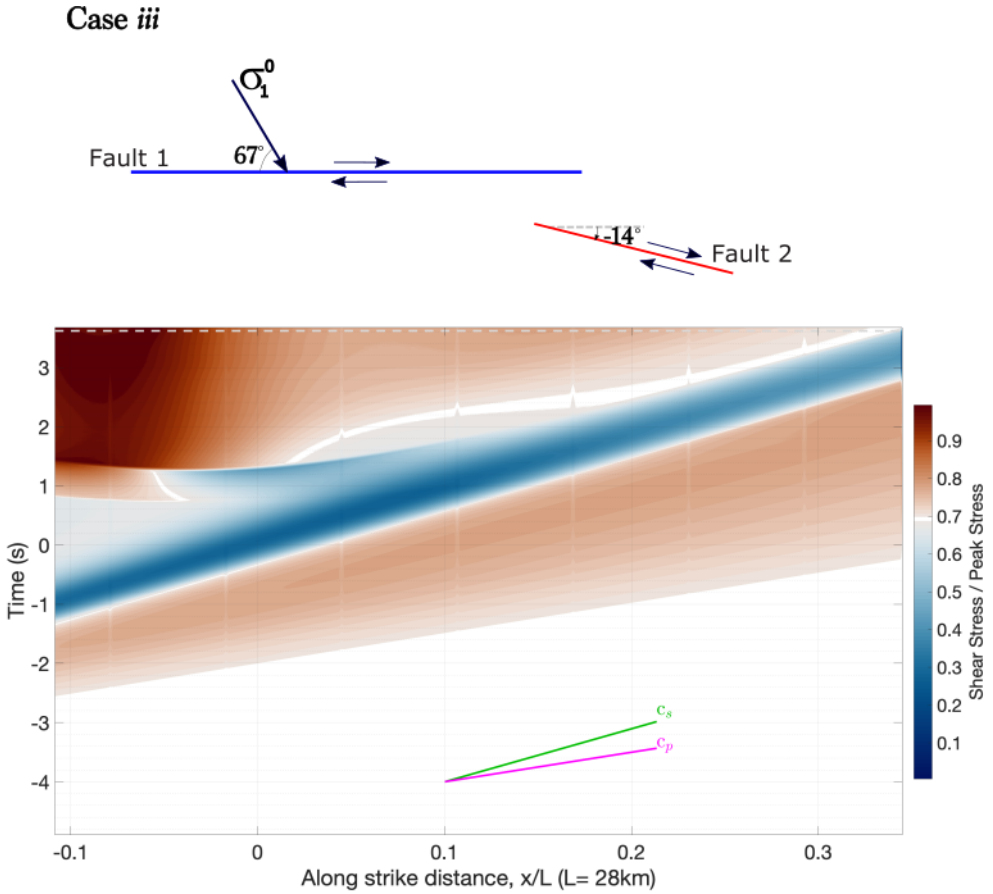

Figure 5.14: **Temporal evolution of the ratio Shear stress / Peak stress at the fault 2 for extensional stepover system, (a) case *iii* , with high angle Ψ.** Time = 0 : time when rupture reaches the end of fault 1. x/L = 0 : location where the end of fault 1 is projected at fault 2. Gray dashed line represents triggering time at fault 2. White color labels the initial stress state.

For cases *vi* and *vii* of a compressional stepover fault with a high angle Ψ, figures 5.15 and 5.16 display the stress ratio and normal stress, respectively. We observe a difference in the contribution of dynamic effects to enable jumping rupture between cases *vi* and *vii*. Notably, in case *vii*, the role of wave-mediated stress transfer on the right side of fault 2 is crucial in enabling jumping rupture, more so than in case *vi*. Regarding the stress ratio (figures 5.15a), for case *vi*, nucleation on the second fault is less likely to occur within the compressional side than the extensional side of fault 1. This condition is also observed in the static solution (see figure 5.17a).

Figure 5.18 illustrates a uniform stress ratio increment, represented by the transition from white to darker red color, occurring uniformly across a specific area on the right side of the fault 2, starting from time t = 0. This uniform increment in stress is attributed to the orientation of the second fault. For instance, in case *vi*, figure 5.15 shows that the stress increment surrounding the right side of fault 2 is closely perpendicular to the strike orientation. This consistent distribution is evident in figure 5.18 until jumping rupture is permitted. However, in case *vii*, the influence of the P-stopping phase becomes evident in the stresses exerted on the second fault, becoming noticeable approximately 0.5 seconds prior to nucleation on the second fault.

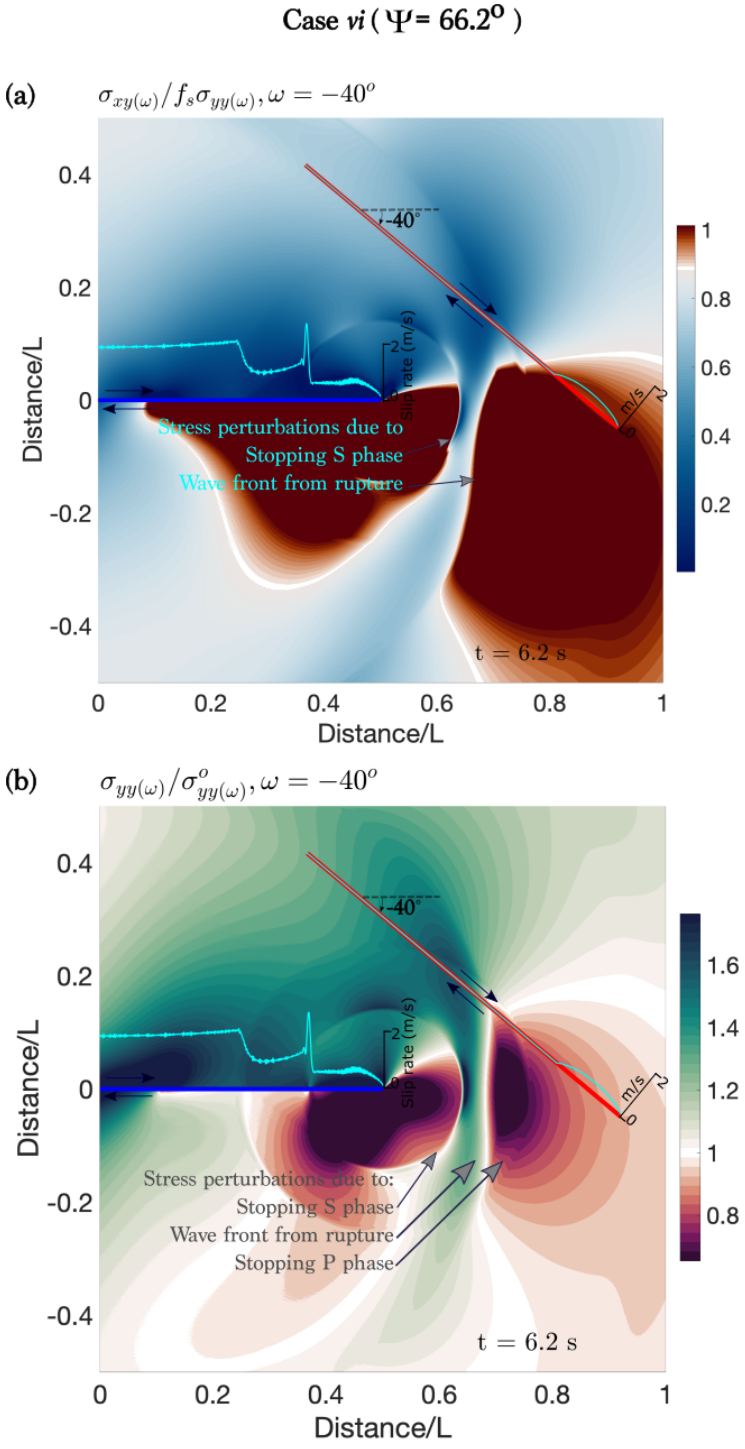

Figure 5.15: **Case *vi* ($\Psi = 66.2^o$, $\omega = -40^o$) : (a) Ratio Shear stress/Peak stress ($\sigma_{xy(\omega)}/f_s\sigma_{yy(\omega)}$) and (b) Normalized normal stress ($\sigma_{yy(\omega)}/\sigma^o_{yy(\omega)}$) at time t = 6.2 s, for a dynamic rupture on compressional stepover faults embedded in a linear elastic medium.** Strike-slip faults are represented by straight lines colored in blue (fault 1) and red (fault 2). Stresses are rotated respect to the orientation ω of the fault 2. Initial orientation of the maximum principal stress σ_1 defined by angle Ψ is measured respect to the strike of the fault 1. White color labels the value that corresponds to the initial stress state. Slip rate on the faults (curves colored in cyan) is superimposed on the snapshots. Parameters are summarized in table 5.1 and 5.2.

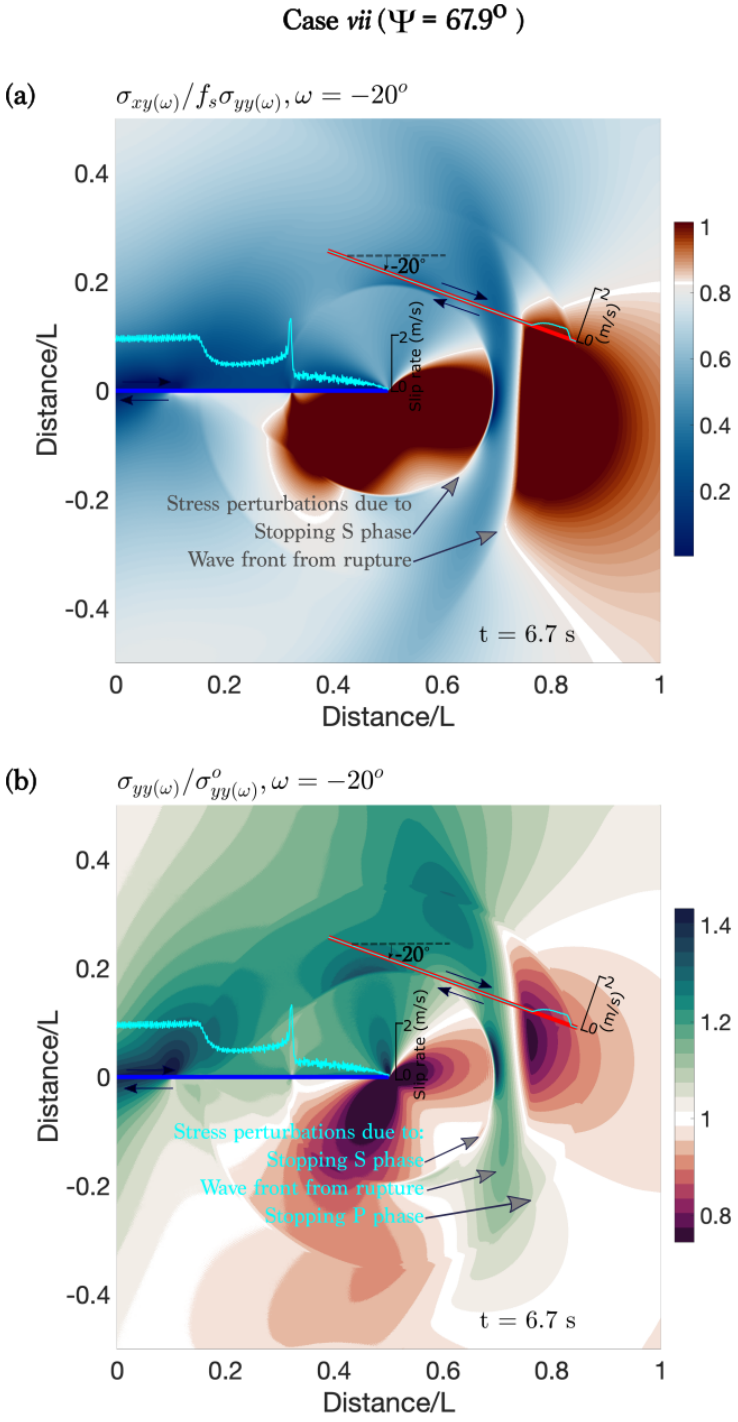

Figure 5.16: **Case *vii* ($\Psi = 67.9^o$, $\omega = -20^o$) : (a) Ratio Shear stress/Peak stress ($\sigma_{xy(\omega)}/f_s\sigma_{yy(\omega)}$) and (b) Normalized normal stress ($\sigma_{yy(\omega)}/\sigma^o_{yy(\omega)}$) at time t = 6.7 s, for a dynamic rupture on compressional stepover faults embedded in a linear elastic medium.** Strike-slip faults are represented by straight lines colored in blue (fault 1) and red (fault 2). Stresses are rotated respect to the orientation ω of the fault 2. Initial orientation of the maximum principal stress σ_1 defined by angle Ψ is measured respect to the strike of the fault 1. White color labels the value that corresponds to the initial stress state. Slip rate on the faults (curves colored in cyan) is superimposed on the snapshots. Parameters are summarized in table 5.1 and 5.2.

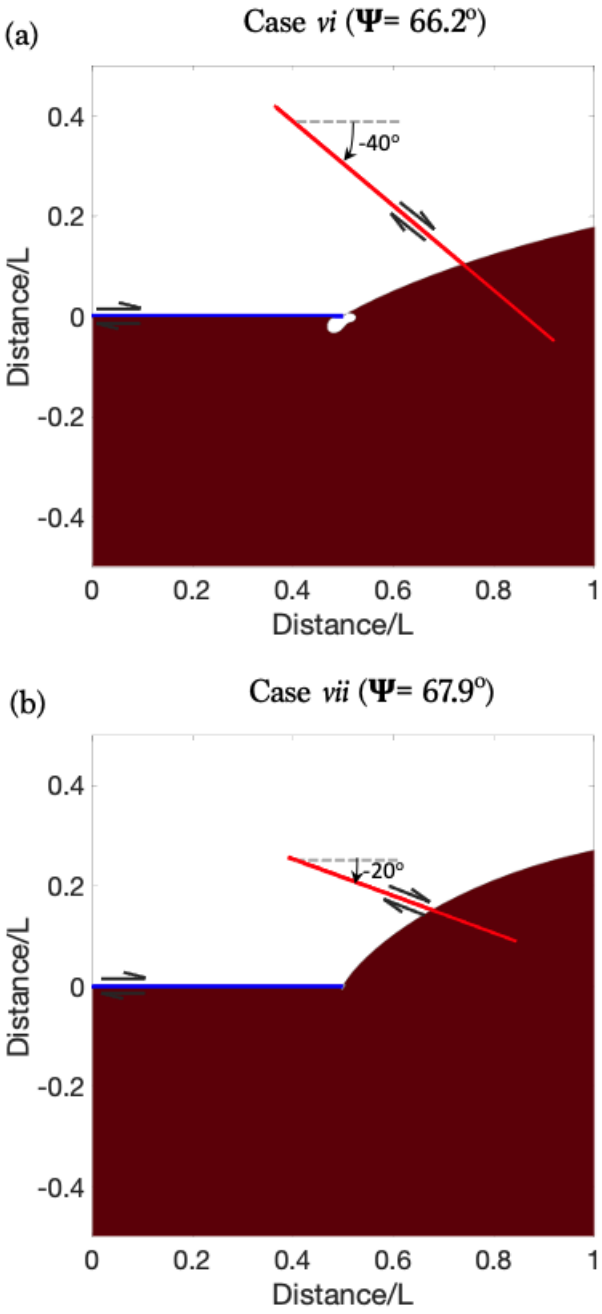

Figure 5.17: **Static solution of the ratio Shear stress/Peak stress for compressional stepover system, (a) case *vi* and (b) case *vii* , with high angle Ψ.** Strike-slip faults are represented by straight lines colored in blue (fault 1) and red (fault 2). Stresses correspond to the orientation ω of the fault 2. Inside the red area, there is the required stress to overcome the frictional resistance for any fault with the strike orientation of fault 2. Initial orientation of the maximum principal stress σ_1 defined by angle Ψ is measured respect to the strike of the fault 1. L is the length of fault 1. Value 0 of normalized distance corresponds to the middle of the fault 1. Further detailed on the static solution, see chapter 4.

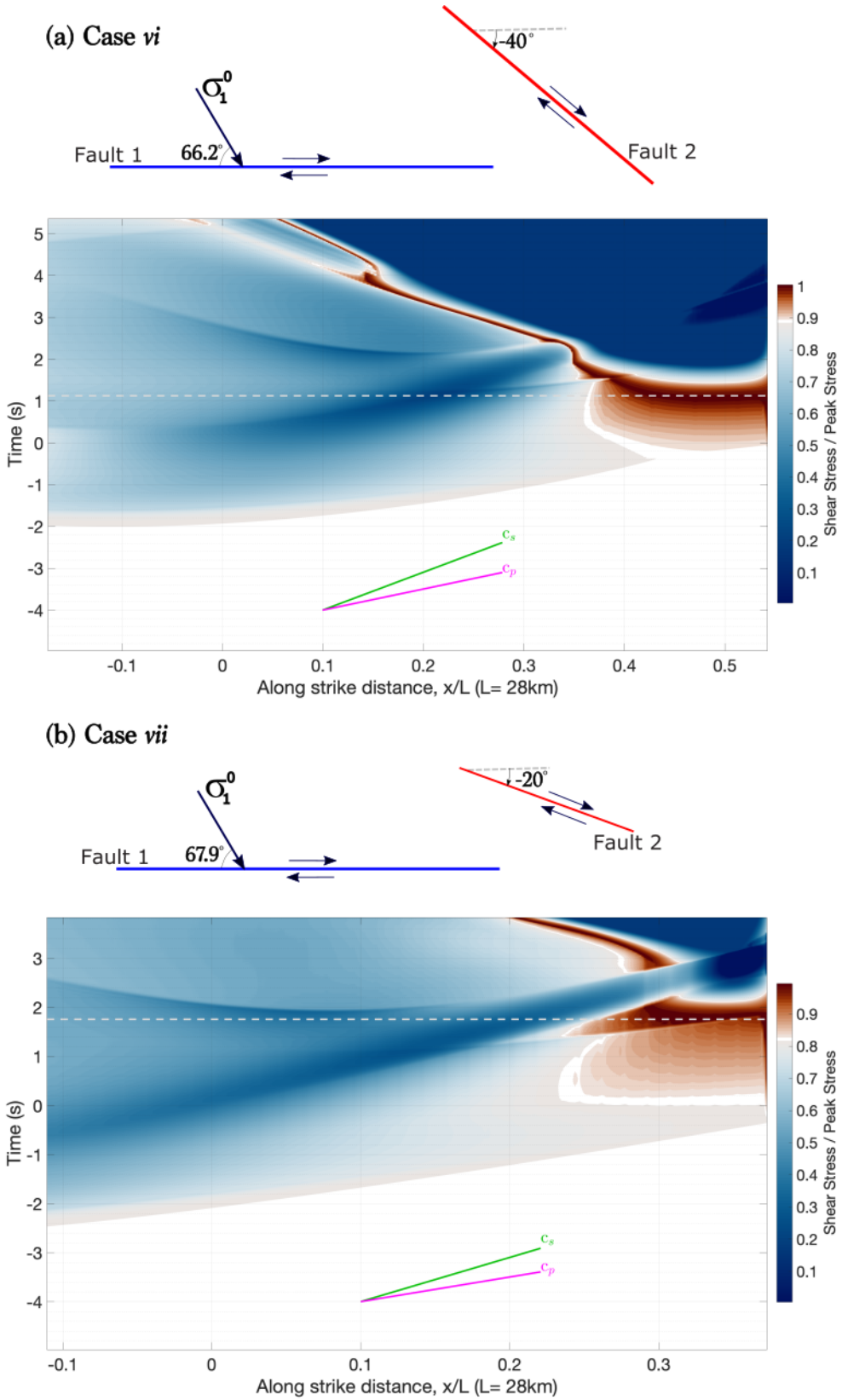

Figure 5.18: **Temporal evolution of the ratio Shear stress / Peak stress at the fault 2 for compressional stepover system, (a) case *vi* and (b) case *vii*, with high angle Ψ.** Time = 0 : time when rupture reaches the end of fault 1. x/L = 0 : location where the end of fault 1 is projected at fault 2. Gray dashed line represents triggering time at fault 2. White color labels the initial stress state.

5.4 Effects of off-fault damage on jumping rupture

In previous section for 2D earthquake rupture simulation around stepover faults in elastic medium, we reported that different parameters play a role in promoting rupture jumping (1) the geometry of the second fault (2) the orientation of the initial stress field (3) the amount of slip on fault 1 and (4) the wave-mediated stress trasnfer. In this section, we explore the additional contribution of dynamic off-fault damage.

The 2D earthquake rupture simulations previously conducted in elastic medium are run again with a brittle damage rheology. As discussed in chapter 3, the angle Ψ substantially impacts on the spatial distribution of damage (e.g. *Poliakov et al.*, 2002; *Templeton and Rice*, 2008). As a consequence, results are grouped in two categories: a low and a high angle Ψ. Additionally, in this section, we discuss how dynamic damage impacts different stepover systems (extensional or compressional).

5.4.1 Low angle ψ

5.4.1.a Extensional stepover system

Comparison between damage and elastic results for extensional stepover fault with low angle Ψ is shown in figure 5.20. Since cases *i* and *ii* display similar contrasts between the damage and the elastic simulations, we only analyse here case *i*. For a better comparison, we choose the snapshots so that the initial rupture fronts in damage and elastic simulations are located at the same position on fault 1. We do not observe any differences which is directly attributed to the absence of any damage as shown in figure 5.19a. In this figure, values of damage around the stepover faults are in the interval between 0 and 1. Our initial damage state is 0.1 (table 5.1) and the maximum value, equals 1, represents the damage state of pulverized rock. Nonetheless, after the initial rupture reaches the end of the first fault, there are

substantial changes in damage, and hence the elastic properties around the end of the fault (figure 5.21). For instance, reduction of P wave speed, calculated using equation 2.34, reaches ∼25%. This suggests that the strong stress perturbation due to the rupture arrest allows the growth of microcracks, even in cases with low angle Ψ where no significant damage is expected (e.g. *Templeton and Rice*, 2008). This high damage density at the end of a fault agrees with different numerical studies and geological observation of damage fault zone (e.g. *Kim et al.*, 2004; *Rice et al.*, 2005; *Ostermeijer et al.*, 2020). In our results, we notice that these changes on the elastic properties present preferred orientations at the edge of the first fault that nearly matches with the shape patterns of the static solution (see figure 5.6a).

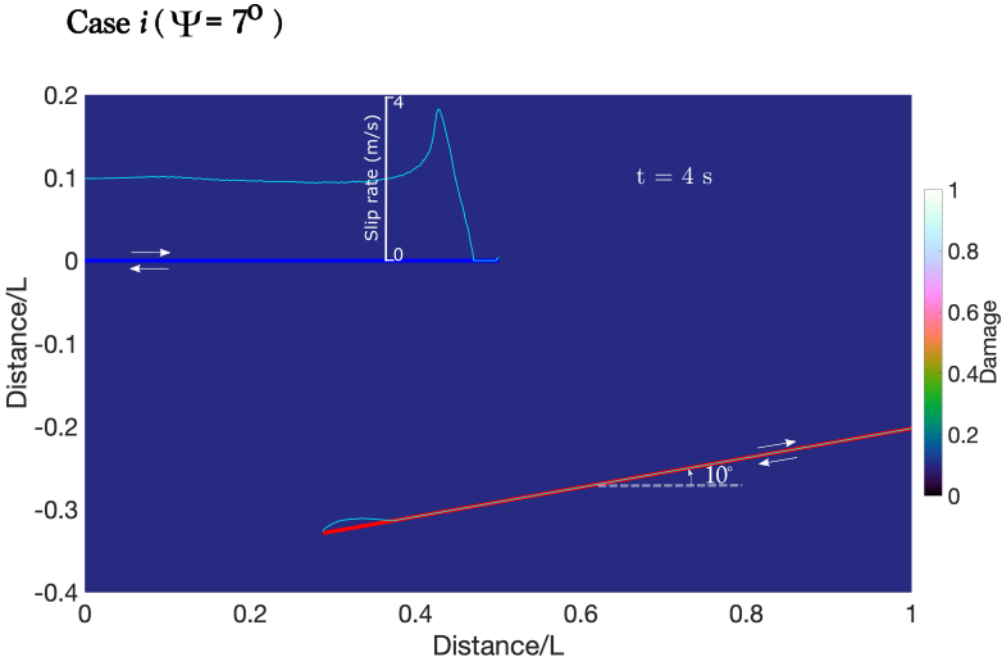

Figure 5.19: **Damage state at time when jumping rupture is allowed on extensional stepover faults embedded in a brittle off-fault medium, with low angle Ψ.** Extensional stepover system correspond to case *i* ($\Psi = 7^o$, $\omega = 10^o$). Strike-slip faults are represented by straight lines colored in blue (fault 1) and red (fault 2). Initial orientation of the maximum principal stress σ_1 defined by the angle Ψ is measured respect to the strike of the fault 1. Slip rate on the faults (curves colored in cyan) is superimposed on the snapshots. Length of fault 1, L =28 km. Parameters are summarized in table 5.1 and 5.2.

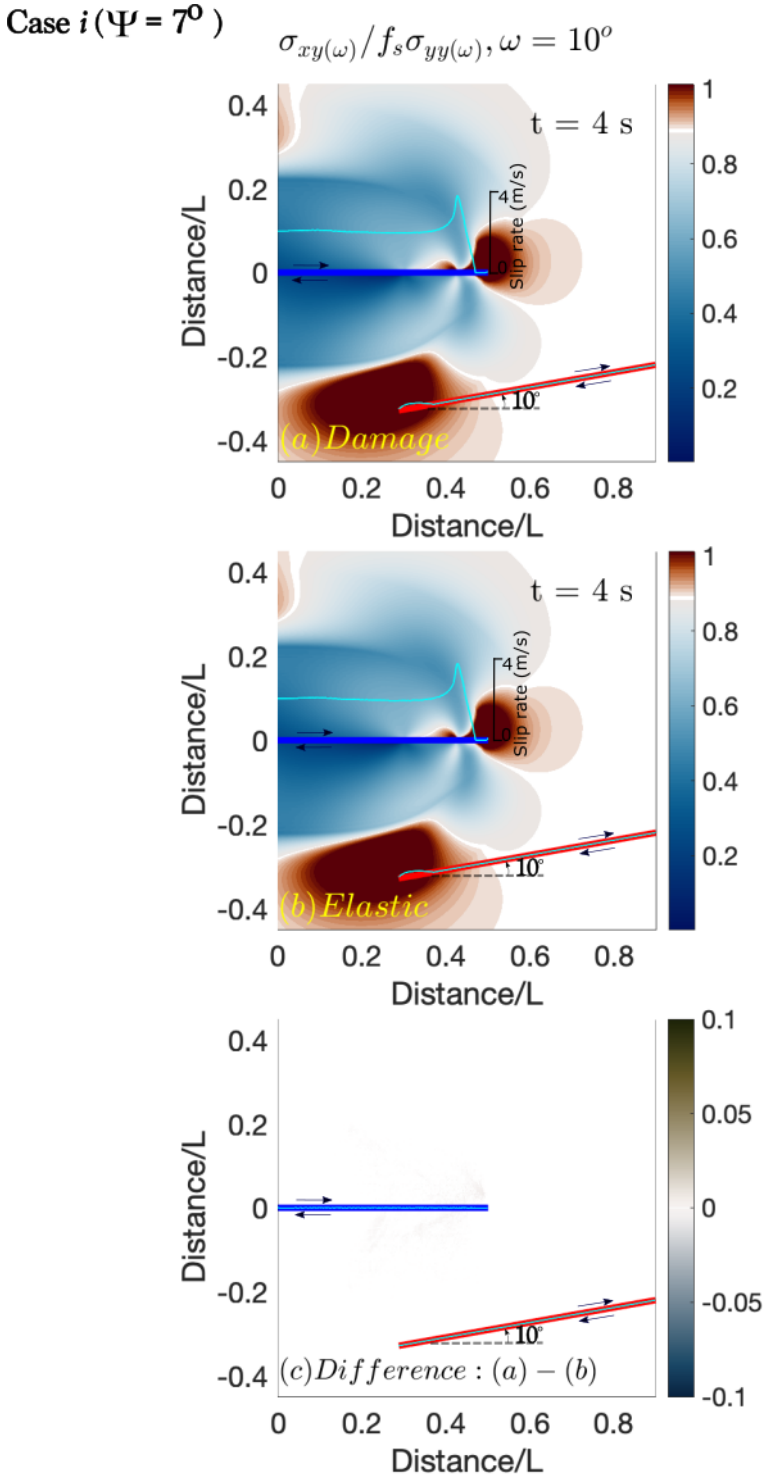

Figure 5.20: **Case i ($\Psi = 7^o$, $\omega = 10^o$) : (c) comparison of ratio shear stress / peak stress ($\sigma_{xy(\omega)}/f_s\sigma_{yy(\omega)}$) for a dynamic rupture on extensional stepover faults embedded in (a) damage and (b) elastic medium.** Strike-slip faults are represented by straight lines colored in blue (fault 1) and red (fault 2). Stresses are rotated respect to the orientation ω of fault 2. Initial orientation of the maximum principal stress σ_1 defined by the angle Ψ is measured respect to the strike of the fault 1. White color in figures (a) and (b) labels the initial stress state. Slip rate on the faults (curves colored in cyan) is superimposed on the snapshots. Length of fault 1, L =28 km. Parameters are summarized in table 5.1 and 5.2.

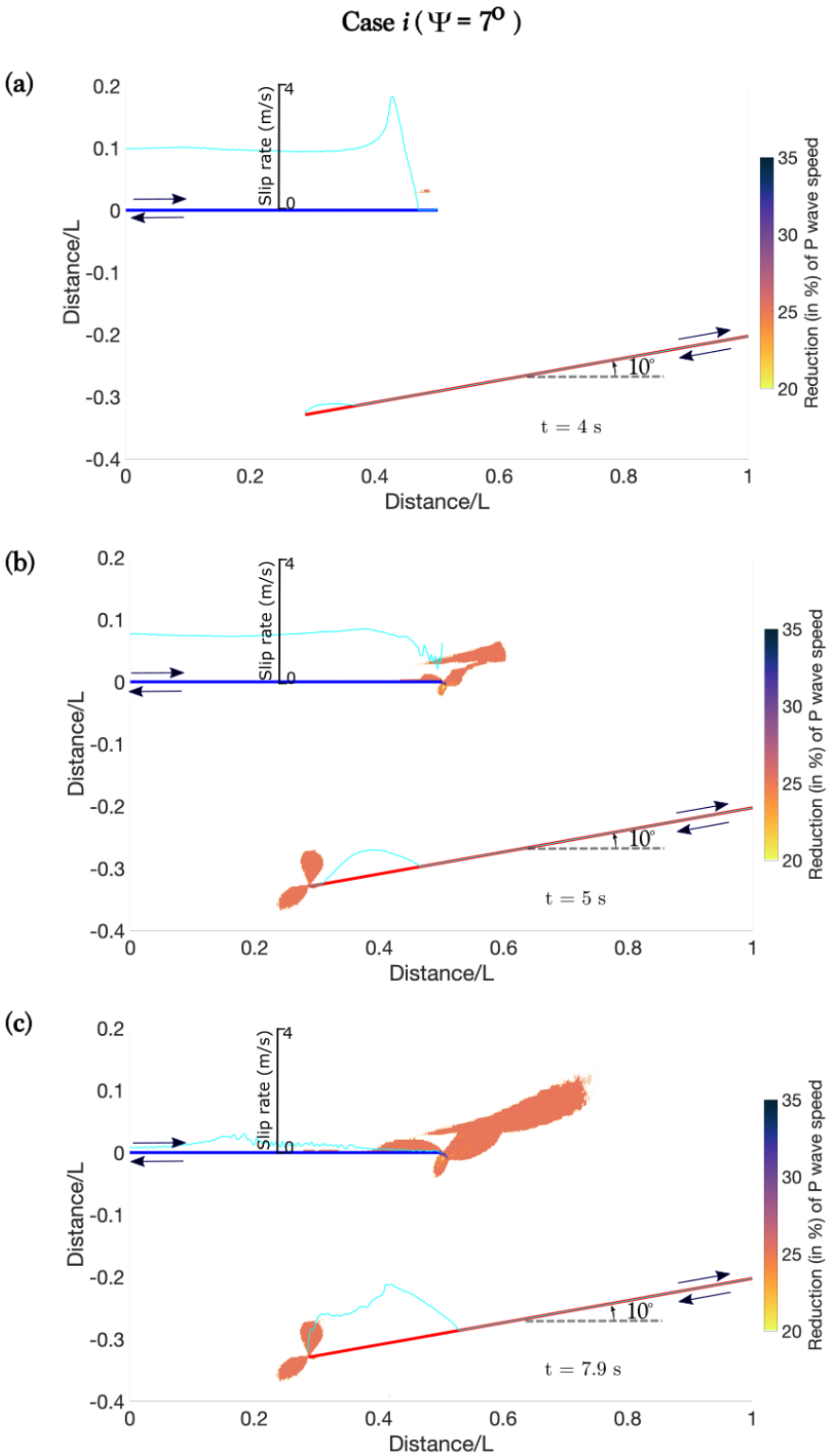

Figure 5.21: **Reduction (in %) of P wave speed at times (a) $t = 4$ s, (b) $t = 5$ s and (c) $t = 7.9$ s for a dynamic rupture on extensional stepover faults embedded in a brittle off-fault medium, with low angle Ψ.** Extensional stepover system corresponds to case i ($\Psi = 7^o$, $\omega = 10^o$). Strike-slip faults are represented by straight lines colored in blue (fault 1) and red (fault 2). Initial orientation of the maximum principal stress σ_1 defined by the angle Ψ is measured respect to the strike of the fault 1. Slip rate on the faults (curves colored in cyan) is superimposed on the snapshots. Length of fault 1, L =28 km. Parameters are summarized in table 5.1 and 5.2.

5.4.1.b Compressional stepover system

Comparison between damage and elastic results for compressional stepover fault with low angle Ψ is shown in figure 5.23. In this part, we analyse only case v since both cases vi and v present similar results. We observe that the strongest stress perturbation resulting from damage is localized at the end of the first fault, due to the rupture arrest (see figure 5.23c). According to the time delay $\Delta t_j^{d/e}$ (table 5.5) required to allow jumping rupture after the rupture arrest on fault 1, damage tends to favor jumping rupture (Δt_j^d is slightly small than Δt_j^e) or at least it does not prevent it. Two factors are affected by damage: (1) We observe a slight increase in cumulative slip on fault 1 (figure 5.25) and (2) the seismic waves are impacted by the reduction of P and S wave speeds around the end of the fault 1 (figure 5.26). This increase of fault slip enhances the stresses on the second fault, yet the discrepancy is very small in comparison to the elastic case. Reduction in P wave speed ($\sim 25\%$) and S wave speed ($\sim 20\%$), as we can observe in figure 5.26, are significant but very localized. In fact, there is no remarkable difference in the stress ratio between the elastic and the damage cases (figure 5.24c). A closer examination reveals a small difference in the temporal evolution of the stress ratio along the second fault. Figure 5.24 displays that during the positive increase of stress at the triggering location, around x/L = 0.3, there are additional slight stress perturbations since time t $\sim$ 2, in comparison with the elastic case. These perturbations arise from the impact of wave-mediated stress transfer that has passed through the localized damage at the end of fault 1. However, it is important to note that these effects are not substantial. Overall, even if more damage was produced compare to case i, it is still minor and it does not have an impact on rupture dynamics.

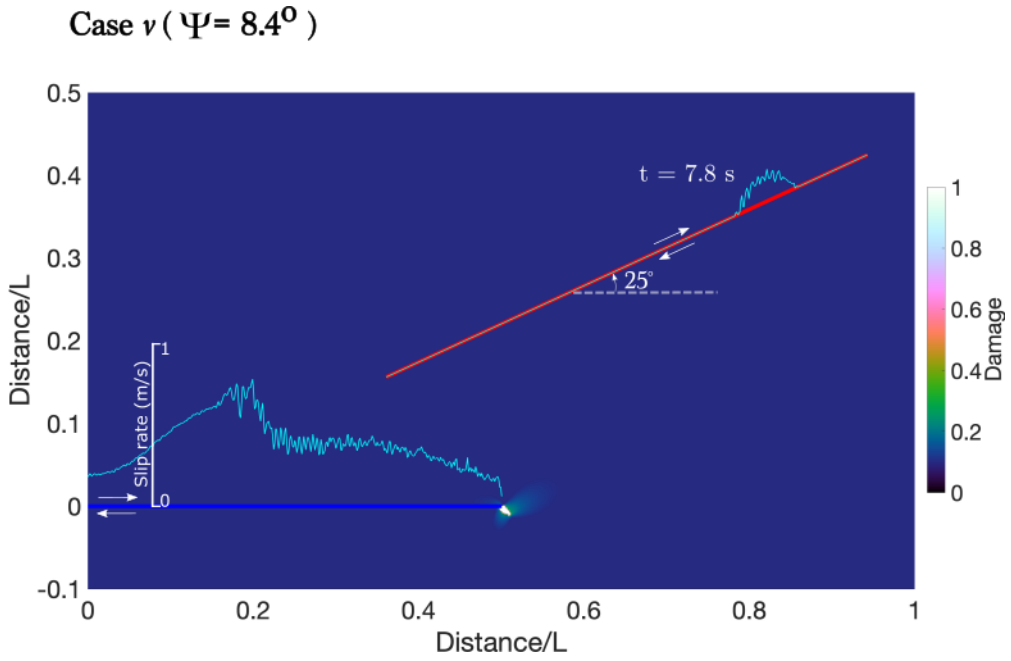

Figure 5.22: **Damage state at time when jumping rupture is allowed on compressional stepover faults embedded in a brittle off-fault medium, with low angle Ψ.** Compressional stepover system correspond to case v ($\Psi = 8.4^o$, $\omega = 25^o$). Strike-slip faults are represented by straight lines colored in blue (fault 1) and red (fault 2). Initial orientation of the maximum principal stress σ_1 defined by the angle Ψ is measured respect to the strike of the fault 1. Slip rate on the faults (curves colored in cyan) is superimposed on the snapshots. Length of fault 1, L =28 km. Parameters are summarized in table 5.1 and 5.2.

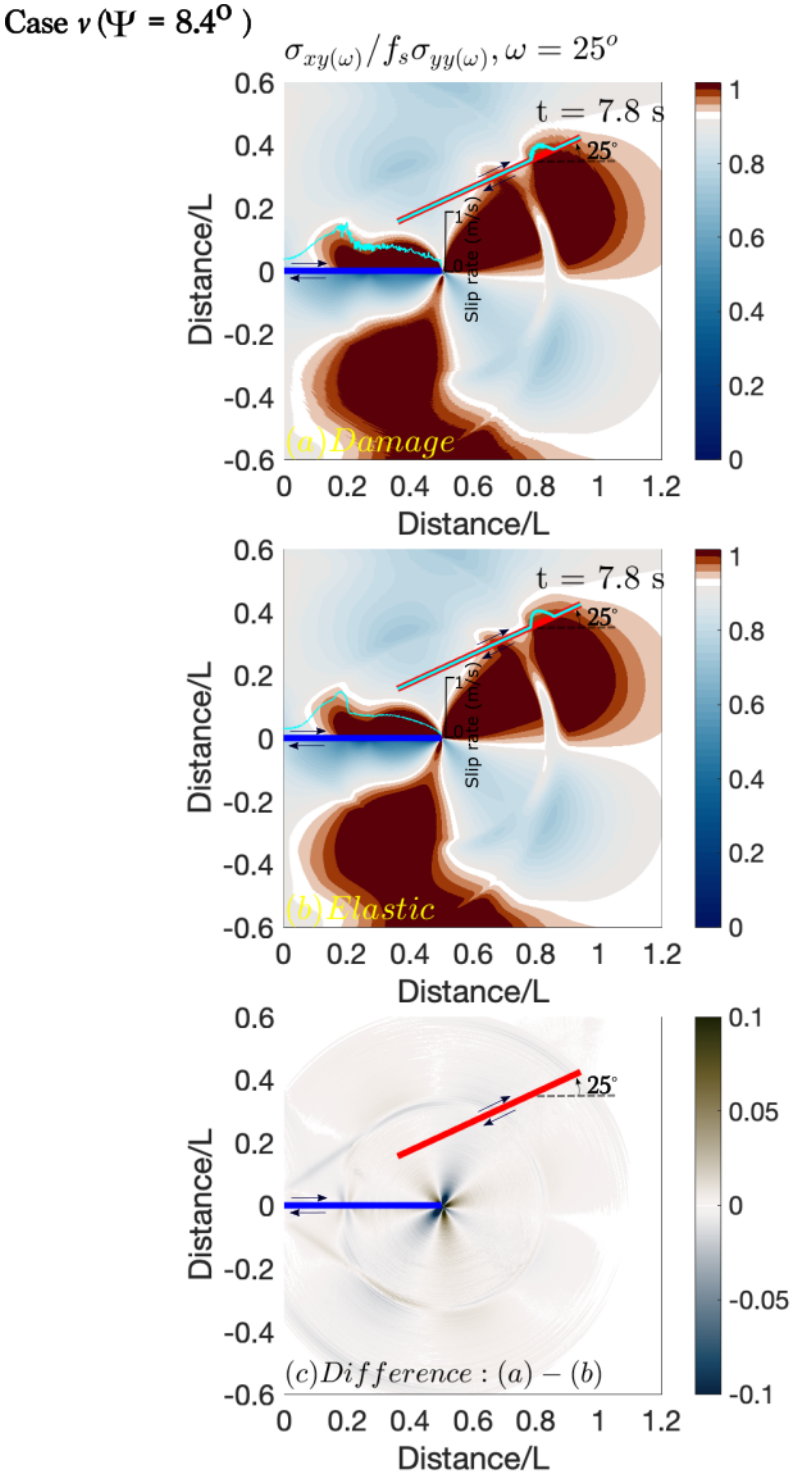

Figure 5.23: **Case v ($\Psi = 8.4^o$, $\omega = 25^o$) : (c) comparison of ratio shear stress / peak stress ($\sigma_{xy(\omega)}/f_s\sigma_{yy(\omega)}$) for a dynamic rupture on compressional stepover faults embedded in (a) damage and (b) elastic medium.** Strike-slip faults are represented by straight lines colored in blue (fault 1) and red (fault 2). Stresses are rotated respect to the orientation ω of fault 2. Initial orientation of the maximum principal stress σ_1 defined by the angle Ψ is measured respect to the strike of the fault 1. White color in figures (a) and (b) labels the initial stress state. Slip rate on the faults (curves colored in cyan) is superimposed on the snapshots. Length of fault 1, L =28 km. Parameters are summarized in table 5.1 and 5.2.

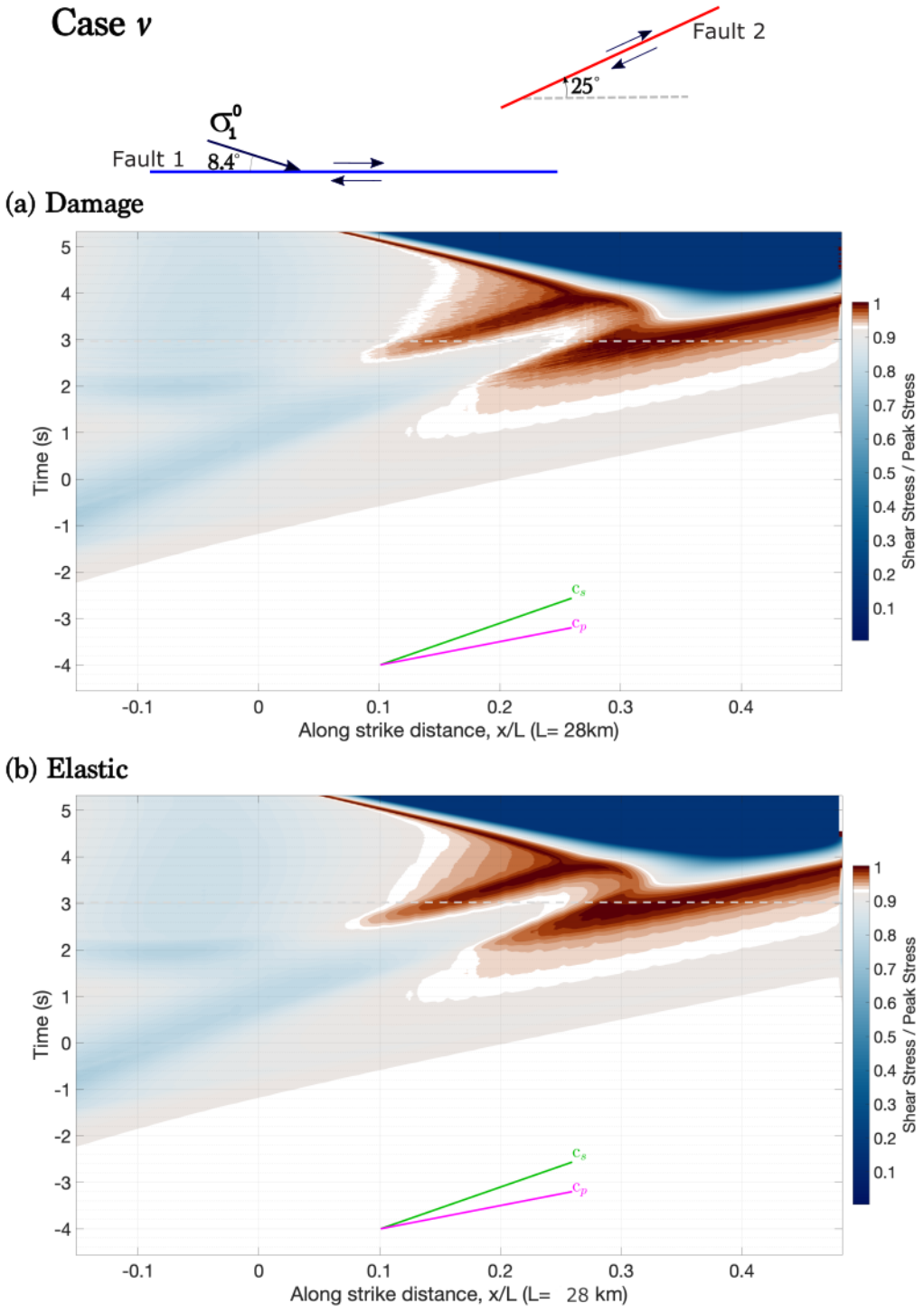

Figure 5.24: **Temporal evolution of the ratio Shear stress / Peak stress at the fault 2 for a dynamic rupture on compressional stepover faults embedded in (a) damage and (b) elastic medium, with low angle Ψ.** Compressional stepover system correspond to case v ($\Psi = 8.4^o$, $\omega = 25^o$). Time = 0 : time when rupture reaches the end of fault 1. x/L = 0 : location where the end of fault 1 is projected at fault 2. Gray dashed line represents triggering time at fault 2. White color labels the initial stress state.

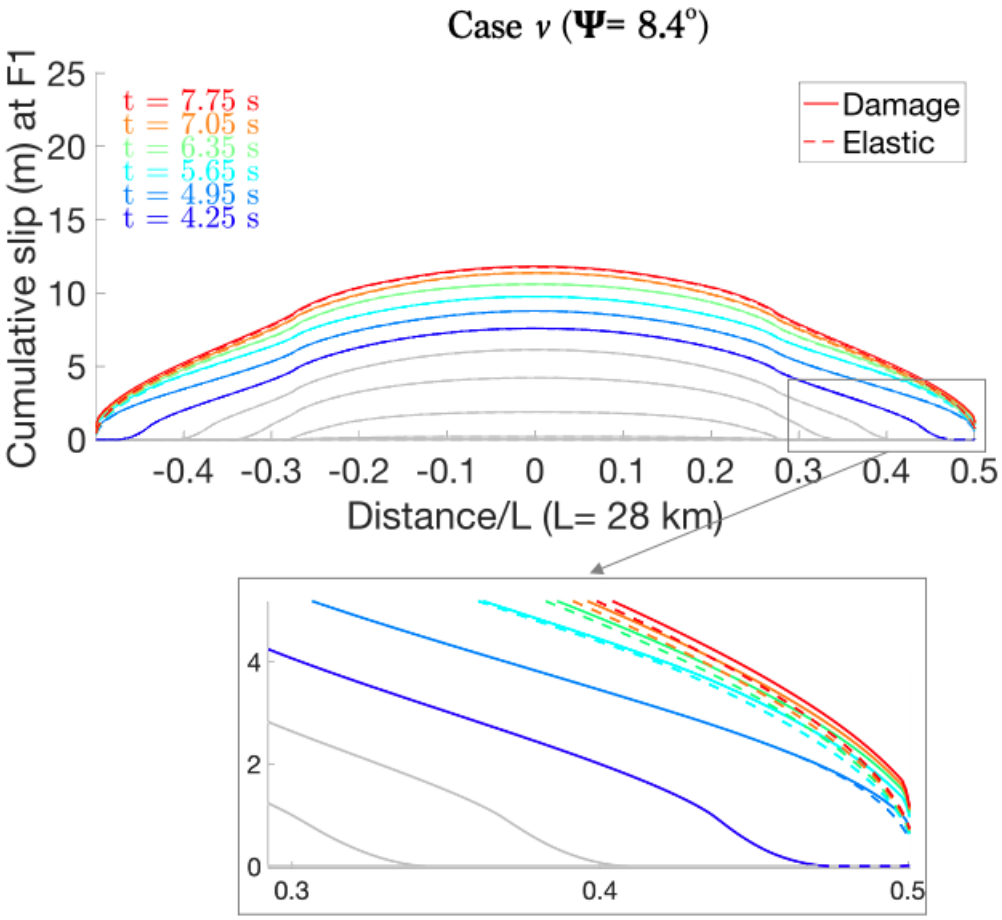

Figure 5.25: **Impact on fault slip: Temporal evolution of the cumulative slip at fault 1 for a dynamic rupture on compressional stepover faults with low angle Ψ ($\Psi = 8.4^o$, $\omega = 25^o$).** Comparison of simulations with dynamic damage (continuous lines) and elastic medium (dashed lines).

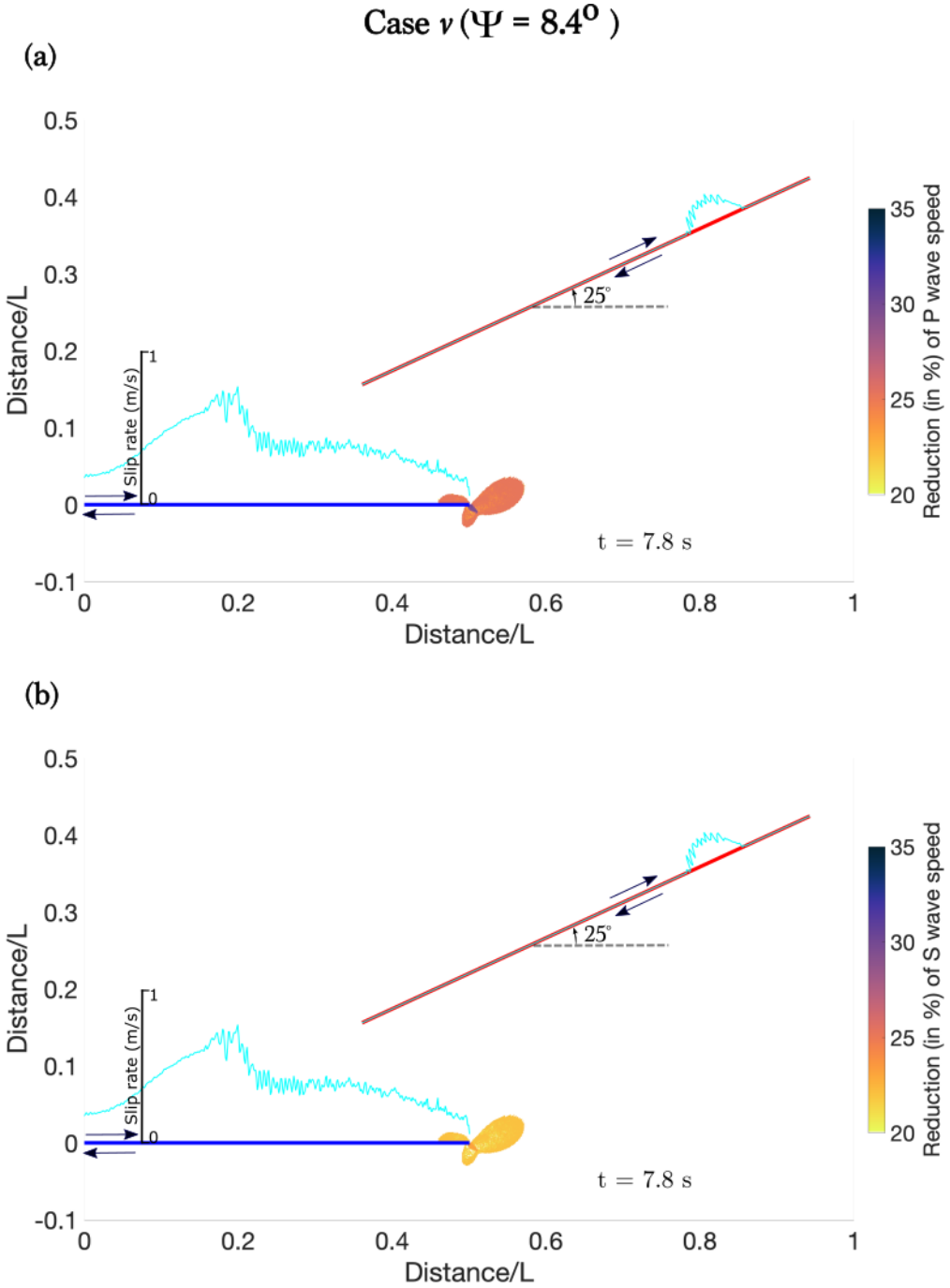

Figure 5.26: **Impact on seismic waves: Reduction (in %) of (a) P and (b) S wave speed at time t = 7.8 s for a dynamic rupture on compressional stepover faults embedded in a brittle off-fault medium, with low angle Ψ.** Compressional stepover system corresponds to case υ ($\Psi = 8.4^o$, $\omega = 25^o$). Strike-slip faults are represented by straight lines colored in blue (fault 1) and red (fault 2). Initial orientation of the maximum principal stress σ_1 defined by the angle Ψ is measured respect to the strike of the fault 1. Slip rate on the faults (curves colored in cyan) is superimposed on the snapshots. Length of fault 1, L =28 km. Parameters are summarized in table 5.1 and 5.2.

5.4.2 High angle ψ

5.4.2.a Extensional stepover system

Figure 5.27 shows two time steps of the damage state for case *iii*. This case corresponds to an extensional stepover faults with $\Psi = 67^o$ and ω = -14^o. The first snapshot corresponds to the instant, time t = 5.7 s, before the rupture jumps onto the second fault. The second snapshot, at time t = 8.5 s, corresponds to the moment after the earthquake is triggered at the second fault. There is generation of dynamic damage via the growth of microcracks located on the tensional side of the first fault. The fact that off-fault cracks grow in the direction of the maximum principal stress, σ_1 (*Thomas and Bhat*, 2018), promotes a positive change of stress aligned towards the fault 2. Figure 5.28 presents a comparison of the stress ratio between the damage and elastic simulations at three distinct time steps: t = 3.4 s, 4.4 s, and 5.4 s, relative to the damage simulation, before nucleation occurs on the second fault. It highlights, at the extensional side of the fault 1, the stress localization (labeled by darker brown color in figure 5.28d) at the tips of the growing cracks. This stress concentration will eventually interact with the stresses on fault 2 facilitating jumping rupture at earlier time than in elastic simulation. Regarding the normal stress, figure 5.29b for damage simulation shows that the previously mentioned stress concentration is favored by a significant reduction of normal stress (labeled by darker red color). This is one of the key effects generated by damage. When the rupture reaches the end of fault 1, higher damage density is generated at the stepover zone, increasing further its impacts. Further analysis can be observed from the stress ratio along the second fault. Figure 5.30 shows the stress ratio on fault 2 as a function of time for simulations with damage and elastic medium. We can observe that damage strongly favors jumping rupture, for this particular case, as it substantially reduces the time difference between the rupture arrest at the first fault (time = 0) and the triggering at the second fault.

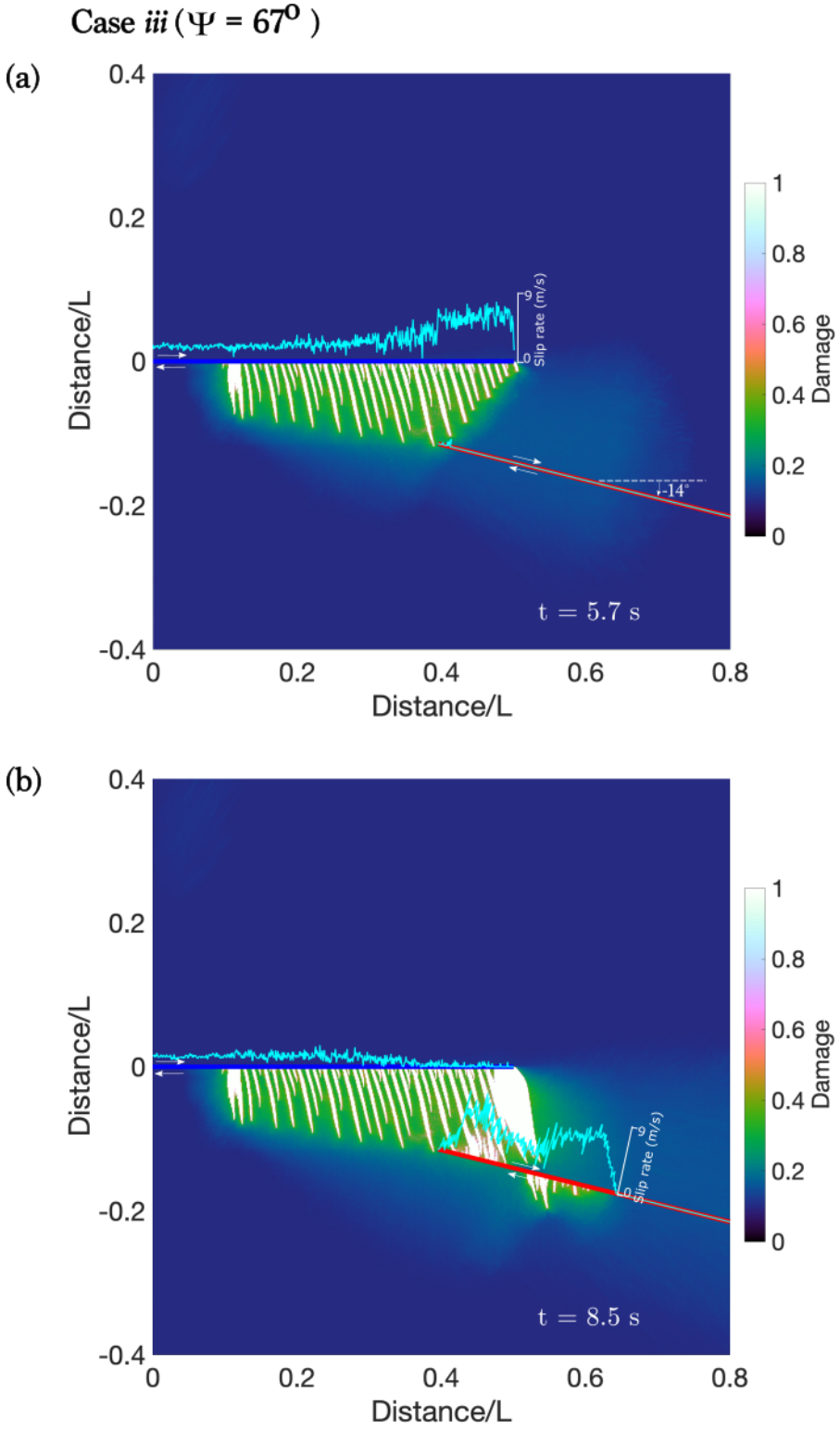

Figure 5.27: **Damage state at times (a) t = 5.7 s and (b) t = 8.5 s for a dynamic rupture on extensional stepover faults embedded in a brittle off-fault medium, with high angle Ψ.** Extensional stepover system correspond to case *iii* ($\Psi = 67^o$, ω = -14^o). Strike-slip faults are represented by straight lines colored in blue (fault 1) and red (fault 2). Initial orientation of the maximum principal stress σ_1 defined by the angle Ψ is measured respect to the strike of the fault 1. Slip rate on the faults (curves colored in cyan) is superimposed on the snapshots. Length of fault 1, L =28 km. Parameters are summarized in table 5.1 and 5.2.

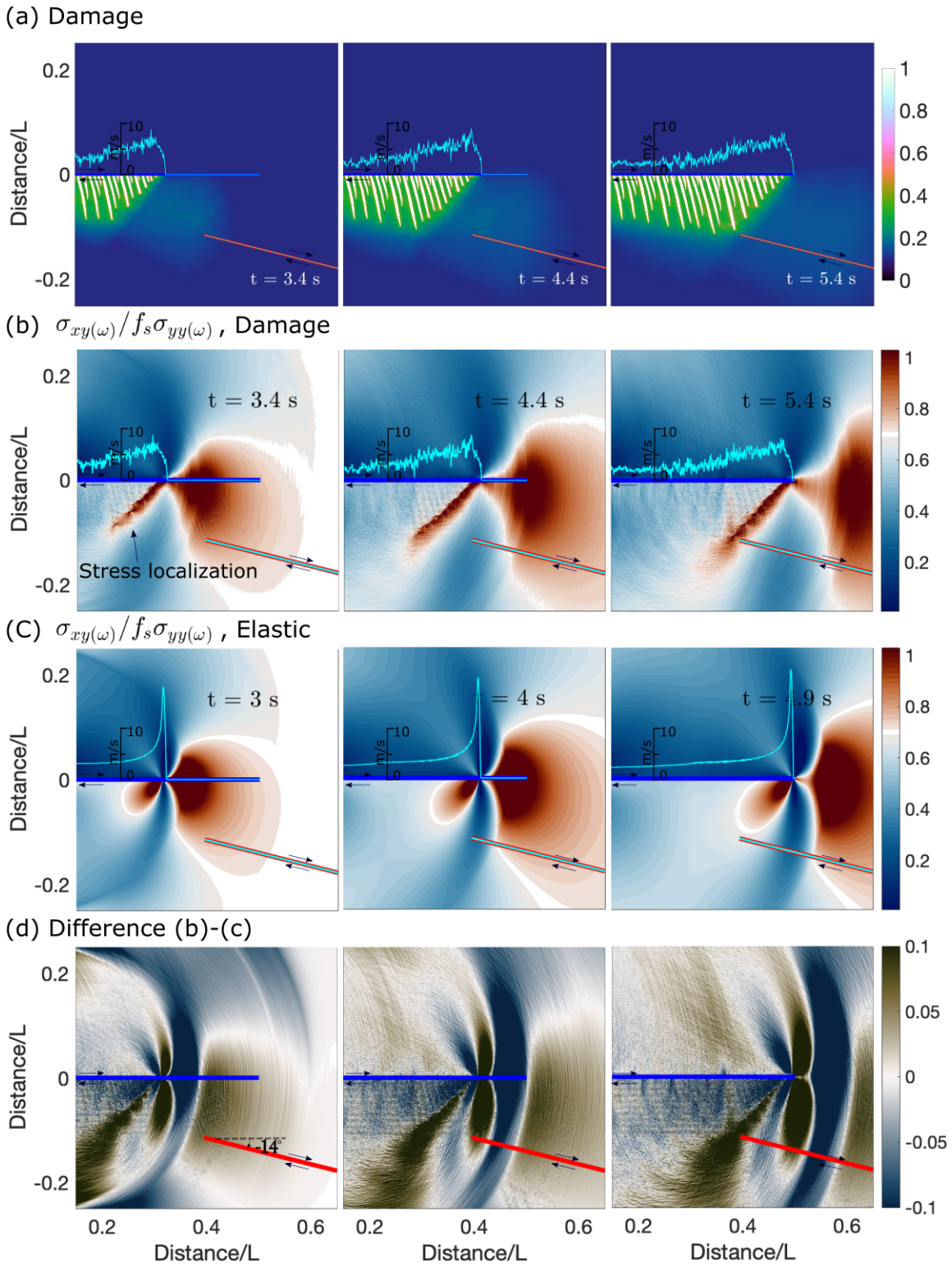

Figure 5.28: **Stress localization: Snapshots of (a) damage state, (b) stress ratio for damage medium, (c) stress ratio for elastic medium and (d) difference (b)-(c), for dynamic rupture on extensional stepover faults.** Extensional stepover system corresponds to case *iii* ($\Psi = 67^o$, ω = -14^o). White color in figures (b) and (c) labels the initial stress state. Slip rate on the faults (curves colored in cyan) is superimposed on the snapshots. Length of fault 1, L =28 km. Parameters are summarized in table 5.1 and 5.2.

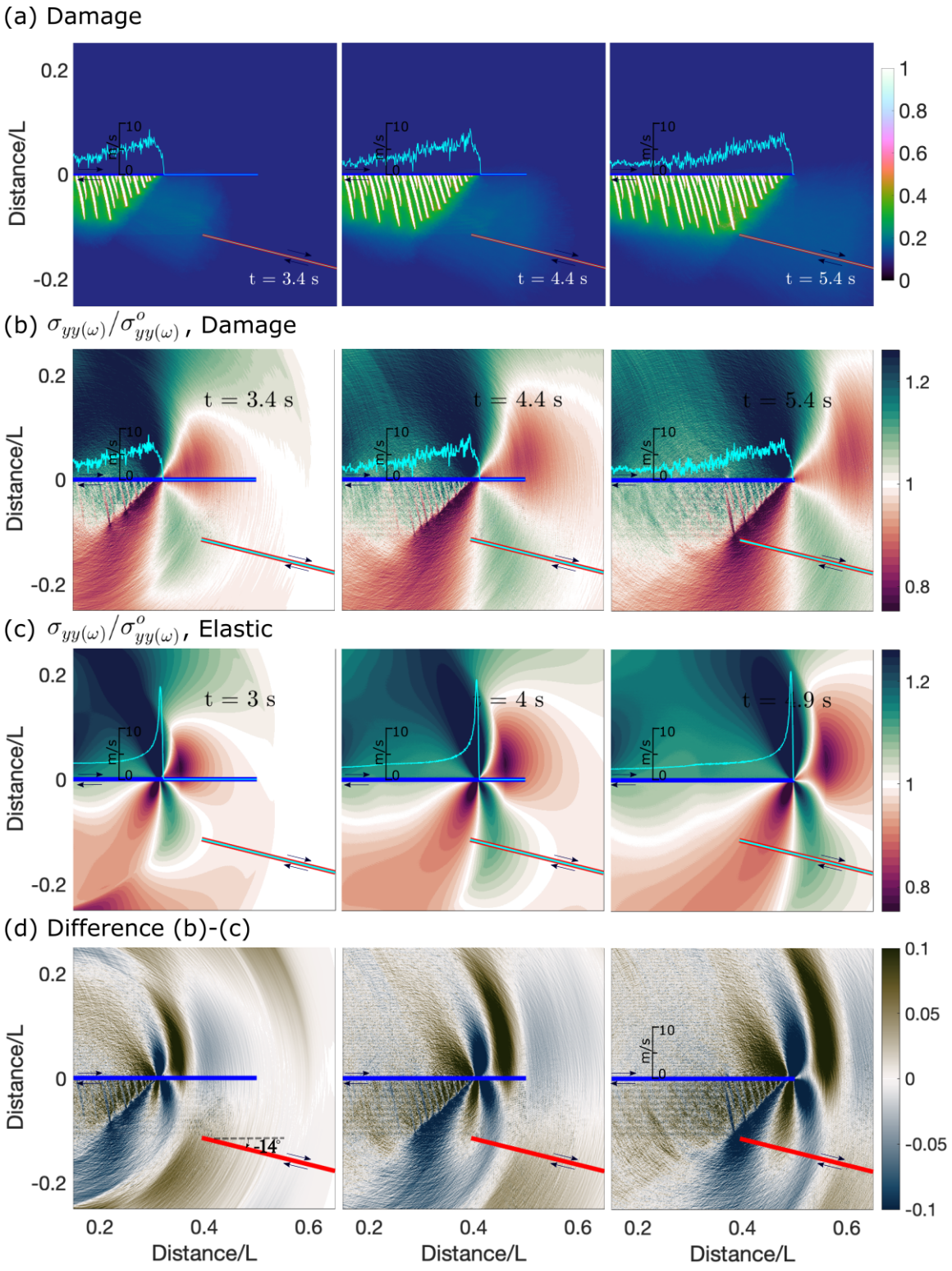

Figure 5.29: **Stress localization: Snapshots of (a) damage state, (b) normalized normal stress for damage medium, (c) normalized normal stress for elastic medium and (d) difference (b)-(c), for dynamic rupture on extensional stepover faults.** Extensional stepover system corresponds to case *iii* ($\Psi = 67^o$, ω = -14^o). White color in figures (b) and (c) labels the initial stress state. Slip rate on the faults (curves colored in cyan) is superimposed on the snapshots. Length of fault 1, L =28 km. Parameters are summarized in table 5.1 and 5.2.

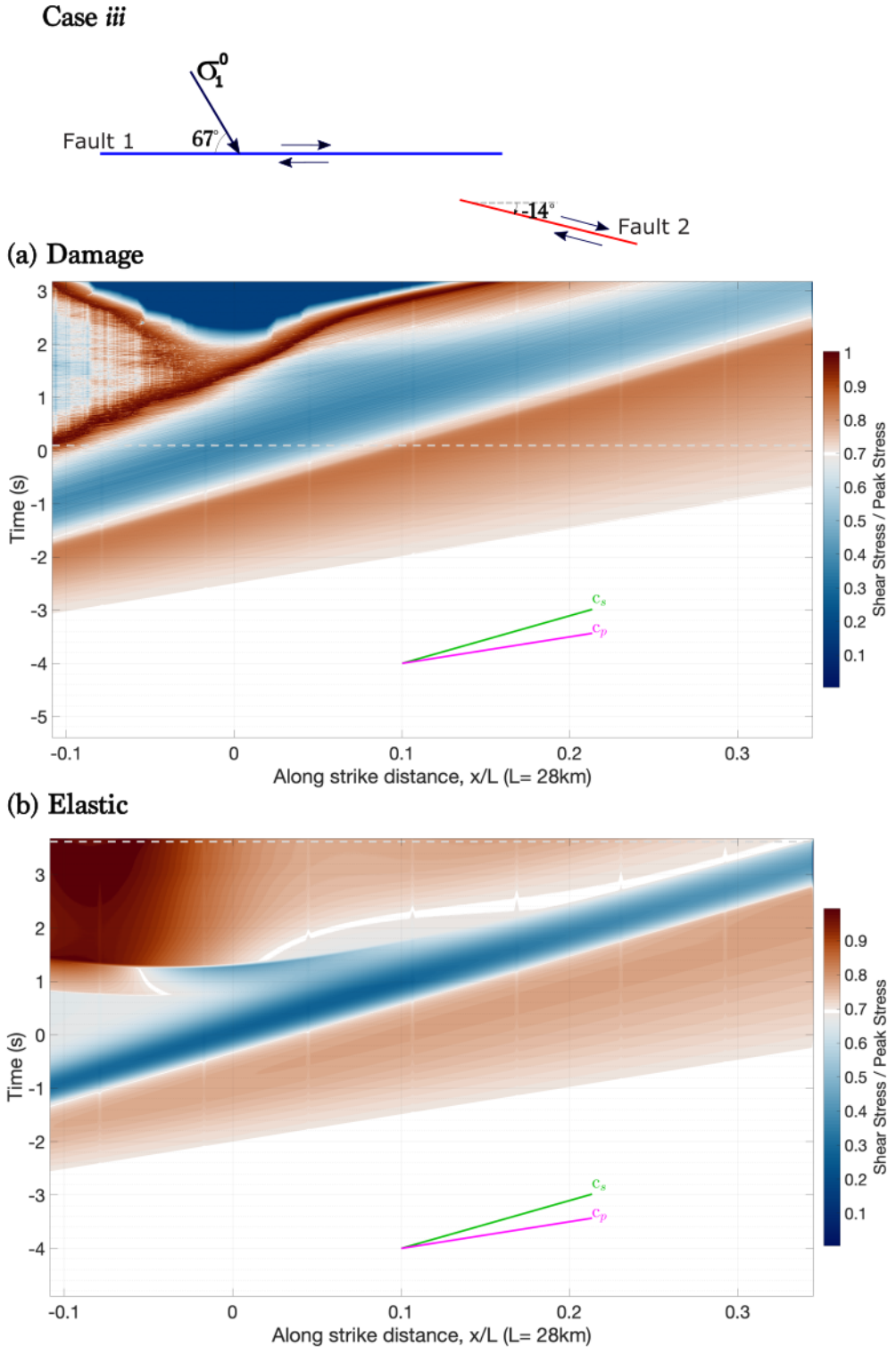

Figure 5.30: **Temporal evolution of the ratio Shear stress / Peak stress at the fault 2 for a dynamic rupture on extensional stepover faults embedded in (a) damage and (b) elastic medium, with high angle Ψ.** Extensional stepover system correspond to case *iii* ($\Psi = 67^o$, ω = -14^o). Time = 0 : time when rupture reaches the end of fault 1. x/L = 0 : location where the end of fault 1 is projected at fault 2. Gray dashed line represents triggering time at fault 2. White color labels the initial stress state.

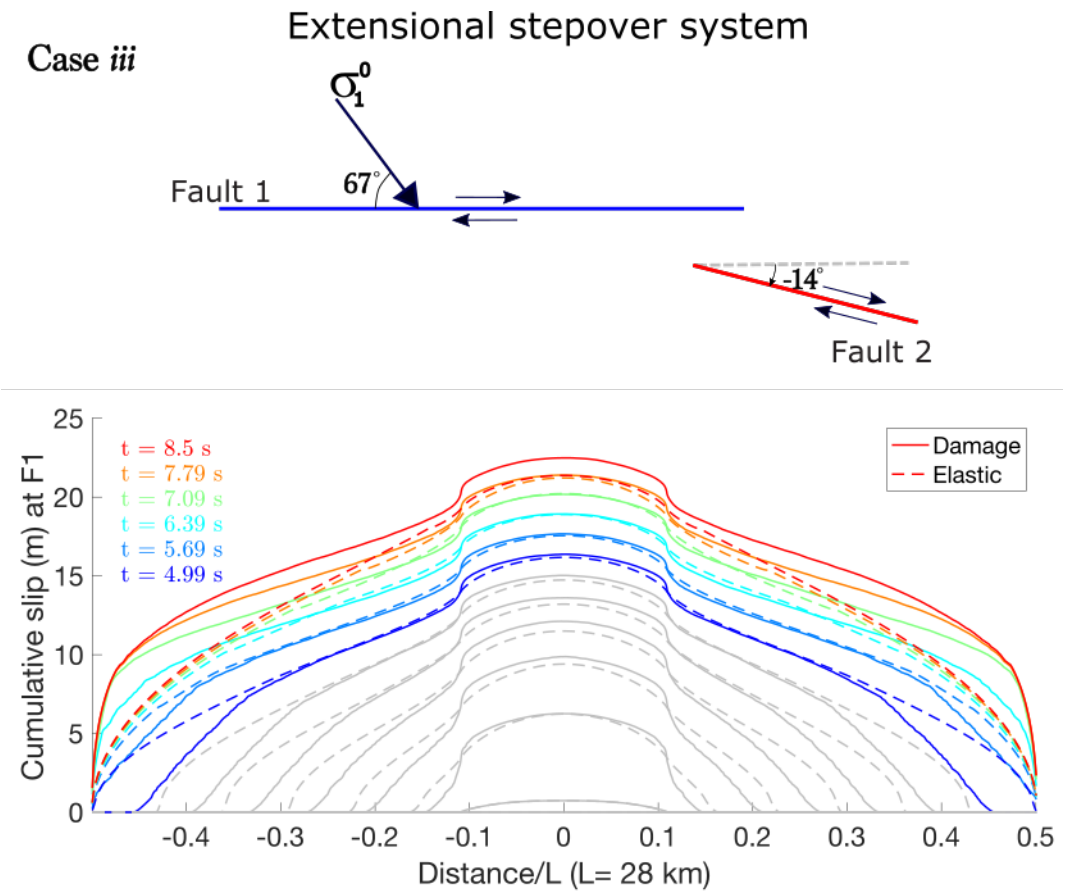

Figure 5.31: **Impact on fault slip: Temporal evolution of the cumulative slip at fault 1 for a dynamic rupture on extensional stepover faults with high angle Ψ. Comparison of simulations with dynamic damage and elastic medium.** Extensional stepover system corresponds to case *iii* ($\Psi = 67^o$, ω = -14^o).

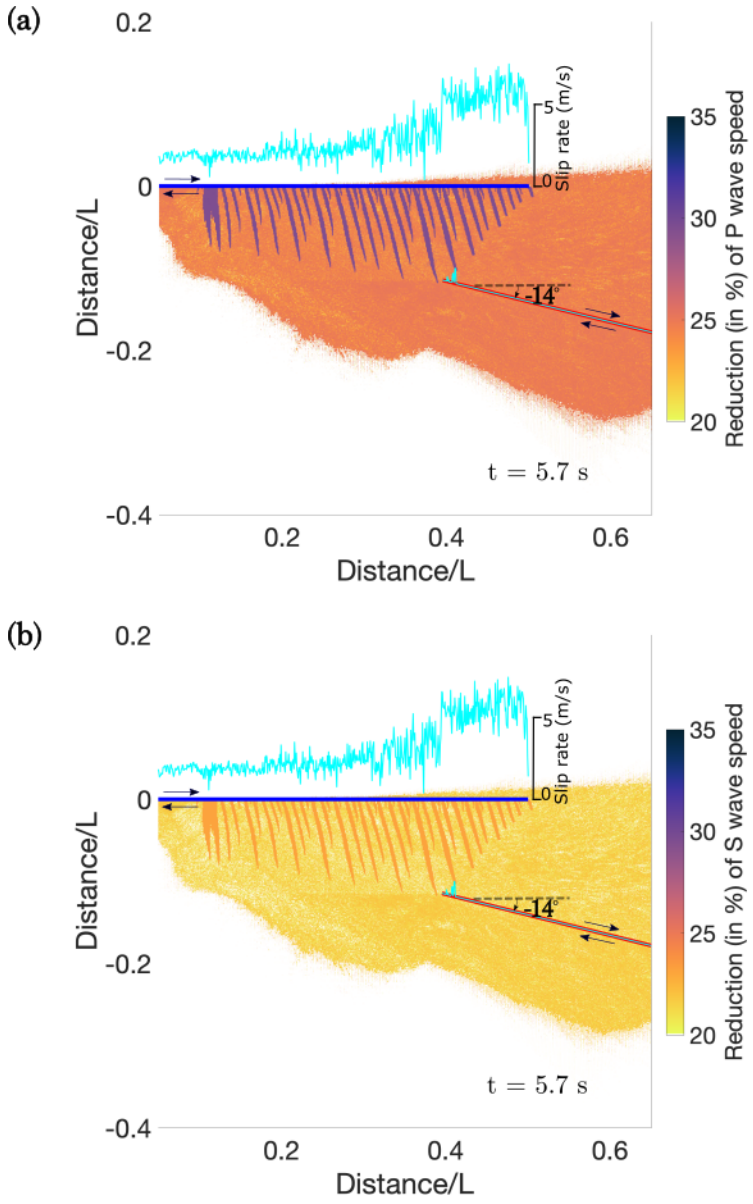

Figure 5.32: **Impact on seismic waves: Reduction (in %) of (a) P and (b) S wave speed at time t = 5.7 s for a dynamic rupture on extensional stepover faults embedded in a brittle off-fault medium, with high angle Ψ.** Extensional stepover system corresponds to case *iii* ($\Psi = 67^o$, ω = -14^o). Strike-slip faults are represented by straight lines colored in blue (fault 1) and red (fault 2). Initial orientation of the maximum principal stress σ_1 defined by the angle Ψ is measured respect to the strike of the fault 1. Slip rate on the faults (curves colored in cyan) is superimposed on the snapshots. Length of fault 1, L =28 km. Parameters are summarized in table 5.1 and 5.2.

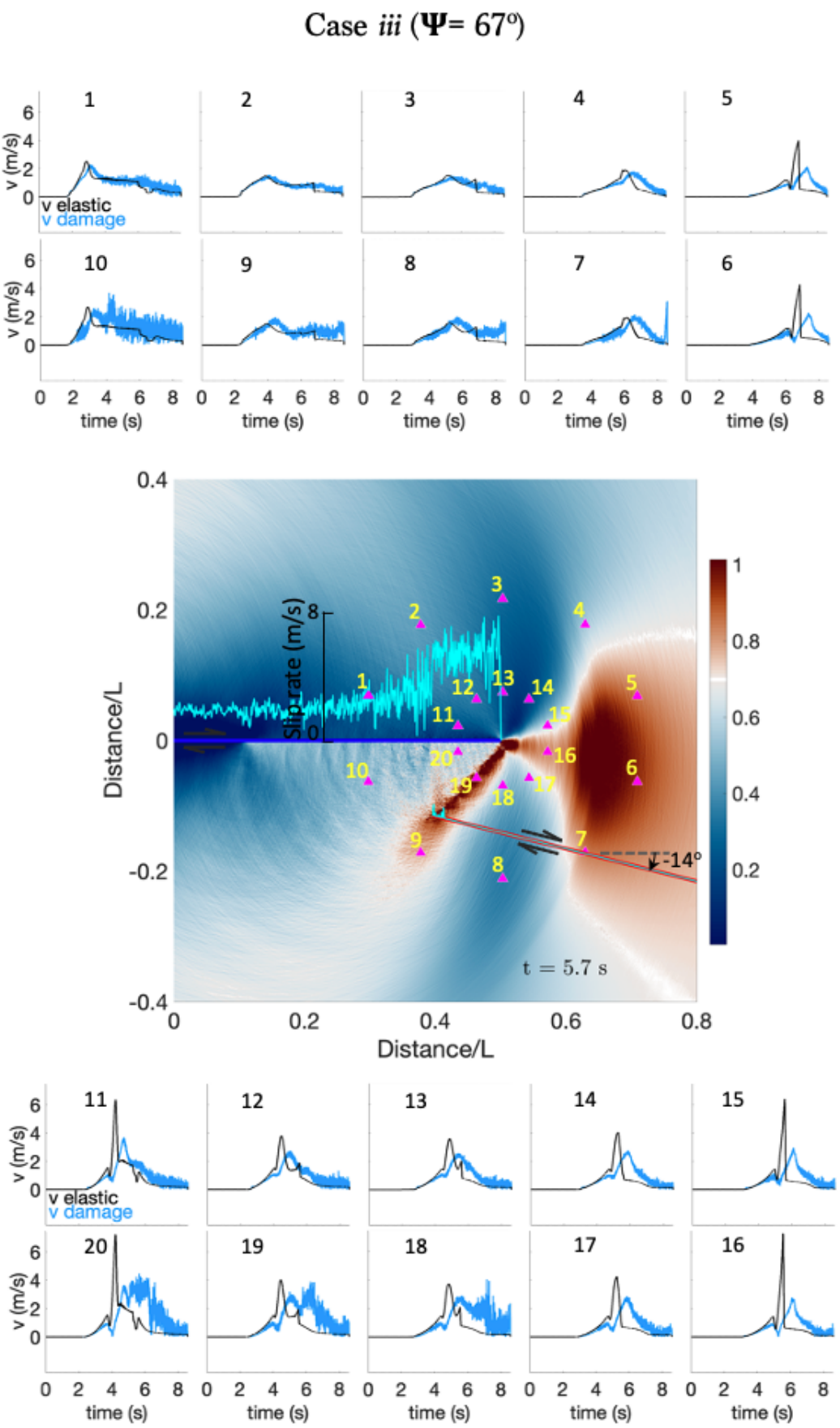

Figure 5.33: **Seismograms for case** *iii* **($\Psi = 67^o$, ω = -14^o).** Black curves correspond to the elastic case and blue curves to the damage case. Parameters are summarized in table 5.1 and 5.2.

5.4.2.b Compressional stepover system

In figure 5.34, we observe the damage state for case *vii* at time t=7.3 s. This case corresponds to a compressional stepover fault with $\Psi = 67.9^o$ and ω = -20^o. At this particular time step, which occurs after the rupture arrest on fault 1, we can clearly observe the extensive damage in the tensional quadrant of fault 1, with the highest concentration of damage localized at the end of the fault.

Comparison of the stress ratio between rupture in elastic medium and damage medium is shown in figure 5.35. The difference presented in figure 5.35c shows that the wave-mediated stress transfer are higher enhanced in the elastic simulation than in damage medium. This difference is also observed in the comparison of normal stress shown in figure 5.36. Normal stress at the triggering location in the second fault is lower in the elastic simulation compared to the simulation with a damaged medium. Figure 5.37 shows the evolution of the stress ratio along the second fault. It is noticeable that in damage medium, the required stress to allow jumping is reached. However, for this case this overstressed area was not as large enough to trigger a nucleation on the second fault.

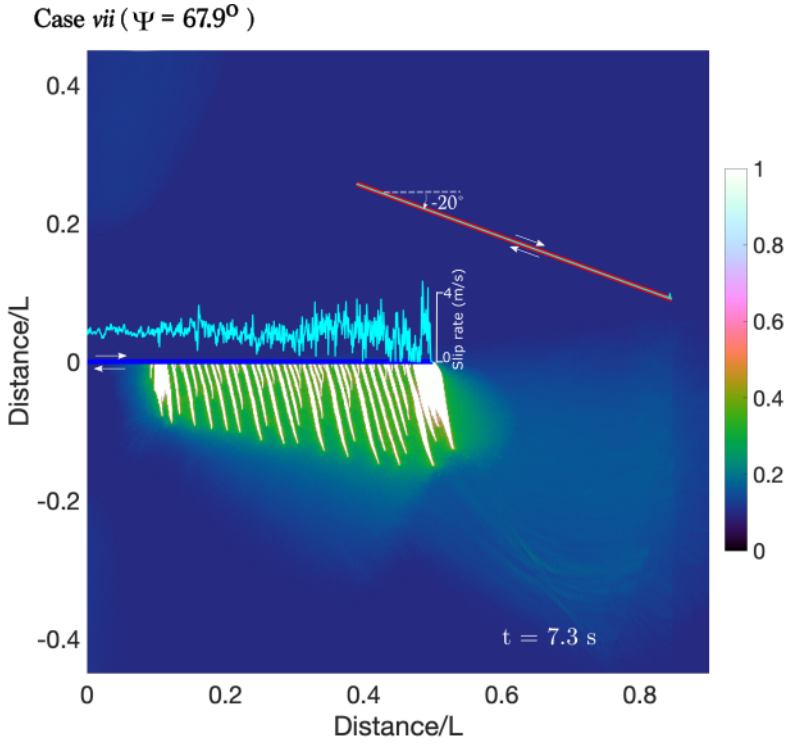

Figure 5.34: **Damage state at time t = 7.3 s for a dynamic rupture on compressional stepover faults embedded in a brittle off-fault medium, with high angle Ψ.** Compressional stepover system correspond to case *vii* ($\Psi = 67.9^o$, ω = -20^o). Strike-slip faults are represented by straight lines colored in blue (fault 1) and red (fault 2). Initial orientation of the maximum principal stress σ_1 defined by the angle Ψ is measured respect to the strike of the fault 1. Slip rate on the faults (curves colored in cyan) is superimposed on the snapshots. Length of fault 1, L =28 km. Parameters are summarized in table 5.1 and 5.2.

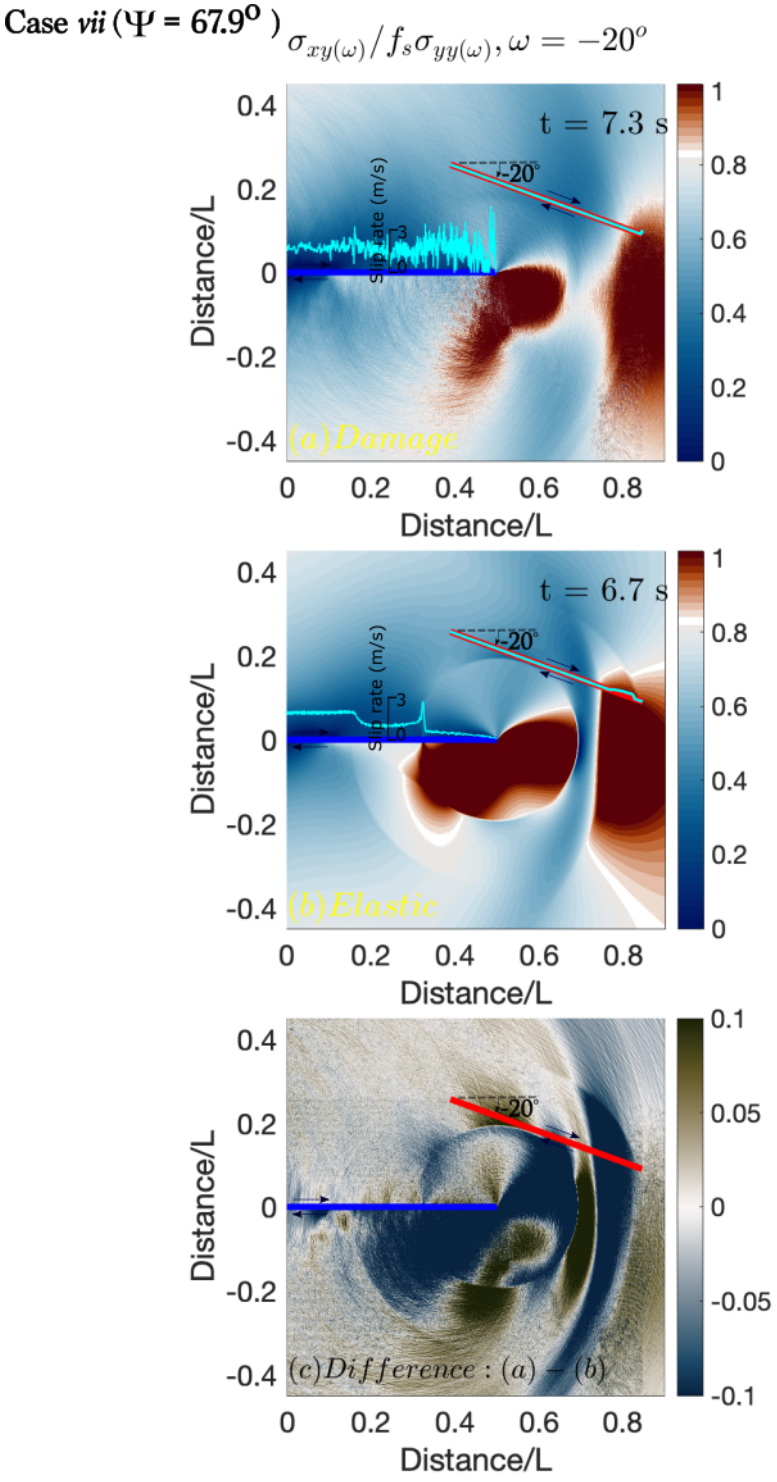

Figure 5.35: **Case** *vii* **($\Psi = 67.9^o$, ω = -20^o) : (c) comparison of ratio shear stress / peak stress ($\sigma_{xy(\omega)}/f_s\sigma_{yy(\omega)}$) for a dynamic rupture on compressional stepover faults embedded in (a) damage and (b) elastic medium.** Strike-slip faults are represented by straight lines colored in blue (fault 1) and red (fault 2). Stresses are rotated respect to the orientation ω of fault 2. Initial orientation of the maximum principal stress σ_1 defined by the angle Ψ is measured respect to the strike of the fault 1. White color in figures (a) and (b) labels the initial stress state. Slip rate on the faults (curves colored in cyan) is superimposed on the snapshots. Length of fault 1, L =28 km. Parameters are summarized in table 5.1 and 5.2.

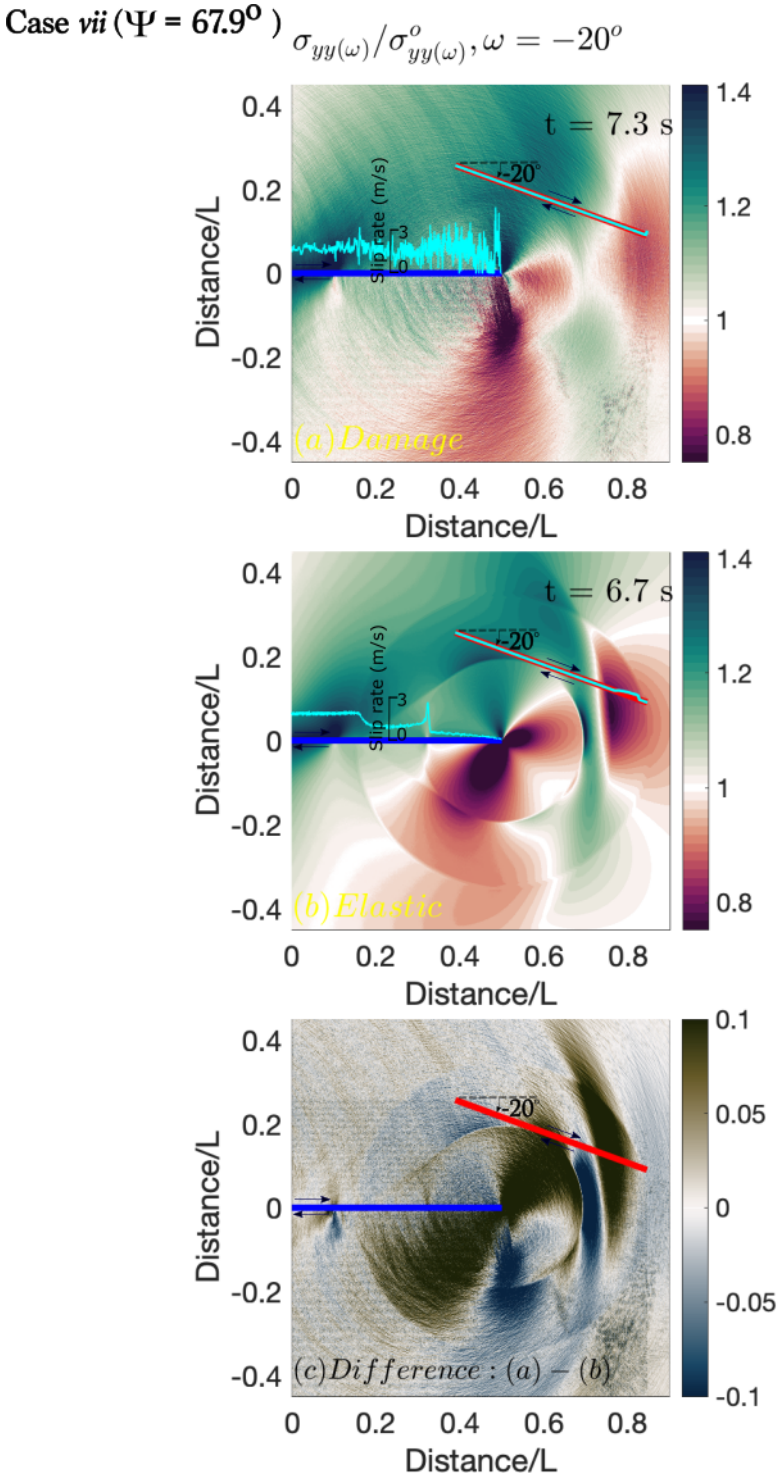

Figure 5.36: **Case** *vii* **($\Psi = 67.9^o$, ω = -20^o) : (c) comparison of normalized normal stress ($\sigma_{yy(\omega)}/\sigma^o_{yy(\omega)}$) for a dynamic rupture on compressional stepover faults embedded in (a) damage and (b) elastic medium.** Strike-slip faults are represented by straight lines colored in blue (fault 1) and red (fault 2). Stresses are rotated respect to the orientation ω of fault 2. Initial orientation of the maximum principal stress σ_1 defined by the angle Ψ is measured respect to the strike of the fault 1. White color in figures (a) and (b) labels the initial normal stress. Slip rate on the faults (curves colored in cyan) is superimposed on the snapshots. Length of fault 1, L =28 km. Parameters are summarized in table 5.1 and 5.2.

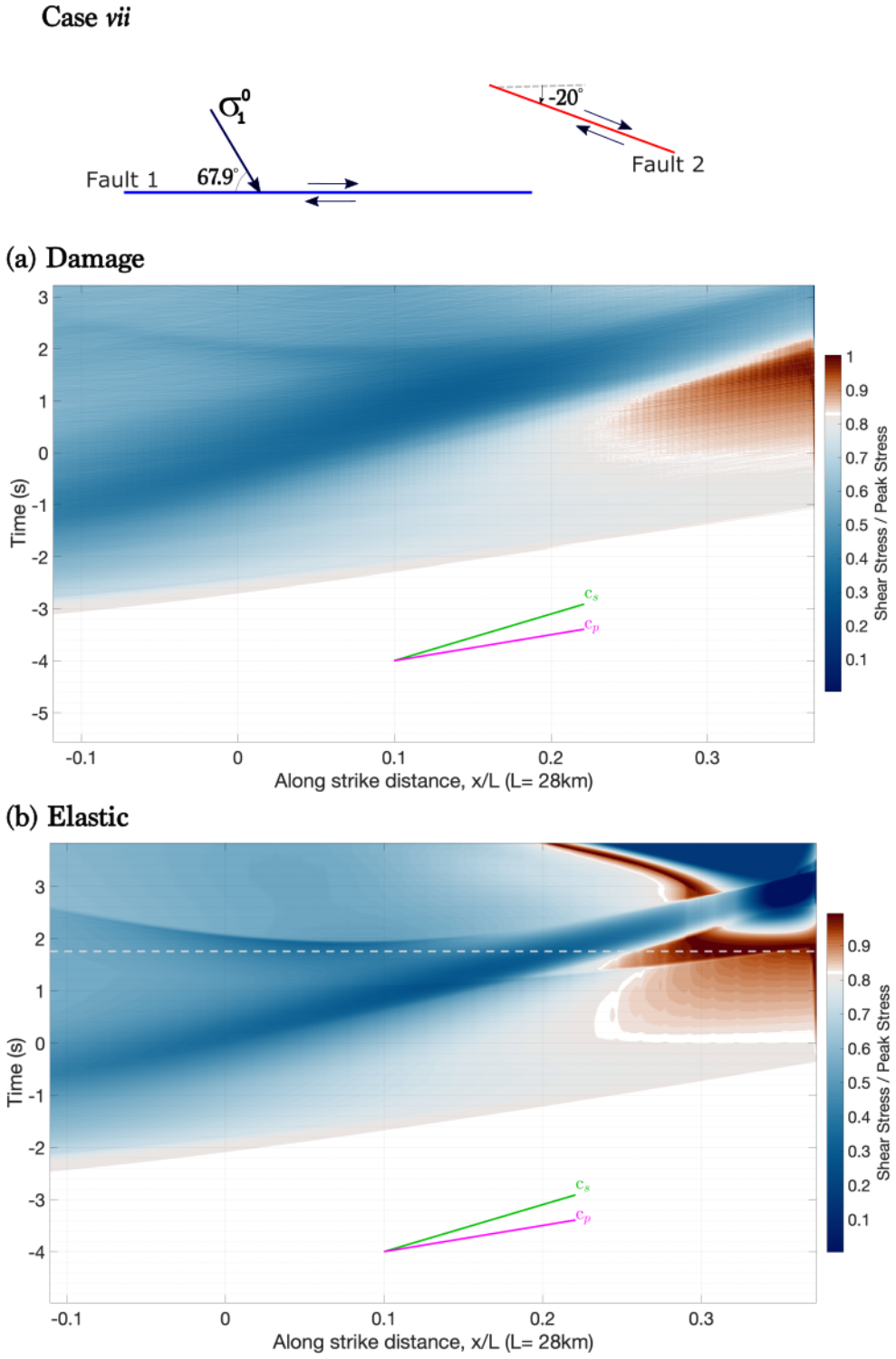

Figure 5.37: **Temporal evolution of the ratio Shear stress / Peak stress at the fault 2 for a dynamic rupture on compressional stepover faults embedded in (a) damage and (b) elastic medium, with high angle Ψ.** Compressional stepover system correspond to case *vii* ($\Psi = 67.9^o$, ω = -20^o). Time = 0 : time when rupture reaches the end of fault 1. x/L = 0 : location where the end of fault 1 is projected at fault 2. Gray dashed line represents triggering time at fault 2. White color labels the initial stress state.

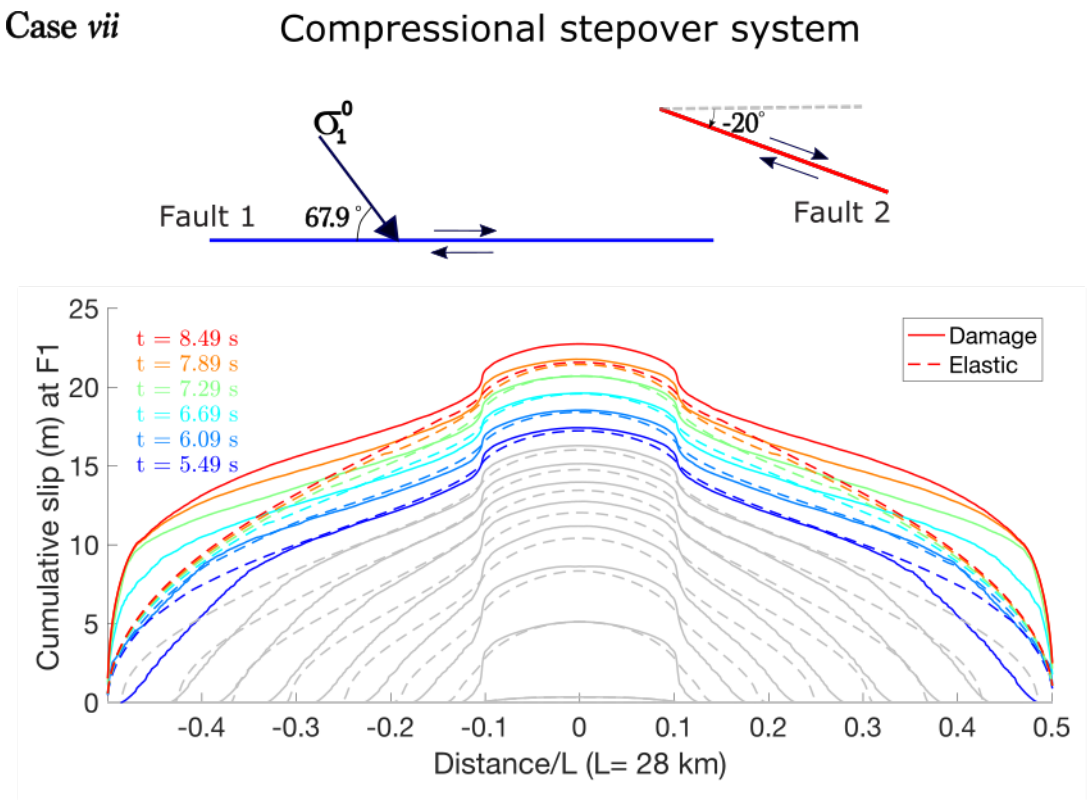

Figure 5.38: **Impact on fault slip: Temporal evolution of the cumulative slip at fault 1 for a dynamic rupture on compressional stepover faults with high angle Ψ. Comparison of cases with dynamic damage and elastic medium.** Compressional stepover system corresponds to case *vii* ($\Psi = 67.9^o$, ω = -20^o).

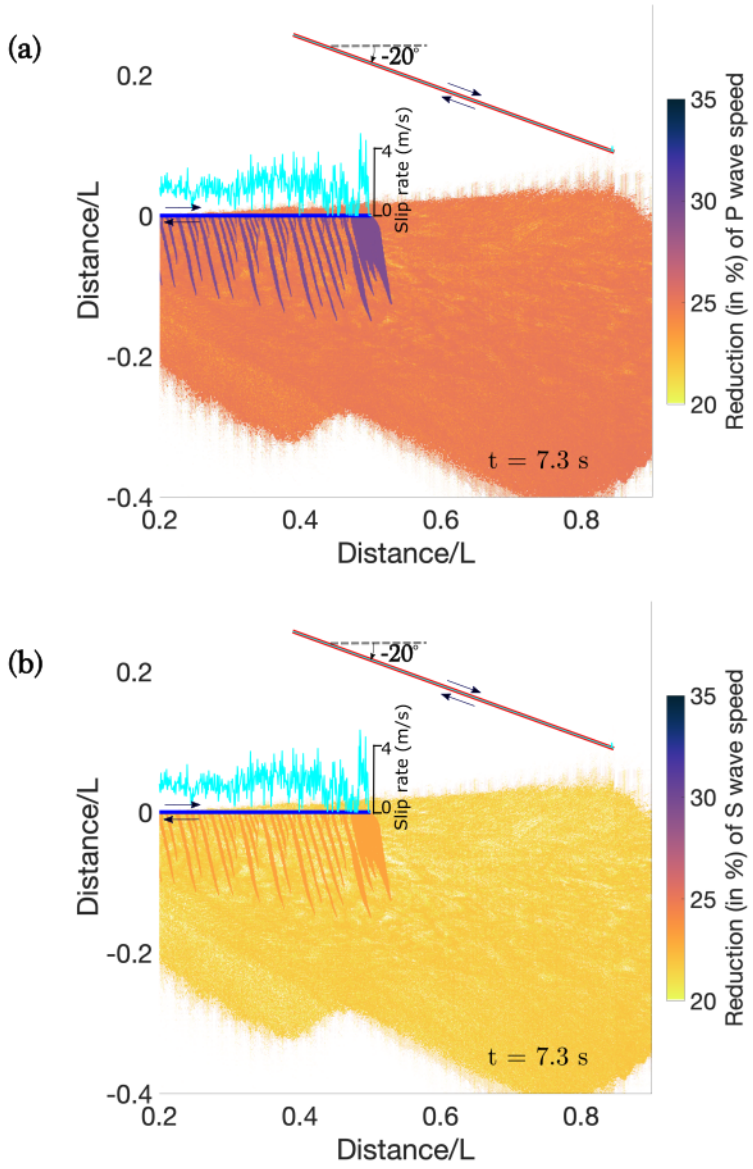

Figure 5.39: **Impact on seismic waves: Reduction (in %) of (a) P and (b) S wave speed at time t = 7.3 s for a dynamic rupture on compressional stepover faults embedded in a brittle off-fault medium, with high angle Ψ.** Compressional stepover system corresponds to case *vii* ($\Psi = 67.9^o$, ω = -20^o). Strike-slip faults are represented by straight lines colored in blue (fault 1) and red (fault 2). Initial orientation of the maximum principal stress σ_1 defined by the angle Ψ is measured respect to the strike of the fault 1. Slip rate on the faults (curves colored in cyan) is superimposed on the snapshots. Length of fault 1, L =28 km. Parameters are summarized in table 5.1 and 5.2.

Finally case *vi* is a compressional stepover fault with $\Psi = 66.2^o$ and ω = -40^o. In this case, the fault 2 is partially located on the tensional quadrant of fault 1. In figure 5.40a, we can observe the damage state right before the rupture jumps to the second fault. We can observe, as for previous cases, that damage essentially develops in the tensional quadrant. Figure 5.40b, corresponds to a latter time step, where the rupture propagates on the second fault. It is noticeable it does not generate significant damage. This is related to the angle between the maximum principal stress σ_1 and the strike orientation of the second fault, which is $\sim 26^o$. Figure 5.41c, when comparing stress ratios, reveals that at the time of the snapshot, the positive stress increment is slightly higher in the damage simulation compared to the elastic simulation, particularly surrounding the right side of fault 2. Similarly, in Figure 5.42c, when comparing normal stresses, it is evident that the reduction in normal stress is more pronounced in the damage simulation compared to the elastic simulation, specifically at the triggering location.

The stress ratio along the second fault for damage and elastic medium is shown in figure 5.43. We observe that in the damage simulation, the overstressed area that allows nucleation is smaller compared to the elastic simulation. This is attributed to the reduction in the nucleation size, as this side of the fault is closer to the area where elastic properties have been significantly reduced. The figures depicting the reduction in P and S wave speeds (refer to Figure 5.44) show that the reduction reaches up to 25% and 20% respectively, particularly in the area closer to the second fault.

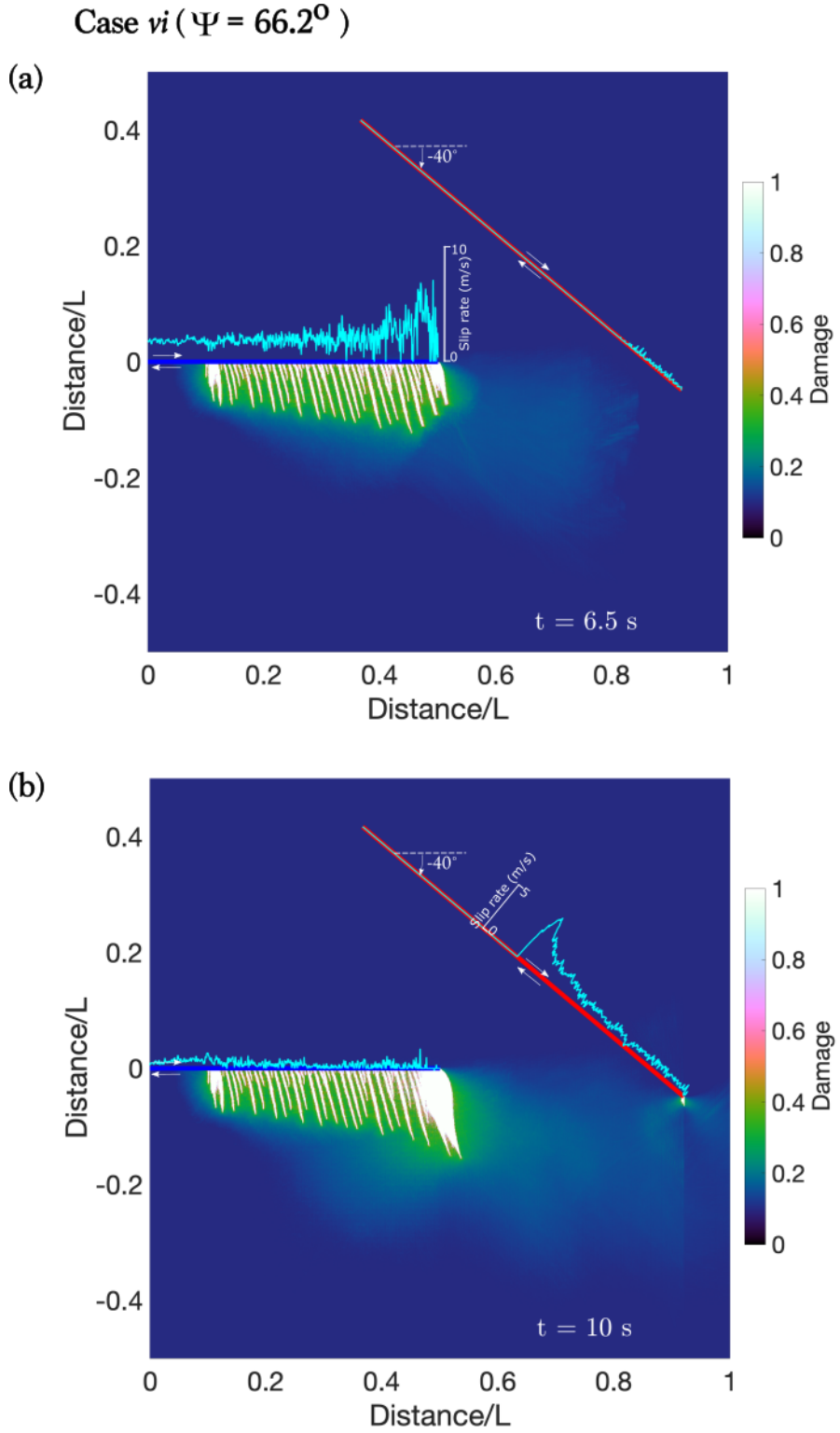

Figure 5.40: **Damage state at times (a) t = 6.5 s and (b) t = 10 s for a dynamic rupture on compressional stepover faults embedded in a brittle off-fault medium, with high angle Ψ.** Compressional stepover system correspond to case *vi* ($\Psi = 66.2^o$, ω = -40^o). Strike-slip faults are represented by straight lines colored in blue (fault 1) and red (fault 2). Initial orientation of the maximum principal stress σ_1 defined by the angle Ψ is measured respect to the strike of the fault 1. Slip rate on the faults (curves colored in cyan) is superimposed on the snapshots. Length of fault 1, L =28 km. Parameters are summarized in table 5.1 and 5.2.

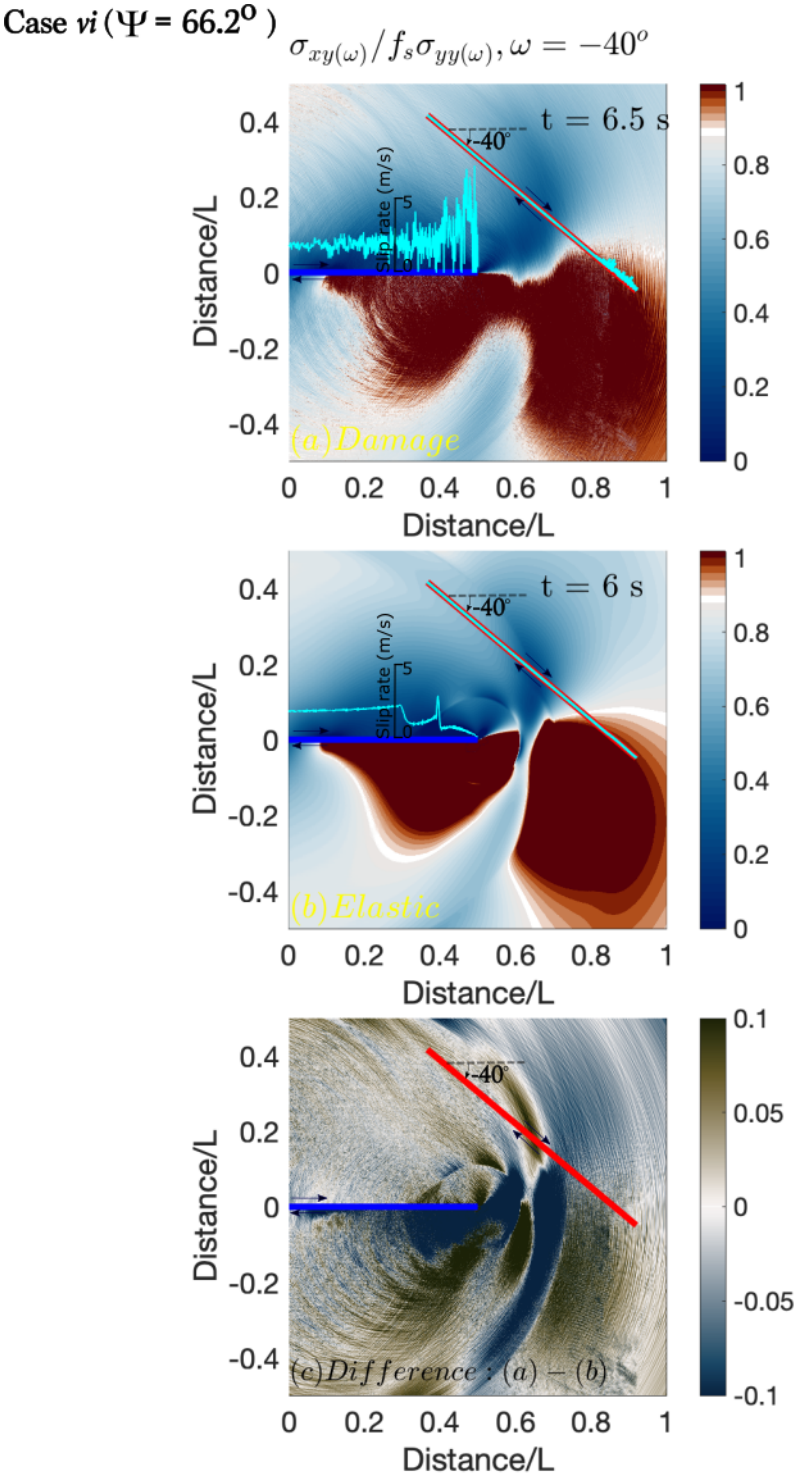

Figure 5.41: **Case** *vi* **($\Psi = 66.2^o$, ω = -40^o) : (c) comparison of ratio shear stress / peak stress ($\sigma_{xy(\omega)}/f_s\sigma_{yy(\omega)}$) for a dynamic rupture on compressional stepover faults embedded in (a) damage and (b) elastic medium.** Strike-slip faults are represented by straight lines colored in blue (fault 1) and red (fault 2). Stresses are rotated respect to the orientation ω of fault 2. Initial orientation of the maximum principal stress σ_1 defined by the angle Ψ is measured respect to the strike of the fault 1. White color in figures (a) and (b) labels the initial stress state. Slip rate on the faults (curves colored in cyan) is superimposed on the snapshots. Length of fault 1, L =28 km. Parameters are summarized in table 5.1 and 5.2.

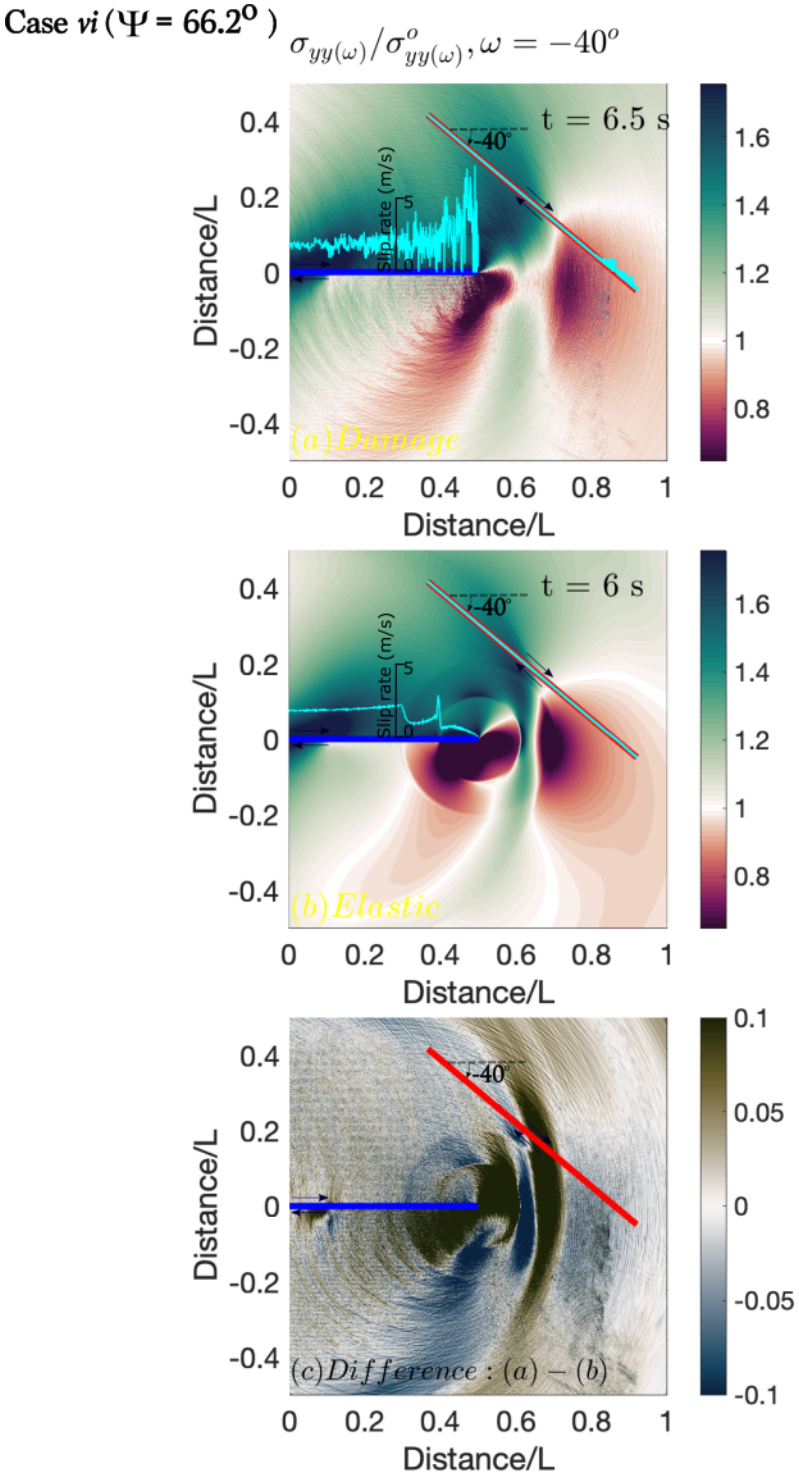

Figure 5.42: **Case** *vi* **($\Psi = 66.2^o$, $\omega =$ -40^o) : (c) comparison of normalized normal stress ($\sigma_{yy(\omega)}/\sigma^o_{yy(\omega)}$) for a dynamic rupture on compressional stepover faults embedded in (a) damage and (b) elastic medium.** Strike-slip faults are represented by straight lines colored in blue (fault 1) and red (fault 2). Stresses are rotated respect to the orientation ω of fault 2. Initial orientation of the maximum principal stress σ_1 defined by the angle Ψ is measured respect to the strike of the fault 1. White color in figures (a) and (b) labels the initial normal stress. Slip rate on the faults (curves colored in cyan) is superimposed on the snapshots. Length of fault 1, L =28 km. Parameters are summarized in table 5.1 and 5.2.

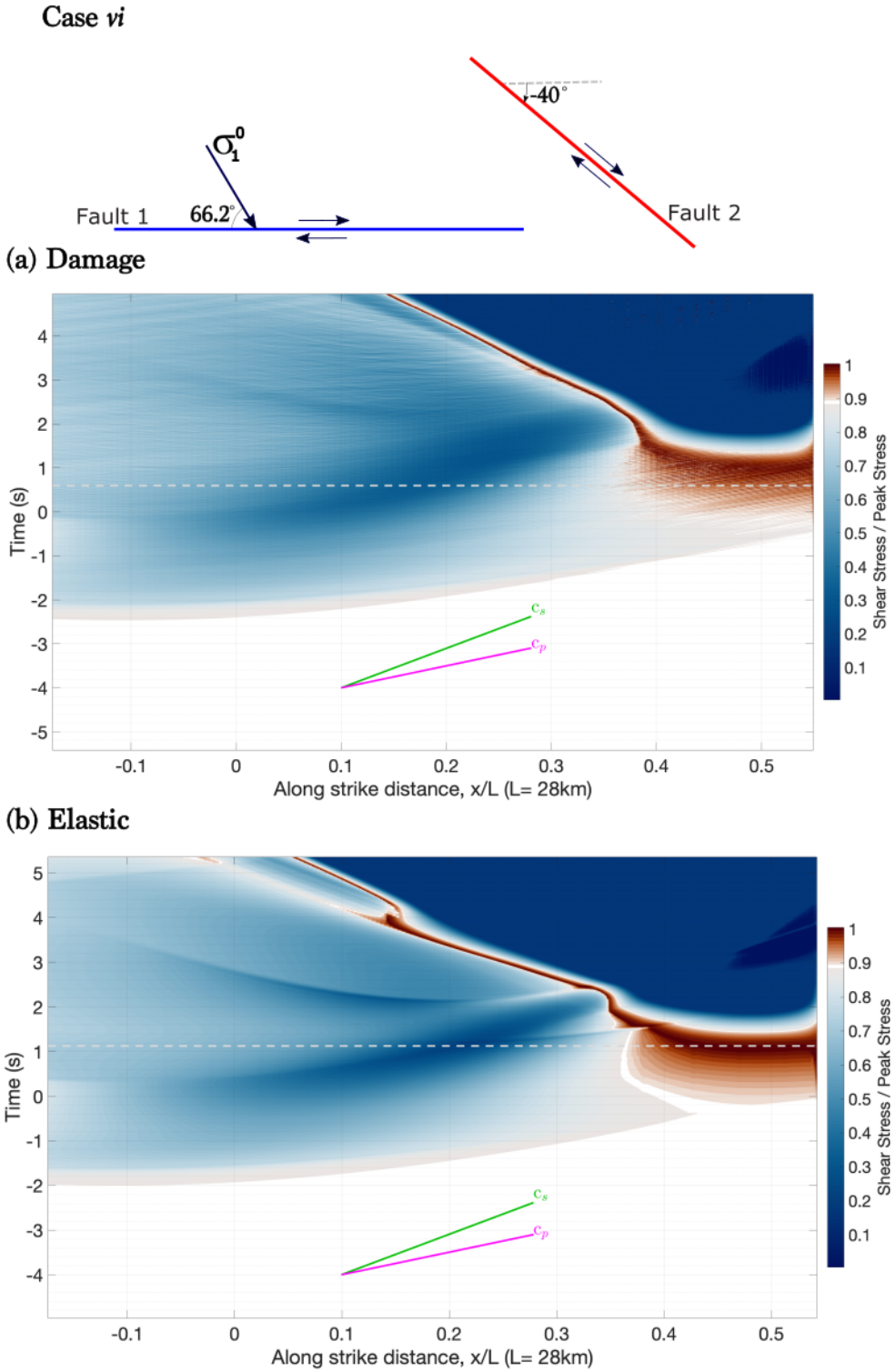

Figure 5.43: **Temporal evolution of the ratio Shear stress / Peak stress at the fault 2 for a dynamic rupture on compressional stepover faults embedded in (a) damage and (b) elastic medium, with high angle Ψ.** Compressional stepover system correspond to case *vi* ($\Psi = 66.2^o$, ω = -40^o). Time = 0 : time when rupture reaches the end of fault 1. x/L = 0 : location where the end of fault 1 is projected at fault 2. Gray dashed line represents triggering time at fault 2. White color labels the initial stress state.

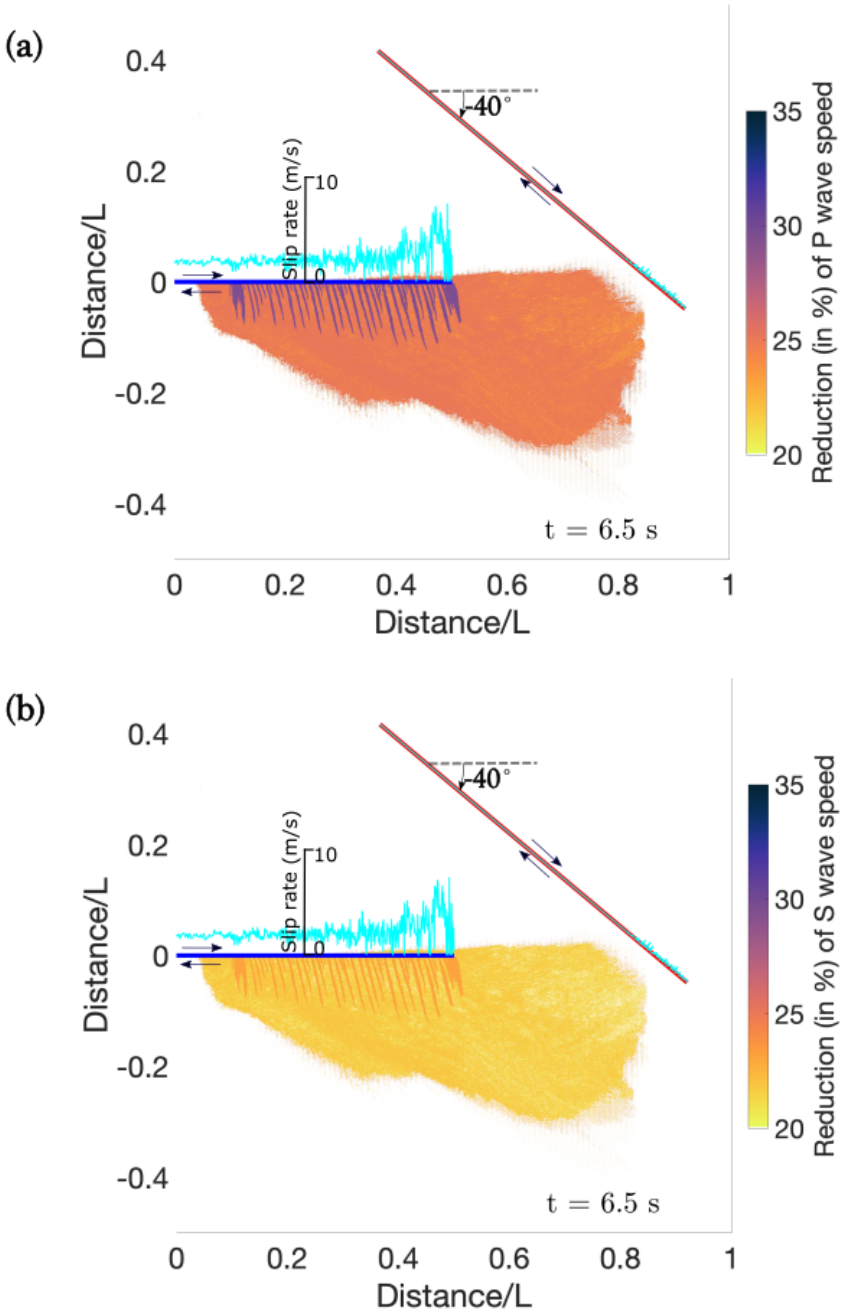

Figure 5.44: **Impact on seismic waves: Reduction (in %) of (a) P and (b) S wave speed at time t = 6.5 s for a dynamic rupture on compressional stepover faults embedded in a brittle off-fault medium, with high angle Ψ.** Compressional stepover system corresponds to case *vi* ($\Psi = 66.2^o$, ω = -40^o). Strike-slip faults are represented by straight lines colored in blue (fault 1) and red (fault 2). Initial orientation of the maximum principal stress σ_1 defined by the angle Ψ is measured respect to the strike of the fault 1. Slip rate on the faults (curves colored in cyan) is superimposed on the snapshots. Length of fault 1, L =28 km. Parameters are summarized in table 5.1 and 5.2.

5.5 Discussion

In this section, we describe the damage effects associated with jumping rupture. To provide an overview, we have summarized these effects in the following table.

		Low angle $7^o < \Psi < 8.5^o$	**High angle** $66^o < \Psi < 68^o$
	Damage effects	No significant damage	Significant damage
Extensional	(1) Greater slip on F1	No	No
	(2) Impact on seismic waves	No	No
	(3) Reduction of nucleation size on F2	No	Yes
	(4) Stress localization	No	Yes
	Jumping rupture:	Yes (e.g. case *i*)	Yes (e.g. case *iii*)
Compressional	(1) Greater slip on F1	slight	Yes
	(2) Impact on seismic waves	slight	Yes
	(3) Reduction of nucleation size on F2	No	No
	(4) Stress localization	No	No
	Jumping rupture:	Yes (e.g. case *v*)	No (e.g. case *vii*)

Table 5.4: **Summary table of damage effects associated with jumping rupture**

We initially conducted an analysis of the mechanisms that lead to jumping rupture in seven cases of stepovers embedded in a linear elastic medium. These cases were selected based on a systematic static stress analysis, which allowed us to estimate the maximum distance over which jumping rupture can occur. Subsequently, we examined these cases considering the evolution of off-fault damage. We grouped according to the angle Ψ. Cases with a low angle Ψ are i, ii, iv, v with $\Psi = 7^o$, 8.1^o, 8.5^o and 8.4^o, respectively. Cases with a high angle Ψ are iii, vi, vii with $\Psi = 67^o$, 66.2^o and 67.9^o, respectively. This criterion, based on the angle Ψ, is applied to simplify the interpretation as it has been observed that significant damage is more likely to occur at higher angles Ψ (e.g., *Poliakov et al.*, 2002; *Templeton and Rice*, 2008).

A first insight of the damage effect can be obtained from the comparison of time delay Δt_j for rupture to jump, between the elastic and the damage models. It is displayed in table 5.5. We can remark that the impact is higher for high angle Ψ (cases *iii*, *vi* and *vii*). Damage significantly reduces Δt_j in case *iii*, or inhibit jumping rupture in case *vii*. For these specific cases it goes against previously published studies that suggested that damage favors jumping rupture (e.g. *Finzi and Langer*, 2012a).

Although damage has a minor influence for low angle Ψ, it is worth noting that its impact is less noticeable in extensional stepovers compared to compressional stepovers. This is related to the fact that jumping rupture in compressional stepovers is allowed after the rupture arrest on fault 1 (see figure 5.24), when the most significant damage (located at the fault end) is developed. Whereas in extensional stepovers, jumping rupture is allowed before the initial rupture reaches the end of the fault 1 (see figure 5.20), when dynamic damage is almost negligible.

Extensional stepover system						
Case	angle Ψ	angle ω	t^e_{F1}	Δt^e_j	t^d_{F1}	Δt^d_j
i	7^o	10^o	4.4 s	-0.5 s	4.4 s	-0.5 s
ii	8.1^o	20^o	4.6 s	-0.8 s	4.6 s	-0.8 s
iii	67^o	-14^o	4.9 s	3.6 s	5.4 s	0.1 s
Compressional stepover system						
Case	angle Ψ	angle ω	t^e_{F1}	Δt^e_j	t^d_{F1}	Δt^d_j
iv	8.5^o	15^o	4.5 s	3.5 s	4.5 s	3.5 s
v	8.4^o	25^o	4.5 s	3.1 s	4.5 s	3 s
vi	66.2^o	-40^o	4.9 s	1.1 s	5.4 s	0.6 s
vii	67.9^o	-20^o	4.9 s	1.7 s	5.6 s	-

Table 5.5: **Results in linear elastic medium and dynamic off-fault damage for 2D earthquake rupture simulation in stepover faults.** Parameters and geometrial features are summarized in table 5.1 and table 5.2, respectively. Results in linear elastic medium and dynamic off-fault damage are labelled by superscripts $()^e$ and $()^d$, respectively. $t^{e/d}_{F1}$: time when rupture propagation reaches the end of fault 1. $\Delta t^{e/d}_j$: Difference between the time of triggering nucleation on fault 2 and $t^{e/d}_{F1}$. Negative values of $\Delta t^{e/d}_j$ means that the nucleation on fault 2 happened before the earthquake rupture reaches the end of fault 1.

Stepover faults with a high angle Ψ exhibit significant coseismic off-fault damage, which leads to substantial modifications in the observed rupture scenarios compared to those in an elastic medium. In these cases, four noteworthy damage effects can be observed and should be highlighted:

1. Greater slip on fault 1
2. Impact of seismic waves
3. Reduction in the nucleation size on fault 2
4. Stress localization

In the following, we will describe these effects.

1. Greater slip on fault 1

Different studies have underlined the slip distribution sensitivity to off-fault damage density (e.g. *Perrin et al.*, 2016; *Gombert et al.*, 2017). First, as the rupture propagates, off-fault damage induces a dynamic change of elastic properties which slown down the rupture front (*Thomas and Bhat*, 2018). For instance, this effect can be observed in case *iii*, where the comparison of cumulative slip in fault 1 between the elastic and damage simulations is depicted in Figure 5.31. The blue isochrones clearly demonstrate that the rupture front in the damage simulation is slower compared to the elastic simulation. Then, towards the end of the fault, at the location of rupture arrest, the damage density is higher (see Figure 5.27b). This higher damage density results in an increase in the compliance of the off-fault material, especially in the vicinity of the fault end. The increased compliance allows for greater slip to be accommodated in this region. This additional slip has the potential to modify the surrounding stress field and, as a consequence, can lead to alterations in the stresses at the second fault. As a result, the impact of slip on jumping rupture becomes more pronounced. For case *iii*, since jumping rupture happened right after the rupture arrest (see table 5.5). Hence, the increase of fault slip after the rupture arrest is not what triggers the jumping rupture. Nonetheless, in cases where jumping rupture is expected to occur after a certain time following the rupture arrest, such as in our compressional stepover fault cases *vi* and *vii*, the effect of damage on fault slip can potentially influence the occurrence of jumping rupture.

2. Impact of seismic waves

Regarding the impact on seismic waves, damage has implications in the following aspects:

The evolution of off-fault damage involves the generation of waves from the

growing cracks (e.g., *Thomas and Bhat*, 2018). Furthermore, waves originating from the rupture at fault 1 interact with the damage zone. This interaction of waves with the damage zone modulates their velocity and amplitude (e.g., *Langer et al.*, 2015; *Gomez et al.*, 2019; *Gomez and Ionescu*, 2021). Additionally, during rupture arrest, the reduction in earthquake rupture speed caused by damage (e.g., *Sammis et al.*, 2009; *Okubo et al.*, 2019a; *Thomas et al.*, 2017; *Thomas and Bhat*, 2018) leads to lower-amplitude stopping phases (*Madariaga*, 1977) compared to the elastic simulation. Moreover, these stopping phases also interact with the damage. These phenomena collectively modulate the amplitude of dynamic stress perturbations, which can either facilitate or inhibit jumping rupture.

Further analysis of damage effect on seismic waves can be obtained from synthetic seismograms located around the stepover zone. At the center of the figure 5.33, for case *iii*, we show the location of 20 receivers (triangles colored in magenta) that recorded synthetic seismograms for simulation in elastic medium and damage medium, colored in black and blue, respectively. For reference, receivers are superimposed on a snapshot of stress ratio, at the instant before jumping rupture. Receivers are organized into two circular distributions, so that seismograms can be recorded in the stepover zone and far from it. At the top of the figure 5.33, we find the 10 seismograms located far from the stepover zone, i.e. for the circular distribution with the largest radius. Whereas at the bottom of the figure 5.33, we find the 10 seismograms located in the stepover zone, i.e. for the circular distribution with the smallest radius. In the simulations with the damage medium, it is evident that the seismograms located near the end of fault 1 (numbered from 11 to 20) exhibit lower amplitudes compared to the seismograms from the elastic simulation. This difference is particularly pronounced for seismograms 15 and 16, which are situated to the right side of fault 1. However, as we move further away from the fault, the differences in amplitude between the damage and elastic simulations become less significant, with the exception of seismograms 5 and 6, where the

difference in amplitude remains notable. This non-uniform reduction in amplitude on seismograms suggests that the impact of damage on seismic waves is spatially variable. In certain areas, there is a higher reduction in amplitude velocity, which may not favor the occurrence of jumping rupture. For instance, in the case of compressional stepover faults (case *vii*), it is evident from Figure 5.35 that the stress perturbation induced by seismic waves around the right side of fault 2 exhibits a lower amplitude in the damage simulation compared to the elastic simulation. This observation suggests that damage effect on seismic waves leads to a reduction in the amplitude of wave-mediated stress transfer on fault 2, thereby hindering jumping rupture in this scenario. In the case of extensional stepover faults (case *iii*), Figure 5.32 demonstrates a substantial reduction in S-wave speed, reaching up to 25%, and P-wave speed, reaching up to 30%, in the vicinity of fault 2. Comparable reductions in seismic wave speed have been reported in various studies (e.g., *Li et al.*, 1994, 2007; *Peng et al.*, 2003). Based on the location and timing of the nucleation, it is unlikely that the impact of damage on wave speed alone is responsible for triggering seismic slip on the second fault. However, it is plausible that seismic waves emanating from the rupture in fault 1 and the growing cracks have potentially contributed to the rupture propagation on fault 2.

3. Reduction of the nucleation size on fault 2

When the area of reduced elastic properties, specifically in the shear modulus, surrounds fault 2, it directly contributes to a decrease in the nucleation size. This direct relationship between the nucleation size and the shear modulus has been extensively demonstrated in several studies (e.g. *Andrews*, 1976; *Campillo and Ionescu*, 1997; *Favreau et al.*, 1999; *Ionescu and Campillo*, 1999; *Uenishi and Rice*, 2003). The reduction in nucleation size significantly facilitates jumping rupture, as it allows for nucleation on the second fault with a smaller overstressed area compared to the elastic simulation. Furthermore, the value and the area of the reduction in elastic

properties play a crucial role in determining the impact of this effect. This condition is observed in case *vii* of compressional stepover faults. Figure 5.44 demonstrates that the region of reduced wave speed is in close proximity to the nucleation area on fault 2, resulting in a reduction in the nucleation size compared to the elastic simulation (see figure 5.43). In contrast, in case *vii*, there is no reduction in nucleation size, or at least its reduction is not sufficient to enable jumping rupture (see figure 5.37). This is because the area where a significant reduction of P and S wave speeds, greater than 20%, is generated is not located close to the second fault (see Figure 5.39), unlike in case *vi*.

4. Stress localization

The case *iii* of extensional stepover faults allows us to analyze this effect. Figure 5.28 illustrates the evolution of (a) the damage state, (b) the stress ratio in damage simulation, (c) the stress ratio in elastic simulation and (d) the difference between the damage and the elastic simulations. The snapshots correspond to three different time steps, t=3.4 s, t=4.4 s and t=5.4 s, relative to the damage simulation. We can observe where damage is generated there is a darker-red color band in the stress ratio, at the tip of the growing cracks. This band carries the stress required to allow nucleation on the second fault. Similarly, the evolution of normal stress is analyzed in Figure 5.29. It is evident that a reduction in normal stress occurs along a darker-red color band, extending to a larger distance in the tensional quadrant of fault 1. These factors contribute to the facilitation of jumping rupture. However, an additional factor is necessary to enable jumping rupture. The nucleation size at the second fault needs to be comparable to the size of the stress localization. This condition is achieved by the previously mentioned effect, i.e. through the reduction of elastic properties caused by damage. Thus, the combined the stress localization and reduction of nucleation size plays a crucial role in enabling jumping rupture. This mechanism is what enables jumping rupture in the case *iii* of the extensional

stepover faults. However, in our cases of compressional stepover faults, there is a notable difference. Despite the development of damage in the tensional quadrant (see figures 5.34 and 5.40), similar to the extensional stepover faults, there is no direct interaction between the microcracks and fault 2. Consequently, stress localization due to damage will not have an influence on jumping rupture in these cases of compressional stepover faults.

Chapter 6

Conclusion

Earthquake rupture length has been the subject of numerous investigations and extensively examined by seismic hazard studies (e.g. *Klinger*, 2010; *Field et al.*, 2014; *Mignan et al.*, 2015; *Gombert et al.*, 2017; *Cheng et al.*, 2021). This is because it potentially determines the earthquake features that impact the strong ground motion (e.g. *Baker et al.*, 2021). These features include the earthquake magnitude, the amount of slip, radiated seismic energy, the location of rupture arrest. Hence, as can be inferred, the larger the earthquake rupture, the more hazardous the strong ground motion. Several devastating earthquakes have been generated in strike-slip fault systems (e.g. *Lettis*, 2002; *Klinger*, 2005; *Wesnousky*, 2006; *Gombert et al.*, 2017). Strike-slip fault systems consist of variety of geometrical complexities like branches, kinks and stepovers. Especially, the presence of stepover structure can impact on the determination of the earthquake rupture length. Rupture propagation can jump from one fault to another, across the overlapped zone, due to stress perturbations that activates sliding dynamics on the second fault. The role of stepovers on earthquake rupture has been mostly analysed in numerical studies considering a two-overlapped parallel faults embedded in an elastic medium (e.g. *Harris and Day*, 1993, 1999; *Wang et al.*, 2020). However, in nature, we observe that stepovers are characterized not only by geometrical features, but also by the presence of an

intricate damage zone, particularly generated during earthquake ruptures (e.g. see figure 1.17). In that sense, numerical studies in elastic medium have limitations to do a meaningful comparative analysis with realistic stepover structures. Then, the key questions that arise is how can we capture the evolution of dynamic off-fault damage? and how does damage impact on the role of stepovers in earthquake rupture dynamics? In this thesis, we approached these research questions, using a micromechanical model that accounts for crack growth and opening and its impact on the dynamic evolution of elastic moduli. We reported that the presence of dynamic damage zone can significantly change the earthquake rupture scenario suggested in results with linear elastic medium. In particular, we highlighted that dynamic off-fault damage has a significant impact on the maximum jumpable distance and the consequent earthquake rupture length.

Our central investigation initially followed a systematic static analysis of a singular elastic crack, which is considered as the first fault of a stepover structure (see chapter 4). Then, we selected 7 scenarios with the highest potential jumpable distance from the static solution to conduct 2D earthquake rupture simulations in elastic and damage medium (see chapter 5).

The static analysis allowed us to estimate the maximum jumpable distance, H_{max}, for a potential secondary fault. Providing the seismic ratio S, static frictional coefficient f_s, dynamic frictional coefficient f_d and the depth z, the static solution of the maximum jumpable distance, $H_{max}(\Psi, \omega)$, is defined as a function of the angles Ψ and ω. With respect to the strike orientation of the first fault; Ψ is the initial orientation of the maximum principal stress ($0^o < \Psi < 90^o$); whereas ω, is the orientation of the second fault ($-90^o < \omega < 90^o$). We pointed out that there is a trade-off between these angles, which substantially modify the maximum jumpable distance. This trade-off indicates that as the angle Ψ increases, the angle ω tends

towards negative values, and vice-versa, in order to reach the maximum jumpable distance. It implies that the combination of these two angles determines the initial proximity of the second fault to sliding, thus favoring jumping rupture.

Results of 2D earthquake rupture simulations of 7 cases of stepover faults embedded in elastic and damage medium, were discussed in chapter 5. Among these cases, we had 3 extensional stepover faults and 4 compressional stepover faults. Rupture simulations in elastic medium show that jumping rupture is mainly controlled by two factors: (1) slip of the first fault and (2) seismic waves that come from the rupture and its arrest on fault 1. This observation agrees with previous studies for parallel strike-slip stepover faults (e.g. *Segall and Pollard*, 1980; *Harris and Day*, 1993). In our findings, we have observed that the influence of the aforementioned factors on jumping rupture is influenced by the orientation of the second fault, characterized by the angle ω, and the orientation of the initial stress field, characterized by the angle Ψ. This observation aligns with our static analysis, which indicates that the maximum distance for jumping rupture is sensitive to both angles.

We then conducted rupture simulations with a higher-order of complexity: the presence of dynamic off-fault damage. As was suggested in previous studies (e.g. *Poliakov et al.*, 2002; *Templeton and Rice*, 2008), the angle Ψ has a significant impact on the development of damage evolution. In this study, we observed that as the angle Ψ increases, the spatial extension of the off-fault damage also increases, resulting in a stronger impact on the jumping rupture.

We now summarize conclusions from our results to explain how damage impact on the role of stepovers in earthquake rupture dynamics. As a first-order of conclusion, we observed that damage evolution tends to favor jumping rupture in extensional stepovers. In contrast, it might prevent jumping rupture in compre-

ssional stepovers.

The effects of coseismic dynamic damage are identified as follows:

1. Greater slip on fault 1
2. Impact of seismic waves
3. Reduction in the nucleation size on fault 2
4. Stress localization

In the following, we describe the previously mentioned four effects of damage. These effects have been highlighted in cases (*iii*, *vi* and *vii*) with the most significant damage:

1. Related to the sliding at the first fault, coseismic damage generated along the first fault, in crack models, increases the material compliance, which increases the cumulative slip compare to elastic models, particularly at the end of the first fault. The direct consequence of this increment is the alteration of the stress field, which can ultimately trigger jumping rupture.
2. In relation to the impact on seismic waves, the evolution of off-fault damage has a significant influence on wave-mediated stress transfers, resulting in the modulation of their velocity and amplitude. This effect is spatially variable, leading to either inhibition or facilitation of jumping rupture.
3. The reduction in nucleation size on fault 2 is a result of the reduction of the elastic properties caused by damage in the surrounding area. This reduction facilitates jumping rupture by requiring a smaller overstressed area compared to the elastic model.
4. In relation to stress localization, dynamic damage induces stress perturbations localized at the tips of growing cracks. As these cracks propagate towards

fault 2, the localized stress can interact with the fault, influencing the rupture process. Another contributing factor is the reduction in nucleation size on the second fault due to damage. This reduction in nucleation size, along with the stress localization effect, facilitates jumping rupture. It is noteworthy that the combined effects mentioned above have a greater impact on extensional stepovers.

Overall, these combined effects play a critical role in determining the occurrence of jumping rupture on stepover faults. It is important to highlight that within the analyzed parameters, additional factors, such as the angle Ψ, the length, and the strike orientation of the second fault, introduce a higher level of complexity in modulating the aforementioned effects. These factors can have a significant impact on the behavior of jumping rupture and should be carefully considered in the analysis of stepover fault systems.

This work provided further analysis on the determination of the jumping rupture considering a model that aims to capture the key features of an stepover fault, particularly the presence of off-fault damage.

6.1 Perspectives

The analysis of damage effects conducted in this thesis provides valuable insights for further exploration of specific cases that are crucial for earthquake hazard assessments. It is recommended to conduct additional analyses to investigate various conditions of the damaged fault zone and different geometrical features. One of the most notable effects of damage we observed is stress localization. Therefore, it is highly interesting to further understand its evolution in other scenarios. Future investigations are proposed as follows:

One perspective involves analyzing the effect of stress localization in non-overlapping faults, with a particular focus on cases where the second fault is located on the extensional side of the first fault. This is of interest because, based on the results of extensional stepovers, nucleation on the second fault is observed near the end of the first fault. Our findings in stepover faults have indicated that the orientation of stress localization is influenced by the angle Ψ. Therefore, it is recommended to conduct a systematic analysis involving the evaluation of different values of the angle Ψ. A research question that arises from this investigation is: under what conditions of damage (D) and angle Ψ can damage dynamically create linking structures within non-overlapping faults that lead to jumping rupture?

The second perspective involves analyzing the influence of depth on the effects of damage. While our study focused on a depth of 2 km, it is crucial to investigate how damage effects vary at different depths. Deeper damage zones are known to result in a narrower zone with a higher density of growing cracks (e.g., *Cochran et al.*, 2009; *Okubo et al.*, 2019a). Therefore, a dedicated analysis will be conducted to evaluate the depth at which damage can promote stress localization. This analysis will provide insights into the maximum depth at which damage-induced dynamic stress concentration can facilitate jumping rupture.

Other proposed future works are aimed at analyzing fault roughness, heterogeneous initial damage density, and variations in lithology across the stepover zone. We believe that these different complexities will have an impact on the generation and distribution of damage, frequency content of radiation, as well as the complexity of slip distribution along the first fault, among other effects.

Bibliography

Aben, F. M., M.-L. Doan, J.-P. Gratier, and F. Renard, Coseismic damage generation and pulverization in fault zones, in *Fault Zone Dynamic Processes*, pp. 47–80, John Wiley & Sons, Inc., 2017.

Ampuero, J. P., Sem2dpack, a spectral element software for 2d seismic wave propagation and earthquake source dynamics, v2.3.8, 2012.

Andrews, D. J., Rupture velocity of plane strain shear cracks, *Journal of Geophysical Research*, *81*, 5679–5687, 1976.

Andrews, D. J., Dynamic plane-strain shear rupture with a slip-weakening friction law calculated by a boundary integral method, *Bulletin of the Seismological Society of America*, *75*, 1–21, 1985.

Andrews, D. J., Rupture dynamics with energy loss outside the slip zone, *Journal of Geophysical Research*, *110*, 2005.

Armijo, R., et al., Submarine fault scarps in the sea of marmara pull-apart (north anatolian fault): Implications for seismic hazard in istanbul, *Geochemistry, Geophysics, Geosystems*, *6*, 2005.

Ashby, M. F., and C. G. Sammis, The damage mechanics of brittle solids in compression, *Pure and Applied Geophysics PAGEOPH*, *133*, 489–521, 1990.

Aydin, A., and A. Nur, Evolution of pull-apart basins and their scale independence, *Tectonics*, *1*, 91–105, 1982.

Aydin, A., and A. Nur, The types and role of stepovers in strike-slip tectonics, in *Strike-Slip Deformation, Basin Formation, and Sedimentation*, pp. 35–44, SEPM (Society for Sedimentary Geology), 1985.

Bai, K., and J.-P. Ampuero, Effect of seismogenic depth and background stress on physical limits of earthquake rupture across fault step overs, *Journal of Geophysical Research: Solid Earth*, *122*, 2017.

Baker, J., B. Bradley, and P. Stafford, *Seismic Hazard and Risk Analysis*, Cambridge University Press, 2021.

Ben-Zion, Y., and Z. Shi, Dynamic rupture on a material interface with spontaneous generation of plastic strain in the bulk, *Earth and Planetary Science Letters*, *236*, 486–496, 2005a.

Ben-Zion, Y., and Z. Shi, Dynamic rupture on a material interface with spontaneous generation of plastic strain in the bulk, *Earth and Planetary Science Letters*, *236*, 486–496, 2005b.

Bernard, P., and D. Baumont, Shear mach wave characterization for kinematic fault rupture models with constant supershear rupture velocity, *Geophysical Journal International*, *162*, 431–447, 2005.

Bhat, H. S., R. Dmowska, G. C. P. King, Y. Klinger, and J. R. Rice, Off-fault damage patterns due to supershear ruptures with application to the 2001 Mw 8.1 Kokoxili (Kunlun) Tibet earthquake, *Journal of Geophysical Research*, *112*, 2007.

Bhat, H. S., A. J. Rosakis, and C. G. Sammis, A micromechanics based constitutive model for brittle failure at high strain rates, *Journal of Applied Mechanics*, *79*, 2012.

Biasi, G. P., and S. G. Wesnousky, Steps and gaps in ground ruptures: Empirical

bounds on rupture propagation, *Bulletin of the Seismological Society of America*, *106*, 1110–1124, 2016.

Bruhat, L., Near-field radiation from stopping ruptures, Master's thesis, Institut de Physique du Globe de Paris, 2012.

Byerlee, J., Friction of rocks, *Pure and Applied Geophysics PAGEOPH*, *116*, 615–626, 1978.

Campillo, M., and I. R. Ionescu, Initiation of antiplane shear instability under slip dependent friction, *Journal of Geophysical Research: Solid Earth*, *102*, 20,363–20,371, 1997.

Cappa, F., C. Perrin, I. Manighetti, and E. Delor, Off-fault long-term damage: A condition to account for generic, triangular earthquake slip profiles, *Geochemistry, Geophysics, Geosystems*, *15*, 1476–1493, 2014.

Chen, R., K. Xia, F. Dai, F. Lu, and S. Luo, Determination of dynamic fracture parameters using a semi-circular bend technique in split Hopkinson pressure bar testing, *Engineering Fracture Mechanics*, *76*, 1268–1276, 2009.

Cheng, J., X. Xu, J. Ren, S. Zhang, and X. Wu, Probabilistic multi-segment rupture seismic hazard along the Xiaojiang fault zone, southeastern Tibetan Plateau, *Journal of Asian Earth Sciences*, *221*, 104,940, 2021.

Chester, F. M., and J. M. Logan, Implications for mechanical properties of brittle faults from observations of the Punchbowl fault zone, California, *Pure and applied geophysics*, *124*, 79–106, 1986.

Chester, F. M., J. P. Evans, and R. L. Biegel, Internal structure and weakening mechanisms of the San Andreas Fault, *Journal of Geophysical Research: Solid Earth*, *98*, 771–786, 1993.

Choi, J.-H., et al., Geologic inheritance and earthquake rupture processes: The 1905 M $\geq$ 8 Tsetserleg-Bulnay strike-slip earthquake sequence, Mongolia, *Journal of Geophysical Research: Solid Earth*, *123*, 1925–1953, 2018.

Clayton, R., and B. Engquist, Absorbing boundary conditions for acoustic and elastic wave equations, *Bulletin of the Seismological Society of America*, *67*, 1529–1540, 1977.

Cochard, A., and R. Madariaga, Dynamic faulting under rate-dependent friction, *Pure and Applied Geophysics PAGEOPH*, *142*, 419–445, 1994.

Cochran, E. S., Y.-G. Li, P. M. Shearer, S. Barbot, Y. Fialko, and J. E. Vidale, Seismic and geodetic evidence for extensive, long-lived fault damage zones, *Geology*, *37*, 315–318, 2009.

Cochran, E. S., R. J. Skoumal, D. McPhillips, Z. E. Ross, and K. M. Keranen, Activation of optimally and unfavourably oriented faults in a uniform local stress field during the 2011 Prague, Oklahoma, sequence, *Geophysical Journal International*, *222*, 153–168, 2020.

Cruikshank, K. M., G. Zhao, and A. M. Johnson, Analysis of minor fractures associated with joints and faulted joints, *Journal of Structural Geology*, *13*, 865–886, 1991.

Dalguer, L., K. Irikura, and J. Riera, Simulation of tensile crack generation by three-dimensional dynamic shear rupture propagation during an earthquake, *Journal of Geophysical Research: Solid Earth*, *108*, 2003.

Das, S., and K. Aki, A numerical study of two-dimensional spontaneous rupture propagation, *Geophysical Journal International*, *50*, 643–668, 1977.

Day, S. M., L. A. Dalguer, N. Lapusta, and Y. Liu, Comparison of finite differ-

ence and boundary integral solutions to three-dimensional spontaneous rupture, *Journal of Geophysical Research*, *110*, 2005.

Dooley, T., and K. McClay, Analog modeling of pull-apart basins, *AAPG Bulletin*, *81*, 1804–1826, 1997.

Dooley, T., K. McClay, and M. Bonora, 4d evolution of segmented strike-slip fault systems: applications to NW Europe, *Geological Society, London, Petroleum Geology Conference Series*, *5*, 215–225, 1999.

Dooley, T. P., and G. Schreurs, Analogue modelling of intraplate strike-slip tectonics: A review and new experimental results, *Tectonophysics*, *574-575*, 1–71, 2012.

Dunham, E. M., and H. S. Bhat, Attenuation of radiated ground motion and stresses from three-dimensional supershear ruptures, *Journal of Geophysical Research: Solid Earth*, *113*, 2008.

Erickson, B. A., E. M. Dunham, and A. Khosravifar, A finite difference method for off-fault plasticity throughout the earthquake cycle, *Journal of the Mechanics and Physics of Solids*, *109*, 50–77, 2017.

Faugere, E., and J.-P. Brun, Modélisation expérimentale de la distention continentale, *Comptes-rendus des séances de l'Académie des sciences. Série 2, Mécanique-physique, chimie, sciences de l'univers, sciences de la terre*, *299*, 365–370, 1984.

Faulkner, D., A. Lewis, and E. Rutter, On the internal structure and mechanics of large strike-slip fault zones: field observations of the carboneras fault in southeastern spain, *Tectonophysics*, *367*, 235–251, 2003.

Faulkner, D., T. Mitchell, E. Rutter, and J. Cembrano, On the structure and mechanical properties of large strike-slip faults, *Geological Society, London, Special Publications*, *299*, 139–150, 2008.

Favreau, P., M. Campillo, and I. R. Ionescu, Initiation of in-plane shear instability under slip-dependent friction, *Bulletin of the Seismological Society of America*, *89*, 1280–1295, 1999.

Field, E. H., et al., Uniform california earthquake rupture forecast, version 2 (UCERF 2), *Bulletin of the Seismological Society of America*, *99*, 2053–2107, 2009.

Field, E. H., et al., Uniform california earthquake rupture forecast, version 3 (UCERF3)–the time-independent model, *Bulletin of the Seismological Society of America*, *104*, 1122–1180, 2014.

Finzi, Y., and S. Langer, Damage in step-overs may enable large cascading earthquakes, *Geophysical Research Letters*, *39*, 1–5, 2012a.

Finzi, Y., and S. Langer, Predicting rupture arrests, rupture jumps and cascading earthquakes, *Journal of Geophysical Research: Solid Earth*, *117*, 1–11, 2012b.

Fliss, S., H. S. Bhat, R. Dmowska, and J. R. Rice, Fault branching and rupture directivity, *Journal of Geophysical Research*, *110*, 2005.

Gamond, J., Bridge structures as sense of displacement criteria in brittle fault zones, *Journal of Structural Geology*, *9*, 609–620, 1987.

Gao, G., W. Yao, K. Xia, and Z. Li, Investigation of the rate dependence of fracture propagation in rocks using digital image correlation (DIC) method, *Engineering Fracture Mechanics*, *138*, 146–155, 2015.

Gombert, B., Z. Duputel, R. Jolivet, C. Doubre, L. Rivera, and M. Simons, Revisiting the 1992 Landers earthquake: a Bayesian exploration of co-seismic slip and off-fault damage, *Geophysical Journal International*, *212*, 839–852, 2017.

Gomez, Q., and I. R. Ionescu, Micro-mechanical fracture dynamics and damage

modelling in brittle materials, *Philosophical Transactions of the Royal Society A: Mathematical, Physical and Engineering Sciences*, *379*, 20200,125, 2021.

Gomez, Q., O. Ciobanu, and I. R. Ionescu, Numerical modeling of wave propagation in a cracked solid, *Mathematics and Mechanics of Solids*, *24*, 2895–2913, 2019.

Harris, R. A., and S. M. Day, Dynamics of fault interaction: Parallel strike-slip faults, *Journal of Geophysical Research: Solid Earth*, *98*, 4461–4472, 1993.

Harris, R. A., and S. M. Day, Dynamic 3d simulations of earthquakes on en echelon faults, *Geophysical Research Letters*, *26*, 2089–2092, 1999.

Harris, R. A., R. J. Archuleta, and S. M. Day, Fault steps and the dynamic rupture process: 2-d numerical simulations of a spontaneously propagating shear fracture, *Geophysical Research Letters*, *18*, 893–896, 1991.

Hu, F., Z. Zhang, and X. Chen, Investigation of earthquake jump distance for strike-slip step overs based on 3-d dynamic rupture simulations in an elastic half-space, *Journal of Geophysical Research: Solid Earth*, *121*, 994–1006, 2016.

Huang, Y., and J.-P. Ampuero, Pulse-like ruptures induced by low-velocity fault zones, *Journal of Geophysical Research: Solid Earth*, *116*, 2011.

Huang, Y., J.-P. Ampuero, and D. V. Helmberger, Earthquake ruptures modulated by waves in damaged fault zones, *Journal of Geophysical Research: Solid Earth*, *119*, 3133–3154, 2014.

Ida, Y., Cohesive force across the tip of a longitudinal-shear crack and Griffith's specific surface energy, *Journal of Geophysical Research*, *77*, 3796–3805, 1972.

Ionescu, I. R., and M. Campillo, Influence of the shape of the friction law and fault finiteness on the duration of initiation, *Journal of Geophysical Research: Solid Earth*, *104*, 3013–3024, 1999.

Jaeger, C., *Rock Mechanics and Engineering*, Cambridge University Press, 1979.

Jeandet-Ribes, L. J., M. Y. Thomas, and H. S. Bhat, On the importance of 3d stress state in 2d earthquake rupture simulations with off-fault deformation, 2023.

Jolivet, L., P. Huchon, J. P. Brun, X. L. Pichon, N. Chamot-Rooke, and J. C. Thomas, Arc deformation and marginal basin opening: Japan sea as a case study, *Journal of Geophysical Research: Solid Earth*, *96*, 4367–4384, 1991.

Kame, N., J. R. Rice, and R. Dmowska, Effects of prestress state and rupture velocity on dynamic fault branching, *Journal of Geophysical Research: Solid Earth*, *108*, 2003.

Kaneko, Y., and Y. Fialko, Shallow slip deficit due to large strike-slip earthquakes in dynamic rupture simulations with elasto-plastic off-fault response, *Geophysical Journal International*, *186*, 1389–1403, 2011.

Kim, Y.-S., J. R. Andrews, and D. J. Sanderson, Damage zones around strike-slip fault systems and strike-slip fault evolution, Crackington Haven, southwest England, *Geosciences Journal*, *4*, 53–72, 2000.

Kim, Y.-S., D. Peacock, and D. J. Sanderson, Mesoscale strike-slip faults and damage zones at Marsalforn, Gozo Island, Malta, *Journal of Structural Geology*, *25*, 793–812, 2003.

Kim, Y.-S., D. C. Peacock, and D. J. Sanderson, Fault damage zones, *Journal of Structural Geology*, *26*, 503–517, 2004.

Klinger, Y., High-resolution satellite imagery mapping of the surface rupture and slip distribution of the Mw 7.8, 14 november 2001 Kokoxili earthquake, Kunlun fault, northern Tibet, China, *Bulletin of the Seismological Society of America*, *95*, 1970–1987, 2005.

Klinger, Y., Relation between continental strike-slip earthquake segmentation and thickness of the crust, *Journal of Geophysical Research*, *115*, 2010.

Klinger, Y., C. Ji, Z.-K. Shen, and W. H. Bakun, Introduction to the special issue on the 2008 Wenchuan, China, earthquake, *Bulletin of the Seismological Society of America*, *100*, 2353–2356, 2010.

Klinger, Y., J.-H. Choi, and A. Vallage, Fault branching and long-term earthquake rupture scenario for strike-slip earthquakes, in *Fault Zone Dynamic Processes*, pp. 217–228, John Wiley & Sons, Inc., 2017.

Langer, S., Y. Finzi, and L. M. Olsen-Kettle, Dynamic triggering of earthquakes is promoted by crustal heterogeneities and bimaterial faults, *Physics of the Earth and Planetary Interiors*, *238*, 34–41, 2015.

Lecomte, E., L. Jolivet, O. Lacombe, Y. Denèle, L. Labrousse, and L. L. Pourhiet, Geometry and kinematics of Mykonos detachment, Cyclades, Greece: Evidence for slip at shallow dip, *Tectonics*, *29*, 2010.

Lefevre, M., Y. Klinger, M. Al-Qaryouti, M. L. Béon, and K. Moumani, Slip deficit and temporal clustering along the dead sea fault from paleoseismological investigations, *Scientific Reports*, *8*, 2018.

Lettis, W., Influence of releasing step-overs on surface fault rupture and fault segmentation: Examples from the 17 august 1999 Izmit earthquake on the North Anatolian fault, Turkey, *Bulletin of the Seismological Society of America*, *92*, 19–42, 2002.

Li, H., L. Zhu, and H. Yang, High-resolution structures of the Landers fault zone inferred from aftershock waveform data, *Geophysical Journal International*, *171*, 1295–1307, 2007.

Li, Y.-G., K. Aki, J. E. Vidale, W. H. K. Lee, and C. J. Marone, Fine structure of the Landers fault zone: Segmentation and the rupture process, *Science*, *265*, 367–370, 1994.

Liu, J., L. Zhang, and Y. Du, Seismic hazard assessment of the mid-northern segment of Xiaojiang fault zone in southwestern China using scenario earthquakes, *Bulletin of the Seismological Society of America*, *110*, 1191–1210, 2020.

Liu, Z., and B. Duan, Dynamics of parallel strike-slip faults with pore fluid pressure change and off-fault damage, *Bulletin of the Seismological Society of America*, *104*, 780–792, 2014.

Lyakhovsky, V., Y. Ben-Zion, and A. Agnon, Distributed damage, faulting, and friction, *Journal of Geophysical Research: Solid Earth*, *102*, 27,635–27,649, 1997a.

Lyakhovsky, V., Z. Reches, R. Weinberger, and T. E. Scott, Non-linear elastic behaviour of damaged rocks, *Geophysical Journal International*, *130*, 157–166, 1997b.

Madariaga, R., Dynamics of an expanding circular fault, *Bulletin of the Seismological Society of America*, *66*, 639–666, 1976.

Madariaga, R., High-frequency radiation from crack (stress drop) models of earthquake faulting, *Geophysical Journal International*, *51*, 625–651, 1977.

Mann, P., Global catalogue, classification and tectonic origins of restraining- and releasing bends on active and ancient strike-slip fault systems, *Geological Society, London, Special Publications*, *290*, 13–142, 2007.

Mann, P., M. R. Hempton, D. C. Bradley, and K. Burke, Development of pull-apart basins, *The Journal of Geology*, *91*, 529–554, 1983.

McClay, K., and M. Bonora, Analog models of restraining stepovers in strike-slip fault systems, *AAPG Bulletin*, *85*, 233–260, 2001.

McClay, K. R., Deformation mechanics in analogue models of extensional fault systems, *Geological Society, London, Special Publications*, *54*, 445–453, 1990.

Mignan, A., L. Danciu, and D. Giardini, Reassessment of the maximum fault rupture length of strike-slip earthquakes and inference on Mmax in the Anatolian Peninsula, Turkey, *Seismological Research Letters*, *86*, 890–900, 2015.

Mitchell, T., and D. Faulkner, The nature and origin of off-fault damage surrounding strike-slip fault zones with a wide range of displacements: A field study from the Atacama fault system, northern Chile, *Journal of Structural Geology*, *31*, 802–816, 2009.

Mitchell, T., and D. Faulkner, Towards quantifying the matrix permeability of fault damage zones in low porosity rocks, *Earth and Planetary Science Letters*, *339-340*, 24–31, 2012.

Moore, D., and D. Lockner, The role of microcracking in shear-fracture propagation in granite, *Journal of Structural Geology*, *17*, 95–114, 1995.

Mori, H., S. Wallis, K. Fujimoto, and N. Shigematsu, Recognition of shear heating on a long-lived major fault using raman carbonaceous material thermometry: Implications for strength and displacement history of the MTL, SW Japan, *Island Arc*, *24*, 425–446, 2015.

Okubo, K., H. S. Bhat, E. Rougier, S. Marty, A. Schubnel, Z. Lei, E. E. Knight, and Y. Klinger, Dynamics, radiation, and overall energy budget of earthquake rupture with coseismic off-fault damage, *Journal of Geophysical Research: Solid Earth*, *124*, 11,771–11,801, 2019a.

Okubo, K., H. S. Bhat, E. Rougier, S. Marty, A. Schubnel, Z. Lei, E. E. Knight, and Y. Klinger, Dynamics, radiation, and overall energy budget of earthquake rupture with coseismic off-fault damage, *Journal of Geophysical Research: Solid Earth*, *124*, 11,771–11,801, 2019b.

Ostermeijer, G. A., T. M. Mitchell, F. M. Aben, M. T. Dorsey, J. Browning, T. K. Rockwell, J. M. Fletcher, and F. Ostermeijer, Damage zone heterogeneity on seismogenic faults in crystalline rock; a field study of the Borrego fault, Baja California, *Journal of Structural Geology*, *137*, 104,016, 2020.

Palmer, A. C., and J. R. Rice, The growth of slip surfaces in the progressive failure of over-consolidated clay, *Proceedings of the Royal Society of London. A. Mathematical and Physical Sciences*, *332*, 527–548, 1973.

Peacock, D., and D. Sanderson, Strike-slip relay ramps, *Journal of Structural Geology*, *17*, 1351–1360, 1995a.

Peacock, D., and D. Sanderson, Pull-aparts, shear fractures and pressure solution, *Tectonophysics*, *241*, 1–13, 1995b.

Peng, Z., Y. Ben-Zion, A. J. Michael, and L. Zhu, Quantitative analysis of seismic fault zone waves in the rupture zone of the 1992 Landers, California, earthquake: Evidence for a shallow trapping structure, *Geophysical Journal International*, *155*, 1021–1041, 2003.

Perrin, C., I. Manighetti, J.-P. Ampuero, F. Cappa, and Y. Gaudemer, Location of largest earthquake slip and fast rupture controlled by along-strike change in fault structural maturity due to fault growth, *Journal of Geophysical Research: Solid Earth*, *121*, 3666–3685, 2016.

Petit, J.-P., and M. M, Palaeostress superimposition deduced from mesoscale structures in limestone: The Matelles exposure, Languedoc, France, *Journal of Structural Geology*, *17*, 245–256, 1995.

Poliakov, A. N. B., R. Dmowska, and J. R. Rice, Dynamic shear rupture interactions with fault bends and off-axis secondary faulting, *Journal of Geophysical Research: Solid Earth*, *107*, 6–18, 2002.

Reches, Z., and D. A. Lockner, Nucleation and growth of faults in brittle rocks, *Journal of Geophysical Research: Solid Earth*, *99*, 18,159–18,173, 1994.

Rempe, M., T. Mitchell, J. Renner, S. Nippress, Y. Ben-Zion, and T. Rockwell, Damage and seismic velocity structure of pulverized rocks near the San Andreas Fault, *Journal of Geophysical Research: Solid Earth*, *118*, 2813–2831, 2013.

Rice, J. R., Mathematical analysis in the mechanics of fracture, *Fracture: an advanced treatise*, *2*, 191–311, 1968.

Rice, J. R., C. G. Sammis, and R. Parsons, Off-fault secondary failure induced by a dynamic slip pulse, *Bulletin of the Seismological Society of America*, *95*, 109–134, 2005.

Rispoli, R., Stress fields about strike-slip faults inferred from stylolites and tension gashes, *Tectonophysics*, *75*, T29–T36, 1981.

Sammis, C. G., A. J. Rosakis, and H. S. Bhat, Effects of off-fault damage on earthquake rupture propagation: Experimental studies, *Pure and Applied Geophysics*, *166*, 1629–1648, 2009.

Savage, J. C., The stopping phase on seismograms, *Bulletin of the Seismological Society of America*, *55*, 47–58, 1965.

Savage, J. C., Radiation from a realistic model of faulting, *Bulletin of the Seismological Society of America*, *56*, 577–592, 1966.

Scholz, C., and A. Gupta, Fault interactions and seismic hazard, *Journal of Geodynamics*, *29*, 459–467, 2000.

Schulz, S. E., and J. P. Evans, Mesoscopic structure of the punchbowl fault, southern california and the geologic and geophysical structure of active strike-slip faults, *Journal of Structural Geology*, *22*, 913–930, 2000.

Segall, P., and D. D. Pollard, Mechanics of discontinuous faults, *Journal of Geophysical Research: Solid Earth*, *85*, 4337–4350, 1980.

Sibson, R. H., Stopping of earthquake ruptures at dilational fault jogs, *Nature*, *316*, 248–251, 1985.

Sibson, R. H., Rupture interaction with fault jogs, in *Earthquake Source Mechanics*, pp. 157–167, American Geophysical Union, 1986.

Skoumal, R. J., J. O. Kaven, and J. I. Walter, Characterizing seismogenic fault structures in Oklahoma using a relocated template-matched catalog, *Seismological Research Letters*, 2019.

Summers, R., and J. Byerlee, A note on the effect of fault gouge composition on the stability of frictional sliding, *International Journal of Rock Mechanics and Mining Sciences & Geomechanics Abstracts*, *14*, 155–160, 1977.

Suzuki, T., Understanding of dynamic earthquake slip behavior using damage as a tensor variable: Microcrack distribution, orientation, and mode and secondary faulting, *Journal of Geophysical Research: Solid Earth*, *117*, 1–20, 2012.

Tchalenko, J. S., and N. N. Ambraseys, Structural analysis of the Dasht-e Bayaz (Iran) earthquake fractures, *Geological Society of America Bulletin*, *81*, 41, 1970.

Templeton, E. L., and J. R. Rice, Off-fault plasticity and earthquake rupture dynamics: 1. dry materials or neglect of fluid pressure changes, *Journal of Geophysical Research*, *113*, 2008.

Thomas, M. Y., and H. S. Bhat, Dynamic evolution of off-fault medium during an earthquake: A micromechanics based model, *Geophysical Journal International*, *214*, 1267–1280, 2018.

Thomas, M. Y., H. S. Bhat, and Y. Klinger, Effect of brittle off-fault damage on earthquake rupture dynamics, in *Fault Zone Dynamic Processes: Evolution of*

Fault Properties During Seismic Rupture, pp. 255–280, John Wiley & Sons, Inc., 2017.

Uenishi, K., and J. R. Rice, Universal nucleation length for slip-weakening rupture instability under nonuniform fault loading, *Journal of Geophysical Research: Solid Earth*, *108*, 2003.

Vallage, A., Y. Klinger, R. Grandin, H. Bhat, and M. Pierrot-Deseilligny, Inelastic surface deformation during the 2013 Mw 7.7 Balochistan, Pakistan, earthquake, *Geology*, pp. 1079—1082, 2015.

Vendeville, B., P. R. Cobbold, P. Davy, P. Choukroune, and J. P. Brun, Physical models of extensional tectonics at various scales, *Geological Society, London, Special Publications*, *28*, 95–107, 1987.

Visage, S., P. Souloumiac, N. Cubas, B. Maillot, S. Antoine, A. Delorme, and Y. Klinger, Evolution of off-fault deformation of strike-slip fault in a sand-box experiment, *SSRN Electronic Journal*, 2022.

Wakabayashi, J., Stepovers that migrate with respect to affected deposits: Field characteristics and speculation on some details of their evolution, *Geological Society, London, Special Publications*, *290*, 169–188, 2007.

Wakabayashi, J., J. V. Hengesh, and T. L. Sawyer, Four-dimensional transform fault processes: Progressive evolution of step-overs and bends, *Tectonophysics*, *392*, 279–301, 2004.

Wang, H., M. Liu, B. Duan, and J. Cao, Rupture propagation along stepovers of strike-slip faults: Effects of initial stress and fault geometry, *Bulletin of the Seismological Society of America*, *110*, 1011–1024, 2020.

Wang, L., S. Hainzl, M. S. Özeren, and Y. Ben-Zion, Postseismic deformation in-

duced by brittle rock damage of aftershocks, *Journal of Geophysical Research*, *115*, 2010.

Wesnousky, S. G., Seismological and structural evolution of strike-slip faults, *Nature*, *335*, 340–343, 1988.

Wesnousky, S. G., Predicting the endpoints of earthquake ruptures, *Nature*, *444*, 358–360, 2006.

Wesnousky, S. G., Displacement and geometrical characteristics of earthquake surface ruptures: Issues and implications for seismic-hazard analysis and the process of earthquake rupture, *Bulletin of the Seismological Society of America*, *98*, 1609–1632, 2008.

Wibberley, C. A., and T. Shimamoto, Internal structure and permeability of major strike-slip fault zones: The Median Tectonic Line in Mie Prefecture, southwest Japan, *Journal of Structural Geology*, *25*, 59–78, 2003.

Wibberley, C. A. J., G. Yielding, and G. D. Toro, Recent advances in the understanding of fault zone internal structure: A review, *Geological Society, London, Special Publications*, *299*, 5–33, 2008.

Wilson, J., J. Chester, and F. Chester, Microfracture analysis of fault growth and wear processes, Punchbowl Fault, San Andreas system, California, *Journal of Structural Geology*, *25*, 1855–1873, 2003.

Wu, J. E., K. McClay, P. Whitehouse, and T. Dooley, 4d analogue modelling of transtensional pull-apart basins, *Marine and Petroleum Geology*, *26*, 1608–1623, 2009.

Xu, J., H. Zhang, and X. Chen, Rupture phase diagrams for a planar fault in 3-d full-space and half-space, *Geophysical Journal International*, *202*, 2194–2206, 2015.

Xu, X., W. Chen, W. Ma, G. Yu, and G. Chen, Surface rupture of the Kunlunshan earthquake (Ms 8.1), northern Tibetan Plateau, China, *Seismological Research Letters*, *73*, 884–892, 2002.

Yamashita, F., E. Fukuyama, and K. Omura, Estimation of fault strength: Reconstruction of stress before the 1995 Kobe earthquake, *Science*, *306*, 261–263, 2004.

Yamashita, T., Generation of microcracks by dynamic shear rupture and its effects on rupture growth and elastic wave radiation, *Geophysical Journal International*, *143*, 395–406, 2000.

Yang, H., Recent advances in imaging crustal fault zones: A review, *Earthquake Science*, *28*, 151–162, 2015.

Zehnder, A. T., *Fracture Mechanics*, Springer Netherlands, 2012.

Zhang, Q., and J. Zhao, Effect of loading rate on fracture toughness and failure micromechanisms in marble, *Engineering Fracture Mechanics*, *102*, 288–309, 2013.